La croissance plasma de nanofils de silicium catalysée par l'étain et l'indium et applications dans les cellules solaires à jonctions radiales.

Benedict O'Donnell

Benedict O'Donnell

PLASMA GROWN SILICON NANOWIRES CATALYZED BY POST-TRANSITION METALS & APPLICATIONS IN RADIAL JUNCTION SOLAR CELLS

Doctoral Thesis in Materials Science

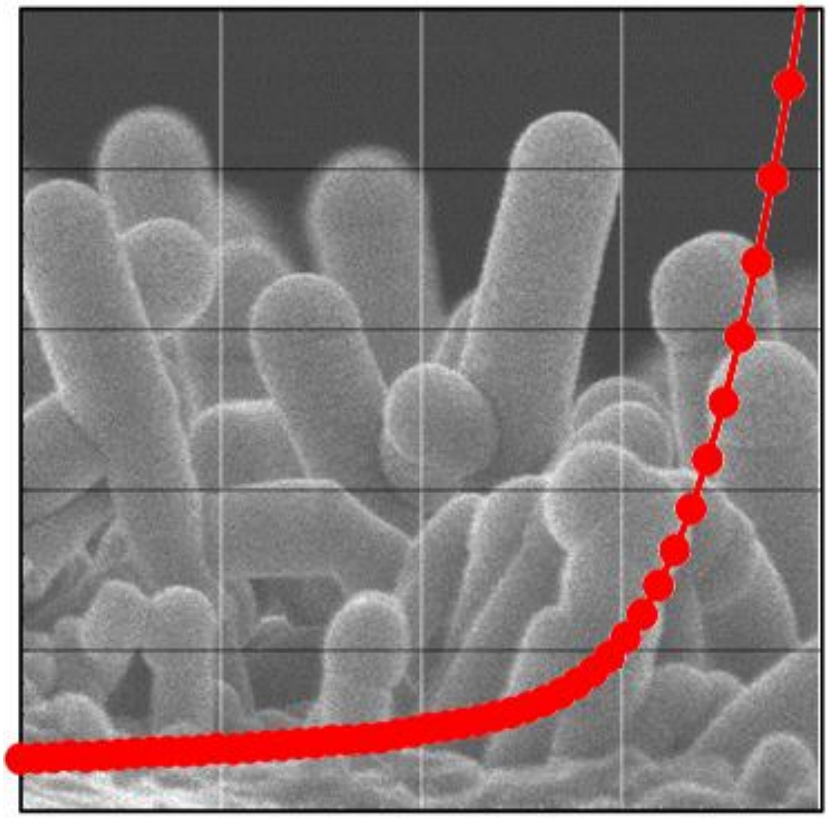

École Polytechnique

Thèse

présentée en vue d'obtenir le grade de

Docteur de l'École Polytechnique

Spécialité « Science des Matériaux »

par

BENEDICT O'DONNELL

benedict.odonnell@polytechnique.edu

PLASMA GROWN SILICON NANOWIRES CATALYZED BY POST-TRANSITION METALS & APPLICATIONS IN RADIAL JUNCTION SOLAR CELLS

Thèse à soutenir le 3 décembre 2012 devant le jury composé de:

DR.	SILKE CHRISTIANSEN	RAPPORTEUR
DR.	JEAN-CHRISTOPHE HARMAND	RAPPORTEUR
DR.	ANTONÍN FEJFAR	EXAMINATEUR
PROF	ANNA FONTCUBERTA I MORRAL	EXAMINATRICE
PROF.	THIERRY GACOIN	EXAMINATEUR
DR.	VOLKER SCHMIDT	EXAMINATEUR
DR.	MARC VERMEERSCH	EXAMINATEUR
PROF.	PERE ROCA I CABARROCAS	DIRECTEUR DE THESE

A Carmen Gonzalez Martinez & Pere Roca i Cabarrocas,

por darme ollos i ensenyar-me a veure.

Contents

List of Tables

List of Figures

List of Acronyms

		Units
a-Si:H	Hydrogenated amorphous silicon	
c-Si	Crystalline Silicon	
CVD	Chemical Vapor Deposition	
FF	Fill factor	%
ITO	Indium-Tin-Oxide	
J_{SC}	Short-circuit current density	$mA.cm^{-2}$
PA-VLS	Plasma Assisted Vapor-Liquid-Solid	
PECVD	Plasma Enhanced Chemical Vapor Deposition	
PV	Photovoltaic	
R_S	Series resistance	$\Omega.cm^2$
R_{SH}	Shunt resistance	$\Omega.cm^2$
sccm	Standard Cubic Centimeters per Minute	
SEM	Scanning Electron Microscopy	
SiNW	Silicon Nanowire	
UHV	Ultra-Hugh Vacuum (pressures < 10^{-6} mbar)	
VLS	Vapor-Liquid-Solid	
V_{OC}	Open circuit voltage	mV
µc-Si:H	Hydrogenated microcrystalline silicon	

1. Introduction

"We are all in the gutter, but some of us are looking at the stars."

The frenetic activity of mankind is fed predominantly by fuels which are finite, located in politically sensitive areas and emit gases that destabilize the Earth climate. As the human species grows more numerous and wealthier, consumption of these risk-prone resources is set to accelerate. In this chapter, we explore the potential of photovoltaic solar energy conversion to meet future demands sustainably. The history of the technology is outlined to highlight the developments which have permitted its recent expansion. The most common industrial practices involved in their fabrication process are also described, in order to draw attention to some of the difficulties in lowering their cost and identifying how radial junction solar cells can contribute to the widespread adoption of photovoltaics.

Quote from Lady Windermere's Fan, Oscar Wilde, 1892.

1. Sustainable economics

When averaged over 2010, human activity consumed energy resources at the staggering rate of 16 TW.[1] There are few forces in nature which compare to this figure. It surpassed the annual power output of lightning bolts (0.01 TW),[2, 3] earthquakes (0.4 TW),[4] waves (3 TW)[5] and tides (3.7 TW).[6] Considering that the payload of the 1945 Fatman nuclear bomb unleashed 10^{14} J,[7] its scale may be glimpsed by considering that, each day, mankind employs enough energy to destroy every city of over 500 000 inhabitants it has ever built.[8] Although daunting, this ravenous appetite for energy reflects highly desirable increases in food production, housing construction, travel, living standards... The grave threat shackled to our current energy consumption does not lie in its scale, but in its source.

1.1. Volatile fuels

Since the industrial revolution, human development has been powered predominantly by burning fossil fuels. These fuels are the remains of living organisms buried over millions of years in the planet crust. While alive, they stored energy from the Sun in chemical bonds which have gradually decayed into forms which include coal, natural gas and oil. These fuels present several advantages over living vegetation. Their energy density is generally higher, making it possible to store more Joules in a lighter load.[9] Their production occupies little agricultural land. Their liquid or gaseous form can make them easier to handle. And they are substantially cheaper to "produce" than any crop.[10] These advantages have historically outweighed some of their less flattering attributes. Reserves of fossil fuels are locally concentrated, leading to political tension between exporter and consumer countries (characteristically between the West and the Middle East or Eastern Europe and Russia) or over territorial ownership (as in the case of Darfur or the South China Sea).[11] Their extraction and combustion lead to health hazards,[12] acid rains,[13] ground contamination,[14] water contamination[15] and are beginning to disrupt the world climate.[16] In addition to these concerns, there is also the unsettling threat of their depletion.

Box 1: Fossil fuels and greenhouse gases.

The combustion of fossil fuels releases greenhouse gases (notably CO_2, CH_4 and N_2O) which build up in the atmosphere and raise the average temperature of the planet by reflecting heat leaving its surface. Since the industrial revolution, the atmospheric concentration of these gases has soar to values unprecedented in over half a billion years.[17, 18] Global temperatures have risen by 0.5 °C and are expected to increase by several degrees Celsius within the next five decades.[19] These figures verge on the difference between current temperatures and those of the last ice age.[20] Such rapid changes to the Earth climate threaten its biosphere with massive extinction.[21, 22] They are already affecting weather patterns and drying agricultural land in regions prone to food shortages.[23] They are intensifying extreme meteorological events such as tornadoes and they are causing mountain glaciers[19] and ice sheets to melt, raising flood risks across entire countries.[23] The complexity of the climate system leaves many disturbing questions unanswered. However the effects mentioned are

all set to worsen as more fossil fuels are burnt and the concentration of greenhouse gases increases in the atmosphere.

1.2. Unknown reserves

The amount of oil, gas and coal which remains to be recovered from the ground is unknown. The International Energy Agency estimates that, at current consumption rates, proven reserves (fuel deposits with a 90% chance of being profitably extracted, depending on future prices and technology) can supply the world with oil for the coming 40 years, gas for 60 years and coal for 200 years.[24] Optimistic estimates with regards to progress in exploration, extraction techniques and energy prices could possibly boost these figures by a factor of 3 for oil, 4 for gas[24] and 20 for coal.[25] However, current consumption rates are far from static. The world population is growing fast and two thirds of it resides in rapidly developing economies in which patterns of energy consumption are booming from Third World to Western standards. Over the past three decades, oil, coal and natural gas consumption rates have increased by 30%, 90% and 100% respectively and energy demand will continue to increase in the decades to come.[24]

There are also considerable uncertainties regarding calculations of recoverable reserves. Although coal is plentiful, only a fraction of it has the energy content expected from the variants used today. There is little evidence as to how much of the rest will ever be energetically favorable to mine, and official sources have recently downgraded their estimates of useable reserves by as much as 90%.[26, 27] Several disconcerting observations imply that global oil production may already have reached a tipping point. Despite massive investment in exploration, the size and number of newly discovered oil fields has dwindled over the past decades.[24, 28] Stubbornly high energy prices since the turn of the millennium suggest that incremental advances (e.g. offshore drilling or hydraulic fracturing) are hard pressed to follow even current demand trends.[29-31] Recent industry figures also indicate that the imbalance in the market is growing, with increases in global oil production lagging behind increases in consumption in 7 of the past 10 years.[1]

As the supply of fossil fuels contracts, their prices will rise, bringing fuels from previously unprofitable sources to the market. However, these substitutes will not prevent recession in sectors relying on cheap fuel. Such a shift from increasing to decreasing energy supplies is unprecedented in human history and bodes ill for economies which function on the prospect of sustained growth.[32]

1.3. The solar resource

The words of Oscar Wilde retain wisdom through the ages. How perverse to scavenge for toxic fossils in the bowels of the lithosphere, when the answer to the problem shines right above our heads. The Earth orbits a nuclear reactor which continuously radiates 90’000 TW of clean and ubiquitous power to its surface.[33] This input raises storms, runs rivers and breathes life into an otherwise desolate rock. It dwarfs the already-colossal rate of human energy consumption thousands of times over. In fact each year the land and oceans absorb close to 3000 ZJ from the Sun. This is dozens of times larger than the proven reserves of all fossil fuels combined, and even several times their total resource base (Figure 1.1). This vast amount of energy is not cheap; it is free. However the machines that convert it

into the kind of energy we can use are currently expensive. One of the greatest challenges of our time is to find an economical way of harnessing it.

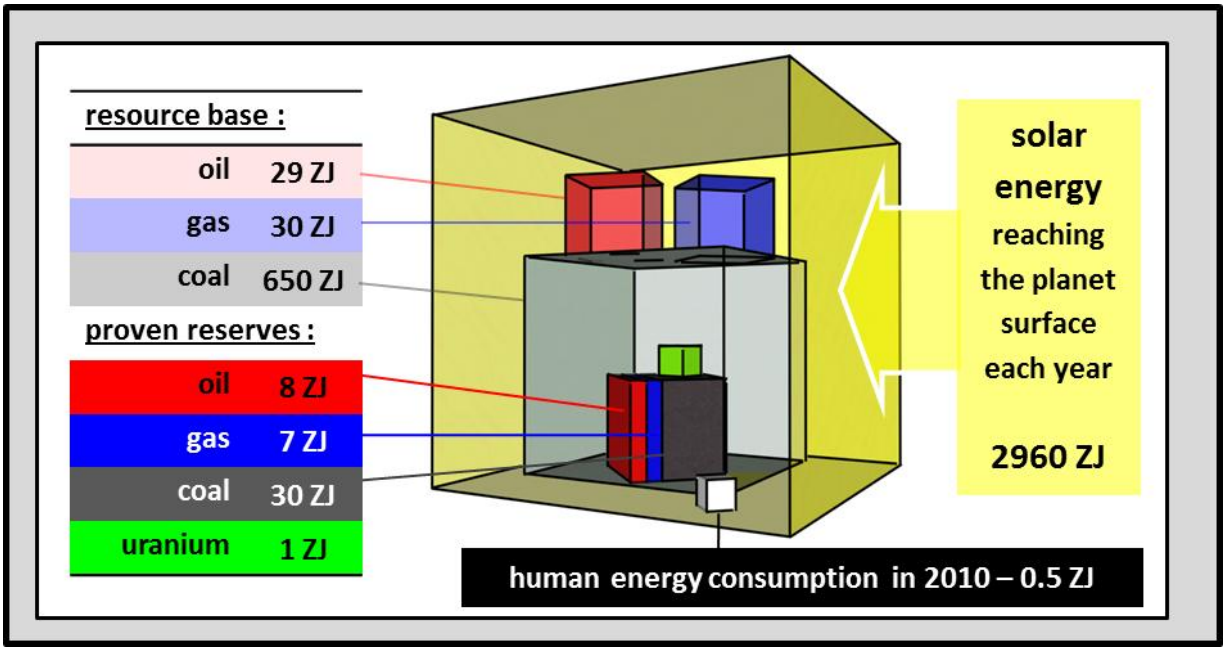

1.1 - Global energy resources.
Geometric representation comparing the scale of remaining energy resources.[24, 25, 33, 34] The resource base includes all deposits geologically expected (but not necessarily discovered) and proven reserves are known deposits with a 90% chance of being profitably extracted. (1 zetajoule (ZJ) = 10^{21} J)

2. The physics of photovoltaic energy conversion

One way of tapping into the vast resource of solar energy is to convert it into electricity using photovoltaic cells. To understand the conversion process, let us define the nature of the energy we are harnessing, and what it is that we want to transform it into. Electricity manifests the redistribution of electrons as they minimize their potential energy. Photons, the elementary particles which compose light, can easily be converted into the potential energy of electrons by exposing them to an opaque material. When they interact, the electrons in the material can absorb the photons which excite them to higher energy states. However, the energy is generally lost within picoseconds to heat in the material. This process is illustrated in Figure 1.2.a, in which the electron cascades back to a state with lower potential energy by conferring the energy gained from the photon to phonons (i.e. vibrations in the atomic lattice). A photovoltaic cell must fulfill two essential conditions to convert the potential energy of its electrons into electricity. The first is to trap the electrons in states which will not decay for as long as it takes to harness their energy. The second is to transform this energy into a form which can be used.

Both these conditions can be met quite elegantly using semiconductors. Semiconductors are a category of materials which conduct electricity only when stimulated to do so (e.g. Si, Ge, GaAs,…). Their main characteristic is that the distribution of energy levels occupied by their electrons is interrupted by what is commonly referred to as a bandgap. At equilibrium, the highest energy state occupied in a semiconductor is at the top of its valence band (and is occupied by the electrons which

Box 2: Alternatives

Our comparison has so far neglected the potential of other energy sources to contribute to the global energy mix. The following is a brief overview of the relative merits of biomass, nuclear, wind, geothermal, wave and tidal energy. The interested reader is referred to MacKay[35] or Tester et al.[5] for further information.

Biomass (in the form of wood, sugar cane, agricultural waste…) remains the fourth most widespread fuel used on Earth. In 2010, it provided 0.05 ZJ of potentially carbon neutral energy. In principle, biomass is free from the environmental and depletion constraints of fossil fuels and work is going into increasing its yield and profitability.[36] In practice, large-scale adoption entails a risk of competing with food production for agricultural land (another commodity in short supply).

Nuclear fission is currently the most established and profitable alternative. However in its current form, it is also plagued with concerns regarding uranium fuel supplies.[37, 38] Given adequate funding for development, breeder reactors could foreseeably overcome this obstacle. However, the technology would still suffer from issues of nuclear safety, proliferation and waste which, with each passing generation, seem less likely to be solved.[39] Nuclear fusion is a commendable pursuit. But it remains too far removed in the future to deal with any imminent risks of fossil fuels.[40]

The share of wind energy has increased rapidly over the past two decades and grew to account for 0.2 TW of global power capacity in 2010.[41] In certain regions, its price has even converged with that of nuclear and coal generated electricity.[42, 43] There remains considerable uncertainty on the amount of power which could ultimately be recovered from the wind; however several academic estimates have placed the upper limit at dozens of terawatts.[44, 45]

Geothermal energy generation consists of extracting heat in the ground which originates predominantly from radioactive decay in the Earth crust. It is extracted by injecting water down boreholes and collecting heat or steam. Depending on the depth at which one drills, 10 – 50 mW/m² can be harnessed virtually anywhere on the planet. At tectonic fault lines (notably in Iceland, the Philippines…) geothermal energy is already a profitable business which contributed 0.01 TW to the global energy mix in 2010.[46] However if used sustainably on a large scale, it would be hard pressed to contribute more than 2.6 TW to the global power output.[35]

Energy from the motion of water flows has been harnessed for millennia. Hydroelectric dams currently contribute 0.4 TW to the global energy mix,[24] a handful of tidal dams add another 0.05 TW and the first prototypes for wave energy systems are being tested. However, the technical potential for hydropower is estimated at 1.9 TW [47] and the power driving global marine flows represents 6.7 TW,[5, 6] (of which only a fraction can possibly be harnessed). While substantial, the scale of hydrological resources is insufficient to cater for global energy demand.

bind the material together). Because there are no energy levels directly above the valence band, photons with less energy than the bandgap cannot be absorbed by electrons in the material. Instead they shine through it as is demonstrated by glass and water which appear transparent because their bandgap exceeds the energy of visible light. In contrast, photons with energy greater than the bandgap can excite valence band electrons to a second continuum of energy states above the bandgap. Because electrons in these higher energy states can conduct electricity, the continuum of states is referred to as the conduction band. The energy barrier provided by the bandgap is of particular interest in photovoltaics because, to a limited extent, it works both ways. When excited electrons reach the lowest energy state in the conduction band, the bandgap makes low-energy phonon decay impossible (Figure 1.2.b) and the electrons remain excited until they release the energy in the form of a photon. In an indirect bandgap semiconductor such as silicon, this can take up to milliseconds. The timescale is long enough to carry the charges across the semiconductor to external contacts where the energy that they have gained from photons can be harvested.

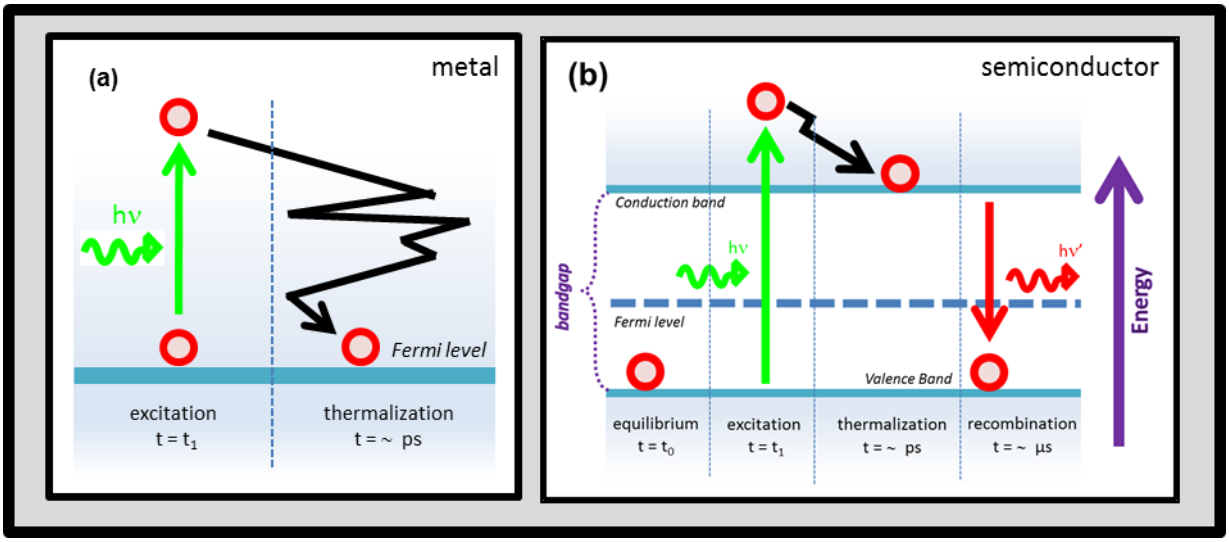

1.2 - The energetic decay of excited electrons.
Schematic representation of electronic de-excitation in metals (a) and semiconductors (b).

The second condition can be met by using a PN junction to convert the excited electrons into a source of voltage. A PN junction is a semiconductor in which one extremity has been doped p-type and the other n-type. Doping is a process whereby atoms with a different number of valence electrons are incorporated into the semiconductor matrix. For instance, silicon can be doped n-type by adding phosphorous atoms to it. Because phosphorous has a valence of 5, one electron in each phosphorous atom will be unable to bond in the tetravalent Si crystal and will be free to diffuse through the semiconductor. Phosphorous is therefore known as an electron *donor* in silicon. If instead the dopant is boron, which has a valence of 3, an electron vacancy will be created in the silicon matrix (which can be represented as a positively charged quasiparticle known as a hole). Hence, boron is an electron *acceptor* in Si. Electrons and holes will diffuse across the interface between the p and n-type regions and recombine, depleting the region surrounding their interface of free charges. In doing so, the ions in the depletion region will remain locked in the crystal matrix, establishing an electric field across the depletion region. When valence electrons are excited by rays

of sunlight to the conduction band, they are subject to the field and drift towards the n-type region of the PN junction. Likewise, the holes they leave in the valence band drift towards the p-type region. Charges will continue to accumulate in this way until the electric field which they generate compensates the built-in field of the PN junction. The accumulation of charges can be used as a voltage source. By connecting the two extremities of the cell, electrons accumulated in the n-type region can circulate to the p-type region through an external circuit in the form of an electric current.

It is useful to describe this process in terms of the band diagram of the device. The tendency of a semiconductor to incorporate or surrender electrons is expressed by the energy separating its conduction band from its Fermi level. When bringing p- and n-type doped semiconductors together, electrons flow from the n-doped region to the p-doped region (and vice-versa for holes) until the density of charge carriers reaches thermodynamic equilibrium. This aligns the Fermi levels between the two materials and establishes a gradient in the energy of the conduction and valence bands across the depletion region (Figure 1.3), preventing further electron diffusion from n-type to the p-type material. It is this gradient in the energy of the band states which causes the photovoltaic effect.

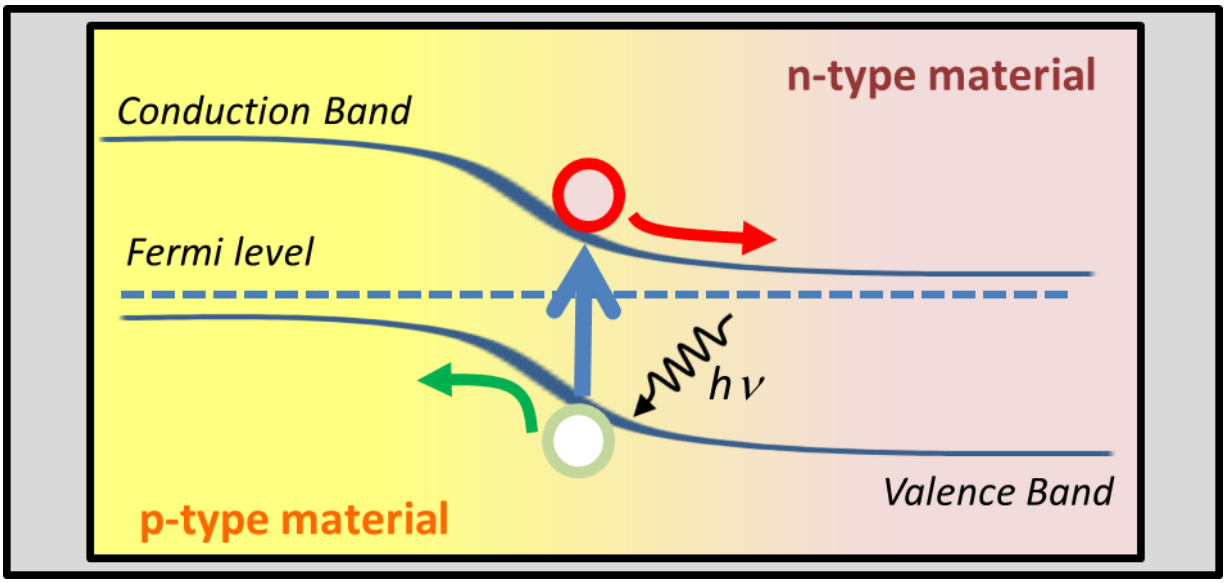

1.3 - Schematic representation of the band diagram within the PN junction.

When a photo-excited electron diffuses within the space charge region, it minimizes its potential energy by drifting to the n-type region (and vice-versa for holes). As more charges are excited and accumulate in either region of the cell, they bend the conduction and valence bands against the initial gradient of the PN junction. The accumulation of charges saturates when the bands are realigned to the extent that there is no longer an energetic gain for newly photo-excited electrons and holes to drift to separate extremities of the cell.

2.1. The equivalent circuit representation of the photovoltaic cell

There is a subtlety involved in extracting the energy from photogenerated electrons efficiently. To grasp this point, it is useful to represent the solar cell as a series of basic electronic components as

illustrated in Figure 1.4.a. The charges built up at the extremities of the cell can produce a current in an external circuit. This aspect of the PV cell is therefore modeled as a current source in the equivalent circuit. Resistive losses can be expected within the cell (arising from charge transport within materials and at the interfaces between different layers). These losses are summed up as a resistor placed in series with the current source. The PN junction also drives electrons towards the n-type layer, but prevents them from approaching the p-type layer. A diode placed in parallel with the external circuit represents this asymmetric behavior with respect to the direction of current flow. Last, the PN junction is not a perfect diode and charges can leak through it. There is therefore another path through which electrons can reach the p-layer, which is referred as the shunt path. It is represented by a resistor, also in parallel to the external circuit. Its resistance represents the quality of the junction (the higher the resistance, the fewer charges leak through the PN junction).

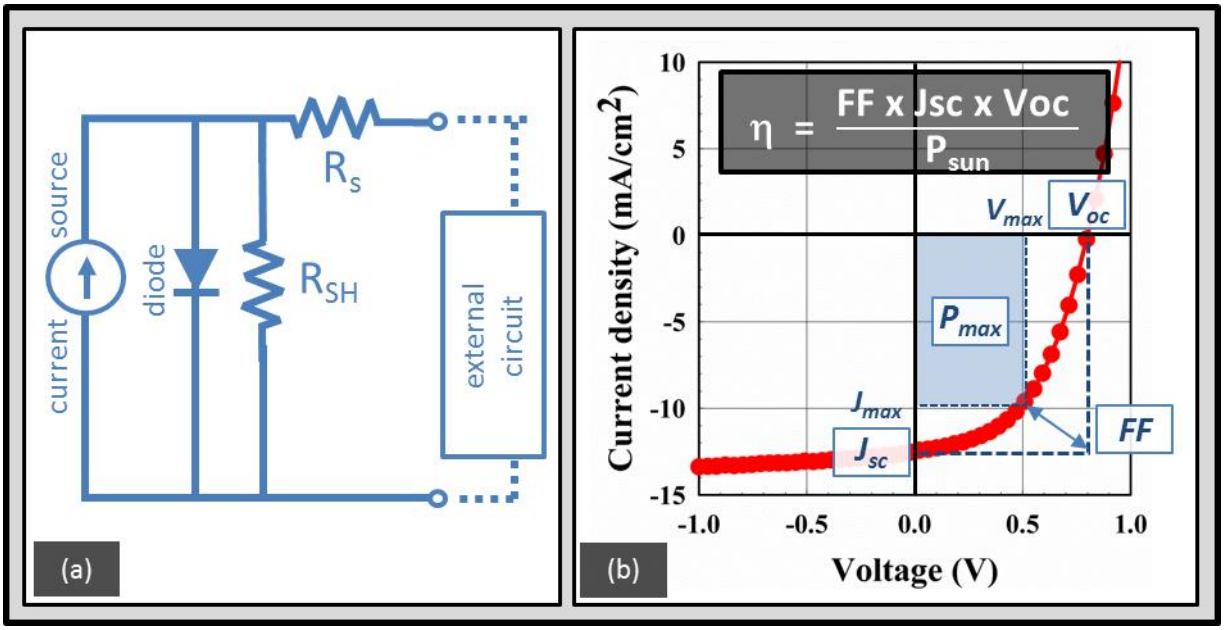

1.4 - The electronics of a solar cell.
Equivalent electric circuit (a) and *J(V)* characteristics of a photovoltaic cell (b).

As a general rule, the power output of a current source with a fixed voltage is maximized when connected to a lighter load. However, for very small resistances in the external electric circuit, resistive losses (R_S) within the material and contacts of the cell will account for a larger share of the voltage drop and reduce the external power output. For large loads, as the voltage drop across the external circuit reaches values close to the break-down voltage of the diode, current leaks through the parallel loop rather than the external circuit in Figure 1.4.a. The optimum is a compromise between a load not too light to be overshadowed by resistive losses, but not too large to induce reverse currents through the junction.

2.2. How to read a current-voltage characteristic

To determine the optimum voltage and test the performance of a solar cell, *J(V)* (current-voltage) measurements are carried out. In this experiment, the temperature is maintained at 25 °C while illuminating the cell with a light source that replicates the solar output through a cloudless

atmosphere when the sun is at a zenith angle of 48.2°. These standardized conditions are referred to as air mass 1.5 (AM1.5) and correspond to a radiative power input of 100 mW/cm² (with the same wavelength distribution as the solar spectrum). The p-type and n-type layers of the cell are connected to both a voltage source and current meter which apply a range of voltages to the cell to replicate the effect of loads with increasing resistivity and measure the current produced by the cell for each.

The current generated by the cell when no voltage is applied s referred to as its short-circuit current (I_{sc}). The applied voltage at which the detected current is zero corresponds to the open circuit voltage (V_{oc}) of the cell. The voltage at which the maximum *current x voltage* product is recorded is known as V_{max} and corresponds to the optimal load for which the solar cell can deliver its maximal power output (the current at this point is known as I_{max}). The energy conversion efficiency η can be determined by dividing I_{max} x V_{max} by the power of incident radiation. The values of I_{sc} and V_{oc} are related to I_{max} x V_{max} by a property known as the fill factor (FF) which can be deduced from the ratio of the product of I_{max} *x* V_{max} over I_{sc} *x* V_{oc}. It is often more practical to normalize the current over the area of the cell which is tested and refer to the current density (*J)* in mA/cm² rather than the absolute current (*I*) in A.

The objective in optimizing solar cells is to achieve the highest possible energy conversion efficiency η. However, it is insightful to compare the values of V_{OC}, J_{sc} and FF as these parameters offer information on what is contributing to (or diminishing) the performance of the cell. The open-circuit voltage is determined by the maximum density of charge carriers which can be separated by the PN junction. This depends largely on the bandgap of the material in the depletion region but also on a variety of other factors including the presence of recombination centers in the doped layers of the cell. The short-circuit current of the cell quantifies the rate at which it generates new charge carriers. It is notably correlated to the intensity of incident radiation and therefore limited by optical losses in the device. The fill factor primarily represents recombination across the PN junction and resistive losses within the materials of the cell (modeled in the equivalent circuit of Figure 1.4.a by two resistors, respectively in parallel and in series to the voltage source). The parameters are related to each other, and many common problems (contamination, defaults, excessive doping…) are liable to affect several of them at same time.

2.3. What is a Watt peak?

A Watt peak (W_p) is the unit adopted by the solar industry to quantify the maximal power output of a solar panel (its capacity) under AM1.5 testing conditions. The unit is not normalized with respect to the area of the solar panel (which needs to be taken into account to assess its energy conversion efficiency). Watts peak are rarely quoted in scientific research. However they are useful when calculating the total energy that a solar installation will produce over its lifetime, or the ultimate contribution of installed photovoltaic capacity to the global energy mix. The conditions under which photovoltaic cells operate outside the laboratory rarely coincide with AM1.5 norms. Practical considerations including night time, cloud cover and the angle of inclination of the sun typically lead to averaged annual power outputs of ~20% the capacity of the solar panel.[48, 49] This fraction is known

as the capacity factor. It applies with different degrees to all energy technologies, as nuclear reactors and fossil fuel plants do not always operate at full capacity either. In the case of photovoltaics, the capacity factor also depends on the region in which the panel is installed, as solar insolation varies across the globe.

3. PV markets and manufacturing costs

In addition to large-scale arguments relating to the future of the world energy supply, there is an immediate business incentive to developing photovoltaics: annual fuel exports are worth $2.3 trillion.[50] Generating power is by far the vastest industrial endeavor ever to have occupied mankind. Seven out of the ten largest public companies in the world deal in fossil fuels[51] (and are modest players in comparison with the state owned titans not listed on the stock exchange). Global exports in this sector tower over those in financial services ($0.27 trillion),[50] agriculture ($1.4 trillion)[50] and defense spending ($1.5 trillion).[52] Given the scale of the market, even marginal profits in novel energy technologies could reap gigantic rewards. In this section, we assess the obstacles blocking the path of current PV manufacturing to these rewards. Paradoxically, some of the most promising paths to overcoming them can be found by looking, not at the encouraging predictions for future photovoltaic growth,[53] but at the meanders of its past. A brief history of photovoltaics is therefore presented before describing the present status of the field and identifying how the following chapters of this thesis may contribute to its development.

3.1. A history of photovoltaics

The prospect of harnessing the energy of the Sun emerged at the tail end of the Enlightenment, when Alexandre Becquerel reported to the French Academy of Sciences that compounds of noble metals immersed in acid could generate a voltage when exposed to light.[54] By the 1880s, scientists in the UK and America had shown that a solid state version of the device could also work using metal coated with selenium.[55, 56] Interest in these photovoltaic systems remained largely scientific until the 1940s, when researchers at Bell Laboratories steered the field towards solidified silicon melts.[57] These highly pure and ordered semiconductors were being developed for the nascent field of microelectronics. They brought energy conversion efficiencies up to an unprecedented 6 percent.[58] However, due to their initial fabrication costs, applications remained limited to markets with exceptionally high energy prices. Fortunately, a niche market soon emerged with the advent of the aerospace industry. As of the 1960s, private companies, including Bell Laboratories, Texas Instruments and Sharp, were turning profits from powering satellites with crystalline silicon solar cells.

The oil crises of the 1970s radically changed the landscape of photovoltaics. Concerns in the West about the security of energy imports led to increased funding in renewable energy. Whereas research had previously focused on boosting the conversion efficiency of solar cells, it shifted to bringing down costs for utility-scale applications. Microscopically thin layers of a-Si:H[59], CdTe,[60, 61] CIGS[62] and GaAs[63] were developed as potentially economical alternatives to wafers of crystalline silicon. However cheaper materials invariably suffered from lower energy conversion efficiencies,

leading to overall electricity prices which remained higher than those of conventional power plants. By the 1980s, the price of oil had crashed and the price of photovoltaics had not. Although scientific advances continued throughout the following two decades, most notably in areas which interface with organic semiconductors[64] and quantum physics[65], government and industrial attention waned and solar cells remained largely confined to niche markets.

3.2. The photovoltaics sector in the 2010s

Since the turn of the millennium, the escalation of fuel prices and a growing perception of the risks of climate change[23, 66] have revived enthusiasm for sustainable energy and led to the development of a booming photovoltaics industry (Figure 1.5.a). This sudden change of events results mainly from political commitment,[67, 68] notably from the introduction of feed-in-tariffs.[69] Feed-in-tariffs are laws which force utilities to buy back renewable energy at a price fixed by the government to allow its producers to recuperate the cost of their installation over its lifetime. The price of solar panels is therefore shared among all utility consumers through their electricity bills. This market distortion was designed to encourage investment and R&D in new energy technologies and reduce their manufacturing costs until they grow competitive.

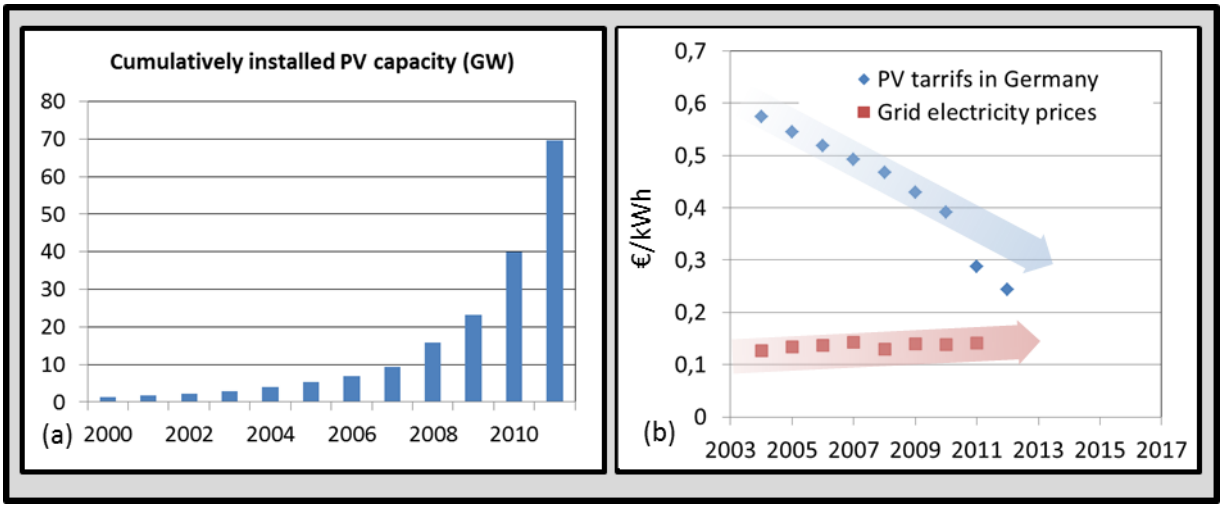

1.5 - Increasing PV capacity and decreasing Feed-in Tariffs.
Cumulative capacity of global photovoltaic installations (a) and the feed-in-tariffs for residential PV systems and electricity prices (€/kWh) in Germany (b) over the past decade.

In many respects, the approach has been remarkably successful. Substantial private funds have been channeled into developing the technology, with demand for solar photovoltaic capacity growing on average by 40% each year over the past decade (Figure 1.5.a).[53] When including system components and installations, the PV market has expanded from $2.5 to 71.2 billion over this period.[70] As a bonus, it has added 70 GW of peak power capacity to the grid [53] and relieved the atmosphere from tens of megatons of CO_2.[24, 53] Outstanding progress has been made towards reducing PV manufacturing costs, as the price of modules has halved with each 10-fold increase in global shipments. [71-73] Trends in electricity prices and feed-in-tariffs indicate that photovoltaics will become competitive in many European markets within the coming decade if the sector can sustain current rates of cost reductions

(Figure 1.5.b). However, with learning curves for established solar technologies saturating and margins across the industry at an all-time low, driving costs down further is likely to require technological innovation. In order to identify where this innovation is most needed, we present a brief overview of current PV manufacturing.

Box 3: The objective and cost of Feed-in-Tariffs.

Germany offers an insightful case study for the global potential of photovoltaics. Because it accounts for the lion's share of global PV installations, political decisions there (i.e. the feed-in-tariffs it sets) have considerable influence on the entire photovoltaic sector. Its utility prices are not particularly high (as in most of the EU, they have remained between €0.10/kWh and €0.15/kWh since 2003) and its annual insolation is modest compared to most inhabited locations around the world. Nonetheless, the price at which its utilities are legally bound to buy solar generated electricity from residential installations has decreased over the past decade from €0.60 to €0.30/kWh without slowing the rate at which PV capacity is being installed within its borders (Figure 1.5). If these trends are sustained, solar energy could drop below German grid prices within the coming decade. Once they do, market forces will massively increase the installed capacity of photovoltaics and bring on a new paradigm in global energy generation. Risks of fuel depletion and climate change will be averted, and further cost-reductions in photovoltaics will provide cheaper energy to the benefit of the world economy. However, *until* they do, feed-in-tariffs constitute an economic burden on the countries implementing them in the form of increased electricity prices. Some governments have already been obliged to reassess legislation in view of financial constraints.[74] Although widespread competitiveness is now well in sight (Figure 1.5.b), the future of photovoltaics hinges on political determination and the capacity for technological innovation over the coming decade.

3.1. Breaking down the manufacturing costs of crystalline silicon PV

Over 80% of solar modules on the market in 2011 were made of crystalline silicon.[70, 72] This material is made from extensively purified and crystallized quartz. The feedstock is initially melted with carbon in an electric arc furnace to remove its oxygen atoms and form 98.5% pure "metallurgical" grade silicon which sells for $2-3/kg.[75] To remove impurities, the metallurgical grade silicon is diluted in HCl and distilled in the form of chlorosilane vapors which condensate as polysilicon crystals.[76] The polysilicon is then melted and gently solidified in the form of a multicrystalline ingot which can reach purities of 99.9999% and prices of $30/kg.[71] The material can undergo further purification and melting cycles to ultimately form monocrystalline silicon. Each improvement in purity and crystallinity leads to better electronic properties but incurs extra costs. In 2011 the photovoltaic market was split evenly between polycrystalline and monocrystalline silicon modules.[72] The crystalline silicon (whether poly- or monocrystalline) is shaped into ingots and sawed into ~180 µm-thick wafers. The material wasted as saw dust during this step can account for up to half the crystalline silicon production. The wafers are doped to establish a PN junction and electrically contacted and connected to create a module. The module is typically encapsulated in a metal frame

between a sheet of plastic and glass. This manufacturing process for polycrystalline silicon solar cells is schematically illustrated in Figure 1.6.

The cost of each step is difficult to ascertain, but estimates from the NREL Internal Cost Model[71] suggest that in a polycrystalline silicon module with a 15% energy conversion efficiency and a price of \$1.25/W_p, manufacturing costs are generally divided four ways between purifying the polysilicon (\$0.29/W_p), sawing the wafers (\$0.32/W_p), making the cells (\$0.34/W_p) and assembling them into a module (0.34/W_p).[71]

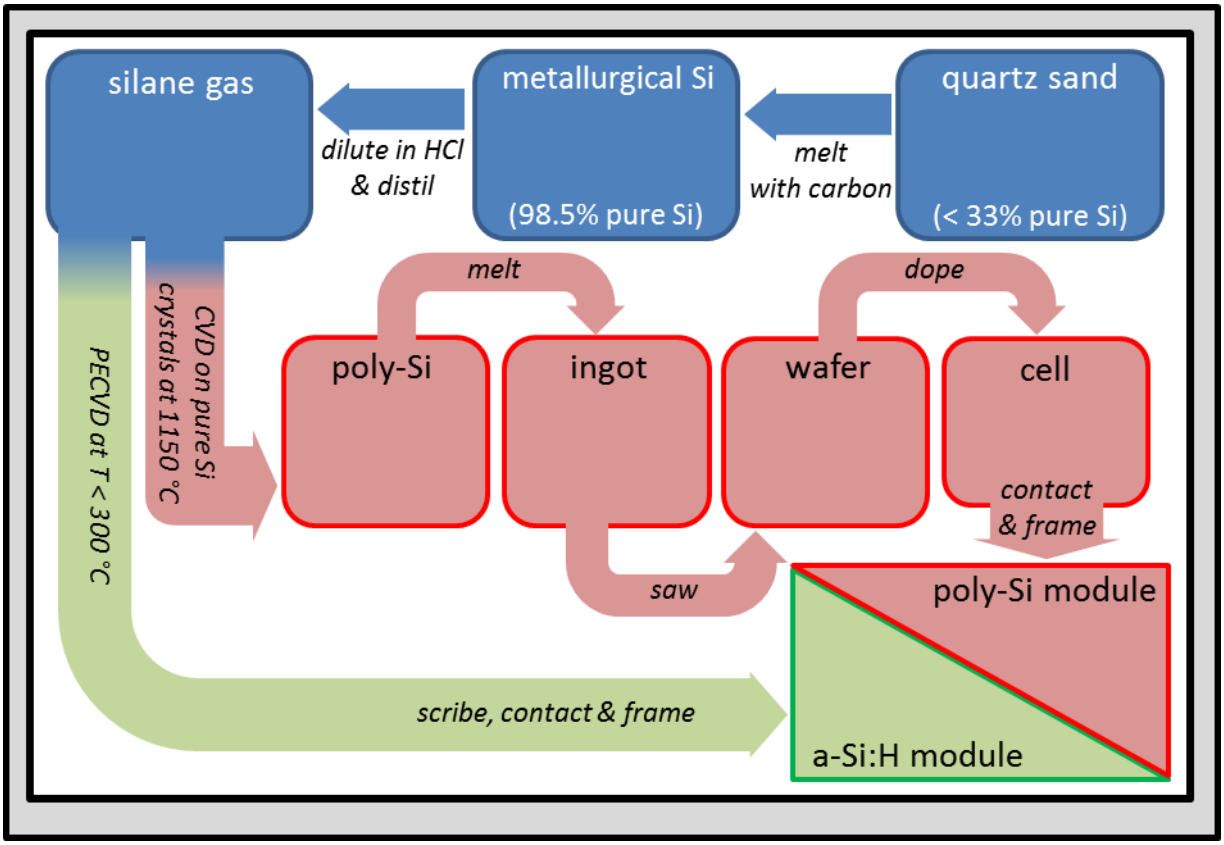

1.6 - Silicon PV manufacturing steps.
Manufacturing steps involved in the industrial production of crystalline and thin-film silicon photovoltaic modules.

Figure 1.7 shows that that the building material (the silicon wafer) accounts for roughly half the cost of the photovoltaic module. While other components of the cell may be replaced as the technology matures, the cost of its active layer raw materials offers an indication of the ultimate limit to which its manufacturing costs can be decreased. Attempts to use less refined silicon crystals[77] and limit sawing losses[78, 79] have been pursued for decades, but their commercial contribution remains marginal to date. Because wafer production is an established industry which has been producing integrated circuits for decades, there are arguably fewer prospects for incremental improvements to dramatically reduce its manufacturing costs.

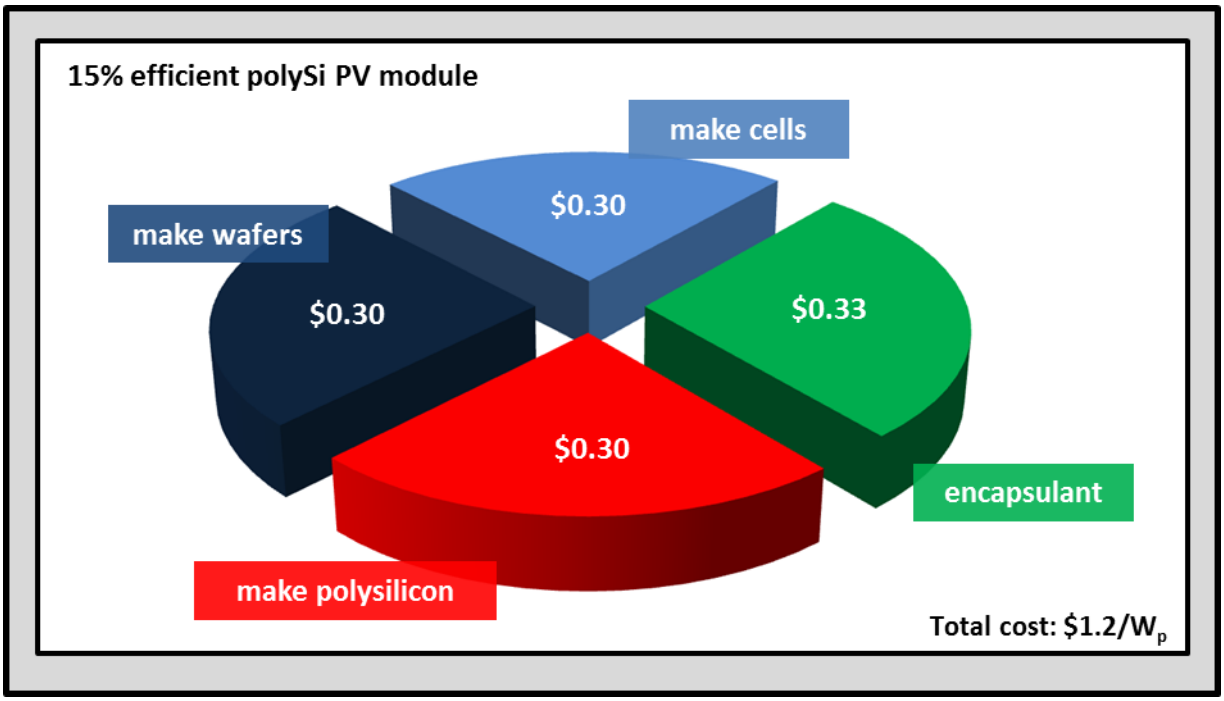

1.7 - Break-down of manufacturing cost per W_P of polycrystalline silicon photovoltaic modules.
Cost estimates for a 15% efficient polycrystalline silicon photovoltaic module fabricated in 2011 inferred from Goodrich[71] and Gielen.[80]

3.2. Short-cuts and hydrogenated amorphous silicon

It is however possible to sidestep wafer manufacturing altogether by depositing silicon directly from the gas phase. This approach was pioneered by David Carlson[59] during the 1970s. The gases in question (most commonly silane or silicon tetrachloride) are the same ones distilled from metallurgical grade silicon in Figure 1.6, but the approach obviates the subsequent high-cost crystallization steps. The gas molecules are cracked by plasma enhanced chemical vapor deposition, releasing Si atoms which bond with foreign substrates. The atoms form thin films of atomically disordered material, the most common of which is known as hydrogenated amorphous silicon (a-Si:H). In 2011, a-Si:H-based photovoltaics accounted for 600 MW_p of installed capacity.[72] Again, the cost breakdown of the technology is tricky to ascertain, but Figure 1.8 combines information from market[80] and industry reports[81] to offer some general guidelines.

The overall cost per W_p for a-Si:H-based modules ($0.8-1.3/$W_p$) can be lower than for crystalline silicon ones ($1.2/$W_p$).[80] In addition, the cost of the raw material (silane and dopant gases) used in the active layers of the module is marginal.[81] The two main expenses in a-Si:H modules are the depreciation of the equipment used to make the module (notably the plasma deposition reactors),[82] and the cost of glass, TCO, metal and other materials required to encapsulate the cell ($0.4/$W_p$). Some of these materials could ultimately be replaced, for instance by depositing the module on sheets of plastic[83] or roof tiles,[84] and because a-Si:H has not yet benefited from the same learning curve as crystalline silicon, it offers brighter prospects in terms of reducing manufacturing costs.

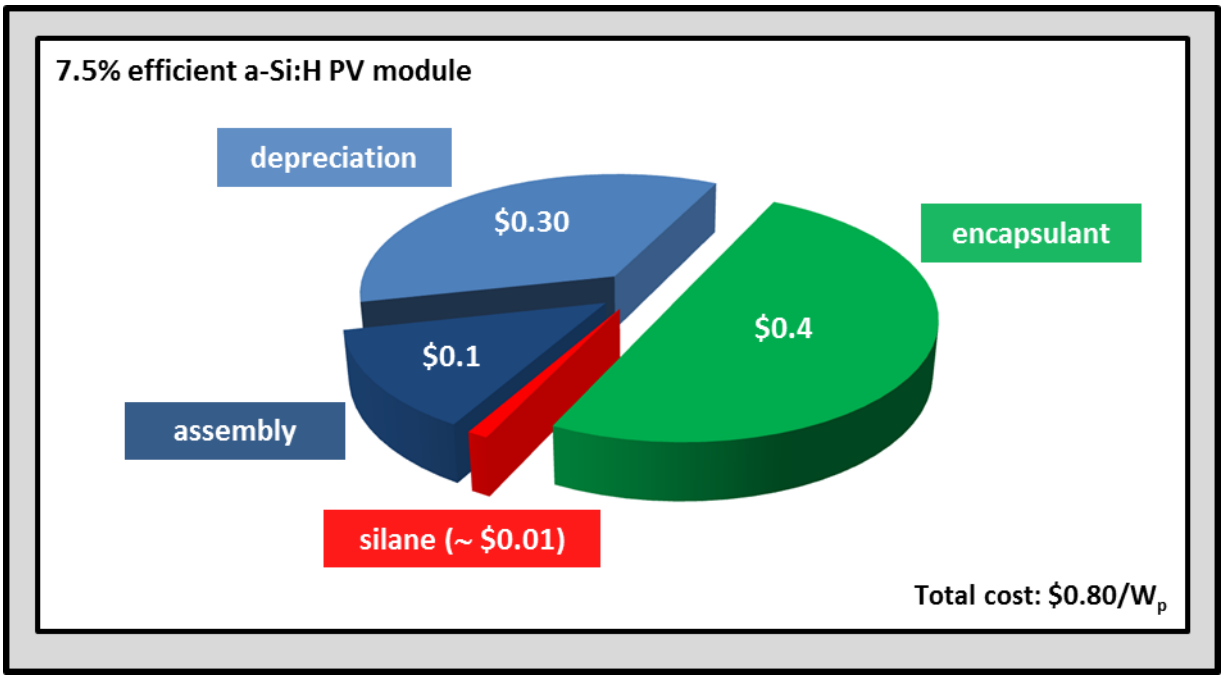

1.8 - Break-down of manufacturing costs per W_P of thin-film silicon photovoltaic modules.
Cost estimates for a single junction a-Si:H-based photovoltaic module in 2011 inferred from Gielen and Carlson.[80, 81]

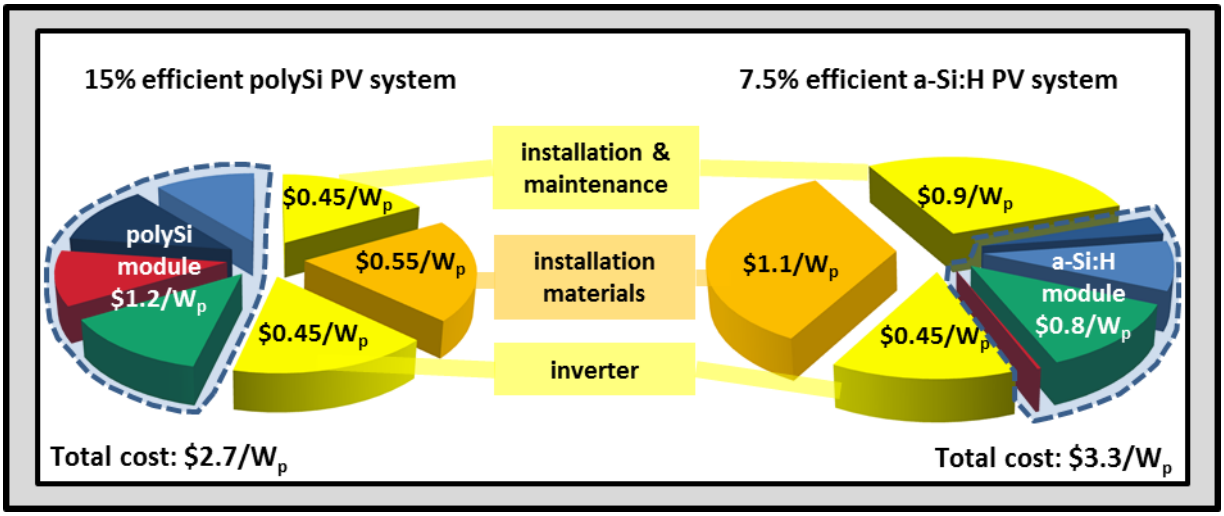

1.9 - Comparing the total cost of polycrystalline and thin-film silicon PV system installations.
Cost estimates for residential photovoltaic systems (installed in Germany using Chinese modules) in 2011. Respective contribution of components inferred from Goodrich[71] and Gielen.[80]

However, these modules suffer from a severe drawback in that their stabilized energy conversion efficiency is typically in the range of 5 – 10%,[80] which is considerably lower than the 15% commonly obtained with crystalline silicon. This is important because installing and operating the photovoltaic module requires additional components and services which tend to scale with its surface area, not its power output. Wiring, mounting materials, inverters, batteries, commissioning, installing the panel, maintenance and land can account for 20 to 70% of the final PV system price.[71, 80] Less efficient devices incur a higher installation penalty which decisively reduces their competitiveness (Figure 1.9). This is a key area where the photovoltaics sector stands to gain from further scientific research. Amorphous materials and thin-film devices present a wealth of unsolved and scientifically rewarding

questions which could lead to higher energy conversion efficiencies in a-Si:H modules and make their cost benefits more attractive.

Box 4: Alternative thin-film technologies

Hydrogenated a-Si:H is not the only promising new material for photovoltaics. In addition to potential advances in producing cheaper crystalline silicon,[77-79] CdTe, CIGS and GaAs modules are also developing rapidly. All three boast higher energy conversion efficiencies than a-Si:H and two of them already occupy larger market shares. However, in all three cases, some of their raw materials (respectively, Te, In and Ga) are in sparse supply. If the dozens of terawatts of global power production are to eventually be supplied by photovoltaics, these technologies will either need to substitute elements of their active layers or engage in recycling operations of unprecedented scales.

Dye sensitized and organic solar cells are also promising technologies but are still tackling issues with chemical stability and are not yet producing modules on the scale of other thin-film materials. Their initial energy conversion efficiencies have reached the benchmark set by a-Si:H[85] and the scope for reducing their manufacturing costs could possibly be greater. The issue of off-setting balance-of-system and installation costs by boosting energy conversion efficiency therefore applies to them all the more.

In brief, although the past sixty years have seen tremendous technological and industrial development of photovoltaic cells, the two have not always overlapped. Crystalline silicon, the material which dominates the PV market today, was inherited from scientific breakthroughs predating the space race. Although incremental advances have since improved the efficiency[58, 85] and reduced the manufacturing costs of these devices considerably,[71, 73] radical innovation will foreseeably be required to drive the cost of solar energy down to grid parity. Novel alternatives include modules based on PECVD deposited a-Si:H which can be produced at lower costs despite the comparatively early stages of their development. However, as the price of photovoltaic systems tends towards their installation costs, materializing the potential of a-Si:H will depend on our ability to improve its energy conversion efficiency. In the following section, some of the causes for the reduced efficiency of a-Si:H-based solar cells are explored and a possible solution is presented.

4. Conducting charges and trapping light in a-Si:H

The main distinction between crystalline and amorphous silicon resides in the arrangement of the atoms constituting the material. To make crystalline silicon, atoms are arranged under high temperatures so as to optimize their bonds in an aligned diamond cubic configuration which can extend over billions of nanometers (Figure 1.10.a). In contrast, because the temperature during silicon PECVD growth is considerably lower, there is less scope for surface diffusion or bond reconfiguration and the atoms generally bond at random. They still adopt covalent bonds, but there

is no order in their distribution beyond lengths of a few atoms (Figure 1.10.b). The short-range order does generate a band structure in the material with an optical bandgap close to 1.8 eV.[86] However, it differs from the band structure of crystalline solids in that the conduction and valence band edges are not clearly defined (Figure 1.10.c). This is due to variations in bond angles between atoms, which lead to localized states in an energy range close to the conduction and valence band edges (called Urbach tail states). In addition, the atomic structure locks the occasional Si atom in a configuration which coordinates it to three or five neighboring atoms[87] rather than four. The resulting dangling or floating bonds constitute recombination centers (localized states in the middle of the bandgap) which limit the charge diffusion and the doping efficiency of the material.

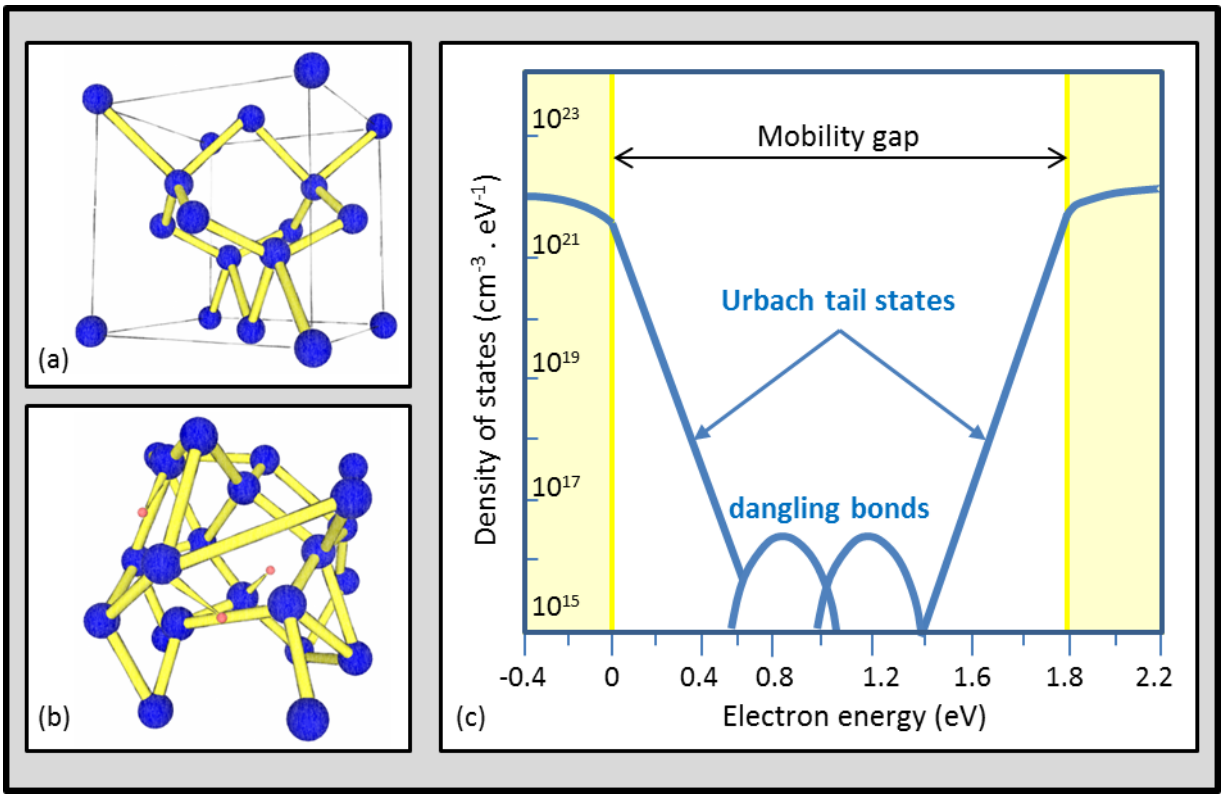

1.10 - Atomic configuration and density of states in a-Si.
Schematic representation of atoms in crystalline (a) and amorphous (b) silicon. Density of states in a-Si:H depicting the spread of the Urbach states into the bandgap due to disorder in the material and the presence of trap states at the center of the bandgap due to dangling bonds, based on Poortmans and Arkhipov[88] (c).

Conduction and doping can be improved in PECVD deposited silicon by adding hydrogen during the growth process to passivate dangling bonds. This results in the formation of a silicon-hydrogen alloy referred to as hydrogenated amorphous silicon (a-Si:H). A fragmented form of crystalline silicon can also be produced by increasing the concentration of hydrogen and the plasma power during PECVD. Silicon atoms then deposit as crystallites embedded in an a-Si:H matrix with diameters reaching hundreds of nanometers and random crystallographic orientations. This material is referred to as hydrogenated microcrystalline silicon (µc-Si:H) and generally has superior conductive properties to a-Si:H, a lower deposition rate and an indirect bandgap. Because the disordered nature of a-Si:H relaxes the quantum mechanical selection rules, the bandgap of a-Si:H is pseudo-direct and the absorption coefficient of a-Si:H is generally larger than that of crystalline silicon.[89]

Layers of a-Si:H and µc-Si:H can be doped by adding trimethylboron (TMB) or phosphine (PH_3) to the silane and hydrogen gas mix during plasma deposition. However, because of recombination centers in these materials, the doping efficiency is lower than in crystalline silicon, requiring higher dopant concentrations to drive the Fermi-level halfway towards the conduction or valence band edges. As this degrades electronic transport, a-Si:H and µc-Si:H solar cells are built by sandwiching an intrinsic layer (which absorbs light and generates charges) between a p-type and n-type layer (which generate the field to separate charge carriers). This architecture is known as a PIN junction. The efficiency of PECVD deposited silicon solar cells can be boosted by stacking a PIN µc-Si:H over a PIN a-Si:H junction in a tandem structure to optimize light absorption in their respective bandgaps.[85]

Another peculiarity of a-Si:H-based photovoltaics is that prolonged light exposure produces dangling bonds in their material which degrades conductivity.[90] This phenomenon, known as the Staebler-Wronski effect, is reportedly less pronounced for thinner[91] or more crystalline layers of silicon.[92] For a recent review on the subject, we refer the reader to the doctoral research of Ka-Hyun Kim.[93] The crucial point which has been tackled in the present thesis relates to the optimal thickness of the intrinsic layer in PECVD deposited solar cells. Although the majority of the above-bandgap solar spectrum can be absorbed in a-Si:H layers about a micron thick,[94] minority carriers in the material only diffuse over lengths of a few hundred nanometers[95] (compared to hundreds of microns in crystalline silicon).[96] This leads to a delicate compromise between charge conduction and light absorption in a-Si:H-based PV devices. A similar question arises with respect to the thickness of intrinsic layers in µc-Si:H solar cells, although more on the grounds of whether gains in light absorption justify increased deposition durations (and hence manufacturing costs). Several drawbacks hindering energy conversion efficiency in cells produced with these promising, low-cost materials are tied to the thickness of their intrinsic layer. Thinning it could increase the electric field across the absorber, improve charge collection, reduce deposition times and minimize Staebler-Wronski degradation. The question is how to achieve this without jeopardizing light absorption in the cell.

4.1. Light trapping and texturing

We have seen that one of the major challenges in a-Si:H and µc-Si:H solar cells lies in making the light absorbing layer thin enough for charges to be collected before they recombine, yet thick enough to absorb the full flux of sunlight. The most common solution is to texture the substrate (typically a transparent conducting oxide) on which the cell is deposited in order to scatter incident light within the plane of the cell (Figure 1.11). This technique is known as light trapping. It relies on differences between the refractive indices of materials in the cell to cause incident light to diffract and reflect at interfaces. Texturing the substrate generally increases the angle of deviation from the initial photon trajectory and hence increases its mean free path through the light absorbing material of the cell.

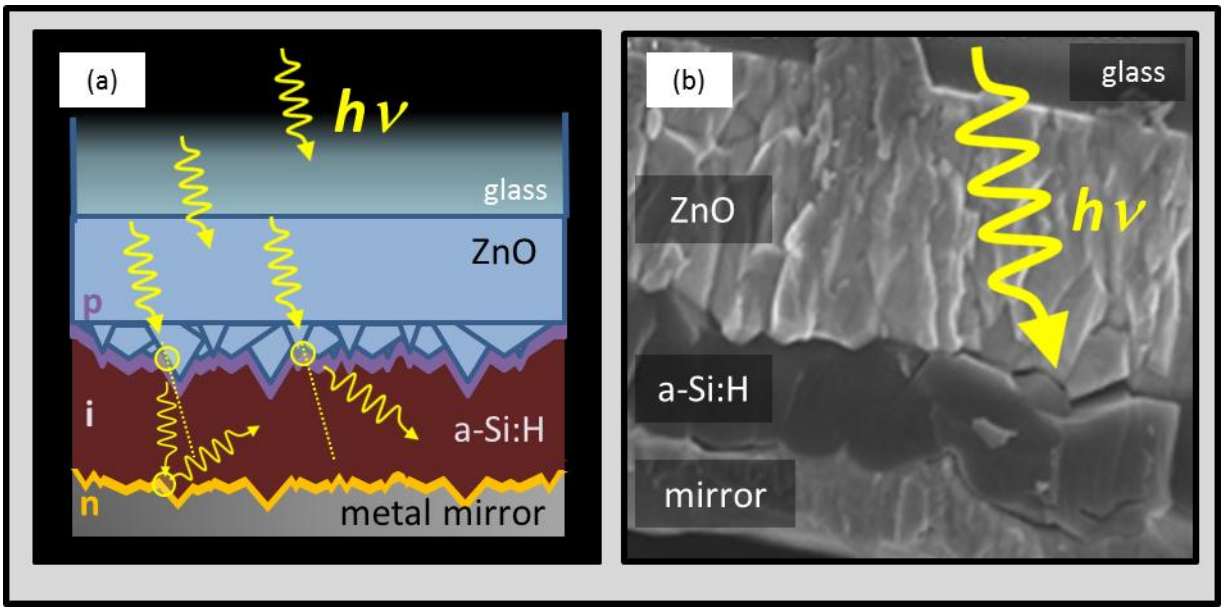

1.11 - Conventional light trapping in an a-Si:H solar cell.
Schematic description (a) and scanning electron microscopy cross-section (b) of planar solar cell composed of p-type, intrinsic and n-type a-Si:H deposited on a layer of ZnO chemically etched to trap light.

There are several drawbacks to this solution. Texturing the transparent conducting oxide layer generally requires additional manufacturing steps. In the case of a ZnO transparent conductive layer, the vacuum process during which the ZnO is sputtered must be interrupted to dip it in a chemical etchant before it is returned to vacuum in order to deposit the subsequent layers of the cell. Another problem is that the random structures obtained on rough transparent conductive oxide layers continue to reflect part of the incident light and are transparent to a considerable fraction of lower energy photons. The approach also imposes an additional constraint on the transparent conductive oxide layer which must already be engineered for high optical transmission, chemical stability and high conductivity. These properties are often in competition (e.g. what improves the layer transparency can degrade its conductivity) and it would be preferable to relieve the layer from the burden of texturing.

One alternative is to texture the silicon itself. This approach has been used for decades to increase light trapping in crystalline silicon cells in which the cell surface can be inclined with respect to incident light by etching pyramids or grooves out of the wafer. A more radical variant of this idea is to incline the entire PN junction with respect to the angle of light incidence so as to maximize the surface texture of the cell without increasing the distance over which charge carriers drift to be separated. This has been achieved for instance by etching areas of ZnO layers over which conformal layers of silicon are deposited.[98] However, these approaches all imply additional manufacturing steps which waste useable material. Ideally, the whole cell would be grown from the start in a three-dimensional configuration and with regions of different refractive indices penetrating through its entire thickness to maximize the effect of light trapping. Over the past five years, this ideal has grown increasing plausible with advances in the fields of silicon nanowire growth and radial junction solar cells.

4.2. Silicon nanowires and the radial junction solar cell

The objective of radial junction silicon solar cells is to absorb more light in thinner layers of material using highly textured surfaces. However the technique used in this case is to fabricate (e.g. p-type) doped pillars of silicon and cover them in intrinsic and (n-type) doped conformal layers of silicon (Figure 1.12). This is a particularly interesting approach for a-Si:H and µc-Si:H solar cells as pillars fitting this description can be fabricated directly by PECVD in the form of silicon nanowires. We will look closer into how silicon nanowires are made in Chapter 3. For now suffice it to say that, during chemical vapor deposition, drops of metal can locally enhance the deposition rate of silicon from the gas phase. This leads to the formation of vertical, cylindrical structures known as silicon nanowires. Arrays of these nanowires can present highly textured surfaces which have been observed to absorb light remarkably well.[99-104] The advantage of using SiNWs to texture PECVD deposited solar cells lies in that remarkably textured devices can be produced in a single deposition run.

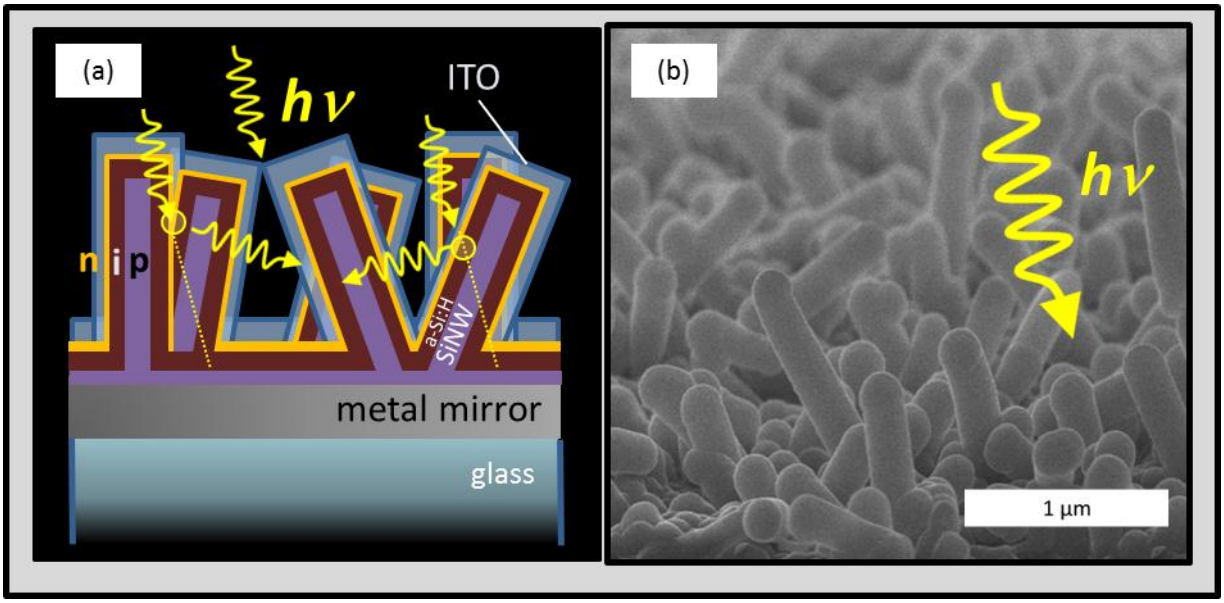

1.12 - Light trapping in a radial junction solar cell.
Schematic description (a) and scanning electron microscopy image (b) of a radial junction solar cell deposited over p-type PECVD-grown silicon nanowires designed for light trapping and covered in intrinsic and n-type layers of a-Si:H.

A full history of how radial junctions reached their current state of development is offered in Chapter 5. Here we simply highlight that at the time that we began to investigate this technology, numerous technical problems remained unsolved. The first attempts at making SiNW-based radial junction devices had led to low short-circuit currents,[50, 105-108] leaving open to debate whether most of the light which they scattered was being absorbed in the cell rather than in surface states[101] or in remnants of the metal particles that catalyze their growth. The cells also suffered from unexplained voltage losses compared to their planar counterparts, with open-circuit voltages typically reaching 300 mV.[105, 106, 109, 110] These flaws raised serious questions over the practicality of SiNW-based radial junctions for photovoltaics - questions which we intend to answer in the following four chapters.

5. Conclusion

In summary, radial junctions offer the prospect of increased the light trapping in a-Si:H and µc-Si:H solar cells. Improved light trapping would make it possible to reduce the thickness of the intrinsic layer in these devices and increase their charge collection. This would in turn lead to higher energy conversion efficiencies, and offset installation costs in a technology which presents enticing prospects for reducing the cost of photovoltaic modules. However, radial junction photovoltaics face considerable technical hurdles and this thesis takes part in the effort to overcome them. We begin with a study on how metal drops can be arranged by self-assembly on a solid substrate with a view to optimize the configuration of the nanowire array for light trapping. We then explore the role of the catalyst in the nanowire growth process in an attempt to identify metals best suited to grow silicon nanowires for radial junction PV applications. The formation mechanism of tin-catalyzed silicon nanowires is studied in further depth to bring out practical issues, advantages and peculiarities of this choice of catalyst. We conclude by bringing together some of these discoveries to build radial junction solar cells and demonstrate how their energy conversion efficiency can be improved.

Box 5: The color code of figures

The figures in the following four chapters have been color coded to assist the reader in differentiating between the substrates and PECVD reactors used. An illustrated guide of these conventions has been included at the end of the manuscript and a brief summary of it follows.

Tables and the outer frame of figures have been colored to identify samples made in the ARCAM reactor in green, those made in the Plasfil reactor in orange, those made in the Nextral reactor in blue. For each scanning electron microscopy (SEM) micrograph, the frame of the image indicates the substrate used. Burgundy Red designates glass substrates covered in a layer of SnO_2 (80 nm thick), orange designates Glass/ZnO substrates over which 1 nm of Sn has been evaporated, blue designates glass or crystalline silicon over which ITO has been sputtered, green designates ZnO (1 µm) covered glass over which ITO has been sputtered, purple designates glass or crystalline silicon over which Sn has been evaporated, black designates ZnO covered glass substrates over which Bi was evaporated and grey designates glass covered in ZnO (1 µm) with no nanowire catalysts present at its surface.

BIBLIOGRAPHY

[1] BP, Statistical Review of World Energy, (2011), www.bp.com/statisticalreview.
[2] W.J. Borucki, W.L. Chameides, Lightning: Estimates of the rates of energy dissipation and nitrogen fixation, *Review Geophysics,* 22 (1984) 363-372, doi:10.1029/RG022i004p00363.
[3] H.J. Christian, R.J. Blakeslee, D.J. Boccippio, W.L. Boeck, D.E. Buechler, K.T. Driscoll, S.J. Goodman, J.M. Hall, W.J. Koshak, D.M. Mach, M.F. Stewart, Global frequency and distribution of lightning as observed from space by the Optical Transient Detector, *Journal Geophysical Research,* 108 (2003) 4005, doi:10.1029/2002jd002347.
[4] USGS, The Preliminary Determination of Epicenters Bulletin, *National Earthquakes Information Center* (2012), http://earthquake.usgs.gov/earthquakes/eqarchives/epic/epic_global.php.
[5] J.W. Tester, E.M. Drake, M.J. Driscoll, M.W. Golay, W.A. Peters, *Sustainable Energy: Choosing Among Options,* MIT Press, 2005, isbn: 9780262201537.
[6] W. Munk, C. Wunsch, Abyssal recipes II: energetics of tidal and wind mixing, *Deep Sea Research Part I: Oceanographic Research Papers,* 45 (1998) 1977-2010, doi:10.1016/s0967-0637(98)00070-3.
[7] J. Malik, J.O. Hirschfelder, J. Magee, R.B. Brode, The Yields of the Hiroshima and Nagasaki Nuclear Explosions, (1985), http://www.hiroshima-remembered.com/documents/00313791.pdf.
[8] UN, World Urbanization Prospects: The 2007 Revision, United Nations Department of Economic and Social Affairs Population Division, (2008) 220, http://www.un.org/esa/population/publications/wup2007/2007WUP_Highlights_web.pdf.
[9] Y.H.P. Zhang, What is vital (and not vital) to advance economically-competitive biofuels production, *Process Biochemistry,* 46 (2011) 2091-2110, doi:10.1016/j.procbio.2011.08.005.
[10] L. Ryan, F. Convery, S. Ferreira, Stimulating the use of biofuels in the European Union: Implications for climate change policy, *Energy Policy,* 34 (2006) 3184-3194, doi:10.1016/j.enpol.2005.06.010.
[11] *The Economist,* Energy policy: A better mix, Special Report on Natural Gas (2012), http://www.economist.com/node/21558455.
[12] *Financial Times,* 750'000 a Year Killed by Chinese Pollution, (2007), www.ft.com/cms/8f40e248-28c7-11dc-af78-000b5df10621.html.
[13] G.E. Likens, F.H. Bormann, Acid Rain: A Serious Regional Environmental Problem, *Science,* 184 (1974) 1176-1179, doi:10.1126/science.184.4142.1176.
[14] R.K. Tiwary, Environmental Impact of Coal Mining on Water Regime and Its Management, *Water, Air, & Soil Pollution,* 132 (2001) 185-199, doi:10.1023/a:1012083519667.
[15] A. Jernelov, How to defend against future oil spills, *Nature,* 466 (2010) 182-183, doi:10.1038/466182a.
[16] M. Parry, O. Canziani, J. Palutikof, P. van der Linden, C. Hanson, *Climate change 2007: impacts, adaptation and vulnerability,* Cambridge University Press, New York, 2007, isbn: ISBN 978 0521 88010-7.
[17] J.R. Petit, J. Jouzel, D. Raynaud, N.I. Barkov, J.M. Barnola, I. Basile, M. Bender, J. Chappellaz, M. Davis, G. Delaygue, M. Delmotte, V.M. Kotlyakov, M. Legrand, V.Y. Lipenkov, C. Lorius, L. Pepin, C. Ritz, E. Saltzman, M. Stievenard, Climate and atmospheric history of the past 420,000 years from the Vostok ice core, Antarctica, *Nature,* 399 (1999) 429-436, doi:10.1038/20859.
[18] U. Siegenthaler, T.F. Stocker, E. Monnin, D. Lüthi, J. Schwander, B. Stauffer, D. Raynaud, J.-M. Barnola, H. Fischer, V. Masson-Delmotte, J. Jouzel, Stable Carbon Cycle–Climate Relationship During the Late Pleistocene, *Science,* 310 (2005) 1313-1317, doi:10.1126/science.1120130.
[19] L. Bernstein, R.K. Pachauri, I.P.o.C. Change, A. Reisinger, Climate Change 2007: Synthesis Report, IPCC, (2008), http://www.ipcc.ch/publications_and_data/publications_ipcc_fourth_assessment_report_synthesis_report.htm.

[20] C. Ritz, *Interpretation of the temperature profile measured at Vostok, east Antarctica,* International Glaciological Society, Cambridge, UK, 1989.
[21] O. Hoegh-Guldberg, J.F. Bruno, The Impact of Climate Change on the World's Marine Ecosystems, *Science,* 328 (2010) 1523-1528, doi:10.1126/science.1189930.
[22] C.D. Thomas, A. Cameron, R.E. Green, M. Bakkenes, L.J. Beaumont, Y.C. Collingham, B.F.N. Erasmus, M.F. de Siqueira, A. Grainger, L. Hannah, L. Hughes, B. Huntley, A.S. van Jaarsveld, G.F. Midgley, L. Miles, M.A. Ortega-Huerta, A. Townsend Peterson, O.L. Phillips, S.E. Williams, Extinction risk from climate change, *Nature,* 427 (2004) 145-148, doi:10.1038/nature02121.
[23] N. Stern, The Economics of Climate Change: The Stern Review*, Cambridge University Press*, 2007.
[24] F. Birol, IEA World Energy Outlook 2010, International Energy Agency, (2010), http://www.iea.org/publications/freepublications/publication/name,27324,en.html.
[25] H. Andruleit, H. Babies, J. Meßner, S. Rehder, M. Schauer, S. Schmidt, Annual Report on Reserves, Resources and Availability of Energy Resources 2011, German Mineral Resources Agency, (2012), http://www.bgr.bund.de/EN/Themen/Energie/Produkte/annual_report_2011-summary_en.html.
[26] *Coal: Research and Development to Support National Energy Policy,* National Academies Press, 2007, isbn: 9780309110228.
[27] W. Zittel, J. Schindler, H. Lehmann, S. Peter, Coal: Resources and Future Production: Background Paper, Energy Watch Group, (2007), http://www.energywatchgroup.org/fileadmin/global/pdf/EWG_Report_Coal_10-07-2007ms.pdf.
[28] A. Witze, Energy: That's oil, folks, *Nature,* 445 (2007) 14-17, doi:10.1038/445014a.
[29] J. Murray, D. King, Climate policy: Oil's tipping point has passed, *Nature,* 481 (2012) 433-435, doi:10.1038/481433a.
[30] R.W. Howarth, A. Ingraffea, T. Engelder, Natural gas: Should fracking stop?, *Nature,* 477 (2011) 271-275, doi:10.1038/477271a.
[31] D. Hughes, Will Natural Gas Fuel America in the 21st Century? , Post Carbon Institute, (2011), http://www.postcarbon.org/report/331901-will-natural-gas-fuel-america-in.
[32] R. Hirsch, R. Bezdek, Peaking of World Oil Production Impacts, Mitigation, & Risk management, (2005), www.netl.doe.gov/publications/others/pdf/oil_peaking_netl.pdf.
[33] K.E. Trenberth, J.T. Fasullo, J. Kiehl, Earth's Global Energy Budget, *Bulletin of the American Meteorological Society,* 90 (2009) 311-323, doi:10.1175/2008bams2634.1.
[34] J.R. Blaise, S. Boitsov, P. Bruneton, M. Ceyhan, F. Dahlkamp, R. Mathieu, A. McKay, J. McMurray, J. Slezak, J. Subhash, World Distribution of Uranium Deposits (UDEPO) with Uranium Deposit Classification, International Atomic Energy Agency (2009), http://www-pub.iaea.org/books/iaeabooks/8175/World-Distribution-of-Uranium-Deposits-UDEPO-with-Uranium-Deposit-Classification-2009-Edition.
[35] D.J.C. MacKay, *Sustainable Energy - Without the Hot Air,* UIT Cambridge Limited, 2009, isbn: 9780954452933.
[36] P. Fairley, Introduction: Next generation biofuels, *Nature,* 474 (2011) S2-S5, doi:10.1038/474S02a.
[37] J.W. Storm van Leeuwen, P. Smith, Can Nuclear Power Provide Energy for the Future; Would it Solve the CO2-Emission Problem?, (2002), http://greatchange.ord/bb-thermochemical-nuclear_sustainability_rev.html.
[38] J.W. Storm van Leeuwen, Energy Security and Uranium Reserves, Oxford Research Group, (2006), www.oxfordresearchgroup.org.uk/publications/briefing_papers/energyfactsheet4.php.
[39] *The Economist,* Special Report on Nuclear Energy, (2012), http://www.economist.com/blogs/babbage/2012/03/special-report-nuclear-energy.
[40] K. Lackner, R. Andreani, D. Campbell, M. Gasparotto, D. Maisonnier, M.A. Pick, Long-term fusion strategy in Europe, *Journal of Nuclear Materials,* 307–311, Part 1 (2002) 10-20, doi:10.1016/s0022-3115(02)00970-4.
[41] GWEC, Global Wind Report: Annual market update 2011, Global Wind Energy Council, (2012), http://gwec.net/wp-content/uploads/2012/06/Annual_report_2011_lowres.pdf.

[42] W.E. Leithead, Wind energy, *Philosophical Transactions of the Royal Society A: Mathematical, Physical and Engineering Sciences,* 365 (2007) 957-970, doi:10.1098/rsta.2006.1955.
[43] S. Chu, A. Majumdar, Opportunities and challenges for a sustainable energy future, *Nature,* 488 (2012) 294-303, doi:10.1038/nature11475.
[44] X. Lu, M.B. McElroy, J. Kiviluoma, Global potential for wind-generated electricity, *Proceedings of the National Academy of Sciences,* 106 (2009) 10933-10938, doi:10.1073/pnas.0904101106.
[45] L.M. Miller, F. Gans, A. Kleidon, Estimating maximum global land surface wind power extractability and associated climatic consequences, *Earth Syst. Dynam.,* 2 (2011) 1-12, doi:10.5194/esd-2-1-2011.
[46] A. Holm, L. Blodgett, D. Jennejohn, K. Gawell, Geothermal Energy: International Market Update, Geothermal Energy Association, (2010), http://www.geo-energy.org/pdf/reports/gea_international_market_report_final_may_2010.pdf.
[47] IEA, Renewable Energy Essentials: Hydropower, International Energy Association, (2010), http://www.iea.org/papers/2010/Hydropower_Essentials.pdf.
[48] C. Wadia, A.P. Alivisatos, D.M. Kammen, Materials Availability Expands the Opportunity for Large-Scale Photovoltaics Deployment, *Environmental Science & Technology,* 43 (2009) 2072-2077, doi:10.1021/es8019534.
[49] L.M. Moore, H.N. Post, Five years of operating experience at a large, utility-scale photovoltaic generating plant, *Progress in Photovoltaics: Research and Applications,* 16 (2008) 249-259, doi:10.1002/pip.800.
[50] WTO, International Trade Statistics 2011, World Trade Organization, (2011), http://www.wto.org/english/res_e/statis_e/its2011_e/its11_toc_e.htm.
[51] Forbes Global 2000 largest companies - listed in terms of sales, (2012), http://www.forbes.com/global2000.
[52] SIPRI, Stockholm International Peace Research Institute Expenditure Database, (2012), http://milexdata.sipri.org/.
[53] G. Masson, M. Latour, D. Biancardi, C. Winneker, Global Market Outlook for Photovoltaics until 2016, European Photovoltaics Industry Association, (2012), http://files.epia.org/files/Global-Market-Outlook-2016.pdf.
[54] A.E. Becquerel, Mémoire sur les effets électriques produits sous l'influence des rayons solaires, *Comptes Rendus des Séances Hebdomadaires,* 9 (1839) 561-567.
[55] W. Adams, R. Day, The Action of Light on Selenium, *Proceedings of the Royal Society of London,* 25 (1877) 113-117, http://www.jstor.org/stable/113462.
[56] C.E. Fritts, A new form of selenium cell, *Proceedings of the American Association for the Advancement of Science,* 33 (1883) 97.
[57] R.S. Ohl, Light-sensitive electric device, US Patent 2402662, *Bell Telephone Laboratories Inc.,*(1946).
[58] D.M. Chapin, C.S. Fuller, G.L. Pearson, A New Silicon p-n Junction Photocell for Converting Solar Radiation into Electrical Power, *Journal of Applied Physics,* 25 (1954) 676-677, doi:10.1063/1.1721711.
[59] D.E. Carlson, C.R. Wronski, Amorphous silicon solar cell, *Applied Physics Letters,* 28 (1976) 671-673, doi:10.1063/1.88617.
[60] D.A. Cusano, CdTe solar cells and photovoltaic heterojunctions in II–VI compounds, *Solid-State Electronics,* 6 (1963) 217-218, doi:10.1016/0038-1101(63)90078-9.
[61] L.M. Fraas, Y. Ma, CdS thin films for terrestrial solar cells, *Journal of Crystal Growth,* 39 (1977) 92-107, doi:10.1016/0022-0248(77)90157-9.
[62] S.D. Mittleman, Investigation of thin film solar cells based on Cu/sub 2/S and CuInS/sub 2/ and ternary compounds, *Department of Engineering,* Brown University, PhD (1974), http://www.osti.gov/energycitations/product.biblio.jsp?osti_id=5002641.
[63] Z.I. Alferov, V.M. Andreev, M.B. Kagan, I.I. Protasov, Solar-energy converters based on p-n AlxGa1-xAs-GaAs heterojunctions, *Soviet Physics: Semiconductors,* 4 (1971).

[64] C.J. Brabec, Organic photovoltaics: technology and market, *Solar Energy Materials and Solar Cells,* 83 (2004) 273-292, doi:10.1016/j.solmat.2004.02.030.
[65] G. Conibeer, Third-generation photovoltaics, *Materials Today,* 10 (2007) 42-50, doi:10.1016/s1369-7021(07)70278-x.
[66] J.J. McCarthy, O.F. Canziani, N.A. Leary, D.J. Dokken, K.S. White, *Climate Change 2001: Impacts, Adaptation, and Vulnerability: Contribution of Working Group II to the Third Assessment Report of the Intergovernmental Panel on Climate Change,* Cambridge University Press, 2001, isbn: 9780521015004.
[67] EU, A scheme for greenhouse gas emission allowance trading within the Community and amending Council Directive 96/61/EC, *Directive 2003/87/EC* (2003), http://ec.europa.eu/clima/policies/ets/documentation_en.htm#Main_legislation.
[68] EU, On the promotion of the use of energy from renewable sources, *DIRECTIVE 2009/28/EC* (2009), http://ec.europa.eu/energy/renewables/targets_en.htm.
[69] S. Jacobsson, V. Lauber, The politics and policy of energy system transformation—explaining the German diffusion of renewable energy technology, *Energy Policy,* 34 (2006) 256-276, doi:10.1016/j.enpol.2004.08.029.
[70] M.D. Platzer, U.S. Solar Photovoltaic Manufacturing: Industry Trends, Global Competition, Federal Support, Congressional Research Service, (2012), http://www.fas.org/sgp/crs/misc/R42509.pdf.
[71] A. Goodrich, M. Woodhouse, T. James, PV Manufacturing Cost Analysis: Future Cost Reduction Opportunities, National Renewable Energy Laboratories, (2012), http://www.nrel.gov/docs/fy12osti/53938.pdf.
[72] B. Burger, K. Kiefer, S. Nold, S. Philipps, R. Preu, S. Roland, T. Schlegl, G. Stryi-Hipp, G. Willeke, H. Wirth, I. Brucker, A. Häberle, V. Schacht, W. Warmuth, R. Wiese, Photovoltaics Report, Fraunhofer ISE, (2012), http://www.ise.fraunhofer.de/de/downloads/pdf-files/aktuelles/photovoltaics-report.pdf.
[73] G.F. Nemet, Beyond the learning curve: factors influencing cost reductions in photovoltaics, *Energy Policy,* 34 (2006) 3218-3232, doi:10.1016/j.enpol.2005.06.020.
[74] B. Sills, Spain Halts Renewable Subsidies to Curb $31 Billion of Debts, *Bloomberg,* (2012), http://www.bloomberg.com/news/2012-01-27/spain-suspends-subsidies-for-new-renewable-energy-plants.html.
[75] L.A. Corathers, Summary on Silicon, *Mineral Commodity Summaries,* United States Geological Society, (2012), http://minerals.usgs.gov/minerals/pubs/commodity/silicon/mcs-2012-simet.pdf.
[76] G. del Coso, I. Tobías, C. Cañizo, A. Luque, Temperature homogeneity of polysilicon rods in a Siemens reactor, *Journal of Crystal Growth,* 299 (2007) 165-170, doi:10.1016/j.jcrysgro.2006.12.004.
[77] N. Yuge, H. Baba, Y. Sakaguchi, K. Nishikawa, H. Terashima, F. Aratani, Purification of metallurgical silicon up to solar grade, *Solar Energy Materials and Solar Cells,* 34 (1994) 243-250, doi:10.1016/0927-0248(94)90046-9.
[78] R.L. Wallace, J.I. Hanoka, A. Rohatgi, G. Crotty, Thin silicon string ribbon, *Solar Energy Materials and Solar Cells,* 48 (1997) 179-186, doi:10.1016/s0927-0248(97)00101-3.
[79] T.F. Ciszek, Edge-defined, film-fed growth (EFG) of silicon ribbons, *Materials Research Bulletin,* 7 (1972) 731-737, doi:10.1016/0025-5408(72)90121-3.
[80] D. Gielen, Solar Photovoltaic: Cost Analysis, *Renewable Energy Technologies: Cost Analysis Series,* International Renewable Energy Agency, Volume 1: Power Sector (2012), http://www.irena.org/DocumentDownloads/Publications/RE_Technologies_Cost_Analysis-SOLAR_PV.pdf.
[81] D.E. Carlson, Monolithic amorphous silicon alloy solar modules, *Solar Energy Materials and Solar Cells,* 78 (2003) 627-645, doi:10.1016/s0927-0248(02)00455-5.
[82] Y. Sobajima, M. Nishino, T. Fukumori, M. Kurihara, T. Higuchi, S. Nakano, T. Toyama, H. Okamoto, Solar cell of 6.3% efficiency employing high deposition rate microcrystalline silicon photovoltaic layer, *Solar Energy Materials and Solar Cells,* 93 (2009) 980-983, doi:10.1016/j.solmat.2008.11.042.

[83] F.J. Haug, T. Söderström, M. Python, V. Terrazzoni-Daudrix, X. Niquille, C. Ballif, Development of micromorph tandem solar cells on flexible low-cost plastic substrates, *Solar Energy Materials and Solar Cells,* 93 (2009) 884-887, doi:10.1016/j.solmat.2008.10.018.
[84] B. Petter Jelle, C. Breivik, H. Drolsum Røkenes, Building integrated photovoltaic products: A state-of-the-art review and future research opportunities, *Solar Energy Materials and Solar Cells,* 100 (2012) 69-96, doi:10.1016/j.solmat.2011.12.016.
[85] M.A. Green, K. Emery, Y. Hishikawa, W. Warta, E.D. Dunlop, Solar cell efficiency tables (version 39), *Progress in Photovoltaics: Research and Applications,* 20 (2012) 12-20, doi:10.1002/pip.2163.
[86] M.F. Thorpe, D. Weaire, Electronic Density of States of Amorphous Si and Ge, *Physical Review Letters,* 27 (1971) 1581-1584, doi:10.1103/PhysRevLett.27.1581.
[87] M.D. Kluge, J.R. Ray, A. Rahman, Amorphous-silicon formation by rapid quenching: A molecular-dynamics study, *Physical Review B,* 36 (1987) 4234-4237, doi:10.1103/PhysRevB.36.4234.
[88] J. Poortmans, V. Arkhipov, *Thin Film Solar Cells: Fabrication, Characterization and Applications,* John Wiley & Sons, 2006, isbn: 9780470091265.
[89] O. Vetterl, F. Finger, R. Carius, P. Hapke, L. Houben, O. Kluth, A. Lambertz, A. Mück, B. Rech, H. Wagner, Intrinsic microcrystalline silicon: A new material for photovoltaics, *Solar Energy Materials and Solar Cells,* 62 (2000) 97-108, doi:10.1016/s0927-0248(99)00140-3.
[90] D.L. Staebler, C.R. Wronski, Reversible conductivity changes in discharge-produced amorphous Si, *Applied Physics Letters,* 31 (1977) 292-294, doi:10.1063/1.89674.
[91] A. Shah, P. Torres, R. Tscharner, N. Wyrsch, H. Keppner, Photovoltaic Technology: The Case for Thin-Film Solar Cells, *Science,* 285 (1999) 692-698, doi:10.1126/science.285.5428.692.
[92] J. Meier, P. Torres, R. Platz, S. Dubail, U. Kroll, J.A. Anna Selvan, N. Pellaton Vaucher, C. Hof, D. Fischer, H. Keppner, A. Shah, K.-D. Ufert, P. Giannoulès, J. Koehler, On the Way Towards High Efficiency Thin Film Silicon Solar Cells by the "Micromorph" Concept. , *MRS Proceedings,* 420 (1996), doi:10.1557/PROC-420-3.
[93] K. Kim, Hydrogenated polymorphous silicon: establishing the link between hydrogen microstructure and irreversible solar cell kinetics during light soaking, Ecole Polytechnique, PhD (2012).
[94] W.B. Jackson, D.K. Biegelsen, R.J. Nemanich, J.C. Knights, Optical absorption spectra of surface or interface states in hydrogenated amorphous silicon, *Applied Physics Letters,* 42 (1983) 105-107, doi:10.1063/1.93762.
[95] J. Dresner, D.J. Szostak, B. Goldstein, Diffusion length of holes in a-Si:H by the surface photovoltage method, *Applied Physics Letters,* 38 (1981) 998-999, doi:10.1063/1.92226.
[96] A.V. Shah, H. Schade, M. Vanecek, J. Meier, E. Vallat-Sauvain, N. Wyrsch, U. Kroll, C. Droz, J. Bailat, Thin-film silicon solar cell technology, *Progress in Photovoltaics: Research and Applications,* 12 (2004) 113-142, doi:10.1002/pip.533.
[97] W.L. Bailey, M.G. Coleman, C.B. Harris, I.A. Lesk, Texture etching of silicon: method, US Patent 4137123, *Motorola Inc.,*(1979).
[98] M. Vanecek, O. Babchenko, A. Purkrt, J. Holovsky, N. Neykova, A. Poruba, Z. Remes, J. Meier, U. Kroll, Nanostructured three-dimensional thin film silicon solar cells with very high efficiency potential, *Applied Physics Letters,* 98 (2011) 163503, doi:10.1063/1.3583377.
[99] K.Q. Peng, Y. Xu, Y. Wu, Y.J. Yan, S.T. Lee, J. Zhu, Aligned single-crystalline Si nanowire arrays for photovoltaic applications, *Small,* 1 (2005) 1062-1067, doi:10.1002/smll.200500137.
[100] L. Hu, G. Chen, Analysis of optical absorption in silicon nanowire Arrays for photovoltaic applications, *Nano Letters,* 7 (2007) 3249-3252, doi:10.1021/Nl071018b.
[101] L. Tsakalakos, J. Balch, J. Fronheiser, M.Y. Shih, S.F. LeBoeuf, M. Pietrzykowski, P.J. Codella, B.A. Korevaar, O. Sulima, J. Rand, A. Davuluru, U. Rapol, Strong broadband optical absorption in silicon nanowire films, *Journal of Nanophotonics,* 1 (2007), doi:10.1117/1.2768999.
[102] O.L. Muskens, J.G. Rivas, R.E. Algra, E.P.A.M. Bakkers, A. Lagendijk, Design of light scattering in nanowire materials for photovoltaic applications, *Nano Letters,* 8 (2008) 2638-2642, doi:10.1021/Nl0808076.

[103] R.A. Street, W.S. Wong, C. Paulson, Analytic model for diffuse reflectivity of silicon nanowire mats, *Nano Letters,* 9 (2009) 3494-3497, doi:10.1021/Nl901683y.
[104] W.Q. Xie, J.I. Oh, W.Z. Shen, Realization of effective light trapping and omnidirectional antireflection in smooth surface silicon nanowire arrays, *Nanotechnology,* 22 (2011) 065704, doi:10.1088/0957-4484/22/6/065704.
[105] L. Tsakalakos, J. Balch, J. Fronheiser, B.A. Korevaar, O. Sulima, J. Rand, Silicon nanowire solar cells, *Applied Physics Letters,* 91 (2007) 233117, doi:10.1063/1.2821113.
[106] O. Gunawan, S. Guha, Characteristics of vapor–liquid–solid grown silicon nanowire solar cells, *Solar Energy Materials and Solar Cells,* 93 (2009) 1388-1393, doi:10.1016/j.solmat.2009.02.024.
[107] C.E. Kendrick, H.P. Yoon, Y.A. Yuwen, G.D. Barber, H. Shen, T.E. Mallouk, E.C. Dickey, T.S. Mayer, J.M. Redwing, Radial junction silicon wire array solar cells fabricated by gold-catalyzed vapor-liquid-solid growth, *Applied Physics Letters,* 97 (2010) 143108, doi:10.1063/1.3496044.
[108] C. Gau, C.Y. Kuo, B.T. Dai, Photovoltaic characteristics of silicon nanowire arrays synthesized by vapor-liquid-solid process, *Solar Energy Materials and Solar Cells,* 95 (2011) 154-157, doi:10.1016/j.solmat.2010.04.028.
[109] B.Z. Tian, X.L. Zheng, T.J. Kempa, Y. Fang, N.F. Yu, G.H. Yu, J.L. Huang, C.M. Lieber, Coaxial silicon nanowires as solar cells and nanoelectronic power sources, *Nature,* 449 (2007) 885-U888, doi:10.1038/Nature06181.
[110] T. Stelzner, M. Pietsch, G. Andra, F. Falk, E. Ose, S. Christiansen, Silicon nanowire-based solar cells, *Nanotechnology,* 19 (2008), doi:10.1088/0957-4484/19/29/295203.

2. Organizing drops of metal

"天下大勢，分久必合，合久必分."

Liquid metal drops catalyze the growth of the silicon nanowires used in our solar cells. To some extent, the diameter and density of these drops determines the diameter and density of the nanowires. As these properties are liable to affect the extent to which the nanowire array traps light, forming these drops is a crucial step in optimizing the performance of our radial junction solar cells. In order to simplify the fabrication process and keep it compatible with a single pump-down process, it is preferable for the organization of the metal catalysts to be executed in vacuum using in situ techniques. Here we study how layers of Sn and In break down into droplets and spread over different substrates. We investigate alternative approaches for controlling the metal distribution by reducing metal oxides and demonstrate that the diameters and density of the metal droplets can be controlled with an appropriate choice of materials, plasma conditions and temperature.

"All things, when divided, strive to unite, and when united, to divide.", Romance of the three kingdoms, Luó Guàn Zhōng, 14th century.

1. Nanowire catalysts and surface science

The objective of this chapter is to control the size and spacing of liquid metal drops on a solid surface using techniques compatible with a single-pump down PECVD deposition process. The importance of the task lies in that the diameter and density of these drops will determine the diameter and density of SiNWs. These same nanowires will in turn determine the diameter and density of radial PIN junctions in our solar cells and hence their ability to trap light.

The term "single pump-down process" refers to depositing and assembling the metal drops (and indeed all other layers of the radial junction solar cell) entirely under vacuum. In practice, this means avoiding lithography steps, wet chemical treatments, or any process which would require removing the sample from vacuum. For instance, templates can be used to position catalysts for SiNW growth (by resorting for instance to lithography[1, 2] or porous alumina masks[3]). However in the interests of simplifying the manufacturing process of these cells, we have here investigated self-assembly methods. Thin films of metal deposited over foreign substrates naturally tend to reconfigure into drops. This occurs because atoms at the surface of a solid or liquid, being bound by fewer neighboring atoms than they would be in the bulk of the material, are in unstable states. Given the opportunity to do so, the film will deform to adopt a less energetic configuration. Its particles diffuse across the surface and bond at thermodynamically favorable sites, sometimes breaking the film down into drops.

Interfaces with liquids have remained an active topic of research for over two centuries.[4, 5] Many aspects on the evolution from a continuous film to dewetted drops remain heatedly debated.[6, 7] Here we present rudimentary guidelines to understand the configuration of the drops formed. Interested readers are referred to Quéré[8] and de Gennes et al.[9]

The surface tension γ is used to describe the energy required to create a new surface divided by the area that it covers. It can be approximated to:

$$E_S \sim \frac{U}{2\,a^2}$$

where *a* is the unit cell (either an atom or a molecule in the material) and *U* is the cohesion energy per unit.[9] For most oils, where interactions are dominated by comparatively weak Van der Waals forces, the surface tension reaches values of around 0.025 J/m². For liquid metals, where the interaction between neighboring atoms is considerably stronger, it ranges from 0.1 to 2.5 J/m².

When a film comes in contact with a surface, it responds to the surface energy of the film, of the substrate and of the interface between the two. The film tends to adopt a shape which minimizes the sum of all three components. If the surface energy of the film is high, it will tend to form a semi-sphere on the substrate surface to minimize the number of atoms at its surface. If the surface energy of the substrate is high, the film will tend to wet to reduce the exposed surface of the substrate. In most cases, equilibrium is reached with the film reconfiguring to both reduce its own surface and partially cover that of the substrate, producing drops as illustrated in Figure 2.1.

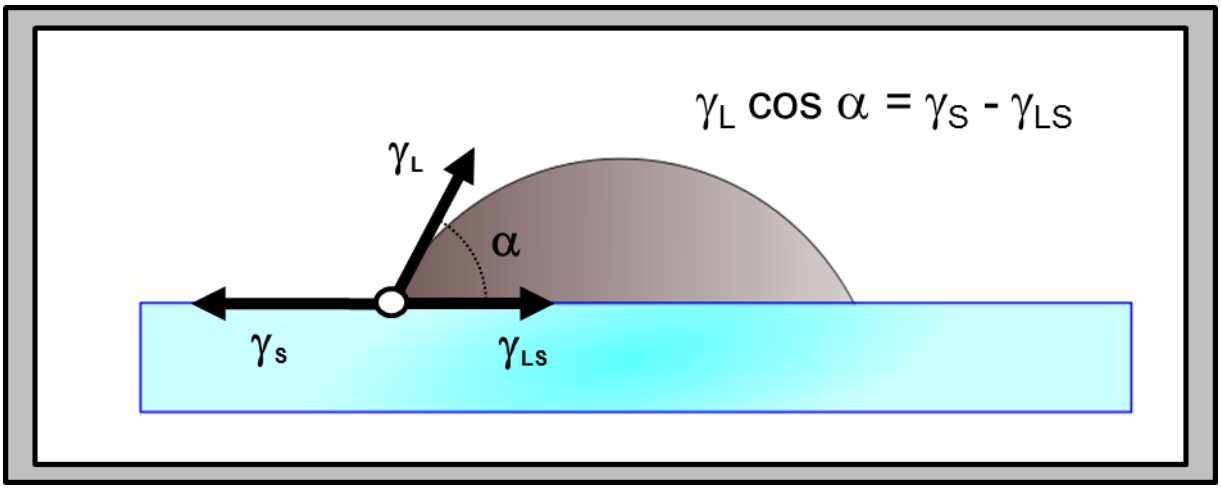

2.1 – Forces acting on the triple phase line of a liquid drop.
Schematic of a liquid drop in equilibrium on a substrate surface and the interfacial tensions acting at its rim.

A useful concept in determining the ultimate shape of the film is the surface tension γ. The surface tension manifests the interfacial energy between the film and the material it is in contact with. It embodies a force pulling at the interface between the two and has the same value as the surface tension but different units (energy per unit area corresponding to force per unit length). The surface tension of the liquid drop (representing in reality its interfacial tension with air) is denoted by γ_L, the surface tension of the substrate on which it rests by γ_S and the interfacial tension between the drop and the substrate by γ_{LS}. If γ_S is larger than the sum of γ_S and γ_{LS}, the substrate wets, if not it forms a drop. The contact angle α between the drop and the substrate is determined by the sum of forces acting on the line of contact between the drop, the surface and their surrounding medium:

$$\gamma_L \cos \alpha = \gamma_S - \gamma_{LS}$$

Looking at the system in terms of energies rather than tensions again, the contact angle defines the shape of the drop which minimizes the area exposed of each surface in the system weighted by its energetic cost. Solid films also have surface energies, but because atoms in solids are less mobile than in liquids, they tend to reconfigure less.

Predicting the shape which the drop adopts is complicated by several practical factors. The surface tension of materials is difficult to determine, in particular for non-crystalline solids. Substrates are rarely entirely flat and their chemical composition can be inhomogeneous. Simply changing their state of oxidation has been observed to alter the configuration of metal drops considerably.[10] The diameter of drops also varies as atoms diffuse out of some and redistribute in others.[11, 12] It varies with the thickness of the film deposited[13] and the height of energetic barriers to atomic diffusion. It also varies with the energy brought to the system to overcome these barriers. This can include differences in the thermal expansion coefficient of the materials in contact,[14,15] and in the temperature and time during which samples are annealed.[10] In brief, Figure 2.1 offers an incomplete picture of how liquid drops configure on real solid surfaces. Fortunately, for the systems which interest us, we can proceed empirically by making the drops and working backwards from our observations to understand how to control them better.

The density and average diameter of droplets in this chapter was determined by treating scanning electron microscopy (SEM) images of the samples with the ImageJ image treating software package. The procedure involved the following steps: Crop, Smooth edges, Enhance contrast, Threshold, Binarize, Watershed and Analyze Particles. Diameters and densities were then extracted from these data. In images where surface roughness prevented the use of this procedure, the drops were counted by hand over representative area and extrapolated. Error bars on the diameter represent the full range of the diameters observed (from maximum to minimum), not the standard deviation. Error bars on the density were set at 20%. Their presence simply indicates that an uncertainty over the value exists but requires a larger set of SEM images to quantify statistically.

2. Dewetting layers of evaporated tin

To study dewetting in metal layers, we deposited Sn on glass substrates in a Joule effect evaporator. For each deposition, a vacuum of 5 x 10^6 mbar was reached in the chamber, a current of 20 A was run through a tungsten boat filled with Sn particles (99.99 % pure) and left for 30 seconds with the shutter shielding the glass substrates so as to evaporate any contaminants from the Sn surface. The shutter was then opened for a duration of a few seconds during which the layer typically deposited at a rate of 1 nm per second according to a quartz microbalance positioned close to the samples inside the evaporator. SEM cross-sections of samples evaporated for durations of 5 to 25 seconds suggest that the quartz microbalance underestimates the thickness of the deposition by a factor of 4 (Figure 2.2).

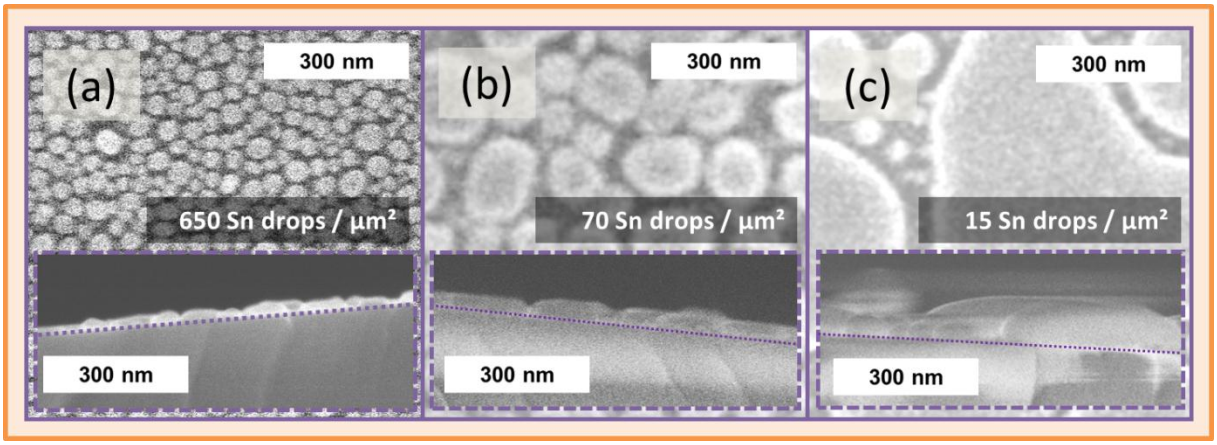

2.2 - Metal drop formations as a function of Sn layer thickness.
Sn evaporated on glass substrates at room temperature for durations of 5 seconds (a), 10 seconds (b) and 25 seconds (c) form drops which extend respectively 20 nm, 40 nm and 100 nm from the substrate surface.

SEM microscopy of the sample surfaces revealed that the Sn atoms form islands which progressively coalesce into a continuous film as more Sn is evaporated (Figure 2.2-3). This nucleation process is referred to as Volmer-Weber growth[16] and commonly occurs when the atoms forming the film bond more favorably with each other than with the surface on which they are being deposited.

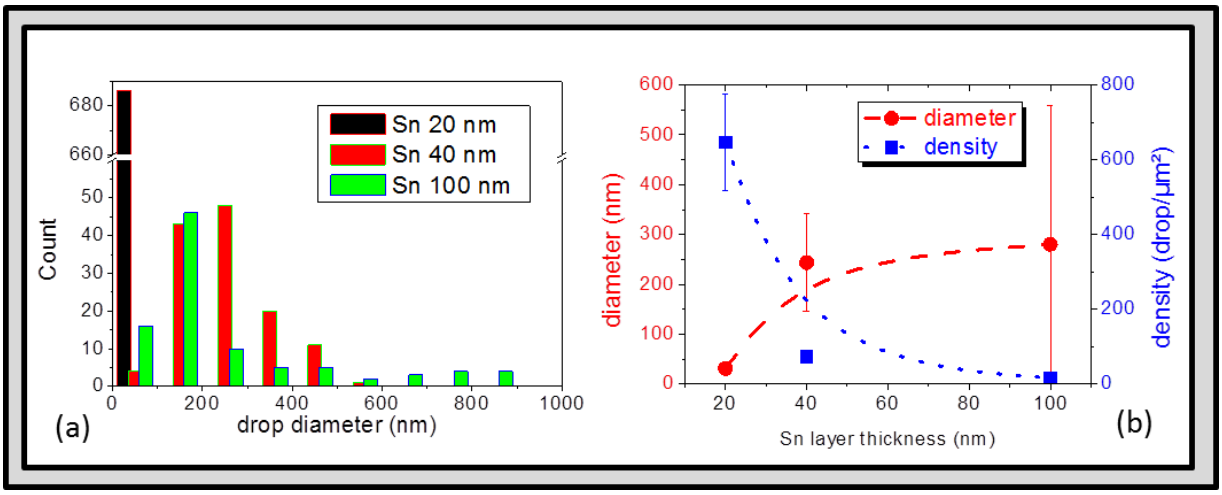

2.3 - Diameters of drops formed as a function of Sn layer thickness.
Histogram of Sn drop diameters (a) and evolution of the density and mean diameter (b) for Sn layers evaporated to a nominal thickness of 20, 40 and 100 nm.

Since the Sn drops are subject to an interfacial tension with the substrate, we investigated whether evaporating the layers on crystalline silicon instead of glass led to different drop configurations. Boron-doped Si wafers were included in the evaporation run alongside glass substrates. Although the wafers differed from the glass substrates in so far as they were conductive and their atomic structure was crystalline, they were covered in a thin native oxide layer. Glass is essentially an amorphous Si oxide, so the difference between the two materials was expected to be modest. Notwithstanding, the density of Sn drops which formed over the crystalline Si wafer was 50% lower than over the glass substrate (Figure 2.4.b & c). Their size was also generally larger (Figure 2.4.a), with average drop diameters increasing from 28 nm on glass to 34 nm on the silicon wafer.

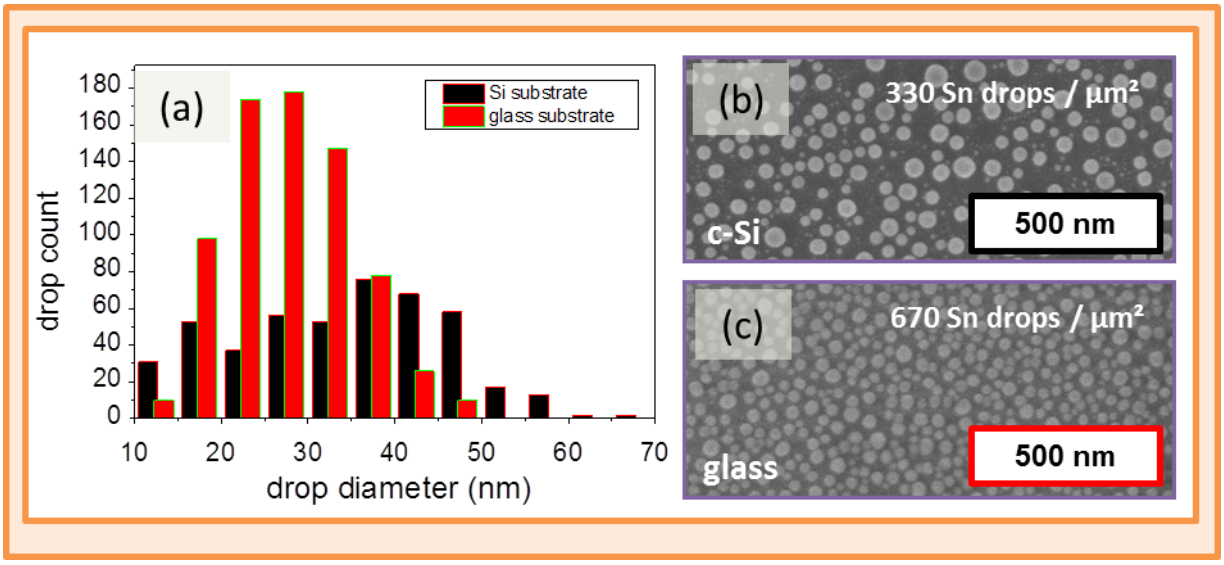

2.4 - Diameters of Sn drops formed on glass and crystalline Si substrates.
Histogram of diameters for Sn drops (a) evaporated in the same run on Si wafers (b) and glass substrates (c).

We attempted to alter the configuration of the Sn droplets by liquefying the metal. Although Sn melts at 231 °C, its surface rapidly reacts with oxygen atoms to form a stable oxide shell which can

remain solid at temperatures in excess of 1000 °C.[17] To prevent oxidation, we heated the samples under a hydrogen plasma. Atomic hydrogen is known to deplete oxygen at the surface of SnO_2 films by reducing the oxide and forming water vapor.[18, 19] This reduction mechanism is detailed further in the next section. Sn layers with a nominal thickness of 40 nm were evaporated on glass and Si wafers and heated in the Plasfil reactor to 250 °C. They were then exposed to a hydrogen plasma with a H_2 pressure of 260 mTorr (gas flow rate of 100 sccm) and a power density of 50 mW/cm² for a duration of 5 minutes.

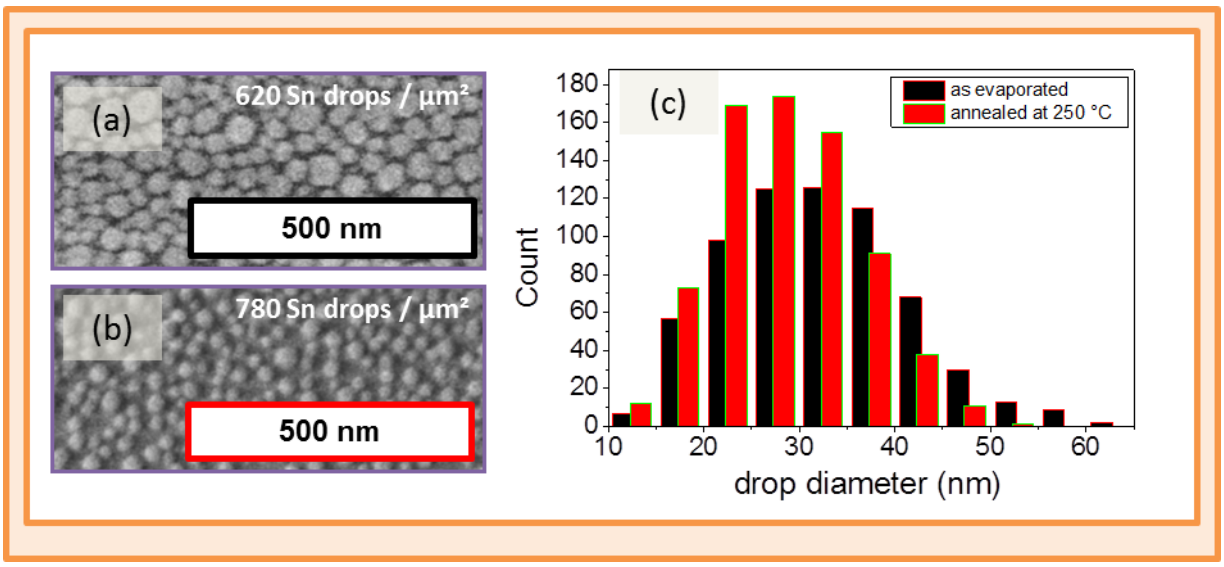

2.5 - Effect of H_2 plasma at 250 °C on the formation of Sn drops.
Sn layers evaporated at room temperature on glass substrates (a) were liquefied under a H_2 plasma at 250 °C (b). Histogram of the Sn drop diameters (c).

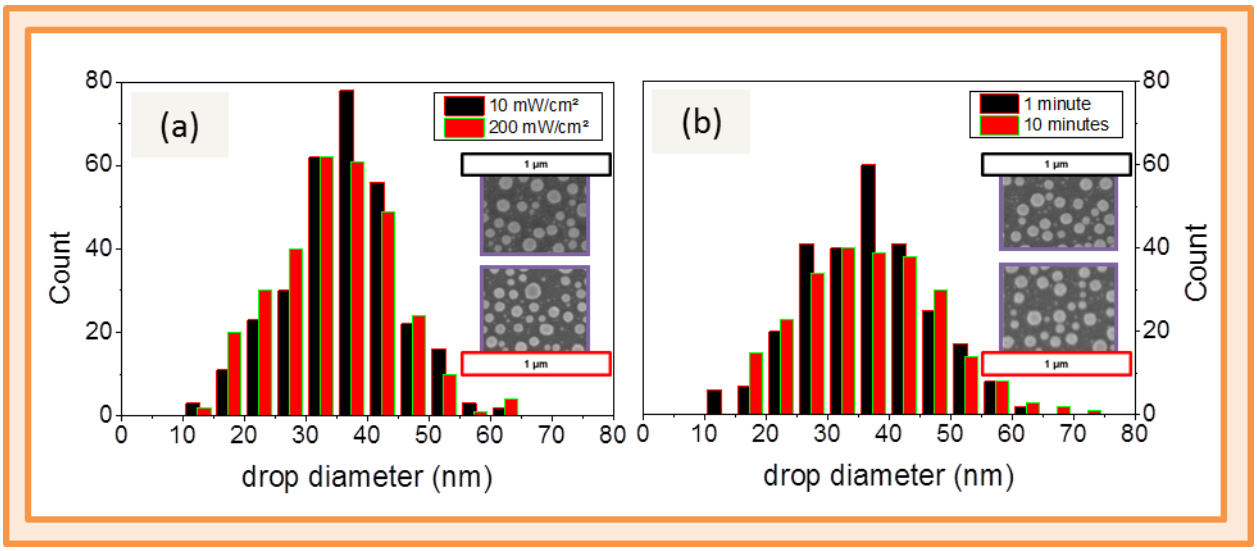

2.6 – Sn drop diameter as a function of plasma power and duration.
Histograms of Sn drop diameters for Sn layers (50 nm thick) evaporated on Si wafers and exposed to H_2 plasmas with increasing power (a) and increasing duration (b).

The treatment led to a modest redistribution of the Sn drops, reducing their average diameter from 32 nm to 26 nm (Figures 2.5.c) and increasing their density from 620 to 780 drops per square micron (Figures 2.5.a-b). Attempts to alter the configuration of Sn drops further by increasing the plasma power density from 10 to 200 mW/cm² (Figure 2.6.a) and its duration from 1 to 10 minutes (Figure 2.6.b) remained unsuccessful. No substantial change in the density and diameter of the Sn drops were observed over this range of conditions.

In conclusion, although evaporated Sn produced metal drops with nanoscopic dimensions, this approach offered little flexibility in terms of their configuration. The diameter of the Sn drops was observed to increase along with the thickness of the evaporated Sn, but the spacing between them remained largely unchanged. Replacing glass substrates with Si wafers modestly reduced the density and increased the diameter of the drops. Heating under a H_2 plasma for 5 minutes marginally reduced their diameter; however further plasma treatments were not observed to alter the drop configuration.

3. Reducing layers of metal oxides

The effect of atomic hydrogen on SnO_2 and ITO has been studied in the field of a-Si:H and µc-Si:H photovoltaics as it is notorious for degrading optical transmission and conductivity.[20] These metal oxides are commonly used as transparent conducting electrodes on which a-Si:H and µc-Si:H solar cells are deposited. However the plasma conditions used do expose them to atomic hydrogen. X-Ray Photoelectron Spectroscopy (XPS) studies have shown that during the initial stages of deposition, hydrogen atoms are liable to reduce the surface of SnO_2[19, 21] and ITO films[22] and contaminate the Si deposition with metal. Observations of the species desorbing from SnO_2 layers exposed to hydrogen suggest that the process involves the reduction of the oxide[18] leading to the formation of water vapor and metal:

$$4\,H^+ + SnO_2 \longrightarrow Sn + 2\,H_2O$$

The thickness of the oxygen deficient layer has been estimated to reach between 0.1 nm[19] and 40 nm into the SnO_2 film.[23] However, during long exposures, the reduced metal particles have been observed to coalesce into microscopic liquid drops, exposing a fresh oxide surface to further reduction.[23] Recently, Alet et al. observed that similar metal drops formed on the surface of reduced ITO substrates and that exposing these drops to a silane plasma could catalyze the growth of SiNWs.[24] This approach side-stepped the need to deposit the metal catalysts on the substrate surface, potentially simplifying the fabrication process of radial junction solar cells.

Building on this discovery, we attempted to optimize the H-plasma conditions to control the density and diameter of metal particles formed at the metal oxide surface. In the previous section we altered the configuration of drops formed from evaporated layers of Sn by changing the layer thickness, the annealing temperature and the nature of the substrate. Here, we detail our attempts in also controlling the duration and rate of Sn production by optimizing the intensity, duration and temperature of the oxide reducing H-plasma applied to SnO_2 and ITO layers.

3.1. The duration of drop formation

Glass substrates covered in 80 nm of SnO_2 with a square resistance of 130 Ω□ (purchased from Asahi) and glass substrates covered in 100 nm of ITO (sputtered in-house under a base vacuum 10^{-6} mbar, 2 sccm of oxygen, 38 sccm of argon, a plasma power density of 2 W/cm², at room temperature and for a duration of 120 seconds) were introduced into the Plasfi reactor. The deposition rate of ZnO and ITO over flat substrates was measured as being 0.5 and 1 nm/s respectively) were introduced into the Plasfil reactor and heated to 250 °C. After reaching a vacuum of 5 x 10^{-6} mbar, they were exposed to a H_2 plasma at a pressure of 600 mTorr (flow rate 200 sccm) with a power density of 50 mW/cm² (Table 2.1).

Table 2.1: Plasma conditions for reducing SnO_2 & ITO layers

H_2 flux	pressure	plasma power	temperature	time
200	600 mTorr	50 mW/cm²	250 °C	5 minutes

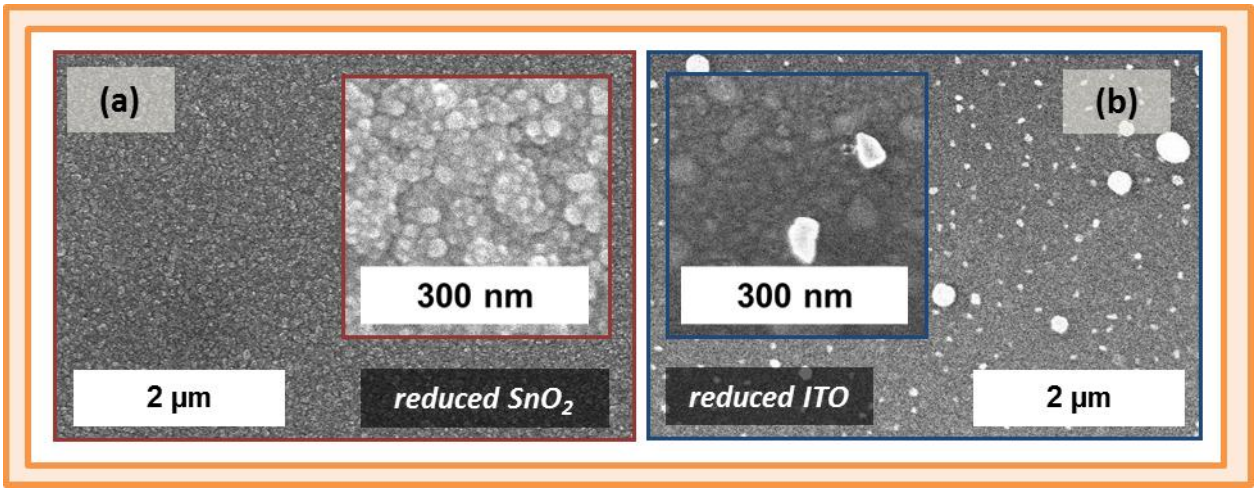

2.7 - SnO2 and ITO substrates exposed to a H_2 plasma.
Glass substrates covered in 80 nm of SnO_2 (a) and ITO (100 nm) (b) were exposed to a H_2 plasma for a duration of 5 minutes in the Plasfil reactor.

The H_2 plasma altered the surface morphology of both substrates. However its impact differed remarkably for the reduced layer of SnO_2 and ITO. In the case of SnO_2, nanoscopic drops (with diameters close to 50 nm) formed over the entire surface of the sample (Figure 2.7.a). Their size was homogeneous and they formed close to each other. In the case of ITO, significantly larger metal drops formed with diameters reaching several hundred nanometers (Figure 2.7.b). The inset in the figure shows that between these larger drops, nanoscopic drops with diameters similar to those found on the SnO_2 substrate (albeit with a lower density) also formed on the ITO substrate. To understand why the morphology adopted by the reduced metal drops differed according to the substrate used, we investigated the formation process of the metal drops both on reduced SnO_2 and ITO substrates by exposing them to a H_2 plasma for periods ranging from 1 to 10 minutes.

Within the first 60 seconds of exposing the SnO_2 substrate to the H_2 plasma, a high density of drops with diameters smaller than 10 nm formed homogeneously over its surface (Figure 2.8.a). Drop diameters increased along with H_2 plasma duration (Figure 2.8.b-c), leading to coalescence and a decrease in drop density. Longer exposures the H_2 plasma also softened the angular surface features of the SnO_2 crystals on which the drops formed (Figure 2.8.b-c) and spread the distribution in drop diameters (Figure 2.8.d).

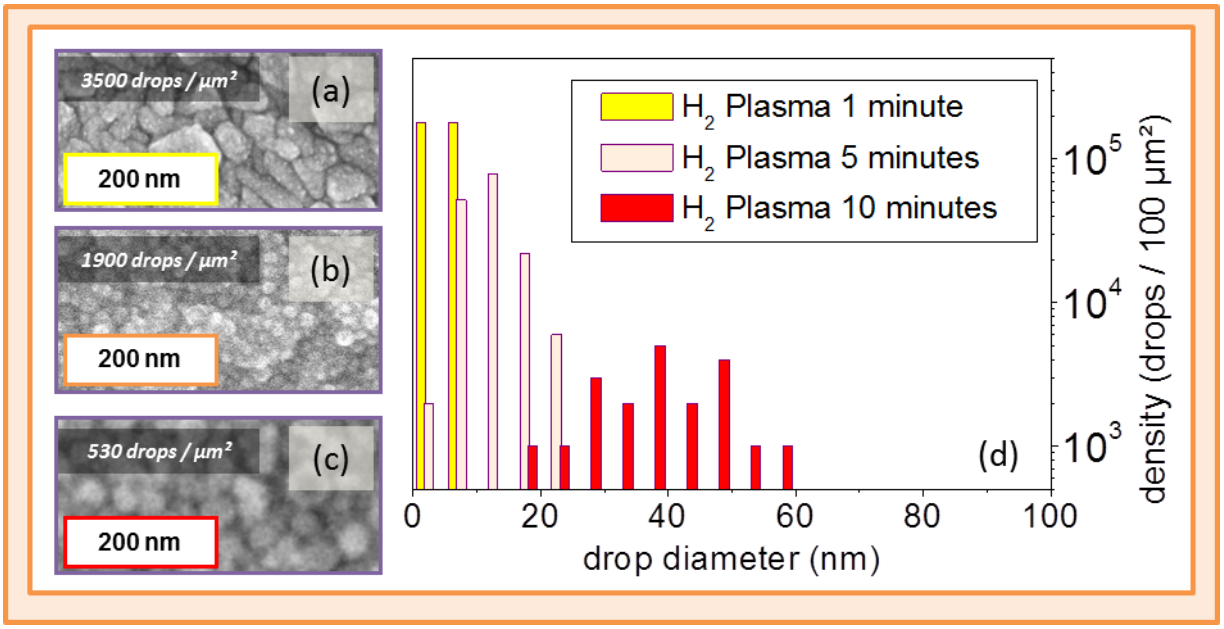

2.8 - Diameter distribution of Sn drops reduced from SnO_2 substrates as a function of H_2 plasma duration.
SEM images (a-c) and diameter distribution (d) of metal drops formed at the surface of SnO_2 substrates exposed to a hydrogen plasma for 1 minute (a), 5 minutes (b) and 10 minutes (c).

The total volume of metal reduced in these samples was inferred from the drop radii by assuming that each drop formed a half-sphere on the sample surface. A more thorough analysis would require cross-sectional profiles of the drops to identify their contact angle. This first estimate suggested that the total volume of metallic Sn progressively increased from 10^4 $nm^3/\mu m^2$ to 10^6 $nm^3/\mu m^2$ for H_2 plasma exposures ranging from 1 to 10 minutes.

The situation differed considerably in the case of ITO substrates. Within the first sixty seconds of exposure to the H_2 plasma, metal drops formed with diameters exceeding several hundred nanometers. They were observed on all ITO samples (for H_2 durations spanning 1 to 10 minutes) and their diameter was not observed to increase along with the duration of the H_2 plasma (Figure 2.9). The regions between these microscopic drops revealed a continuous distribution of smaller drops with diameters ranging from tens to hundreds of nanometers (Figure 2.10.a-c). In contrast to observations on reduced SnO_2 substrates, the size distribution of the small drops extracted from ITO was continuous and faded towards larger diameters. As their inter-drop spacing was substantially larger than their diameter, no coalescence between drops was observed when the plasma duration was extended from 1 to 10 minutesn and drop densities actually increased for longer exposures (Figures 2.10.a-c). Also, the distribution in drop diameters remained largely unaffected when the plasma exposure was extended (Figure 2.10.d).

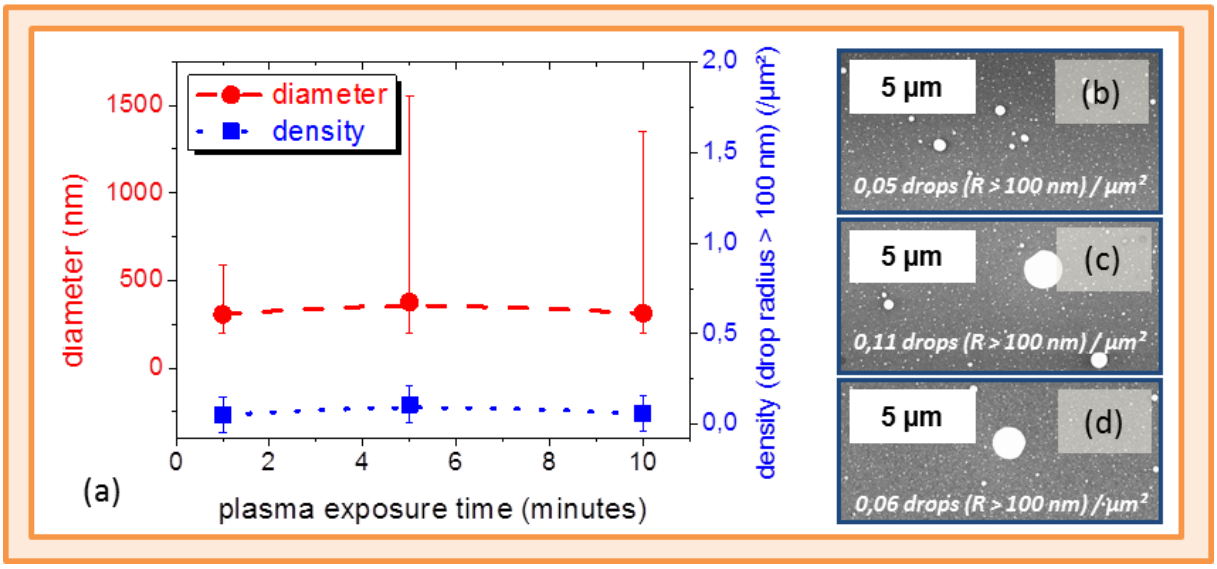

2.9 – Diameter and density of metal drops reduced from ITO substrates as a function H_2 plasma duration.
Diameter, density (a) and SEM images (b-d) of metal drops formed at the surface of ITO substrates exposed to a hydrogen plasma at 250 °C reduction for durations of 1 minute, 5 minutes and 10 minutes.

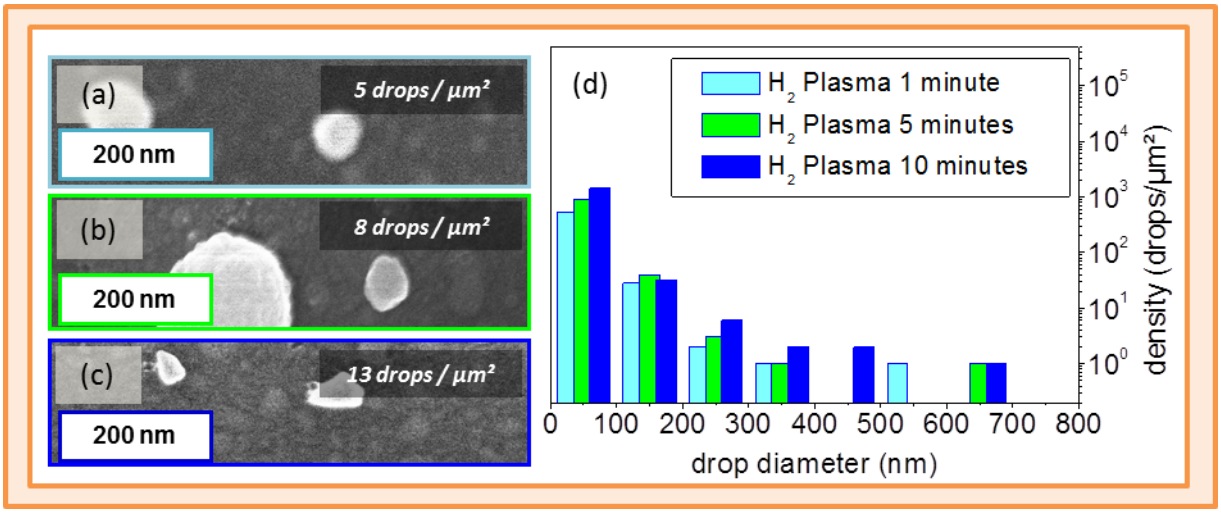

2.10 - Diameter distribution of Sn drops reduced from ITO substrates as a function of H_2 plasma duration.
SEM images (a-c) and histogram of diameters (d) of metal drops formed on ITO substrates reduced at 250 °C in a H_2 plasma for durations of 1, 5 and 10 minutes.

Using the same geometric approach, the volume of metal reduced from ITO exposed to a H_2 plasma was estimated to increase from 0.8 to 2 x 10^6 $nm^3/\mu m^2$ for plasma exposures of 1 to 10 minutes (Figure 2.11.a). This volume corresponds to a homogeneous film of metal 0.8 to 2 nm thick. Figure 2.11.a suggests that the rate at which the metal volume increases in reduced ITO is an order of magnitude lower than in SnO_2.

To investigate the depth of the ITO layer which contributes to the metal drop formation, we sputtered layers of ITO (20 nm thick) over crystalline Si substrates and submitted them to the same plasma treatment as the substrates covered in 100 nm thick layers of ITO. The morphology of the drops reduced at the surface of these new substrates (Figure 2.11.a-b) differed significantly from those obtained on 100 nm-thick ITO layers (Figure 2.9.b-d). No large drops were observed, and for 10

minute exposures the ITO film began to break down, revealing the crystalline silicon substrate beneath it (Figure 2.11.b). It is unlikely that the absence of large drops can be explained by an exhaustion of metal in the ITO layer. As we will see further on, larger drops can be obtained from 20 nm thick layers of ITO by altering some of the conditions during the H_2 plasma process. In addition, the combined volume of metal drops observed for the ITO samples in Figure 2.12 represented a continuous metal layer 0.9 to 2 nm thick, indicating that the ITO layer contained sufficient metal to produce drops with micrometric diameters, but did not do so.

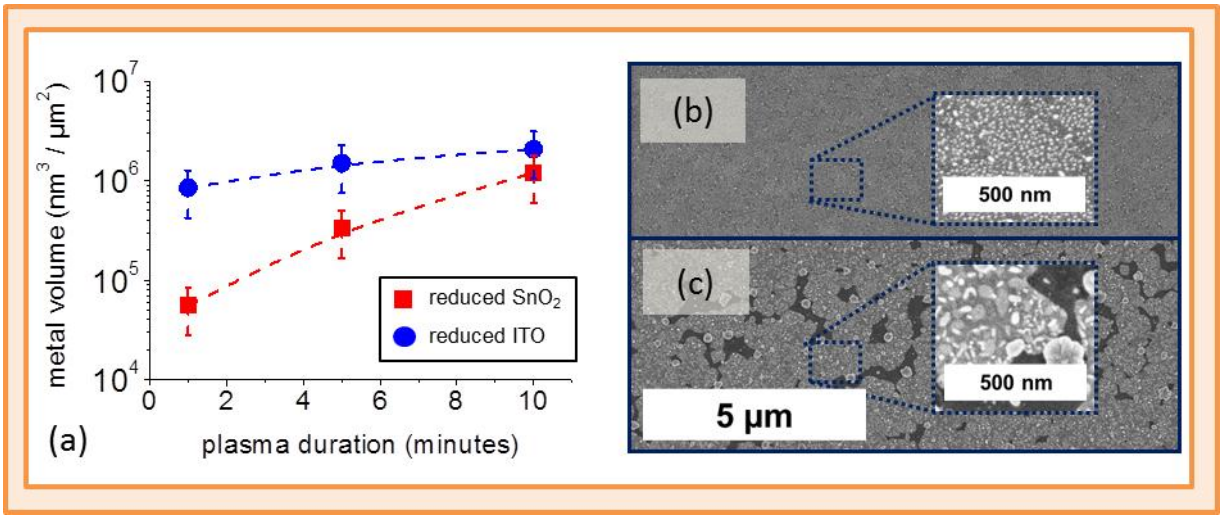

2.11 - Volume of metal reduced at the surface of SnO2 and ITO layers in a H_2 plasma.
Estimated volume of metal present at the surface of SnO_2 and ITO layers exposed to a H_2 plasma for 1, 5 and 10 minutes (a). Thin layers of ITO (20 nm) sputtered over silicon wafers exposed to a H_2 plasma for 1 minute (b) and 10 minutes (c).

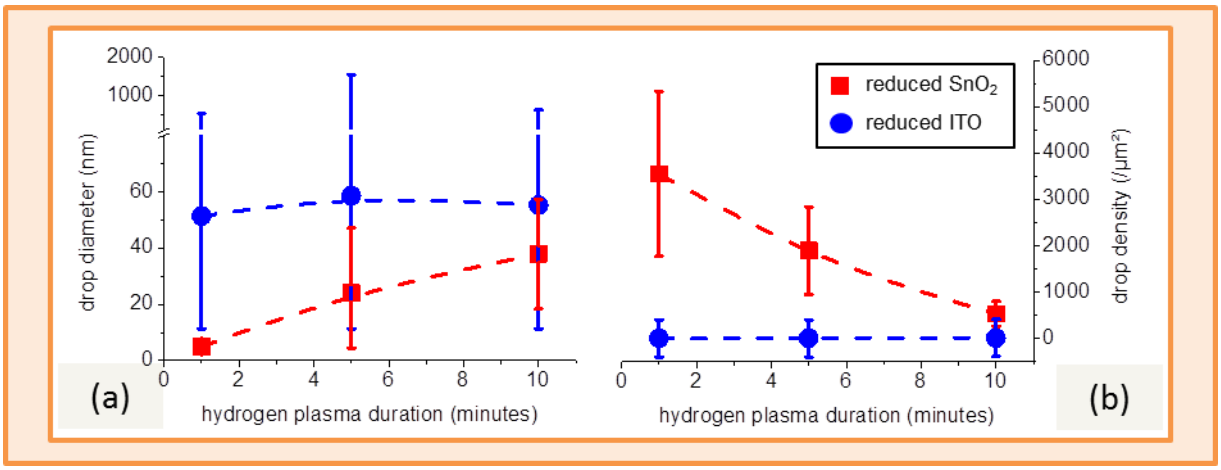

2.12 – Diameter and density of drops reduced from SnO_2 and ITO layers as a function H_2 plasma duration.
Comparison between the diameter (a) and density (b) of metal drops formed at the surface of SnO_2 and ITO layers reduced by progressively longer exposures to a H_2 plasma.

In summary, our study of SnO_2 and ITO layers progressively reduced in a hydrogen plasma points towards several differences in the formation mechanism for metal drops over the surface of these two substrates. In the case of SnO_2, the H_2 plasma reduced Sn atoms which nucleated in high

densities of small drops spread out homogeneously over the substrate surface. As the SnO_2 remained exposed to the plasma, more Sn was extracted from the oxide, leading to a gradual increase in the diameter of the drops, which ultimately resulted in them coalescing, causing their density to decrease. In the case of ITO, considerably larger drops formed (with diameters in the region of 1 micron) within the first 60 seconds of exposure to the H_2 plasma. Prolonged exposure gradually increased the number of metal drops reduced on the ITO surface. However it did not affect their size distribution or their density.

3.2. The rate of drop formation

In order to study the effect of the rate at which metal is reduced at the TCO surface on the diameter and density of the drops produced, we attempted to increase the concentration of reactive hydrogen in the plasma by increasing the RF power. Substrates of flat SnO_2 (80 nm) on glass and of ITO layers (20 nm) sputtered on crystalline silicon wafers and glass were introduced into the Plasfil reactor and subjected to the conditions specified in Table 2.1. We varied the power from 10 mW/cm² to 200 mW/cm², However the impact of plasma power density on the density and diameter of drops reduced from layers of SnO_2 and ITO was marginal.

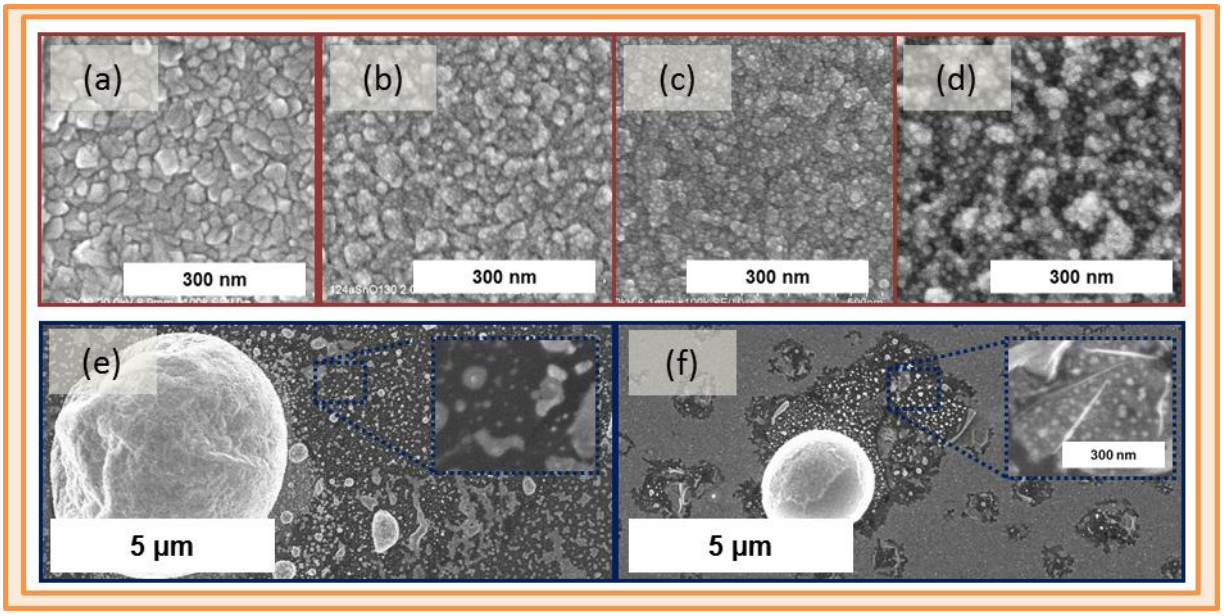

2.13 – Reduction of SnO_2 and ITO as a function of H_2 plasma power density.
Glass/SnO_2 (80 nm) substrates (a) reduced for 5 minutes in a H_2 plasma at 250 °C with a power density of 10 mW/cm² (b), 50 mW/cm² (c), 200 mW/cm² (d). cSi/ITO (20 nm thick) substrates reduced for 5 minutes in a H_2 plasma at 250 °C with a power density of 10 mW/cm² (e) and 200 mW/cm² (f).

In the case of SnO_2, increasing the plasma powers conspicuously softened the surface features of the SnO_2 crystals on which the metal drops formed (Figure 2.13.a-d). However it only modestly increased the diameter and density of the drops themselves (Figure 2.14). The diameter of the metal drops also increased modestly at higher plasma powers, but their average diameter decreased.

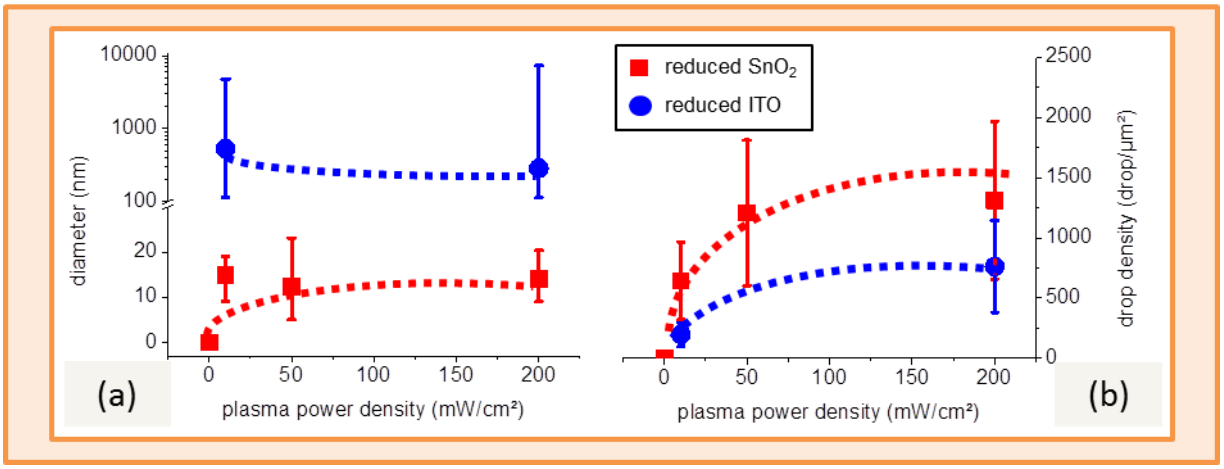

2.14 – Metal drop diameter and density as a function of H_2 plasma power SnO_2 and ITO layers.
Evolution of the diameter (a) and density (b) of metal drops formed at the surface of SnO_2 and ITO substrates exposed to hydrogen plasmas with a power density of 10 mW/cm², 50 mW/cm² and 200 mW/cm².

In summary, the plasma power during the reduction process was not observed to affect the drop configuration over the range studied. However these experiments revealed an important factor which we had previously overlooked in our depositions: the contamination of metal drops by sidewall silicon.

3.3. Sidewall silicon contamination

A layer of foreign material was observed to form over large portions of the sample surface (the homogeneous light grey areas in Figures 2.13.e-f). This could be explained by Si being sputtered or etched from the plasma reactor sidewalls during the H_2 plasma process and depositing over the samples. To observe the potential scale of Si contamination during the H_2 plasma, we reduced two identical SnO_2 samples, one in a chamber that had just been cleaned and conditioned in a stable layer of a-Si:H, the other in a chamber which had undergone high temperature Si deposition conditions typically adopted to grow our SiNWs (resembling those prior to the reduction of the samples in Figure 2.13.e-f). Plasma conditions for the chamber coating are described in Table 2.2.

Table 2.2: Plasma conditions for coating the Plasfil chamber with a-Si:H

	H_2 flux	SiH_4 flux	pressure	plasma power	Temp.	time
H_2 etch	200	0	260 mTorr	300 mW/cm²	100 °C	30 minutes
stable a-Si:H	0	10	120 mTorr	20 mW/cm²	100 °C	15 minutes
high temperature a-Si:H	0	10	380 mTorr	20 mW/cm²	500 °C	15 minutes

In the first case, the reactor sidewalls were exposed to an extensive, high-power H_2 plasma and then coated in a layer of a-Si:H deposited at 100 °C (Table 2.2). A glass/SnO_2 substrate was then exposed within the conditioned chamber to the standard reductive H_2 plasma conditions (Table 2.1). Its

surface emerged with the texture of the SnO_2 crystals still visible behind the reduced metal drops (Figure 2.15.a). We then exposed the reactor sidewalls to a silane plasma at a nominal temperature of 500 °C (see Annex). At this temperature, hydrogen atoms cannot adsorb to the sample surface and will therefore not passivate the growth front during deposition, arguably leading to a less stable material. An identical glass/SnO_2 substrate was loaded in the chamber and exposed to the standard metal reducing H_2 plasma (Table 2.1). Non-circular structures emerged at its surface with a broader size range than the drops observed on the previous sample (Figure 2.15.b). The area between these structures was generally flat and closer inspection revealed several of the structures presented the conical shape of silicon nanowires.

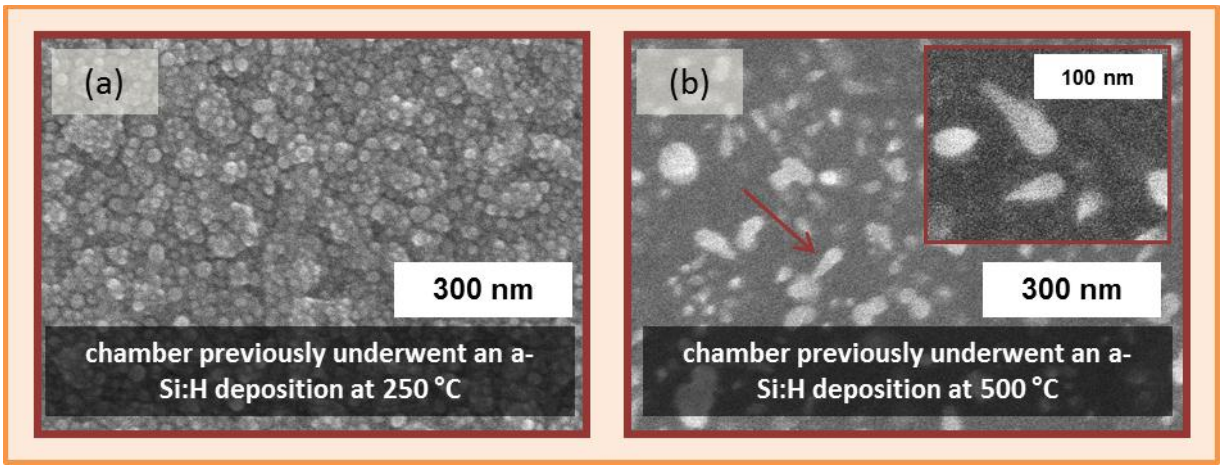

2.15 - Contamination from sidewall Si deposition.
SnO_2 reduced under a H_2 plasma for five minutes in a chamber which had previously underwent a deposition of hydrogenated amorphous silicon at 250 °C (a) and 500 °C (b).

The mechanism by which Si contamination from the sidewalls alters the diameter and distribution of metal drops remains unclear. It can change the chemical composition of the substrate over which the metal particles may diffuse, it can alloy with the metal drops to change their physical properties, it can bury Sn drops and shield the SnO_2 layer from the plasma… Identifying the exact role of this contamination could constitute an interesting and potentially useful topic in controlling the size and density of drops formed. However, considering present difficulties without Si contamination, we opted for keeping the sidewall conditions constant for each batch of samples by regularly conditioning the chamber.

3.4. The substrate temperature

The last plasma process parameter we shall look into is the substrate temperature. Among its many roles, the temperature governs the state (liquid, solid or vapor) of the metal reduced, its tendency to diffuse and, as mentioned above, whether H atoms adsorb at the surface of the sample. To investigate its impact, substrates of glass/SnO_2 (80 nm) and glass/ITO (20 nm) were exposed to standard H_2 plasmas (Table 2.1) at temperatures of 200, 250 and 500 °C. Increases in the temperature were observed to strongly influence the morphology of metal drops reduced, but SnO_2 and ITO substrates responded to them in different manners (Figure 2.16). On SnO_2 substrates, the

diameter of Sn drops formed at 200 °C was 10 to 30 nm (Figure 2.16.a) and increased by a factor of 20 as the temperature was increased to 500 °C (Figure 2.16.a-c). We also observed that the density of drops decreased as the temperature was increased (Figure 2.17.b), which may be ascribed to smaller drops coalescing as they grow. In the case of ITO substrates, drops with diameters larger than a micron formed at temperatures as low as 200 °C (Figure 2.16.d). However when the temperature was increased, their average diameter shrunk to 700 nm at 250 °C and to 50 nm at 500 °C (Figures 2.16.e-f).

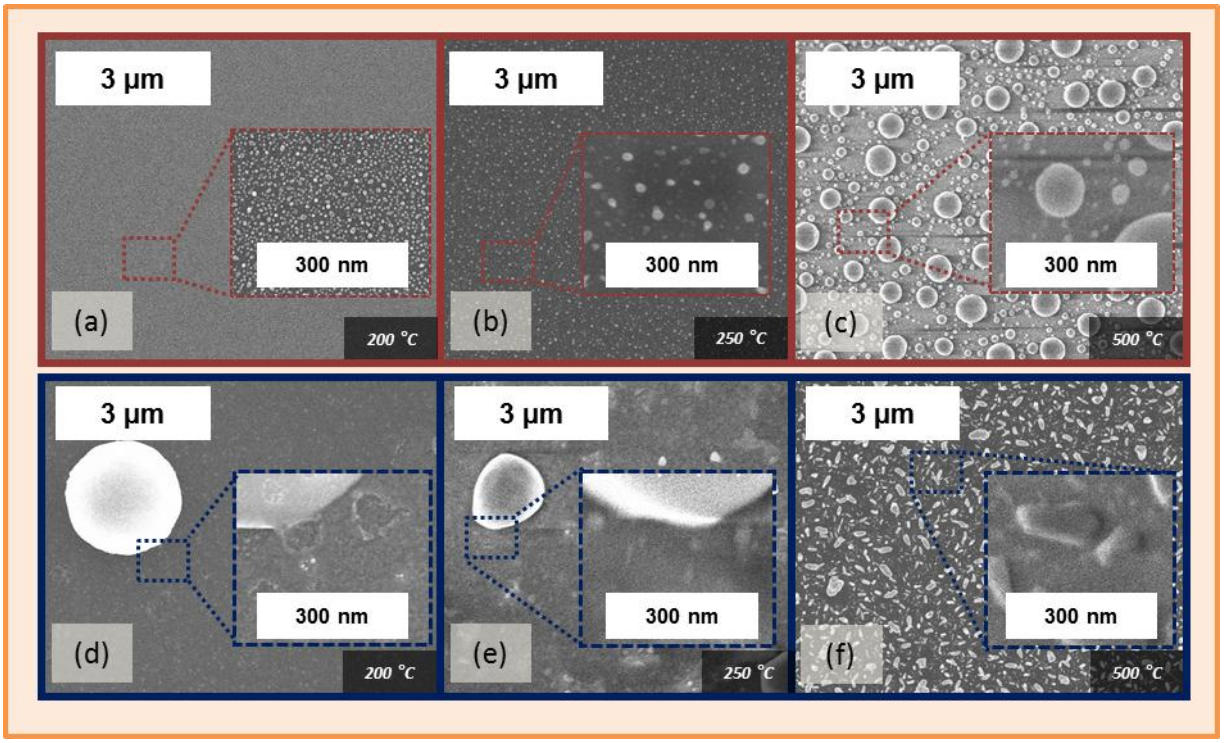

2.16 - Effect of H_2 plasma temperature on metal drops reduced from SnO_2 and ITO layers.
Glass/SnO_2 (80 nm) substrates reduced in a H_2 plasma at 200 °C (a), 250 °C (b) and 500 °C (c). Glass/ITO layers (20 nm) sputtered on glass and reduced in a H_2 plasma at 200 °C (d), 250 °C (e) and 500 °C (f).

At 500 °C, micron-diameter drops were no longer observed on the sample surface (Figure 2.17.b). In summary, reduced layers of SnO_2 and ITO responded in opposite manners. As the substrate temperature increased, drops reduced from SnO_2 grew larger and those reduced from ITO grew smaller (Figure 2.17). In order to gain further insight into the role that the temperature plays on the metal drop distribution, we broke the plasma process down into four steps. Substrates of SnO_2 and ITO were exposed to a standard (Table 2.1) hydrogen plasma at 250 °C. Identical substrates were exposed to the same 250 °C plasma followed by an annealing step during which the sample was heated for one hour at 500 °C under a hydrogen pressure of 1 Torr (but no plasma was ignited). Other identical substrates were exposed to the same 250 °C plasma and heated; however when the temperature had stabilized at 500 °C, they were exposed to a brief (1 second) hydrogen plasma in order to reduce the surface oxide on the sample, and then left under a H_2 gas pressure of 1 Torr at 500 °C for one hour. The final batch of substrates were heated to 500 °C before being exposed to a H_2 plasma (process conditions other than temperature were the same as in Table 2.1). The objective

was to identify whether the heating, the plasma or both effects were responsible for changing the diameter and density of the metal drops.

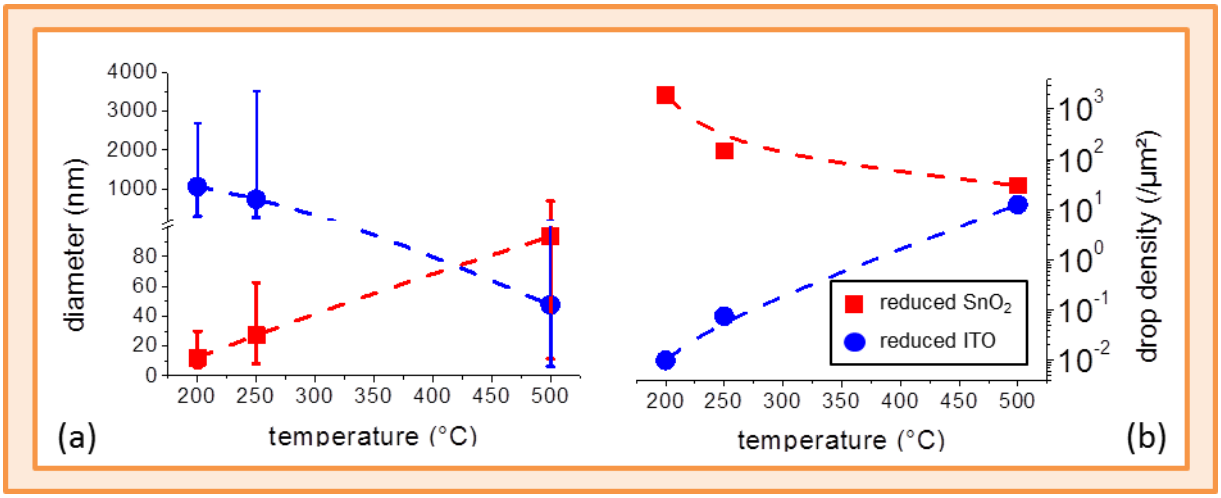

2.17 – Diameter and density of metal drops reduced from ITO and SnO_2 layers as a function of temperature.
The diameter (a) and density (b) of metal drops reduced on the surface of SnO_2 and ITO substrates at increasing temperatures.

In the case of SnO_2, simply increasing the temperature of the metal drops once they had been formed at 250 °C was not observed to alter their configuration (Figure 2.18.b). Likewise, exposing them to a brief H_2 plasma did not lead to larger drops - but was observed to trigger limited VLS growth of SiNWs (Figure 2.18.c).

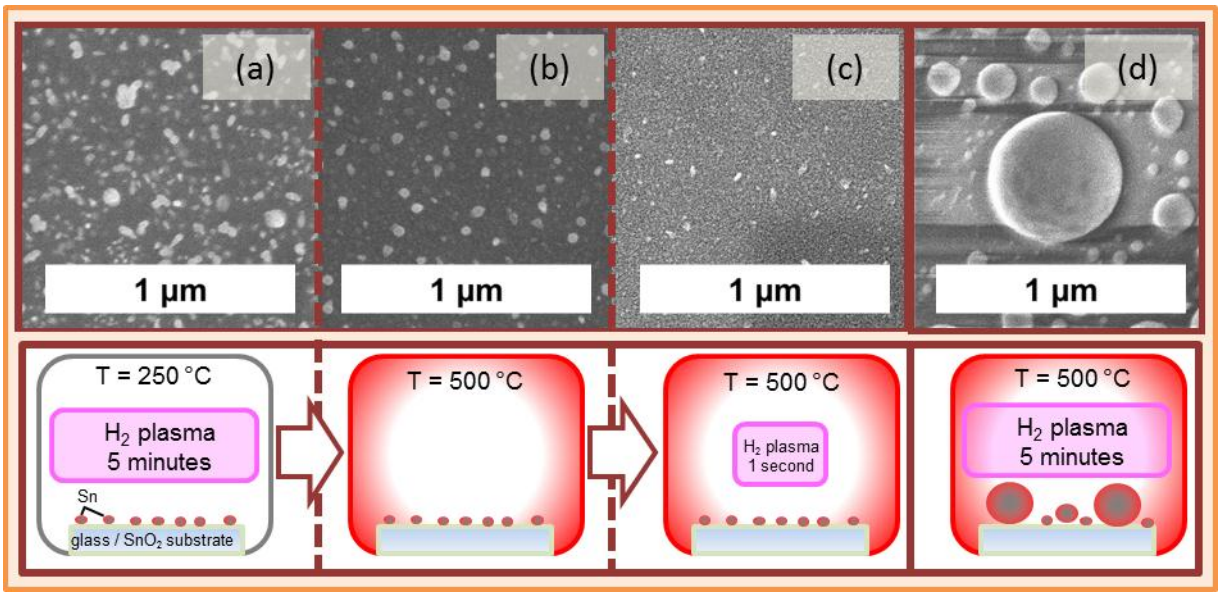

2.18 - Step-by-step response of glass/SnO2 substrates to heating and plasma reduction.
SnO_2 substrates were exposed to a H_2 plasma at 250 °C for 5 minutes (a), heated to 500 °C (b), then exposed again to a H_2 plasma for a duration of 1 second (c). The size and density of the drops contrast starkly with those produced when the substrate was exposed to a H_2 plasma at 500 °C for 5 minutes (d).

In contrast, when the five minute hydrogen plasma was performed at high temperature, the difference in the morphology and distribution of the drops was striking (Figure 2.18.d). The overall surface area covered in Sn was also observed to increase at higher temperature, suggesting that heating may increase the effectiveness of the reduction process. The situation differed considerably for ITO substrates. At low temperatures, large drops of metal formed on the sample surface (Figure 2.19.a) while at high temperatures, small ones did (Figure 2.19.d). Surprisingly, when large drops were formed at low temperature and heated to 500 °C, they remained intact (Figure 2.19.b). However, the second a hydrogen plasma was ignited, they disintegrated (Figure 2.19.c), leading to similar results as if the entire reduction process had taken place at 500 °C (Figure 2.19.d). This substantial reconfiguration of metal drops may signal the presence of a surface oxide shell encapsulating the metal drops. In or Sn oxide would not melt at 500 °C and might hold the liquid metal within it in place. Removing the surface oxide could therefore allow the metal inside the drop to diffuse

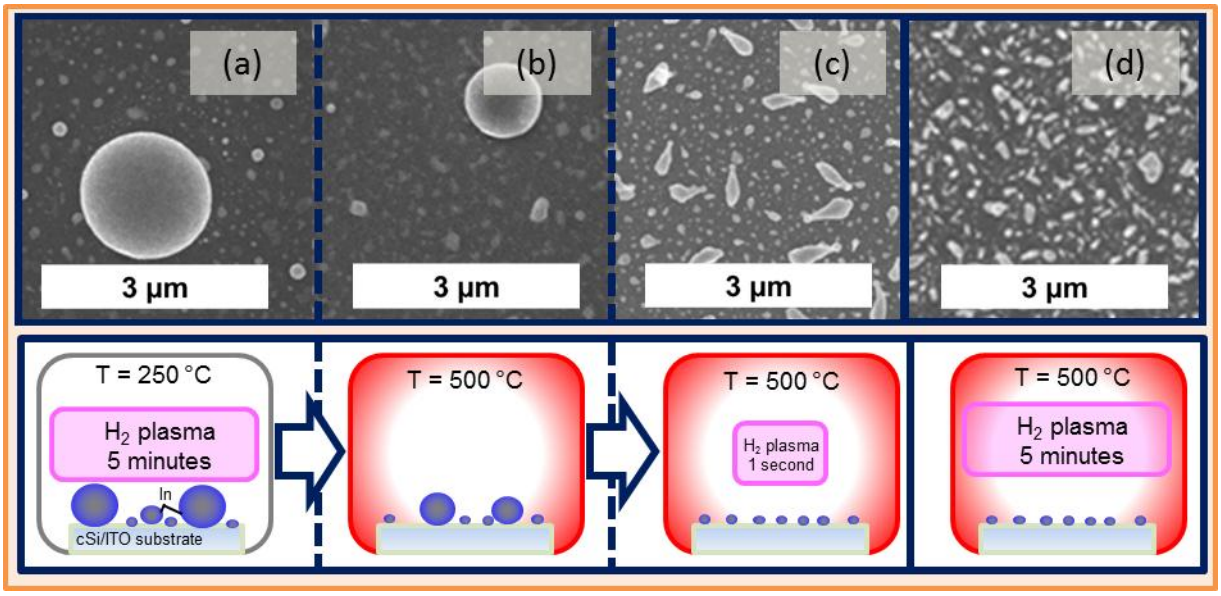

2.19 - Step-by-step response of cSi/ITO substrates to heating and plasma reduction.
Substrates of crystalline Si sputtered with 20 nm of ITO were exposed to a H_2 plasma at 250 °C for 5 minutes (a), heated to 500 °C (b), then exposed again to a H_2 plasma for a duration of 1 second (c). The size and density of the drops contrast starkly with those produced when the substrate was exposed to a H_2 plasma at 500 °C for 5 minutes (d).

Although the mechanism remains unclear, this study shows that the substrate temperature during hydrogen plasma exposure of metal oxide can substantially alter the density and diameter of reduced metal drops. Surprisingly, the way in which the configuration is altered differs very much in the case of SnO_2 or ITO substrates. One important distinction between these two substrates which may shed light on these results is the nature of the two substrates. Metal reduced on the SnO_2 surface diffuses on a conductive and slightly textured material while the metal reduced on thin layers of ITO may be diffusing on dielectric and flat substrates of silica. Measuring the chemical potential of composite surfaces is a delicate matter, and measuring that of the nanoscopic drops we study, all the more so. However, some insight into the potential contribution of the substrate on drop configurations could easily be gathered by altering the substrate on which the ITO was deposited. We therefore sputtered layers of ZnO:Al (1 µm thick) over glass substrates under a vacuum of 10^{-6} mbar, an argon flow rate of 40 sccm, a plasma power density of 2 W/cm² and a temperature of 350 °C for a

duration of 40 minutes. These glass ZnO substrates were then covered in ITO (20 nm) to offer a middle ground between the two substrates previously used.

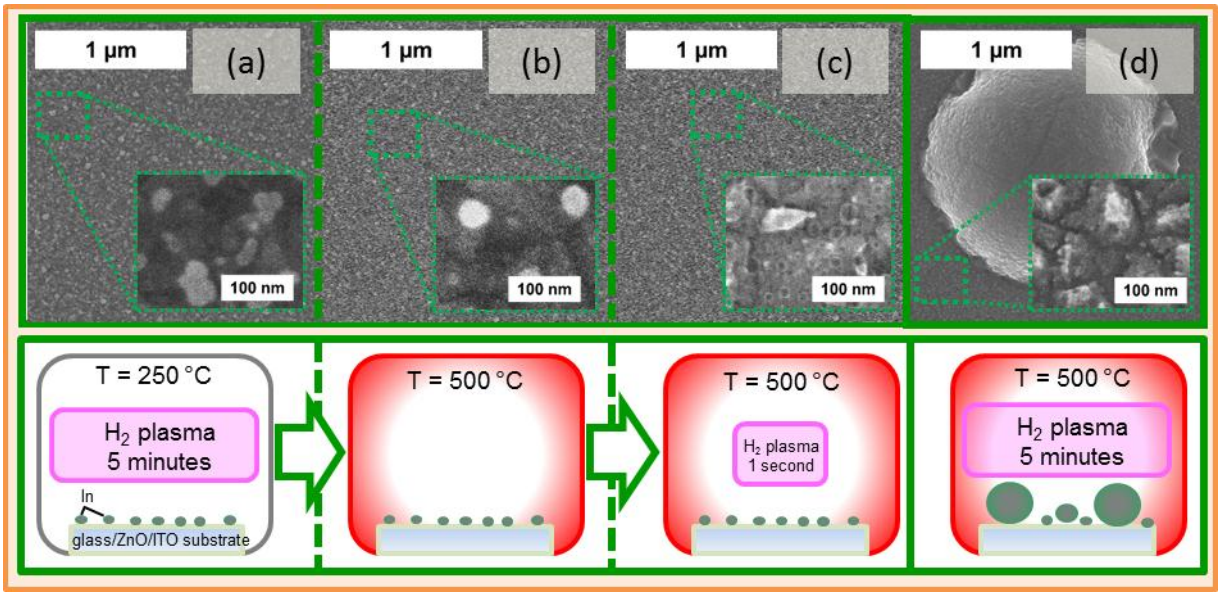

2.20 - Step-by-step response of ZnO/ITO substrates to heating and plasma reduction.
Substrates of glass sputtered with 1 µm of ZnO and 20 nm of ITO were exposed to a H_2 plasma at 250 °C for 5 minutes (a), heated to 500 °C (b), then exposed again to a H_2 plasma for a duration of 1 second (c). The size and density of the drops contrast starkly with those produced when the substrate was exposed to a H_2 plasma at 500 °C for 5 minutes (d).

We submitted these substrates to the same step-by-step treatment of a heated H_2 plasma process and, surprisingly, the drops responded to temperature and plasma exposures according to the same pattern as reduced SnO_2 substrates (Figure 2.18). Drops in the range of 10 to 50 nm formed at low temperature (Figure 2.20.a). Heating them or exposing them to a high temperature plasma for 1 second did not increase their size (Figure 2.20.b-c). However, reducing the ITO layer with a H_2 plasma at 500 °C instead of 250 °C resulted in the formation of drops with diameters hundreds of nanometers wide. The fact that the contribution of the substrate may dominate the configuration of the reduced metal drops rather the metal or the plasma parameters used opens interesting possibilities.

4. Thin layers of tin and ITO over stable zinc oxide

To explore the possibilities offered by this new substrate we investigated the behavior with respect to temperature of reduced ITO layers deposited with increasing thickness over glass/ZnO substrates.

4.1. Layers of ITO with increasing thickness

Substrates were prepared with a layer of 1 µm thick ZnO covered in ITO layers with thicknesses of 1 nm, 10 nm, 20 nm and 120 nm. The substrates were exposed to a H_2 reductive plasma under conditions identical to Table 2.1 except that the temperature was reduced to 200 °C. Reduced layers

of ITO (1 nm thick) formed small drops 5 to 30 nm in diameter (Figure 2.21.a). Their density reached 1800 drops per µm² and their configuration remained largely unaffected by plasma treatments at temperatures as high as 400 °C (Figure 2.23).

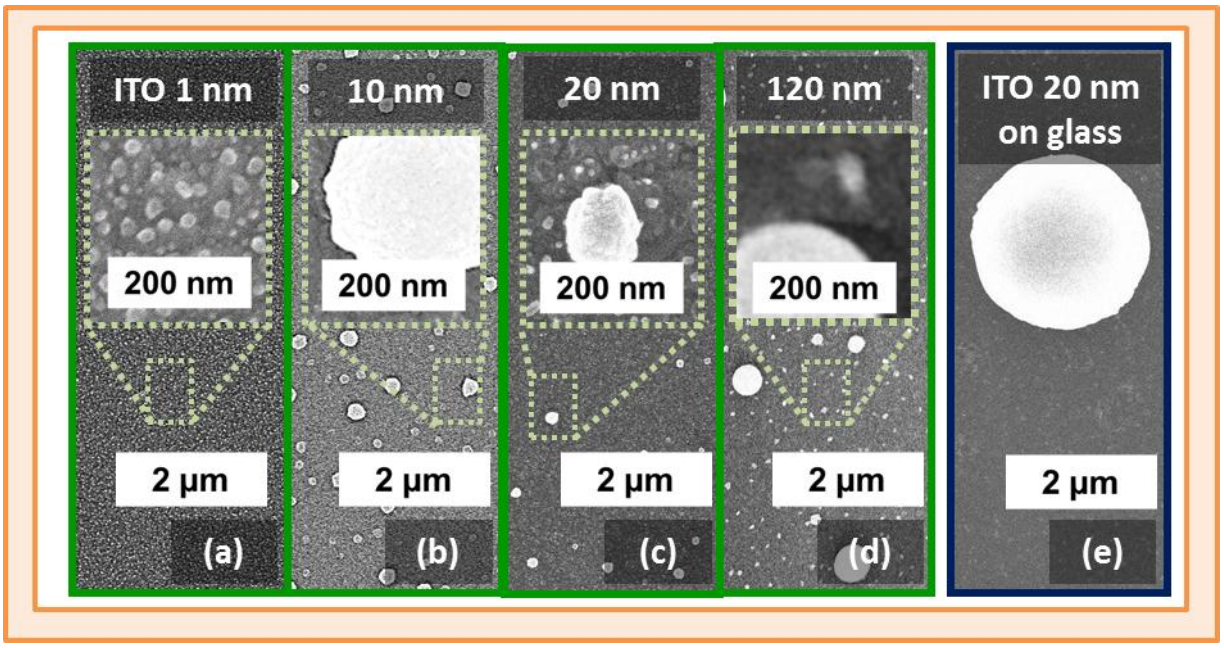

2.21 - Metal drops reduced from increasingly thick ITO layers.
Substrates of glass sputtered with ZnO (1 µm) and a layer of ITO 1 nm (a), 10 nm (b), 20 nm (c) and 120 nm (d) thick were exposed to the same H_2 plasma. A sample of ITO (20 seconds) sputtered on glass was included in the same plasma run.

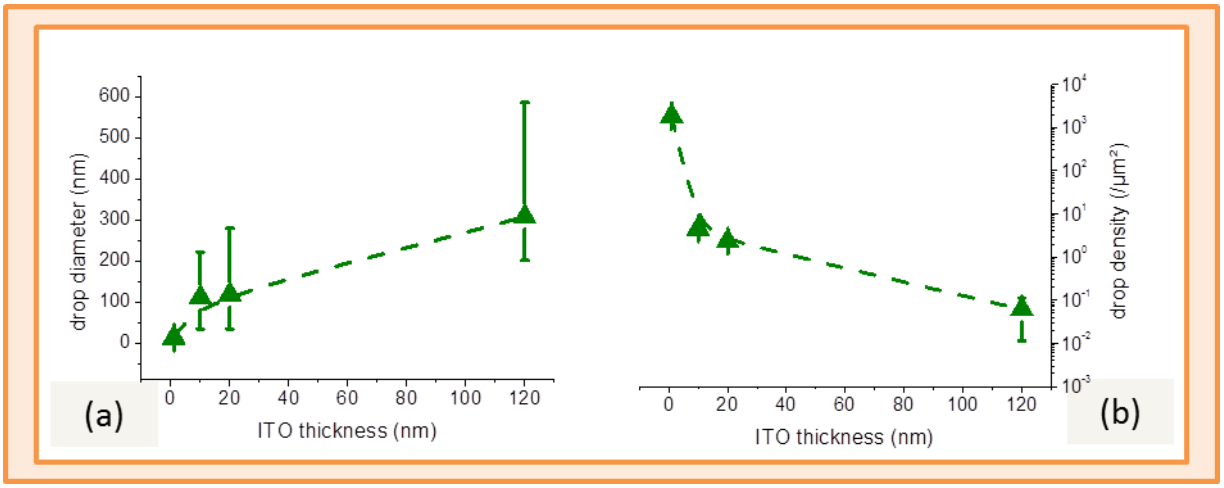

2.22 - Diameter and density of metal drops reduced from increasingly thick layers of ITO.
Diameter (a) and density (b) of metal drops reduced in a H_2 plasma from substrates of glass sputtered with ZnO (1 µm) and a layer of ITO 1 nm, 10 nm, 20 nm and 120 nm thick.

Layers of ITO 10 and 20 nm thick displayed the familiar patterns of drops several hundreds of nanometers in diameter and 2 – 5 drops per µm² (Figure 2.21.b-c). The 120 nm-thick layer of ITO produced a similar spread of drops with diameters ranging from 200 to 600 nm and a density of 0.05 drops per µm² (Figure 2.21.d). These results indicate that (as in the case of reduced SnO_2) the

diameters of the metal drops are related to the thickness of the ITO layer from which they are extracted (Figure 2.22.a), and that the density of drops decreases as their diameters increase (Figure 2.22.b). However, in this case, the considerable distance separating the metal drops from each other raises doubts as to whether this occurs due to coalescence. A substrate of glass covered in ITO (20 nm) was included in the same hydrogen plasma run. The metal drops which formed on its surface were considerably larger than those on the glass/ZnO substrates, highlighting the effect of the substrate surface on the configuration of the drops (Figure 2.21.e). In fact, the nature of the substrate is also liable to play a part in the configuration of the glass/ZnO samples presented in Figure 2.21. Whereas on thicker layers of ITO, the metal drops diffuse over an ITO crystal, in the case of the 1 nm-thick layer of ITO, the drops are most likely in immediate contact with the ZnO substrate. This could alter their behavior and explain why 1-nm thick layers of ITO do not respond to temperature variations during reduction.

4.2. Substrate temperature

We investigated the effect of the substrate temperature on reduced layers of ITO deposited over glass/ZnO substrates. To identify possible implications of the substrate surface, the study was conducted on both 1 nm-thick and 20 nm-thick layers of ITO. The samples were exposed to the same run of H_2 plasmas at temperatures ranging from 200 to 400 °C. In the case of the 1nm-thick layer of ITO, the drop configurations revealed striking similarity regardless of the temperature used (Figure 2.23). Ignoring the effect of VLS growth presumably resulting from sidewall deposition of silicon, the diameter of drops remained largely identical. At higher temperatures, their density was observed to gradually decline; however this may possibly be a result from increased evaporation of the In drops.

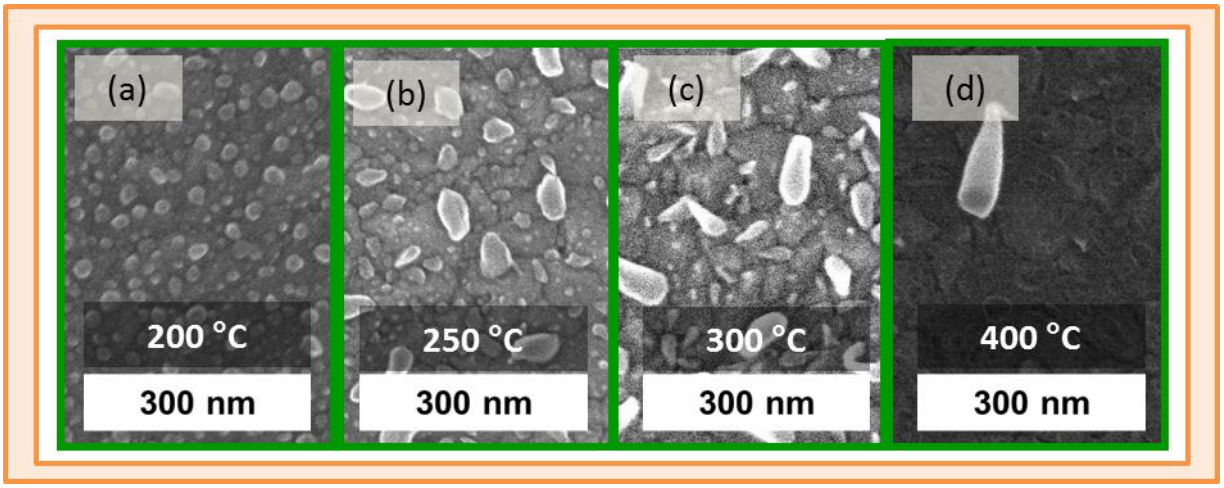

2.23 - Effect of reduction temperature on thin (1 nm) layers of ITO.
Metal drops reduced from 1 nm-thick layers of ITO sputtered over ZnO covered glass substrates show no marked variation in diameter despite increasing the H_2 plasma temperature from 200 °C (a), 250 °C (b), 300 °C (c) to 400 °C (d).

In contrast, glass/ZnO substrates covered in 20 nm-thick layers of ITO showed a strong correlation between the substrate temperature during the reducing H_2 plasma and the diameter of metal drops. At 200 °C, drops formed with diameters of 80 to 110 nm (Figure 2.23.a). As the temperature of the H_2

plasma was increased to 500 °C, their average diameter progressively increased to 5 µm and their density decreased by four orders of magnitude (Figures 2.24.b-d).

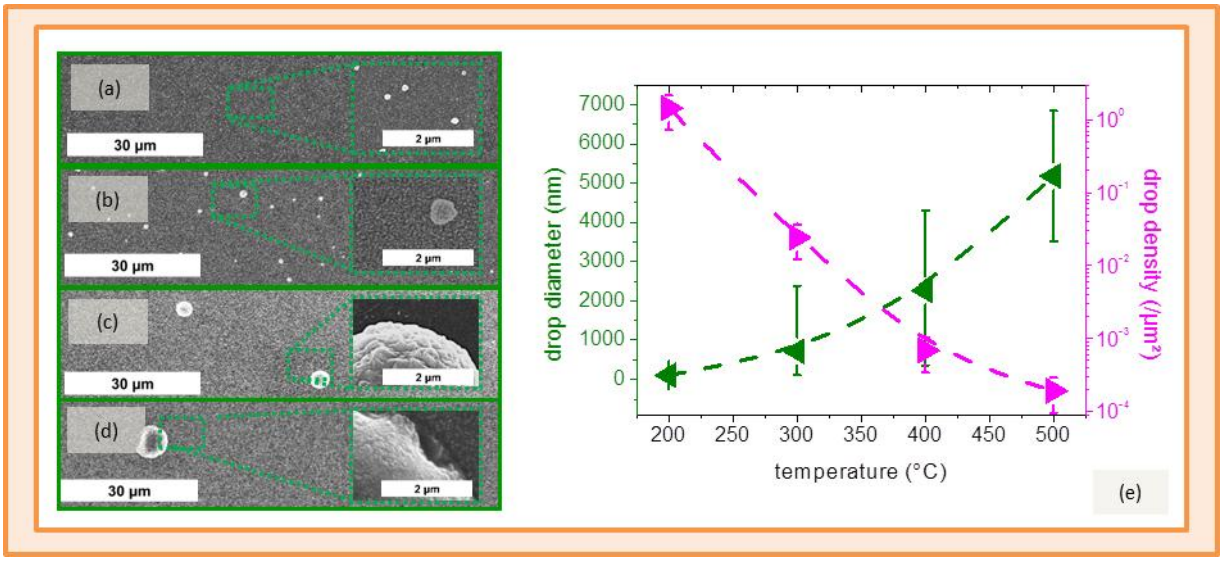

2.24 - Effect of temperature on metal drops reduced from layers of ITO.
Substrates of glass sputtered with ZnO (1 µm) and ITO (20 nm) were exposed to a H_2 plasma at 200 °C (a), 300 °C (b) , 400 °C (c) and 500 °C (d). The diameter and density of the metal drops reduced during this process is presented as a function of temperature (e).

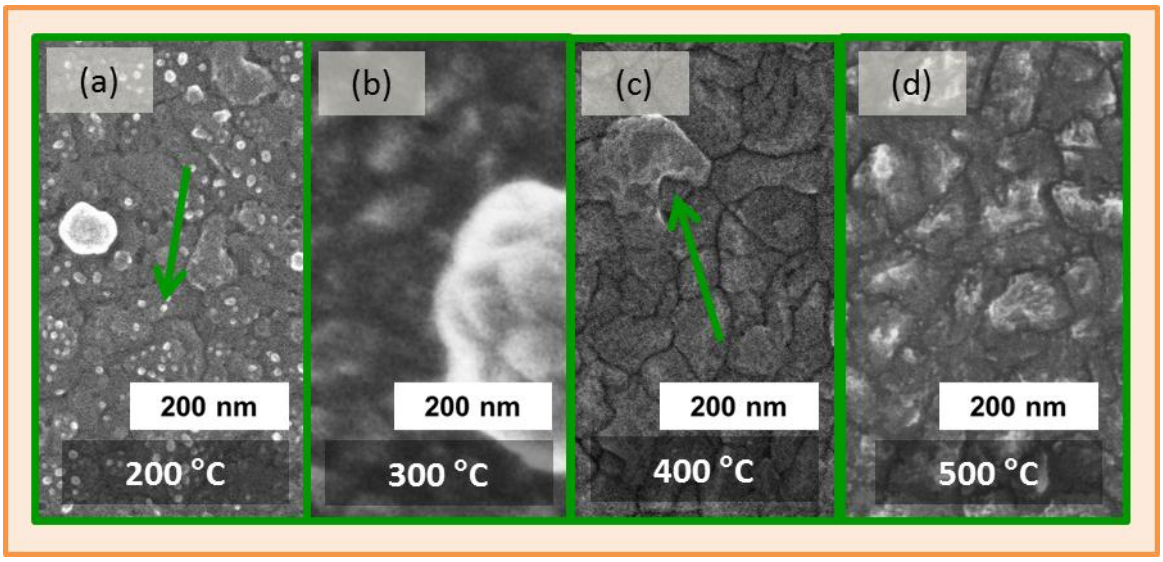

2.25 - Surface features of ITO layers reduced in a H_2 plasma.
Higher magnification SEM micrographs of ITO layers sputtered over glass/ZnO substrates and reduced in a H_2 plasma at 200 °C (a), 300 °C (b), 400 °C (c) and 500 °C (d).

Closer inspection of the sample surface between drops revealed again the crystalline surface of ZnO. At lower temperatures, small metal drops lay scattered over the sample surface (Figure 2.25.a). At higher temperatures, the texture of the ZnO became more apparent and was inhomogeneously covered in a layer which could be metal (Figure 2.25.c). The small ubiquitous quantities of metal may result from the surface migration of atoms from the larger drops observed in Figure 2.24.[11] The

results in Figures 2.24 demonstrate that the radius and density of liquid metal drops reduced from layers of ITO can be controlled by adapting the substrate and plasma conditions.

4.3. Combining temperature, Sn and ZnO

We also turned our attention to Sn catalysts on ZnO surfaces. Combining lessons learnt from previous studies, we investigated the effect of Sn layer thickness, the nature of the substrate and the H_2 reduction plasma temperature.

2.26 - Sn drops formed on ZnO with increasingly thick layers and high reduction temperatures.
Metal drops formed by evaporating increasingly thick layers of Sn on glass/ZnO substrates and submitting them to a H_2 plasma at temperatures of 250 °C (a, e, i), 350 °C (b, f, j), 450 °C (c, g, k) and 600 °C (d, h, l). The nominal thickness of the Sn layers was 0.5 nm (a-d), 1 nm (e-h), 5 nm (j-l).

Sn layers were therefore evaporated with a nominal thickness of 0.5 nm, 1 nm and 5 nm over substrates of glass/ZnO (identical to those used in the previous study). They were exposed to a H_2 plasma under the conditions described in Table 2.1 at temperatures of 250 °C to 350 °C, 450 °C and 600 °C (Figure 2.26). The metal drops which formed on these substrates presented diameters of up to 20 nm. At 250 °C and 350 °C, heating was not observed to affect the distribution of drops on the ZnO surface (which resembled closely the distribution of drops observed when Sn was evaporated on glass substrates in Figure 2.2). However, the thickness of the Sn layer evaporated determined the diameter of the drops. When exposing the substrates to a hydrogen plasma at a temperature higher than 450 °C, drops were no longer visible on the sample surface. Instead a discontinuous film covered the ZnO substrate (Figure 2.26.g,k,d,h,l). Exposing samples with no visible drops to a silane plasma did however lead to the growth of silicon nanowires (Figure 2.27), indicating that metal remained present (although not visible) on the sample surface.

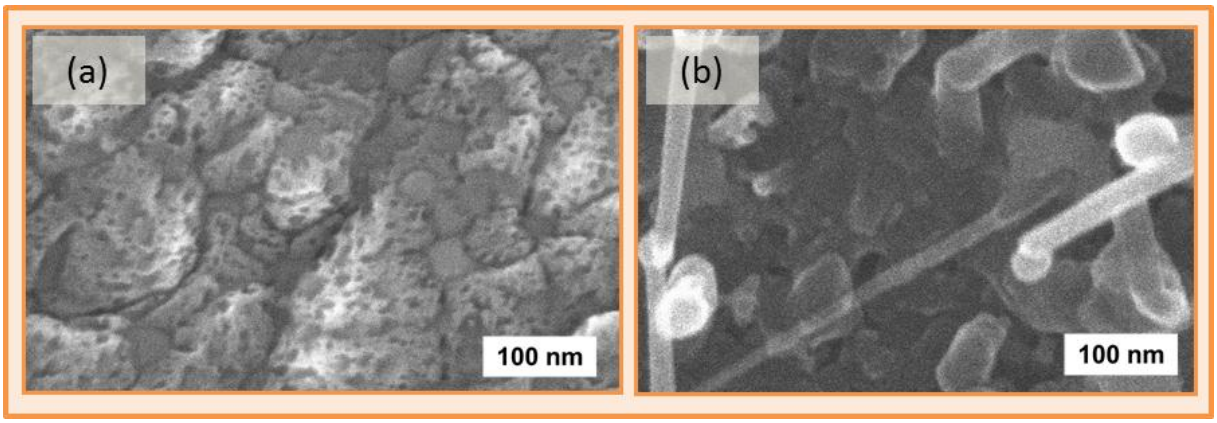

2.27 - Observations of nanowire growth on glass/ZnO substrates covered in wetting Sn.
Sn evaporated over ZnO and exposed to a H_2 plasma at 450 °C showed no drop formations (a) however the substrates nonetheless catalyzed SiNW growth when then exposed to a SiH_4 plasma at 500 °C (b).

While our attempts to control the configuration of Sn drops by heating them were of limited success, the drops formed at 350 °C for layers of Sn 1 – 5 nm thick displayed diameters in the 5 – 20 nm range and comparatively high densities (Figure 2.26.f&j). This configuration proved instrumental in making the tightly packed arrays of low-diameter SiNWs used in Chapter 5.

5. Conclusion

The objective of the studies reported in this chapter was to control the distribution of nanometric metal drops over a solid surface using only techniques compatible with a one-pump-down process (by altering the plasma parameters, substrate material, temperature…). Considerable advances towards this goal have been made and much has been learnt on the behavior of liquid Sn and In in the process. Throughout these studies, it was observed that all metal layers, either evaporated or reduced from the surface of oxides, dewetted on their substrate. The diameter of the drops which they produced depended primarily on the amount of metal provided. Longer evaporations of Sn spontaneously formed drops with larger diameters (Figure 2.2-3), as did reducing thicker layers of ITO (Figure 2.21). These results are qualitatively summarized in Table 2.3.

Table 2.3: Metal drops formed from metal films of different thickness			
Sn **thickness:**	5 nm	40 nm	100 nm
on glass substrates	small and dense	larger and dense	large and dense
ITO thickness:	1 nm	20 nm	120 nm
on glass/ZnO substrates	small and dense	larger and sparse	large and sparse

We attempted to gain more control over the density and diameter of the metal drops by reducing layers of SnO_2 (80 nm) and ITO (20 – 100 nm) in a hydrogen plasma. This approach offered additional levers of control over the system, including the temperature, duration and intensity of the reducing plasma. Striking differences were observed throughout our studies between the configuration of metal drops reduced from layers of SnO_2 and ITO under identical plasma conditions. At temperatures of 250 °C, metal drops reduced from layers of SnO_2 presented high densities and diameters generally in the tens of nanometers (Figure 2.8). In contrast, ITO samples produced much larger drops in lower densities, with diameters reaching several microns (Figure 2.9). Longer or higher power plasmas marginally increased the diameter of metal drops reduced from SnO_2 (Figure 2.8) but affected reduced layers of ITO very little (Figure 2.13). The modest impact of the plasma power and duration on the configuration of metal drops is summarized in Table 2.4.

Table 2.4: Metal drops formed under longer or higher power H_2 plasma					
	no plasma	250 °C 1 minute	250 °C 10 minutes	250 °C 10 mW	250 °C 200 mW
glass/Sn (5 nm)	small and dense	small and dense	small and dense	small and dense	small and dense
cSi/Sn	small and dense	small and dense	small and dense	small and dense	small and dense
glass/SnO_2 (80 nm)	none	small and dense	less small, still dense	small and dense	less small, still dense
cSi/ITO(20nm)	none	large and sparse	large and sparse	large and sparse	large and sparse
glass/ITO (90 nm)	none	large and sparse	large and sparse	not tested	

In contrast, the density and diameter of the metal drops reduced from SnO_2 and ITO layers was observed to vary substantially according to the temperature at which they were exposed to the reductive H_2 plasma. While layers of SnO_2 produced progressively larger metal drops for progressively temperatures, drops reduced from ITO layers tended to grow progressively smaller (Figure 2.16). Intriguingly, micron-large metal drops reduced at low temperature from ITO layers were observed to shatter into small drops (with diameters in the tens of nanometers) when exposed, even briefly, to a H_2 plasma at 500 °C (Figure 2.19). This behavior suggests that an oxide shell forms at the drop surface, containing the liquid metal at high temperature. It remains unclear why the metal reduced from layers of SnO_2 stabilizes as large drops at high temperature, while metal reduced from ITO forms smaller drops under the same conditions. A clue may lie in the substrate on which the metal drops diffuse. When the same layer of ITO was deposited over a thick layer of ZnO instead

of glass, the reduced metal responded to increases in the H_2 plasma temperature by forming larger drops, not smaller ones (Figures 2.18 & 2.19). These results are summarized in Table 2.5.

Table 2.5: Metal drops formed from TCOs reduced by H_2 plasma under different temperatures

	250 °C	250 °C + 500 °C (1 second)	500 °C
glass/SnO_2	small and dense	small and fewer	large and sparse
glass/ITO	large and sparse	small and dense	small and dense
glass/ZnO/ITO	small and dense	small and fewer	large and sparse

On the basis of these observations, we deposited ITO layers with different thicknesses on Glass/ZnO layers and optimized the temperature at which they were reduced. In doing so, it was possible to vary the diameter of the metal drops over a range of 75 – 5000 nm and their density from 1 to 10^{-4} drops per µm² (Figures 2.22 & 2.24). Metal drops with smaller diameters were also obtained by evaporating thin films (0.5 – 5 nm thick) of Sn on glass/ZnO substrates. However varying the temperature and other plasma parameters proved incapable of altering the diameter and density of these drops (Figure 2.26). The same independence from temperature was observed on very thin layers of ITO (also 1 nm thick) deposited on glass/ZnO substrates (Figure 2.21.a).

In these studies, silicon was at times observed to sputter from the reactor sidewalls onto the substrate during the H_2 reduction of the catalysts and to initiate VLS growth when coming in contact with Sn or In drops (Figure 2.15). This constitutes a risk to reproducibility in these samples as the presence of Si drastically alters the density and diameter of the drops. Conditioning the chamber with a high energy H_2 plasma followed by a low temperature coating of a-Si:H was observed to contain this contamination.

In summary, drops of Sn and In were produced using techniques compatible with a single-pump down process at the surface of glass, silicon, ITO, SnO_2 and ZnO covered substrates. Their diameter and density were observed to vary according to the amount of metal provided, the temperature at which they were exposed to a hydrogen plasma and the nature of the substrate on which they formed. By tuning these parameters, it was possible to vary by over three orders of magnitude the diameter and density of In drops formed over ZnO substrates. However we failed to decorrelate the diameter of the drops from their density. Applications in radial junction solar cells favor thin nanowires (with diameters under 100 nm) with low densities (preferably fewer than ten nanowires per µm²) in view of minimizing the thickness of the doped nanowires and facilitating their conformal coverage. Although we have uncovered diverse techniques of producing configurations of small and dense metal drops or large and sparse ones, forming small and sparse drops has remained more challenging. As a compromise, the majority of work conducted on radial junction devices (Chapter 5) was performed on 1 nm-thick layers of Sn evaporated on glass/ZnO substrates. Layers of ITO 10 nm and 20 nm-thick sputtered on glass/ZnO substrates were briefly adopted in attempts to alter the density of nanowires in Chapter 5. In Chapter 4, substrate reproducibility is key, so we look into the growth process for silicon nanowires with standard glass/SnO_2 (80 nm) substrates.

Perspectives

Throughout these studies, we have grouped many factors under the "nature of the substrate" which would be interesting to investigate independently. These include the surface roughness, conductivity and surface tension. High melting point metals (steel, Ag or Al) offer an interesting alternative substrate in this respect as they present flat and conductive surfaces with differing surface tensions. There is no reason to restrict the search to transparent substrates. At the time of these studies, we intended to build our cells in a substrate configuration and therefore wanted to form the metal drops on transparent conductive oxides. Advances presented in Chapter 5 have since lifted this requirement. In a similar way, the thickness of the catalyst containing layer and the temperature of the hydrogen plasma also conceal intricacies. For instance, the dimensions of the metal drops can affect the forces at work on them and the temperature may affect the hydrogen passivation of the substrate on which they diffuse. Dissociating these factors may help identify the ones guiding the dewetting process.

Contamination from sidewall silicon was kept in check throughout most of these studies; however a timely addition of silane to the reducing H_2 plasma might ultimately help achieve the desired drop configuration. We will see in Chapter 4 that, in the case of dense arrays of metal drops, the density and diameter of nanowires does not necessarily correspond to that of their catalysts prior to growth. During the first instants of VLS, the liquid metal reconfigures. Understanding how Si upsets the established distribution of dense arrays of metal drops could help engineer practical and reproducible nanowire arrays.

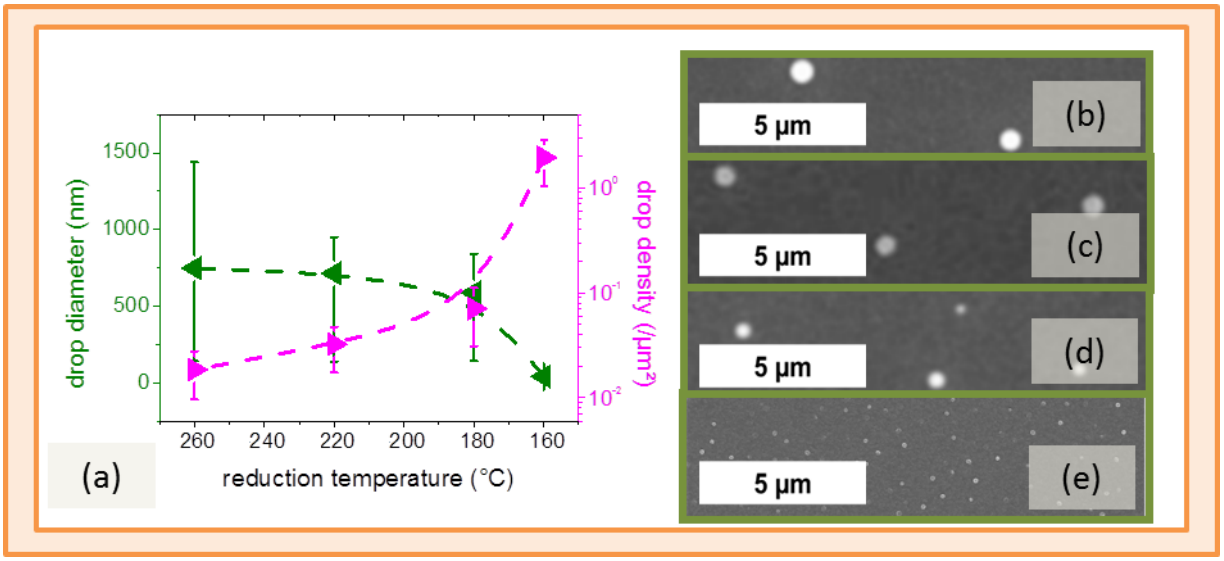

2.28 - Lower density metal drops reduced from layers of ITO in lower temperature H2 plasmas.
The diameter and density (a) of metal drops reduced at the surface of glass substrates sputtered with ZnO (1 μm) and ITO (20 nm) exposed to a H_2 plasma at 260 °C (b), 220 °C (c) , 180 °C (d) and 160 °C (e).

The studies presented on the metal drops formed from layers of ITO sputtered over ZnO resulted in a broad range of drop diameters, but none lower than 100 nm (Figures 2.24). However, we recently

discovered that by decreasing the temperature of the H_2 plasma to 260 °C, 180 °C and 160 °C, drops with average diameters of 750 nm, 600 nm and 40 nm could respectively be produced (Figure 2.28).[25] Conditions at 160 °C also led to an inter-drop spacing of 500 nm which offers a promising configuration for radial junction applications.

Many of the studies conducted in this chapter showed strikingly different behaviors between metal drops reduced from layers of SnO_2 and ITO. However, these differences could be interpreted as complementary or phase shifted. The increase in metal volume (Figure 2.11) or drop diameter (Figure 2.12) resulting from longer reduction plasmas gradually saturates for Sn drops, while under the conditions studied, it appears to have already saturated for In drops. Likewise, higher temperatures initially increase the drop diameter in both Sn and In (Figure 2.17 & 2.28); however the temperature required to observed this increase differs between the two. There is a potentially crucial distinction between In and Sn which has been neglected throughout these studies. Sn has a melting point of 232 °C, which is higher than that of In at 157 °C. Its boiling point and heat of vaporization are also higher. Attempts to understand the behavior of metal drops by comparing the two substrates under identical process conditions may therefore be misguided. Phenomena observed on In might only affect Sn in the same way at higher temperatures. This would imply that the phase response to temperature of each metal determines the window of process conditions within which a given drop configuration can be achieved.

The results in this chapter constitute our first steps into a vast field. The techniques developed have provided some useful building blocks for our radial junction solar cells and offered a glimpse of the potential for producing the metal drop configurations by methods of self-assembly. However there remains a great wealth of physics to be explored in the dewetting process of these liquid metals. We have gained some insight into how the diameter and density of forming metal drops can be changed, but we have barely begun to uncover why. Further studies into the role of the substrate surface or the phase response of the liquid may shed light on the mechanisms guiding these observations, and ultimately offer greater control over the catalyst drops seeding our radial junction cells.

BIBLIOGRAPHY

[1] Y.F. Guan, J.D. Fowlkes, S.T. Retterer, M.L. Simpson, P.D. Rack, Nanoscale lithography via electron beam induced deposition, *Nanotechnology,* 19 (2008), doi:10.1088/0957-4484/19/50/505302.
[2] B. Kayes, M.A. Filler, N.S. Lewis, H. Atwater, Structures of and methods for forming vertically aligned Si wire arrays, US Patent 2009/0020853 A1, 2009).
[3] I. Lombardi, A.I. Hochbaum, P. Yang, C. Carraro, R. Maboudian, Synthesis of High Density, Size-Controlled Si Nanowire Arrays via Porous Anodic Alumina Mask, *Chemistry of Materials,* 18 (2006) 988-991, doi:10.1021/cm052435x.
[4] T. Young, An Essay on the Cohesion of Fluids, *Philosophical Transactions of the Royal Society of London,* 95 (1805) 65-87, doi:http://www.jstor.org/stable/107159.
[5] P.G. Degennes, Soft Matter (Nobel Lecture), *Angewandte Chemie-International Edition in English,* 31 (1992) 842-845, doi:10.1002/anie.199208421.
[6] W.W. Mullins, Theory of Thermal Grooving, *Journal of Applied Physics,* 28 (1957) 333-339, doi:10.1063/1.1722742.
[7] D.J. Srolovitz, S.A. Safran, Capillary instabilities in thin films. I. Energetics, *Journal of Applied Physics,* 60 (1986) 247-254, doi:10.1063/1.337689.
[8] D. Quéré, Rough ideas on wetting, *Physica A: Statistical Mechanics and its Applications,* 313 (2002) 32-46, doi:10.1016/s0378-4371(02)01033-6.
[9] P.G. de Gennes, F. Brochard-Wyart, D. Quéré, *Gouttes, bulles, perles et ondes,* Belin, 2005, isbn: 9782701140551.
[10] M.C. Plante, J. Garrett, S.C. Ghosh, P. Kruse, H. Schriemer, T. Hall, R.R. LaPierre, The formation of supported monodisperse Au nanoparticles by UV/ozone oxidation process, *Applied Surface Science,* 253 (2006) 2348-2354, doi:10.1016/j.apsusc.2006.05.113.
[11] J.B. Hannon, S. Kodambaka, F.M. Ross, R.M. Tromp, The influence of the surface migration of gold on the growth of silicon nanowires, *Nature,* 440 (2006) 69-71, doi:10.1038/Nature04574.
[12] J.D. Carey, S.J. Henley, E. Mendoza, C.E. Giusca, A.A.A.D. T., S.S.R. P., Formation of Three Dimensional Ni Nanostructures for Large Area Catalysts, *MRS Proceedings,* 820 (2004), doi:10.1557/PROC-820-R8.3.
[13] K. Hiruma, K. Haraguchi, M. Yazawa, Y. Madokoro, T. Katsuyama, Nanometre-sized GaAs wires grown by organo-metallic vapour-phase epitaxy, *Nanotechnology,* 17 (2006) S369, doi:10.1088/0957-4484/17/11/S23.
[14] V.I. Merkulov, D.H. Lowndes, Y.Y. Wei, G. Eres, E. Voelkl, Patterned growth of individual and multiple vertically aligned carbon nanofibers, *Applied Physics Letters,* 76 (2000) 3555-3557, doi:10.1063/1.126705.
[15] C. Täschner, F. Pácal, A. Leonhardt, P. Spatenka, K. Bartsch, A. Graff, R. Kaltofen, Synthesis of aligned carbon nanotubes by DC plasma-enhanced hot filament CVD, *Surface and Coatings Technology,* 174–175 (2003) 81-87, doi:10.1016/s0257-8972(03)00712-6.
[16] E. Bauer, Phänomenologische Theorie der Kristallabscheidung an Oberflächen. I, *Zeitschrift für Kristallographie,* 110 (1958) 372-394, doi:10.1524/zkri.1958.110.1-6.372.
[17] H. Okamoto, O−Sn (Oxygen-Tin), *Journal of Phase Equilibria and Diffusion,* 27 (2006) 202-202, doi:10.1007/s11669-006-0063-6.
[18] N. Yamazoe, J. Fuchigami, M. Kishikawa, T. Seiyama, Interactions of tin oxide surface with O2, H2O AND H2, *Surface Science,* 86 (1979) 335-344, doi:10.1016/0039-6028(79)90411-4.
[19] J.H. Thomas, X-ray photoelectron spectroscopy study of hydrogen plasma interactions with a tin oxide surface, *Applied Physics Letters,* 42 (1983) 794-796, doi:10.1063/1.94097.
[20] R. Banerjee, S. Ray, N. Basu, A.K. Batabyal, A.K. Barua, Degradation of tin-doped indium-oxide film in hydrogen and argon plasma, *Journal of Applied Physics,* 62 (1987) 912-916, doi:10.1063/1.339699.
[21] S. Hamma, P. Roca i Cabarrocas, Low-temperature growth of thick intrinsic and ultrathin phosphorous or boron-doped microcrystalline silicon films: Optimum crystalline fractions for solar

cell applications, *Solar Energy Materials and Solar Cells,* 69 (2001) 217-239, doi:10.1016/s0927-0248(00)00391-3.
[22] O. Kuboi, Degradation of ITO Film in Glow-Discharge Plasma, *Japanese Journal of Applied Physics,* 20 (1981), doi:10.1143/JJAP.20.L783.
[23] J. Wallinga, W.M. Arnoldbik, A.M. Vredenberg, R.E.I. Schropp, W.F. van der Weg, Reduction of Tin Oxide by Hydrogen Radicals, *The Journal of Physical Chemistry B,* 102 (1998) 6219-6224, doi:10.1021/jp981447l.
[24] P.J. Alet, L. Yu, G. Patriarche, S. Palacin, P. Roca i Cabarrocas, In situ generation of indium catalysts to grow crystalline silicon nanowires at low temperature on ITO, *Journal of Materials Chemistry,* 18 (2008) 5187-5189, doi:10.1039/B813046a.
[25] L. Yu, B. O'Donnell, M. Foldyna, P. Roca i Cabarrocas, Radial junction amorphous silicon solar cells on PECVD-grown silicon nanowires, *Nanotechnology,* 23 (2012) 194011, doi:10.1088/0957-4484/23/19/194011.

3. VLS Growth Catalyzed by Post-Transition Metals

"Ce n'est pas possible, m'écrivez-vous ; cela n'est pas français. "

In this chapter we discuss the growth mechanism of SiNWs, assess the drawbacks of using conventional catalysts in terms of process temperatures, contamination and raw material costs, and look into post-transition metals as an alternative. Post-transition metals remain to date unusual choices for catalyzing the vapor-liquid-solid growth of silicon nanowires. In contrast with noble metals, they present a low silicon solubility, low surface tension, low melting point, they oxidize rapidly in air and the d-subshells in their electronic configuration are full. While some of these properties present challenges to nanowire growth, others offer bright prospects for their implementation in electronics. Our aim is to illustrate how the obstacles can be overcome using a simple PECVD growth technique and the benefits of these metals can be taken advantage of. We will be brought to reassess certain intricacies of the VLS mechanism in light of these results.

"Impossible? That word is not French." Field orders from Napoléon Bonaparte to General Lemarois, 1813.

1. Nanowires and Vapour-Liquid-Solid growth

Nanowires are small, very small cylinders. They can present diameters barely dozens of atoms across[1] while extending over hundreds, or even millions, of atoms in length.[2] The unnatural dimensions and extraordinary surface to volume ratios of these structures can endow them with a range of exotic physical properties.[3] In the case of our radial junction solar cells, what interests us is that when nanowires are grown in arrays, their abrupt surface texture is particularly effective at trapping light.[4]

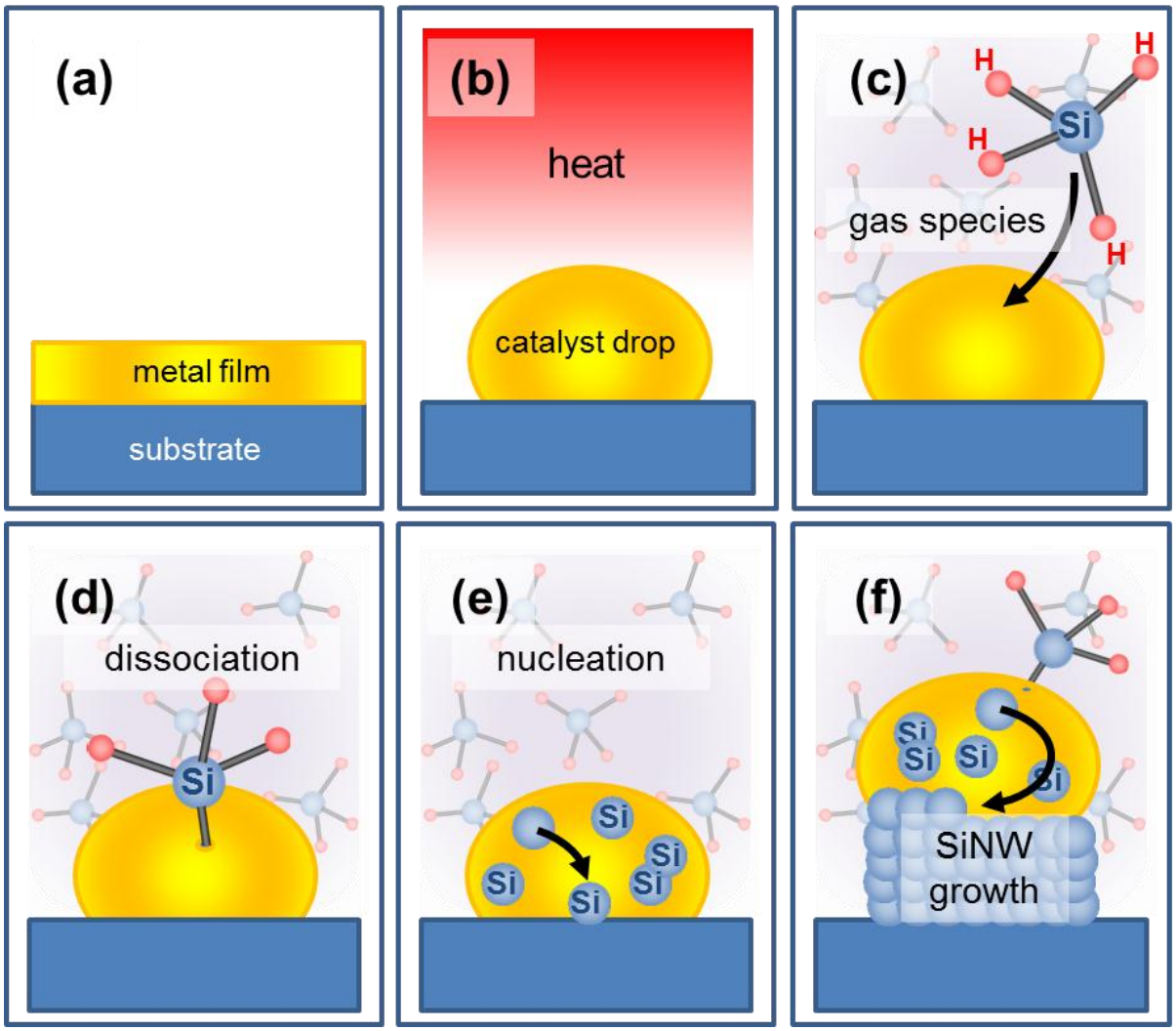

3.1 - The VLS growth mechanism.
Schematic representation of the steps involved in VLS growth. A thin metal film is deposited over a substrate (a). It is heated above its eutectic point with Si (b) and exposed to a silane gas (c). The silane molecules dissociate at the metal surface (d) and the concentration of Si atoms builds up inside the catalyst (e) until it exceeds its equilibrium solubility and begins precipitating at the interface with the substrate forming a silicon nanowire (f).

1.1. The classical picture of VLS

Many techniques are used to make SiNWs. They can be etched out of Si wafers[5] or assembled from chemical solutions.[6] In the interest of compatibility with the equipment used to fabricate a-Si:H solar cells, we have grown our SiNWs from the gas phase using the Vapor-Liquid-Solid (VLS) process. A schematic representation of the main steps in the VLS growth process is illustrated in Figure 3.1.

The essence of VLS is to locally enhance the deposition rate from the gas phase by exposing the growth species to liquid metal drops spread over the substrate. To form the drops a metal film (Figure 3.1.a) is dewetted on the substrate (Figure 3.1.b). In the case of SiNW growth, the metal is heated above its eutectic temperature with silicon and exposed to a gas containing silicon, typically silane (Figure 3.1.c). The silane molecules break down at the surface of the metal drop, causing the Si atoms to bond with the metal and incorporate the drop (Figure 3.1.d-e). The concentration of Si builds up inside the catalyst drop until it reaches the equilibrium solubility. Beyond this concentration, Si atoms precipitate and nucleate at the interface with the substrate. As the Si atoms form a complete solid layer at the base of the metal drop, they drive it upwards by an atomic plane. The metal drop continues to catalyze the silane dissociation and nucleation, resulting in a solid pillar (or nanowire) forming beneath it.

1.2. Open questions on the VLS growth mechanism

The broad lines described above were proposed five decades years ago by Wagner and Ellis[7] and have withstood the test of time remarkably well. However numerous intricacies of the VLS process have remained topics of debate since its discovery. For instance, the means by which the catalyst liquefies are is not necessarily trivial. Although prior to the beginning of the VLS process the metal film contains no silicon, it can liquefy at the eutectic temperature of the Si-metal alloy (which can be hundreds of degrees lower than its own melting point). Observations of an initial incubation time between exposure of the heated metal particles to Si containing gas molecules and the beginning of nanowire growth fit models of a progressively advancing liquid front through the solid metal.[8] This may suggest that at the interface between the Si and the metal, the local concentration of Si is high enough for the system to act as an alloy and thus the retreating solid surface liquefies. In-situ TEM corroborate this description with observation of silicon incorporation in the catalyst initiating at the particle rim before progressively moving towards its center.[9] Decades of debate have also revolved around which of the steps depicted in Figure 3.1 limits the nanowire growth rate. Some studies favor the incorporation of Si from the gas phase into the catalyst drop (Figure 3.1.c-d),[10, 11] others the crystallization of Si at the liquid-solid interface (Figure 3.1.e).[12] It remains unclear why nucleation is not amorphous (as is usually the case for CVD at temperatures below 600 °C) but crystalline,[7] and why it occurs at times at the catalyst surface rather than at the interface with the substrate.[13, 14]

The candid question which runs through this chapter is why the gas precursors incorporate the catalyst drop to start with. Although there is some evidence that Au drops can help dissociate Si-H bonds,[11, 15] the diversity of catalyst materials, gas species and process conditions with which VLS growth has been observed suggest that it is not just the result of a chemical reaction. Wagner and

Ellis postulated that the key property of the catalyst drop was the higher "accommodation coefficient" it presented to gas molecules in virtue of its liquid phase.[16] This would explain the universality of the process, although it fails to account for more recent observations of nanowire growth with solid catalysts[17, 18] or under conditions in which the accommodation coefficient is already close to unity (such as in molecular beam epitaxy).[19] The answer has since been refined in terms of the height of energy barriers presented by interfaces between different phases or materials.[12, 20, 21] This description is more complete, but it still does not account for one recurring puzzle in studies on SiNW growth: why do some metals catalyze growth better than others?

1.3. Post-transition metal catalysts

Numerous studies have found that the ability to catalyze SiNW growth is not shared equally by all metals. Already in 1964, Wagner and Ellis noticed that Au, Ni, Pd, Cu, Gd, Mg, and Os could produce extensive filamentary growth while Zn and Sn did not.[22] Bootsma and Gassen observed VLS growth with Au, Ag, Cu, Ni and Pd catalysts but none with In, Sn and Bi.[10] More recently, Nebol'sin offered an explanation as to why nanowire growth was possible with Au, Cu, Pt and Ni catalysts, but not with Sn, Pb, Sb and Bi.[23] It is striking that in many accounts, the outliers are post-transition metals. Intriguingly, over the past decade, post-transition metals have emerged in isolated reports on silicon nanowire growth. In 2001, Sunkara reported VLS growth with Ga catalysts.[13] In 2006, the Gösele group managed to catalyze straight and epitaxial SiNWs with Al.[18] In 2007, Iacopi et al. presented nanowires grown from In drops.[24] In 2007 and 2008, Parlevliet and Cornish[25] and Yu et al.[26] showed results with Sn.[27, 28] The first account of vertical VLS growth with Bi catalysts appeared only this year.[29]

This chapter sets out to explain what has made these sudden advances possible and infer their implications regarding the role of the catalyst in the VLS growth process. We present our opinions relying primarily on studies from the literature and complementing where necessary with our own results. Although these results are merely stated here, fabrication details and deposition conditions for our catalysts and nanowires are offered in Chapters 2 and 4 of this thesis.

2. Practical considerations in choosing nanowire catalysts

The VLS growth process has been observed with a broad range of feed gases and catalyst metals. Growth of SiNWs alone has been reported with two dozen different catalysts.[30] We therefore begin by addressing their relative merits from an industrial perspective. In particular, we aim to compare their scope for reducing electronic losses and limiting manufacturing costs in SiNW-based devices.

2.1. Contamination and recombination

During the VLS process, particles of the metal drop catalyzing growth inevitably precipitate into the nanowire material.[31, 32] This contamination is liable to affect the electronic properties of the nanowire and of the devices that it is integrated in. How much metal precipitates from the catalyst

into the silicon nanowire can be assessed on the basis of its equilibrium solubility in silicon. The equilibrium solubility defines the concentration of a given impurity which can be dissolved in a foreign material. It is generally determined on bulk crystalline silicon, and can substantially underestimate the concentration of contaminants found in nanowires. For instance, when Au is used as a VLS catalyst, concentrations within SiNWs can reach several orders of magnitude higher than in bulk silicon.[31] Direct measurements of the concentration of metal contaminants in silicon nanowire structures have recently been obtained by transmission electron microscopy[31] and atomic probe tomography,[33], offering new prospects in understanding these materials.

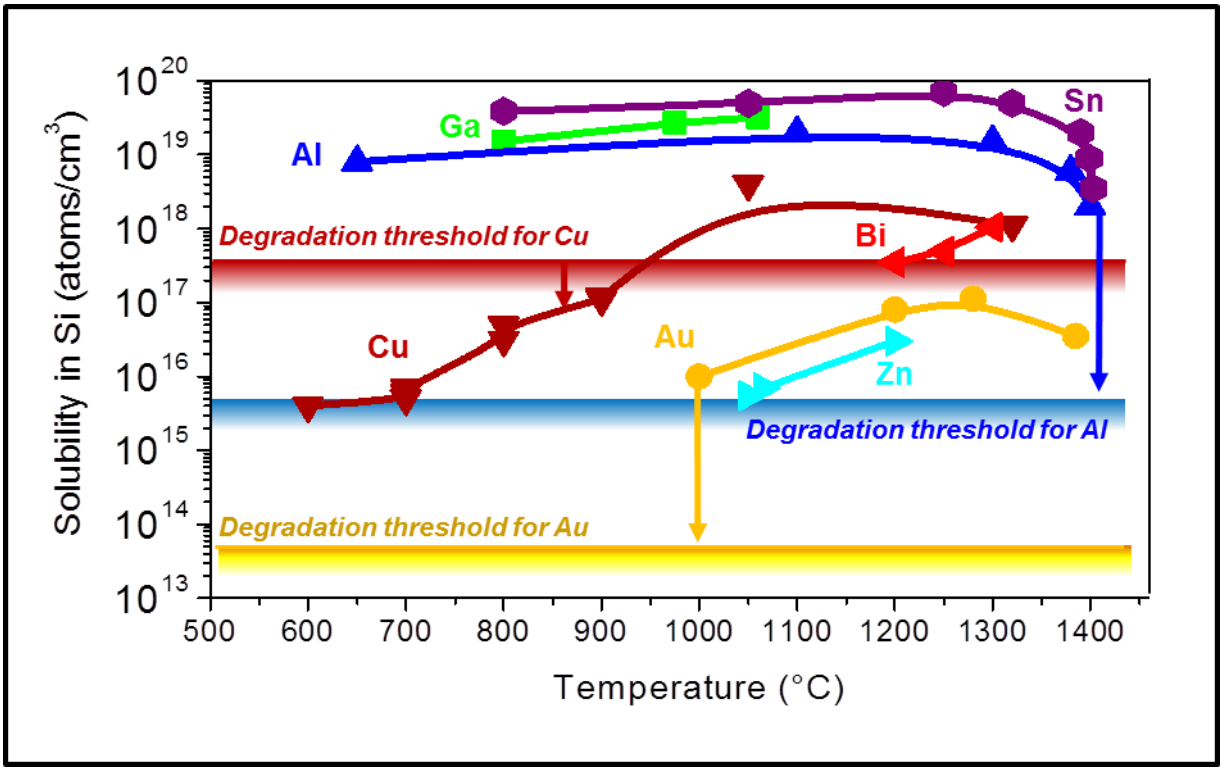

3.2 - Equilibrium solubility and degradation thresholds for various metals in silicon.
Data for the equilibrium solubility of various metals in silicon as a function of the temperature derived from Trumbore.[34] Degradation thresholds for Cu and Al are quoted from Davis et al.[35] and Kayes[36] for Au.

However, even neglecting this complication, the solubility of contaminants provides an incomplete account of their damage to electronic properties. Davis et al. tackled the issue from a different perspective. They intentionally incorporated metal atoms in crystalline silicon wafers which were assembled into solar cells. The concentration at which the metal was observed to substantially degrade the performance of cells was recorded as its degradation threshold.[35] As can be seen in Figure 3.2, some metals with comparatively low solubility in Si (e.g. Au) can prove more damaging to the electronic properties of solar cells than other metals with higher solubility (e.g. Cu). The reason they differ from predictions based on solubility values is that the efficiency with which each contaminant atom causes charges to recombine varies from metal to metal.

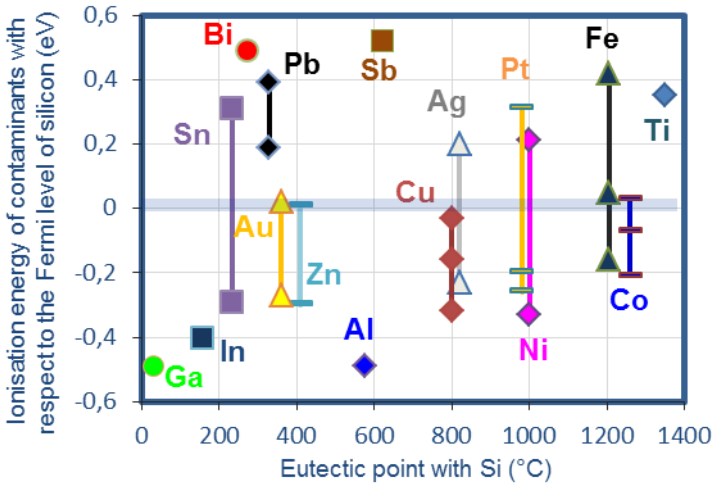

Metal	Degradation Threshold
Au	3 x 10^{13} atoms/cm^3
Mn	2 x 10^{14} atoms/cm^3
Fe	3 x 10^{14} atoms/cm^3
Ni	5 x 10^{15} atoms/cm^3
Al	4 x 10^{15} atoms/cm^3
Cu	4 x 10^{17} atoms/cm^3

3.3 - Ionization energies and degradation thresholds of different metals in crystalline silicon.
Ionization energies of different metal contaminants in silicon with respect to the middle of the crystalline silicon bandgap are taken from Schmitt et al.[37] (a) and degradation thresholds of different metals in crystalline silicon from Davis et al.[35] (b).

Shockley-Read-Hall recombination statistics state that the rate of carrier capture scales exponentially with the energy separating the Fermi level of a Si crystal from the energy level introduced in its bandgap by an impurity.[38] The closer this energy level is to the middle of the bandgap, the higher the recombination rate and the lower the carrier lifetime in the material (Figure 3.3). Au provides particularly efficient centers for recombination in the silicon matrix as a result of the deep energy levels it introduces in the Si bandgap. This may explain its exceptionally low degradation threshold in crystalline silicon solar cells. Other metals, including Sn, Ag, Pt and Ni introduce energy levels within 0.2 and 0.3 eV from the center of the bandgap, foreseeably less damaging to charge conduction in the material. More promising yet are Ga, In, Bi and Al, which introduce energy levels close to the valence or conduction band of Si and may therefore even help dope the material.[29]

2.2. Process temperature

There are several advantages to minimizing heating throughout the fabrication steps of electronic devices. Lower temperatures reduce the energy expenditure of the manufacturing process.[39] They can increase throughput by avoiding cooling phases and simplifying the fabrication process.[39] In the case of photovoltaics, they also allow greater flexibility in terms of the substrate used. Most glasses are not designed to withstand temperatures above 600 °C,[40] and keeping the process temperature beneath 300°C opens prospects for depositing the cells on low-cost, flexible foils and polymers.[41, 42] By definition, VLS growth relies on the presence of a liquid drop. To an extent, this fixes the lower limit of the fabrication process as the Si-catalyst alloy only liquefies at its eutectic point. The eutectic point can differ significantly from the melting point of each element in the alloy (under atmospheric pressure, Au-Si alloys can melt at 363°C while pure Au remains solid up to 1064°C and Si up to 1414 °C) and from one alloy to another (in contrast to Au-Si, the Fe-Si system liquefies at

temperatures above 1200 °C). The eutectic points of Si with metals reportedly capable of catalyzing SiNW growth are represented in the x-axis of Figure 3.3. For the purpose of our study, it is interesting to note that Ga, In, Sn and Bi form alloys with Si that are liquid below 300°C. Au, Pb and Al have a eutectic point below 600°C. And other potential catalysts require temperatures in excess of 800°C.

A note of caution is needed when asserting that the eutectic point fixes the minimum temperature of nanowire growth. Recent studies have shown that metal drops with diameters lower than 10 nm exhibit a range of alterations to their physical properties, including their melting point.[43, 44] There have been reports of VLS growth at temperatures below the eutectic when catalysts are exposed to a silane plasma.[45-47] Červenka et al. notably succeeded in growing SiNWs from silane plasmas at temperatures as low 250 °C.[48] Just as striking is the observation of Vapor-Solid-Solid[18] or oxide assisted growth[49] which can lead to nanowire growth at temperatures substantially lower than the eutectic. These anomalies may ultimately change our understanding of VLS and what can be achieved with it. Nonetheless, they remain matters of on-going research and the eutectic point currently provides the best benchmark for comparing the heating requirements in fabricating SiNWs with different metal catalysts.

2.3. Abundance of raw materials

Concerns over material abundance may seem exaggerated given the nanoscopic layers of catalyst material used for VLS growth. However, such concerns are inevitable when working with the colossal scales of the energy sector. To generate the present world power output of 16 TW with solar panels (operating optimistically at 20% energy conversion efficiency[50] with a 20% capacity factor[51]) would require covering 400'000 km² of land with photovoltaic cells.[52] If these cells are to make use of VLS-grown SiNWs and the thickness of the catalyst layer can be kept to 10 nm, roughly five thousand cubic meters of metal would be needed or, in the case of Au, 700'000 tons of catalyst. If the price of gold remained at $1200/ounce,[53] this would add 0.04 $/$W_p$ to module manufacturing costs and trillions of dollars to the entire installation. However it is unlikely that prices would remain stable as the installation would completely deplete global Au reserves.[53]

The cost of minerals has until now primarily reflected a balance between demand and recovery techniques. However as the first increases and the second matures, the reserves of commodities grow to reflect their natural abundance.[54] The risk is that by mining rare metals such as Au in large quantities, their supply dwindles until they become prohibitively expensive. By and large, the more common metals in the upper continental crust are the lighter ones. Barring the contribution from Si, over 90% of the mass of the lithosphere is accounted for by Al, Fe, Ca, Na, K and Mg.[55] The elemental abundances of Mn, Ni, Zn, Ga, Cu, Co, Pb, Sn are two to four orders of magnitude lower. Metals including Bi, Cd, In, Ag, Hg can be considered rare as their abundance is seven orders of magnitude lower. Nobel metals, notably Au, Pt and Pd, are rarer still.[55]

2.4. Conclusions on the practical choice of catalyst

In summary, the electronic properties of SiNW-based devices are likely to improve if metals introducing shallow energy levels in the Si bandgap are used as catalysts. Manufacturing constraints favor metal whose alloys with Si have eutectic points lower than 300 °C. Long-term cost considerations lean towards metals which are abundant. These three factors have been compared in Figure 3.4, revealing a pattern of more desirable properties to the right of the periodic table. This group of elements (namely Al, Ga, In, Sn, Tl, Pb and Bi) are sometimes referred to as post-transition metals.

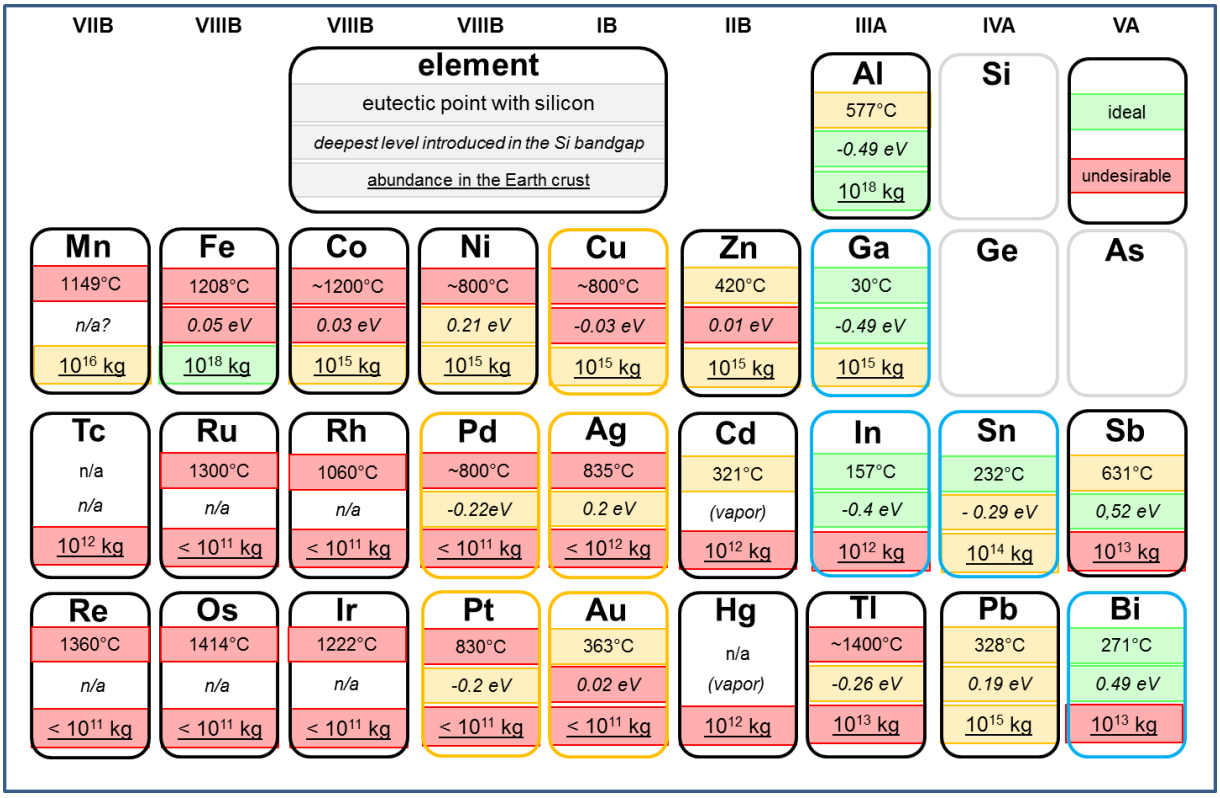

3.4 - Summary of abundances, eutectic points and ionization energies in Si for potential SiNW catalysts.
Periodic table comparing the eutectic point, deepest energy level introduced in the silicon bandgap (with respect to the mid-bandgap), and elemental abundance of different metals.

It may come as a surprise that the most popular VLS catalysts for SiNW growth have historically been Au, Ag, Pt, Pd, Cu and Ni,[7, 10, 56, 57] with Au remaining the most common choice to date.[30, 58] The eutectic points of these metals require process temperatures of 350 – 1100 °C, some of them are among the most rare and expensive elements on Earth and they can introduce recombination levels deep inside the Si bandgap (Figure 3.4). However, they boast a decisive redeeming quality from the perspective of laboratory studies in that they are convenient SiNW catalysts. Au, most notably, is widely used in solid state research, it is non-toxic, available in colloidal suspensions of nanoparticles and chemically stable, which can reduce sample preparation steps.[30] For decades, the growth of SiNWs using Al, Ga, In, Sn, Pb and Bi has been considered uncontrollable or utterly impossible.[10, 22, 23] However technical advances in the VLS fabrication process[18, 59] have recently demonstrated the

contrary and made it possible to explore the practical advantages presented by post-transition metal catalysts.

3. Post-transition metals and plasma enhanced VLS

Strictly speaking, post-transition metals designate Al, Ga, In, Sn, Tl, Pb and Bi, seven elements between columns 13 and 15 of the periodic table. The term sometimes encompasses the transition metals Zn, Cd, Hg or the metalloids Ge, Sb and Po. We will refer here in particular to Sn, In, Ga and Bi, although parts of what follows may also apply to their neighbors. Certain physical properties set these elements apart from transition metals (columns 3 to 11 in the periodic table). They present remarkably low melting points, ranging from close to room temperature to a few hundred degrees, compared to typical values of over 800 °C for transition metals. Liquid Sn, In, Ga and Bi also have unusually low Si solubilities and low surface tensions. They oxidize rapidly and, in stark contrast to transition metals, their d and s electronic subshells are full. This chapter sets out to explore the impact of these properties on their potential as silicon nanowire catalysts. In particular, we look for relations between these properties and one peculiarity which draws interest to post-transition metals in the study of VLS growth: they are notoriously ineffective catalysts[22, 10, 60, 61] until immersed in a reactive environment, such as a plasma.[13, 24, 27-29, 62-67]

3.1. Solubility of Si in the catalyst

The equilibrium solubility of Si tends to be considerably lower in post-transition metals than in transition metals (Table 3.1). It has been proposed that if the Si solubility of a catalyst is low and its volume is small, a single atom of Si may be sufficient to saturate the droplet.[61] In such a case, each nucleation event would deplete the stock of Si in the catalyst, hampering nanowire growth,[10, 30, 58, 68, 69] potentially explaining the lackluster record of In, Sn, Ga and Bi catalysts under standard VLS conditions. However, this assessment applies to catalyst droplets with diameters smaller than 10 nm and solubilities of orders of magnitude lower than 1% which, given the temperature and dimensions of the catalyst drops used during VLS growth, does not necessarily correspond to experimental conditions. Comparative studies between different transition metal catalysts have so far revealed no relation between the growth rate and the equilibrium Si solubility[57] and, over the past six years, abundant evidence has emerged of straight SiNW growth using post-transition metals with some of the lowest Si solubilities in the periodic table.[24, 27, 70]

It is not so much the solubility of Si in the droplet at equilibrium that leads dissolved atoms to nucleate at the nanowire surface but the *supersaturation* of Si with respect to this equilibrium solubility. The supersaturation expresses the excess chemical potential of Si atoms in a given phase compared to that in the surrounding medium.[21] It can be inferred in our case from the concentration of Si atoms in the catalyst before and after exposure to the gas phase species:[63]

$$S = C_{Si} / C_{Si.eq}$$

where C_{Si} and $C_{Si.eq}$ are the dissolved concentration and equilibrium solubility of Si in the catalyst.

Table 3.1: Equilibrium solubility of Si in liquid metals (atomic %)*

Transition Metals			Post-Transition Metals		
	eutectic	1000 °C	1000 °C	eutectic	
Fe	65-75%	solid	12%	45%	Al
Pt	23-67%	30-67%	17%	0.02%	Zn
Ni	21-55%	45-60%	0.01%	0.01%	Pb
Cu	20-30%	40%	< 1%	$< 10^{-4}$	Bi
Au	17%	40%	3%	$< 10^{-6}$	Sn
Pd	15-52%	15-60%	4%	$< 10^{-8}$	In
Ag	11%	19%	15%	$< 10^{-8}$	Ga

*Solubility values for Si in Fe,[71] Pt,[72] Ni,[73] Cu,[74] Au,[75] Pd,[76] Al,[77] Ag,[78] Zn,[79] Pb,[80] Bi,[81] Sn,[82] In[83] and Ga[84] extracted from phase diagrams of their alloys.

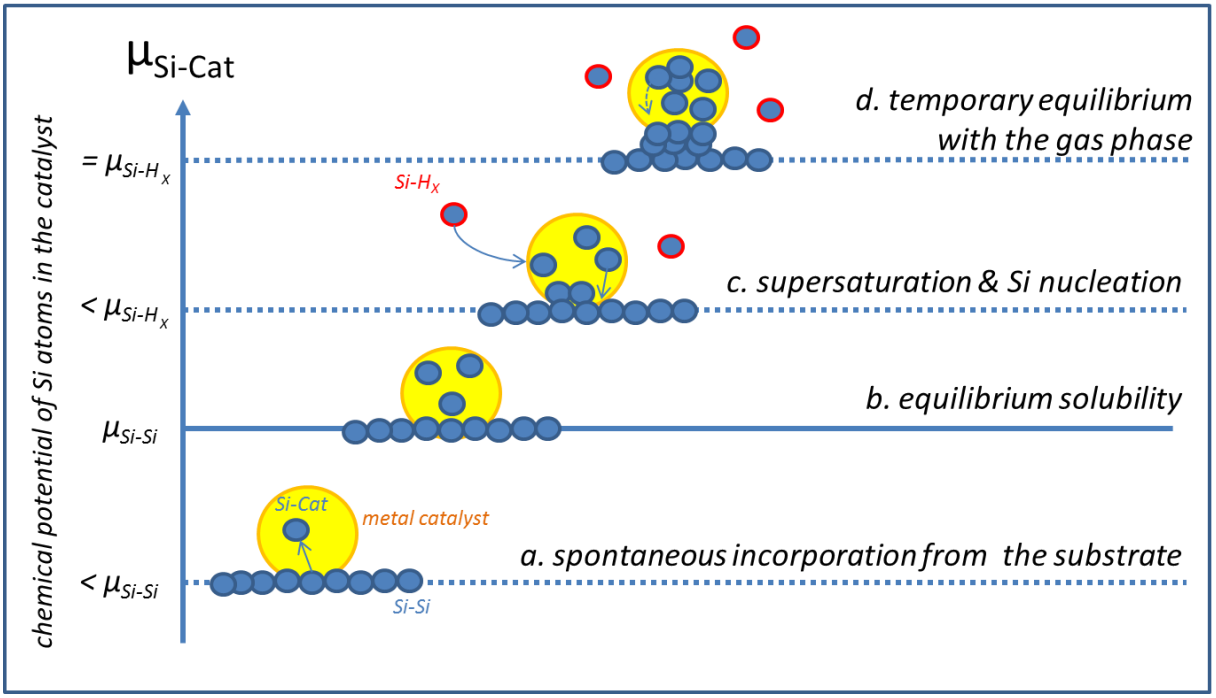

3.5 - The role of Si chemical potential in the VLS growth process.
Schematic representation of the VLS system growth process in terms of the chemical potential $\mu_{Si\text{-}Cat}$ of Si atoms as they build up in the metal catalyst. Si-Si designates bonds between silicon atoms, Si-Cat refers to bonds between dissolved Si and atoms in the catalyst and Si-H_x to bonds between the atoms in the gas species.

The process has been described schematically in Figure 3.5 with respect to the chemical potential of Si atoms in the catalyst drop. When a catalyst drop of pure metal is placed over solid silicon, it can

incorporate atoms from the gas phase or even the substrate (Figure 3.5.a) until their concentration reaches the Si equilibrium solubility in the metal (Figure 3.5.b). However nanowire growth will only occur when the concentration exceeds the equilibrium solubility. This situation arises if the catalyst drop is in a medium containing silicon atoms with a chemical potential higher than that of the Si atoms dissolved within it, for instance when it is exposed to silane radicals (Figure 3.5.c). The silicon from the gas phase will then integrate the drop, increasing the chemical potential of the silicon atoms closer to that of the feed species (Figure 3.5.d). However, because the chemical potential of silicon atoms in a solid crystal is lower than that of the silicon atoms in the drop, Si atoms within the catalyst will precipitate at the interface with the substrate in the form of a nanowire. This reduces their concentration within the drop (and hence their chemical potential), causing the system to revert to the situation described in Figure 3.5.c. The result is a continuous process in which Si atoms from the gas phase continually replace the Si atoms from within the drop which have been incorporated in the nanowire. Each of the processes described above presents an energy barrier which the chemical potential of the Si atoms must overcome for the process to occur. The reason VLS growth tends to be faster than (direct gas phase to solid) CVD deposition is the smaller energy barrier for incorporation into the liquid drop compared to direct nucleation at the crystal surface.

One important role of the plasma during the VLS growth of SiNWs (regardless of the catalyst used) is to reduce the energy barrier for incorporation into the drop by breaking down the feed species (another way of looking at this is to say that it increases their chemical potential).[85] This leads to a higher concentration of Si atoms in the catalyst (for the same Si equilibrium solubility) and hence higher Si supersaturations and growth rates.[45, 47] The only effect that the equilibrium solubility can play in itself on nucleation is that, on changing the source species (say from SiH_4 to GeH_4), a lower solubility will lead to more abrupt interfaces in the nanowire heterostructure as fewer species atoms are stored in the catalyst.[30, 86]

3.2. Surface tension

The surface tension expresses the force of atoms in a material pulling on the atoms at its surface. It is to a large extent determined by the bond energy and distance between atoms.[87] Variations in these properties lead to values of ~ 0.1 – 2.5 N/m for different liquid metals. Table 3.2 was compiled with data from Eusthathopoulos[88] and values for transition metals were cross checked with Lu and Jiang.[89] It shows that conventional SiNW catalysts (Au, Pt, Pd, Cu and Ni) have strikingly higher surface tensions than most post-transition metals.

During VLS growth, the interplay between the surface tensions of the catalyst and nanowire materials plays an important role in determining the morphology of the SiNWs. The forces acting on the Triple Phase Line (at the rim of the catalyst drop where liquid, solid and vapor phases meet) have notably been observed to taper the nanowire base during the early stages of growth.[37] Nebol'sin et al. studied the possible implications of surface tensions on the suitability of different metals to catalyze the VLS growth of SiNWs by assessing the contribution from the surface tension of the liquid catalyst (γ_L), the surface tension of the solid nanowire (γ_S) and the interfacial tension between the catalyst and the nanowire (γ_{LS}) at the triple phase line (Figure 3.6.a).[23, 90]

Table 3.2: Surface tensions of liquid metals - γ_{LV} (in N/m)			
Transition Metals		Post-Transition Metals	
Fe	1.8	0.9 –1.1	Al
Ni	1.8	0.79	Zn
Pt	1.7	0.70	Ga
Pd	1.5	0.55	Sn
Cu	1.4	0.55	In
Au	1.1	0.40	Pb
Ag	0.9	0.35	Bi

Nebol'sin et al. concluded that for the catalyst to promote stable (rectilinear) growth, the horizontal component of the resultant force on the TPL must be zero and the vertical component must be directed upwards in order for the replacement of liquid-vapor interfaces with solid-vapor interfaces to be energetically favorable.[23]

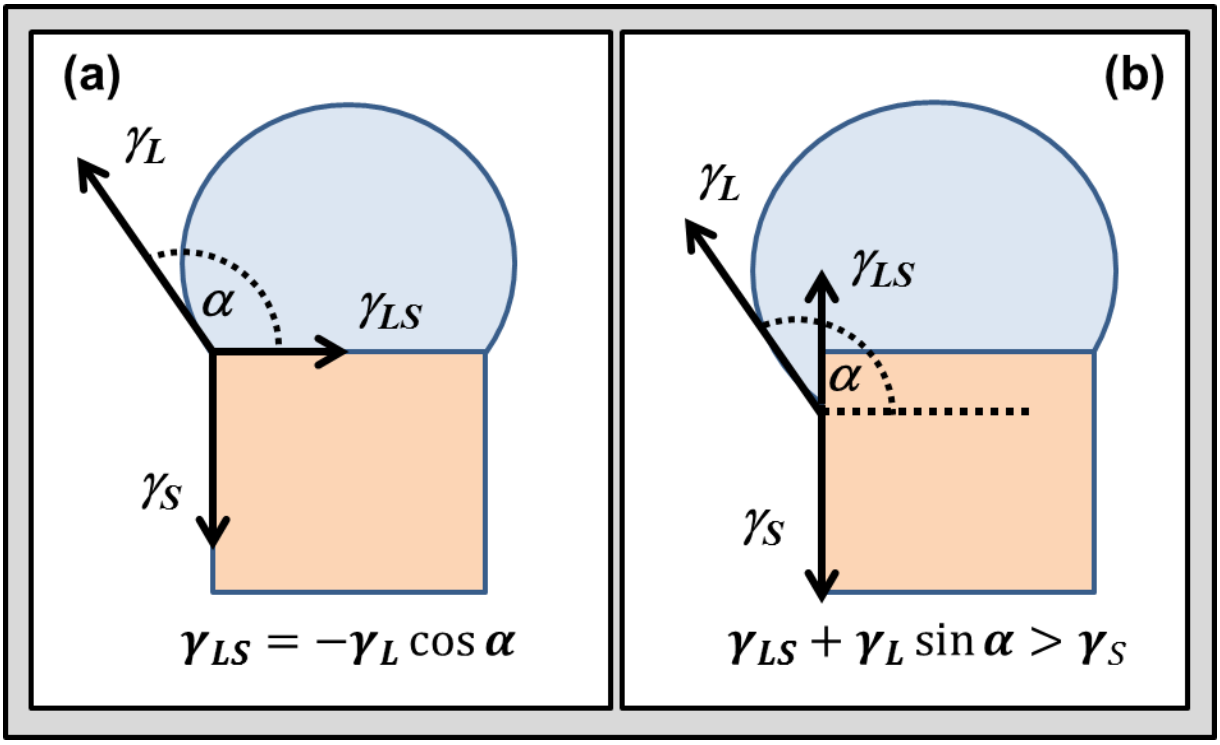

3.6 – Surface tension equilibrium during SiNW growth.
Schematic representation of the forces at work on the TPL during SiNW growth. For stable growth to occur, horizontal components of the interface tensions must balance out (a) and vertical components must pull upwards (b).

Schmidt et al. presented the problem from a different perspective by pointing out that if the resultant force were directed downwards, at each instability of the triple phase line, the liquid metal would wet the nanowire sidewall and leak away from the tip (Figure 3.6.b).[30] Figure 3.6.a shows that for the horizontal components of the surface tensions to balance out, the horizontal component of the catalyst surface tension (γ_L) and the liquid-solid interface tension (γ_{LS}) must be of equal magnitude. The system adapts the contact angle of the liquid drop to meet this condition. Figure 3.6.b shows that if the TPL spreads over the edge of the nanowire tip, the vertical components of the liquid-solid interface tension (γ_{LS}) and liquid surface tension (γ_L) must together be greater than the surface tension of the solid nanowire (σ_{SV}) to bring it back to the nanowire tip. These two conditions can be combined to conclude that the resultant force on the triple phase line will only be directed upwards when the following inequality is met:

$$\gamma_{LV} > \gamma_{LS} / (\sin \alpha - \cos \alpha)$$

As the surface tension of solid Si is in the range of 0.94 - 1.2 N/m[91-93] and ($\sin \alpha - \cos \alpha$) cannot exceed 1.41, the minimum surface tension required for a liquid metal catalyst to promote straight SiNW growth would need to be 0.67 - 0.85 N/m. This has led to predictions that In, Ga, Al and Zn are likely to catalyze only short and unstable growth, while and Sn and Bi should be incapable of catalyzing SiNW growth altogether.[23] However, recent experimental evidence of straight SiNW growth with In,[59] Ga,[70] Al,[18], Zn,[94] Sn,[27, 28, 64] and Bi[29] suggests that this picture is incomplete.

It is possible but unlikely that the plasma ignited during the growth of SiNWs catalyzed by post-transition metals alters their surface tension as this property tends to react weakly to gaseous environments.[95, 96] Surface tensions have been observed to decrease by a factor of up to 30% when metals including Sn and Zn are heated to 1000 °C[95] and when Al oxidizes, but we have found no cause for them to increase on the scales required to fulfill the Nebol'sin stability criterion.[97] As an alternative explanation, we have proposed that the small metal particles, commonly observed over nanowire sidewalls following VLS growth,[98, 99] could constitute the remnants of an atomically thin continuous film wetting the entire sample surface between the catalyst drops during the growth process. Such a layer would alter the geometry of the triple phase line and the forces acting on it, resulting in greater stability of the catalyst drops.[100]

3.3. Oxidation

One crucial difference between post-transition metals and many of the noble metals that have traditionally been used to catalyze SiNW growth is that they oxidize rapidly. Surface oxide shells may prevent Si atoms from incorporating the metal catalyst drop, leading to irregular growth[101] or even burying the catalyst and preventing growth altogether.[59] In the case of transition metals, Au, Pt, Pd and Ag are highly resistant to oxidation and at temperatures above 900°C, which are commonly used for Fe, Cu and Ni catalyzed VLS growth, the surface oxides of base transition metals can break down.[102, 103]

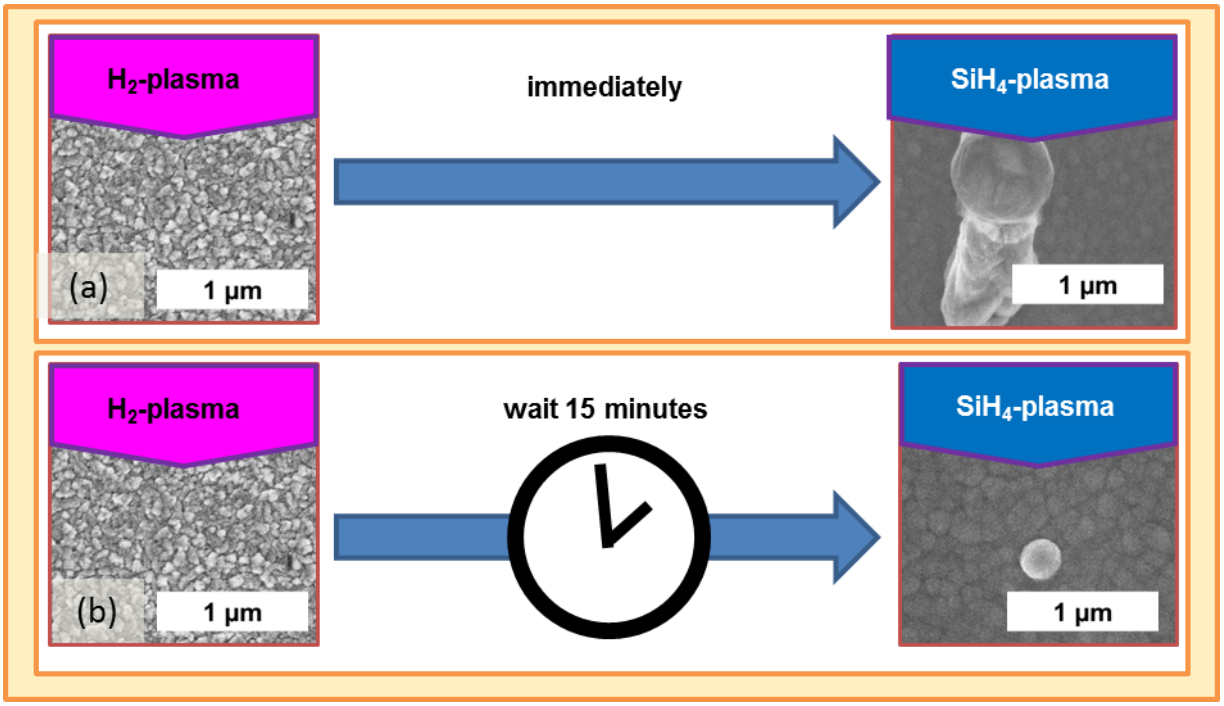

3.7 - The risk of oxidation when growing Sn-catalyzed SiNWs.
When the Sn-covered substrate is exposed to a H_2 plasma, directly followed by a SiH_4 plasma, SiNW growth is observed (a). When the Sn is allowed to reoxidize after the H_2 plasma for fifteen minutes before exposure to the silane plasma, no nanowire growth is observed (b).

The situation is different for post-transition metals as their surface oxides show signs of comparative thermal stability[104] and their growth is often intentionally kept at low temperature. Al is a good example as surface oxidation has prevented its use as a SiNW catalyst until 2006 when Wang et al. managed to evaporate the metal and expose it to a silane gas in a single ultra-high vacuum run.[18] However a reactive environment can reduce the metal oxide at the catalyst surface by dissociating its oxygen bonds.[105, 106] It is likely that oxidation plays a key part in the difficulties encountered until recently in catalyzing SiNW growth with post-transition metals. From our studies on Sn-catalyzed SiNWs, when the catalysts were not exposed to a preliminary H_2 plasma or when a fifteen minute delay separated the (catalyst reducing) H_2 plasma from the (nanowire growing) SiH_4 plasma, no nanowire growth was observed (Figure 3.7). Reports of SiNW growth with Ga[70, 107], In[24], Sn[28] and Bi[29] have also incorporated an exposure to atomic hydrogen in their fabrication process. Our attempts at reducing ZnO and Al_2O_3 with hydrogen plasmas have consistently failed. Whether the outcome of the plasma reduction is decided by the chemical stability of the oxide remains to be studied. It might prove interesting to expose Al_2O_3 to a precursor containing chlorine as bulk alumina is typically reduced using HCl. Oxidation does not rule out SiNW growth altogether. Chung et al. reported that Zn (which forms a notoriously stable oxide) can catalyze the growth of SiNWs under standard CVD conditions at temperatures of 450 °C.[94] Renard et al. reported that a surface oxide over Cu droplets can actually enhance their catalytic activity.[49] Notwithstanding, from our experience, it generally inhibits the incorporation of species into the catalyst and is best avoided.

3.4. Electronic configuration

Simply reducing the surface of post-transition metal catalysts is not sufficient to guarantee SiNW growth. In-situ laser reflectance interferometry measurements have shown that even after reducing the native oxide layer over Ga drops, silicon nanowire growth initiates only when a plasma is ignited in the silane gas.[107] This confirms our own experience with Sn, In and Bi catalysts (Figure 3.8). In 2001, Sunkara suggested that the main role the plasma plays in growing SiNWs from Ga drops is to break down the Si-H bond. He argued that unlike Au, Ga is not capable of catalyzing this reaction.[13] The metals best known to catalyze straight SiNW growth are Au, Cu, Ni, Pt, Pd, Ag and Fe[30]. These are all high valence elements of the d-block transition metals.[108] This is important as the effective medium theory of surface chemical bonds predicts that interactions with d-subshell electrons are responsible for the adsorption of molecules at the metal surface (the first step in catalytic decomposition). Furthermore, Falicov & Somojai have reported that materials in which electrons shift between d- and s-subshells provide a large concentration of low-energy electronic states and vacancies that can readily exchange electrons with adsorbed species.[109] The presence of valence electrons in an incomplete d-subshell is a defining characteristic of transition metals. It makes conventional SiNW catalysts well suited to breaking and reorganizing the chemical bonds of surrounding species.[110, 111]

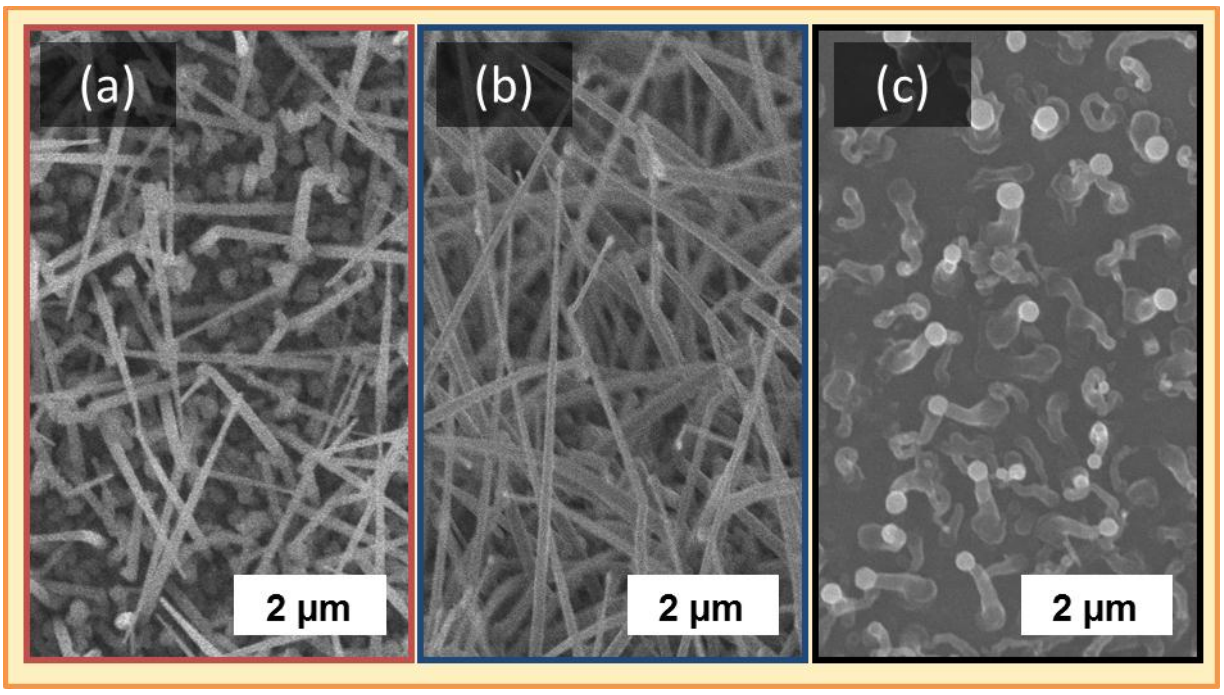

3.8 - SiNWs grown using Sn, In and Bi catalysts.
SiNWs grown using (a) Sn, (b) In and (c) Bi catalysts under identical SiH_4 plasmas at 600°C. When the same substrates were exposed to silane gas with no plasma, no nanowire growth was observed.

It may seem surprising that noble metals, which are renowned for an aversion to react with other elements, are such effective SiNW catalysts. Part of the explanation lies in the distinction between the tendency of a material to interact with its surroundings and to actually form compounds. Although it may be energetically unfavorable for foreign particles to be incorporated into the crystal matrix of noble metals, their surfaces offer sites upon which foreign molecules can loosely bind and

break apart. Au, Pd, Cu, Ni, Pt and Ag can all dehydrogenate alcohols and formic acids[112] and silane has been observed to adsorb and dissociate at the surface of solid Au, Ni, Cu and Pd.[113-116] During VLS growth, the catalytic activity of metals may also be enhanced by the fact that they are in liquid form[16] and of nanoscopic dimensions.[117] In contrast to the electronic configuration of conventional catalysts, the d-subshells of post-transition metals are full and stable (figure 3.9). Their valence electrons originate from s-p subshells, not the long-range, highly reactive d-s subshells of transition metals. This may be the reason that post-transition metal catalysts and the dominant reason for needing a reactive environment (such as a plasma) to catalyze nanowire growth with Sn,[28, 63, 64] In,[24, 27] Ga [13, 65] and Bi.[29, 66, 67] At temperatures too low to thermally dissociate silane, Au helps break down the gas molecules while post-transition metals react very weakly with them. Even under standard thermal CVD conditions, post-transition metals will not locally accelerate the decomposition of gas species in their surrounding and nanowire nucleation may prove too slow to compete with standard CVD thin-film growth. However, when a plasma is ignited, the gas molecules are broken down for them, which may make it possible for higher rates of them to be incorporated into the liquid catalyst.[85]

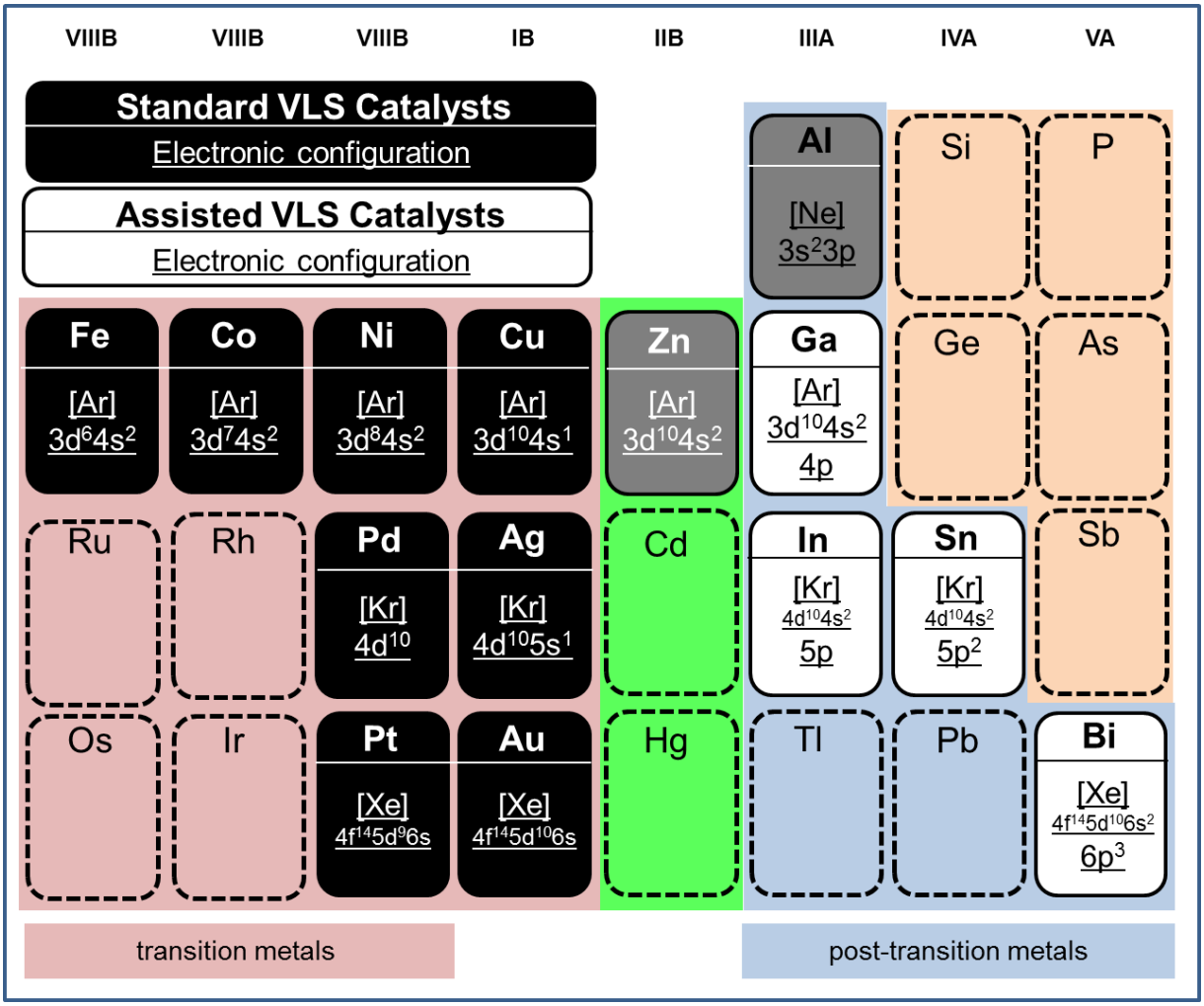

3.9 – The distinction between transition and post-transition metals as SiNW catalysts.
Periodic table of common SiNW catalysts. To the left are the transition metals with incomplete d-s electronic subshells which can catalyze the growth of SiNWs under standard CVD conditions. To the right are the post-

transition metals which require assistance from a reactive environment (e.g. a plasma) to catalyze SiNW growth.

The fact that nanowire growth is still observed when the *chemical catalyst* role of the metal is delegated to the plasma indicates that the liquid drop plays more than one role in VLS, meeting models of a *physical catalyst* role[21] in which the metal drop also provides an energetically favorable site for nucleation.

4. Conclusion

From a practical perspective, SiNW-based devices stand to gain from adopting metal catalysts which introduce shallow energy levels in the silicon bandgap, and offer low eutectic points with silicon and vast material availability. The best compromise between these three conditions was found in post-transition metals, notably Al, Sn, In, Ga and Bi (Figure 3.4). Out of convenience and concerns for the quality of the nanowires produced, reports on SiNW growth generally favor Au catalysts, a metal which fulfills these guidelines for SiNW-based devices particularly poorly. However results published over the past six years have shown that the growth of long, straight SiNWs can be catalyzed by post-transmission metals. We note that with remarkably few exceptions, these studies have required the VLS process to be conducted under plasma conditions. The plasma appears to fulfill several roles in assisting the VLS growth of SiNWs catalyzed by post-transition metals. Its initial contribution is to remove the oxide layer at the catalyst surface. In contrast to noble metals, surface oxides form rapidly over post-transition metals and are unlikely be thermally dissociated given the low temperatures at which they tend to be used. A reactive environment, such as a plasma, provides a simple approach to reduce their surface oxide. The technique has proven successful with Ga[70, 107], In,[24, 27, 118] Sn[28, 100] and Bi.[29] During nanowire growth, the plasma also offers the additional benefit to VLS growth of increasing the chemical potential of Si particles in the gas phase, and hence increasing the supersaturation of Si in the catalyst and the growth rate of the nanowire.[45, 47] However this last point is merely an advantage of plasma-assisted VLS, not a requisite for nanowire growth to occur.

We have argued that the crucial role of the plasma in facilitating VLS growth with post-transition metals lies in dissociating the feed species when the metals themselves are incapable of doing so. Building on the work of Sunkara,[13] Iacopi et al.[59] and Bianco et al.,[107] we advance that transition metals are capable of producing SiNWs under standard CVD conditions while, with the notable exception of Al, post-transition metals require some form of assistance in breaking down the gas species because of a distinction in their electronic configuration (Figure 3.9). The highly delocalized valence electrons of transition metals make them highly reactive with feed species (in our case, silane) molecules. As these subshells are filled in post-transition metals, the plasma may be required to break the Si-H bonds. These observations suggest that the metal catalyst has several roles in the VLS process. In the case of transition metals, it breaks down the feed species and in addition offers a favorable nucleation site. In the case of post-transition metals, it can still fulfill the second role so long as the first is provided by the process conditions (for instance by a plasma).

We have also debated two widespread misconceptions regarding the choice of catalyst for SiNW growth, namely that the liquid metal must present a high Si solubility and a high surface tension. In the case of Si solubility, we argue that nanowire growth results from Si supersaturation in the catalyst drop, which depends primarily on the chemical potential of the feed species and can be achieved regardless of the initial Si equilibrium solubility of the catalyst. In the case of surface tension, experimental evidence demonstrates that the arguments in favor of high surface tensions must be rectified in the case of plasma-grown SiNWs catalyzed by post-transition metals. However, seeing no reason for the plasma itself to affect the surface tension of the metal, we propose that a thin layer of metal covering the SiNW sidewalls alters the forces acting on the triple phase line of the system.[100]

Perspectives

We have concluded that the ability of a metal to catalyze SiNW growth under standard CVD conditions depends largely on whether it presents unfilled d and s electronic subshells. In doing so we have left the glaring exception of Al, which reportedly requires UHV conditions, but no reactive environment. There are several physical properties which single Al out among its neighbors in the periodic table. It is the lightest of post-transition metals, its melting point is considerably higher than that of Sn, In, Ga or Bi, and its surface tension and solubility are closer to those of transition metals. However, none of these properties are expected to influence its ability to break down silane molecules. It would be interesting to study the behavior of other post-transition metals in ultra-high vacuum. If Sn, In, Ga or Bi are also capable of catalyzing nanowire growth under these conditions, we have overestimated the importance of the electronic configuration of the catalyst and the role of the plasma may simply be to ensure continued reduction of the metal surface throughout exposure to the silane gas. If not, Al may present some unusual physical properties which are worth investigating further.

Considerable ground also remains unexplored in the remaining post-transition metals. Pb introduces trap levels not much deeper than those of Sn, its eutectic is not much higher, it is also tetravalent and highly abundant. These properties are promising for a SiNW catalyst. However, with few exceptions,[14] it has remained to date largely unexploited and it would be interesting to confirm that it responds to silane plasmas in the way that other post-transition metals do. There has also been limited work conducted on Zn catalysts, which present something of a riddle as well. The p and s subshells in Zn are nominally full yet it has been observed to catalyze SiNW under standard CVD conditions. Hg and Cd are less likely to offer reliable SiNW catalysts on account of their high vapor pressure.[30] However, if nothing else, the results in this chapter draw attention to the risks of discarding options as impossible too hastily in the history of SiNW research.

In parallel with our studies into the VLS growth mechanism, these investigations have resulted in a pragmatic outcome. SiNW growth has been demonstrated with Sn, In, Ga and Bi – metal catalysts which are abundant and compatible with low-temperature deposition techniques. This alleviates the burden of making the nanowire building blocks of our radial junction cells on a commercial scale. As will be shown in Chapter 5 of this thesis, the prospect of reducing the impact of metal contamination in SiNW-based devices by using post-transition metals may be tremendously significant.

BIBLIOGRAPHY

[1] D.D.D. Ma, C.S. Lee, F.C.K. Au, S.Y. Tong, S.T. Lee, Small-Diameter Silicon Nanowire Surfaces, *Science,* 299 (2003) 1874-1877, doi:10.1126/science.1080313.
[2] W.-S. Shi, H.-Y. Peng, Y.-F. Zheng, N. Wang, N.-G. Shang, Z.-W. Pan, C.-S. Lee, S.-T. Lee, Synthesis of large areas of highly oriented, very long silicon nanowires, *ChemInform,* 32 (2001), doi:10.1002/chin.200103229.
[3] Y. Xia, P. Yang, Y. Sun, Y. Wu, B. Mayers, B. Gates, Y. Yin, F. Kim, H. Yan, One-Dimensional Nanostructures: Synthesis, Characterization, and Applications, *Advanced Materials,* 15 (2003) 353-389, doi:10.1002/adma.200390087.
[4] W.Q. Xie, J.I. Oh, W.Z. Shen, Realization of effective light trapping and omnidirectional antireflection in smooth surface silicon nanowire arrays, *Nanotechnology,* 22 (2011) 065704, doi:10.1088/0957-4484/22/6/065704.
[5] Z.P. Huang, H. Fang, J. Zhu, Fabrication of silicon nanowire arrays with controlled diameter, length, and density, *Advanced Materials,* 19 (2007) 744, doi:10.1002/adma.200600892.
[6] J.D. Holmes, K.P. Johnston, R.C. Doty, B.A. Korgel, Control of Thickness and Orientation of Solution-Grown Silicon Nanowires, *Science,* 287 (2000) 1471-1473, doi:10.1126/science.287.5457.1471.
[7] R.S. Wagner, W.C. Ellis, Vapor-liquid-solid mechanism of single crystal growth, *Applied Physics Letters,* 4 (1964) 89-90, doi:10.1063/1.1753975.
[8] B. Kalache, P. Roca i Cabarrocas, A. Fontcuberta i Morral, Observation of incubation times in the nucleation of silicon nanowires obtained by the vapor-liquid-solid method, *Japanese Journal of Applied Physics,* 45 (2006) L190-L193, doi:10.1143/Jjap.45.L190.
[9] B.J. Kim, J. Tersoff, S. Kodambaka, M.C. Reuter, E.A. Stach, F.M. Ross, Kinetics of Individual Nucleation Events Observed in Nanoscale Vapor-Liquid-Solid Growth, *Science,* 322 (2008) 1070-1073, doi:10.1126/science.1163494.
[10] G.A. Bootsma, H.J. Gassen, A quantitative study on the growth of silicon whiskers from silane and germanium whiskers from germane, *Journal of Crystal Growth,* 10 (1971) 223-234, doi:10.1016/0022-0248(71)90188-6.
[11] S. Kodambaka, J. Tersoff, M.C. Reuter, F.M. Ross, Diameter-Independent Kinetics in the Vapor-Liquid-Solid Growth of Si Nanowires, *Physical Review Letters,* 96 (2006) 096105, doi:10.1103/PhysRevLett.96.096105.
[12] E.I. Givargizov, Fundamental aspects of VLS growth, *Journal of Crystal Growth,* 31 (1975) 20-30, doi:10.1016/0022-0248(75)90105-0.
[13] M.K. Sunkara, S. Sharma, R. Miranda, G. Lian, E.C. Dickey, Bulk synthesis of silicon nanowires using a low-temperature vapor-liquid-solid method, *Applied Physics Letters,* 79 (2001) 1546-1548, doi:10.1063/1.1401089.
[14] J. Zhang, F. Jiang, Y. Yang, J. Li, Molten Pb as a catalyst for large-scale growth of highly aligned silicon oxide nanowires, *Journal of Crystal Growth,* 307 (2007) 76-81, doi:10.1016/j.jcrysgro.2007.06.003.
[15] J. Westwater, D.p. Gosain, K. Yamauchi, S. Usui, Nanoscale silicon whiskers formed by silane/gold reaction at 335 °C, *Materials Letters,* 24 (1995) 109-112, doi:10.1016/0167-577x(95)00091-7.
[16] R.S. Wagner, W.C. Ellis, The vapor-liquid-solid mechanism of crystal growth and its application to silicon, *Transactions of the Metallurgical Society of Aime,* 233 (1965) 1053-1064, http://www.chem.sc.edu/faculty/greytak/chem749/wagner-trans-metall-soc-aime-1965-vls.pdf.

[17] T.I. Kamins, R.S. Williams, Y. Chen, Y.-L. Chang, Y.A. Chang, Chemical vapor deposition of Si nanowires nucleated by TiSi[sub 2] islands on Si, *Applied Physics Letters,* 76 (2000) 562-564, doi:10.1063/1.125852.
[18] Y. Wang, V. Schmidt, S. Senz, U. Gosele, Epitaxial growth of silicon nanowires using an aluminium catalyst, *Nat Nano,* 1 (2006) 186-189, doi:10.1038/nnano.2006.133.
[19] J.L. Liu, S.J. Cai, G.L. Jin, Y.S. Tang, K.L. Wang, Gas-source MBE growth of freestanding Si nanowires on Au/Si substrate, *Superlattices and Microstructures,* 25 (1999) 477-479, doi:10.1006/spmi.1998.0678.
[20] B. Mutaftschiev, R. Kern, C. Georges, Sur le mecanisme vls de croissance des whiskers, *Physics Letters,* 16 (1965) 32-33, doi:10.1016/0031-9163(65)90388-4.
[21] B.A. Wacaser, K.A. Dick, J. Johansson, M.T. Borgström, K. Deppert, L. Samuelson, Preferential Interface Nucleation: An Expansion of the VLS Growth Mechanism for Nanowires, *Advanced Materials,* 21 (2009) 153-165, doi:10.1002/adma.200800440.
[22] R.S. Wagner, W.C. Ellis, K.A. Jackson, S.M. Arnold, Study of the Filamentary Growth of Silicon Crystals from the Vapor, *Journal of Applied Physics,* 35 (1964) 2993-3000, doi:10.1063/1.1713143.
[23] V.A. Nebol'sin, A.A. Shchetinin, Role of surface energy in the vapor-liquid-solid growth of silicon, *Inorganic Materials,* 39 (2003) 899-903, doi:10.1023/A:1025588601262.
[24] F. Iacopi, P.M. Vereecken, M. Schaekers, M. Caymax, N. Moelans, B. Blanpain, O. Richard, C. Detavernier, H. Griffiths, Plasma-enhanced chemical vapour deposition growth of Si nanowires with low melting point metal catalysts: an effective alternative to Au-mediated growth, *Nanotechnology,* 18 (2007), doi:10.1088/0957-4484/18/50/505307.
[25] D. Parlevliet, J.C.L. Cornish, Silicon Nanowires: Growth Studies Using Pulsed PECVD, *MRS Online Proceedings Library,* 989 (2007), doi:10.1557/PROC-0989-A23-03.
[26] L. Yu, P.-J. Alet, G. Picardi, I. Maurin, P.R.i. Cabarrocas, Synthesis, morphology and compositional evolution of silicon nanowires directly grown on SnO2 substrates, *Nanotechnology,* 19 (2008) 485605, doi:10.1088/0957-4484/19/48/485605.
[27] L. Yu, B. O'Donnell, P.J. Alet, S. Conesa-Boj, F. Peiro, J. Arbiol, P. Roca i Cabarrocas, Plasma-enhanced low temperature growth of silicon nanowires and hierarchical structures by using tin and indium catalysts, *Nanotechnology,* 20 (2009) 225604, doi:10.1088/0957-4484/20/22/225604.
[28] M. Jeon, K. Kamisako, Synthesis and characterization of silicon nanowires using tin catalyst for solar cells application, *Materials Letters,* 63 (2009) 777-779, doi:10.1016/j.matlet.2009.01.001.
[29] L. Yu, F. Fortuna, B. O'Donnell, T. Jeon, M. Foldyna, G. Picardi, P. Roca i Cabarrocas, Bismuth-Catalyzed and Doped Silicon Nanowires for One-Pump-Down Fabrication of Radial Junction Solar Cells, *Nano Letters,* 12 (2012) 4153-4158, doi:10.1021/nl3017187.
[30] V. Schmidt, J.V. Wittemann, U. Gösele, Growth, Thermodynamics, and Electrical Properties of Silicon Nanowires, *Chemical Reviews,* 110 (2010) 361-388, doi:10.1021/cr900141g.
[31] J.E. Allen, E.R. Hemesath, D.E. Perea, J.L. Lensch-Falk, Z.Y. Li, F. Yin, M.H. Gass, P. Wang, A.L. Bleloch, R.E. Palmer, L.J. Lauhon, High-resolution detection of Au catalyst atoms in Si nanowires, *Nature Nanotechnology,* 3 (2008) 168-173, doi:10.1038/Nnano.2008.5.
[32] M.C. Putnam, M.A. Filler, B.M. Kayes, M.D. Kelzenberg, Y.B. Guan, N.S. Lewis, J.M. Eiler, H.A. Atwater, Secondary Ion Mass Spectrometry of Vapor-Liquid-Solid Grown, Au-Catalyzed, Si Wires, *Nano Letters,* 8 (2008) 3109-3113, doi:10.1021/Nl801234y.
[33] L. Yu, W. Chen, B. O'Donnell, G. Patriarche, S. Bouchoule, P. Pareige, R. Rogel, A.C. Salaun, L. Pichon, P. Roca i Cabarrocas, Growth-in-place deployment of in-plane silicon nanowires, *Applied Physics Letters,* 99 (2011) 203104-203103, doi:10.1063/1.3659895.
[34] F. Trumbore, Solid solubilities of impurity elements in germanium and silicon, *Bell System Technical Journal,* 39 (1960) 205-233, http://www.alcatel-lucent.com/bstj/vol39-1960/articles/bstj39-1-205.pdf.

[35] J.R. Davis, Jr., A. Rohatgi, R.H. Hopkins, P.D. Blais, P. Rai-Choudhury, J.R. McCormick, H.C. Mollenkopf, Impurities in silicon solar cells, *Electron Devices, IEEE Transactions on,* 27 (1980) 677-687, doi:10.1109/t-ed.1980.19922.
[36] B. Kayes, Radial pn Junction, Wire Array Solar Cells, *Doctoral Thesis, California Institute of Technology,* (2009), http://thesis.library.caltech.edu/3702/.
[37] V. Schmidt, J.V. Wittemann, S. Senz, U. Gosele, Silicon Nanowires: A Review on Aspects of their Growth and their Electrical Properties, *Advanced Materials,* 21 (2009) 2681-2702, doi:10.1002/adma.200803754.
[38] W. Shockley, W.T. Read, Jr., Statistics of the Recombinations of Holes and Electrons, *Physical Review,* 87 (1952) 835-842.
[39] P. Lechner, H. Schade, Photovoltaic thin-film technology based on hydrogenated amorphous silicon, *Progress in Photovoltaics: Research and Applications,* 10 (2002) 85-97, doi:10.1002/pip.412.
[40] A. Luque, S. Hegedus, *Handbook of Photovoltaic Science and Engineering,* John Wiley & Sons, 2003, isbn: 9780471491965.
[41] Y. Ichikawa, T. Yoshida, T. Hama, H. Sakai, K. Harashima, Production technology for amorphous silicon-based flexible solar cells, *Solar Energy Materials and Solar Cells,* 66 (2001) 107-115, doi:10.1016/s0927-0248(00)00163-x.
[42] M. Pagliaro, R. Ciriminna, G. Palmisano, Flexible Solar Cells, *ChemSusChem,* 1 (2008) 880-891, doi:10.1002/cssc.200800127.
[43] K. Dick, T. Dhanasekaran, Z. Zhang, D. Meisel, Size-Dependent Melting of Silica-Encapsulated Gold Nanoparticles, *Journal of the American Chemical Society,* 124 (2002) 2312-2317, doi:10.1021/ja017281a.
[44] Q. Jiang, S. Zhang, M. Zhao, Size-dependent melting point of noble metals, *Materials Chemistry and Physics,* 82 (2003) 225-227, doi:10.1016/s0254-0584(03)00201-3.
[45] S. Hofmann, C. Ducati, R.J. Neill, S. Piscanec, A.C. Ferrari, J. Geng, R.E. Dunin-Borkowski, J. Robertson, Gold catalyzed growth of silicon nanowires by plasma enhanced chemical vapor deposition, *Journal of Applied Physics,* 94 (2003) 6005-6012, doi:10.1063/1.1614432.
[46] H. Hamidinezhad, Y. Wahab, Z. Othaman, A.K. Ismail, Synthesis and analysis of silicon nanowire below Si–Au eutectic temperatures using very high frequency plasma enhanced chemical vapor deposition, *Applied Surface Science,* 257 (2011) 9188-9192, doi:10.1016/j.apsusc.2011.05.130.
[47] P. Aella, S. Ingole, W.T. Petuskey, S.T. Picraux, Influence of plasma stimulation on Si nanowire nucleation and orientation dependence, *Advanced Materials,* 19 (2007) 2603, doi:10.1002/adma.200602944.
[48] J. Červenka, M. Ledinský, J. Stuchlík, H. Stuchlíková, S. Bakardjieva, K. Hruška, A. Fejfar, J. Kočka, The structure and growth mechanism of Si nanoneedles prepared by plasma-enhanced chemical vapor deposition, *Nanotechnology,* 21 (2010) 415604, doi:10.1088/0957-4484/21/41/415604.
[49] V.T. Renard, M. Jublot, P. Gergaud, P. Cherns, D. Rouchon, A. Chabli, V. Jousseaume, Catalyst preparation for CMOS-compatible silicon nanowire synthesis, *Nat Nano,* 4 (2009) 654-657, doi:10.1038/nnano.2009.234.
[50] M.A. Green, K. Emery, Y. Hishikawa, W. Warta, E.D. Dunlop, Solar cell efficiency tables (version 39), *Progress in Photovoltaics: Research and Applications,* 20 (2012) 12-20, doi:10.1002/pip.2163.
[51] L.M. Moore, H.N. Post, Five years of operating experience at a large, utility-scale photovoltaic generating plant, *Progress in Photovoltaics: Research and Applications,* 16 (2008) 249-259, doi:10.1002/pip.800.
[52] F. Birol, IEA World Energy Outlook 2010, International Energy Agency, (2010), http://www.iea.org/publications/freepublications/publication/name,27324,en.html.
[53] M.W. George, Mineral Commodity Summaries: Gold, US Geological Survey, (2011).
[54] V.E. McKelvey, Relation of reserves of the elements to their crustal abundance, *American Journal of Science,* 258-A (1960) 234-241, http://earth.geology.yale.edu/~ajs/1960/ajs_258A_11.pdf/234.pdf.

[55] H.K. Wedepohl, The composition of the continental crust, *Geochimica Et Cosmochimica Acta,* 59 (1995) 1217-1232, doi:10.1016/0016-7037(95)00038-2.
[56] E.I. Givargizov, *Highly Anisotropic Crystals,* Springer, Reidel: Dordrech, 1987, isbn: 9027721726.
[57] V.A. Nebol'sin, A.A. Shchetinin, A.A. Dolgachev, V.V. Korneeva, Effect of the nature of the metal solvent on the vapor-liquid-solid growth rate of silicon whiskers, *Inorganic Materials,* 41 (2005) 1256-1259, doi:10.1007/s10789-005-0296-5.
[58] M.E. Messing, K. Hillerich, J. Johansson, K. Deppert, K.A. Dick, The use of gold for fabrication of nanowire structures, *Gold Bulletin,* 42 (2009) 172-181, doi:10.1007/BF03214931.
[59] F. Iacopi, P.M. Vereecken, M. Schaekers, M. Caymax, N. Moelans, B. Blanpain, C. Detavernier, J. D'Haen, H. Griffiths, Alternative Catalysts For Si-Technology Compatible Growth Of Si Nanowires, *MRS Online Proceedings Library,* 1017 (2007), doi:10.1557/PROC-1017-DD01-10-EE01-10.
[60] T. Stelzner, G. Andrä, F. Falk, E. Wendler, W. Wesch, R. Scholz, S. Christiansen, Silicon nanowire synthesis on metal implanted silicon substrates, *Nuclear Instruments and Methods in Physics Research Section B: Beam Interactions with Materials and Atoms,* 257 (2007) 172-176, doi:10.1016/j.nimb.2007.01.037.
[61] V. Schmidt, Silicon Nanowires: Synthesis, Fundamental Issues, and a First Device, Martin-Luther-Universität, PhD (2006), http://nbn-resolving.de/urn/resolver.pl?urn=nbn%3Ade%3Agbv%3A3-000011060.
[62] H. Griffiths, C. Xu, T. Barrass, M. Cooke, F. Iacopi, P. Vereecken, S. Esconjauregui, Plasma assisted growth of nanotubes and nanowires, *Surface and Coatings Technology,* 201 (2007) 9215-9220, doi:10.1016/j.surfcoat.2007.04.067.
[63] L. Yu, B. O'Donnell, J.L. Maurice, P. Roca i Cabarrocas, Core-shell structure and unique faceting of Sn-catalyzed silicon nanowires, *Applied Physics Letters,* 97 (2010), doi:10.1063/1.3464557.
[64] S.J. Rathi, B.N. Jariwala, J.D. Beach, P. Stradins, P.C. Taylor, X.J. Weng, Y. Ke, J.M. Redwing, S. Agarwal, R.T. Collins, Tin-Catalyzed Plasma-Assisted Growth of Silicon Nanowires, *Journal of Physical Chemistry C,* 115 (2011) 3833-3839, doi:10.1021/Jp1066428.
[65] I. Zardo, L. Yu, S. Conesa-Boj, S. Estrade, P.J. Alet, J. Roessler, M. Frimmer, P. Roca i Cabarrocas, F. Peiro, J. Arbiol, J.R. Morante, A.Fontcuberta i Morral, Gallium assisted plasma enhanced chemical vapor deposition of silicon nanowires, *Nanotechnology,* 20 (2009), doi:10.1088/0957-4484/20/15/155602.
[66] A.T. Heitsch, D.D. Fanfair, H.Y. Tuan, B.A. Korgel, Solution-liquid-solid (SLS) growth of silicon nanowires, *Journal of the American Chemical Society,* 130 (2008) 5436, doi:10.1021/Ja8011353.
[67] Y. Xiang, L. Cao, J. Arbiol, M.L. Brongersma, A. Fontcuberta i Morral, Synthesis parameter space of bismuth catalyzed germanium nanowires, *Applied Physics Letters,* 94 (2009) 163101, doi:10.1063/1.3116625.
[68] H.Y. Kim, J. Park, H. Yang, Synthesis of silicon nitride nanowires directly from the silicon substrates, *Chemical Physics Letters,* 372 (2003) 269-274, doi:10.1016/s0009-2614(03)00428-7.
[69] C.Y. Kuo, C. Gau, Vapor–solid–solid growth of crystalline silicon nanowires using anodic aluminum oxide template, *Thin Solid Films,* 519 (2011) 3603-3607, doi:10.1016/j.tsf.2011.01.280.
[70] I. Zardo, L. Yu, S. Conesa-Boj, S. Estrade, P.J. Alet, J. Roessler, M. Frimmer, P. Roca i Cabarrocas, F. Peiro, J. Arbiol, J.R. Morante, A.Fontcuberta i Morral, Gallium assisted plasma enhanced chemical vapor deposition of silicon nanowires, *Nanotechnology,* 20 (2009), doi:10.1088/0957-4484/20/15/155602.
[71] J. Hu, T.W. Odom, C.M. Lieber, Chemistry and Physics in One Dimension: Synthesis and Properties of Nanowires and Nanotubes, *ChemInform,* 30 (1999), doi:10.1002/chin.199929268.
[72] L.E. Tanner, H. Okamoto, The Pt-Si (Platinum-Silicon) system, *Journal of Phase Equilibria,* 12 (1991) 571-574, doi:10.1007/bf02645072.
[73] P. Nash, A. Nash, The Ni−Si (Nickel-Silicon) system, *Journal of Phase Equilibria,* 8 (1987) 6-14, doi:10.1007/bf02868885.

[74] R. Olesinski, G. Abbaschian, The Cu−Si (Copper-Silicon) system, *Journal of Phase Equilibria,* 7 (1986) 170-178, doi:10.1007/bf02881559.
[75] H. Okamoto, T. Massalski, The Au−Si (Gold-Silicon) system, *Journal of Phase Equilibria,* 4 (1983) 190-198, doi:10.1007/bf02884878.
[76] H. Okamoto, Pd-Si (Palladium-Silicon), *Journal of Phase Equilibria and Diffusion,* 28 (2007) 231-232, doi:10.1007/s11669-007-9039-4.
[77] J. Murray, A. McAlister, The Al-Si (Aluminum-Silicon) system, *Journal of Phase Equilibria,* 5 (1984) 74-84, doi:10.1007/bf02868729.
[78] R. Olesinski, A. Gokhale, G. Abbaschian, The Ag-Si (Silver-Silicon) system, *Journal of Phase Equilibria,* 10 (1989) 635-640, doi:10.1007/bf02877631.
[79] R. Olesinski, G. Abbaschian, The Si-Zn (Silicon-Zinc) system, *Journal of Phase Equilibria,* 6 (1985) 545-548, doi:10.1007/bf02887156.
[80] R. Olesinski, G. Abbaschian, The Pb−Si (Lead−Silicon) system, *Journal of Phase Equilibria,* 5 (1984) 271-273, doi:10.1007/bf02868551.
[81] R. Olesinski, G. Abbaschian, The Bi−Si (Bismuth-Silicon) system, *Journal of Phase Equilibria,* 6 (1985) 359-361, doi:10.1007/bf02880522.
[82] R. Olesinski, G. Abbaschian, The Si−Sn (Silicon−Tin) system, *Journal of Phase Equilibria,* 5 (1984) 273-276, doi:10.1007/bf02868552.
[83] R. Olesinski, N. Kanani, G. Abbaschian, The In−Si (Indium-Silicon) system, *Journal of Phase Equilibria,* 6 (1985) 128-130, doi:10.1007/bf02869223.
[84] R. Olesinski, N. Kanani, G. Abbaschian, The Ga−Si (Gallium-Silicon) system, *Journal of Phase Equilibria,* 6 (1985) 362-364, doi:10.1007/bf02880523.
[85] K. Ostrikov, H. Mehdipour, Rapid, simultaneous activation of thin nanowire growth in low-temperature, low-pressure chemically active plasmas, *Journal of Materials Chemistry,* 21 (2011) 8183-8191, doi:10.1039/C1JM10318K.
[86] C.-Y. Wen, M.C. Reuter, J. Bruley, J. Tersoff, S. Kodambaka, E.A. Stach, F.M. Ross, Formation of Compositionally Abrupt Axial Heterojunctions in Silicon-Germanium Nanowires, *Science,* 326 (2009) 1247-1250, doi:10.1126/science.1178606.
[87] A.S. Skapski, The Surface Tension of Liquid Metals, *The Journal of Chemical Physics,* 16 (1948) 389-393, doi:10.1063/1.1746898.
[88] N. Eustathopoulos, B. Drevet, E. Ricci, Temperature coefficient of surface tension for pure liquid metals, *Journal of Crystal Growth,* 191 (1998) 268-274, doi:10.1016/s0022-0248(98)00012-8.
[89] H.M. Lu, Q. Jiang, Surface Tension and Its Temperature Coefficient for Liquid Metals, *The Journal of Physical Chemistry B,* 109 (2005) 15463-15468, doi:10.1021/jp0516341.
[90] V.A. Nebol'sin, A.A. Shchetinin, T.I. Sushko, E.I. Natarova, Growth stability of silicon whiskers, *Inorganic Materials,* 36 (2000) 419-421, doi:10.1007/BF02758037.
[91] E.I. Givargizov, *Rost nitevidnykh i plastinchatykh kristallov iz para (Vapor Growth of Whiskers and Platelike Crystals),* Moscow: Nauka 1977, isbn: B0000EH71X.
[92] W.R. Tyson, W.A. Miller, Surface free energies of solid metals: Estimation from liquid surface tension measurements, *Surface Science,* 62 (1977) 267-276, doi:10.1016/0039-6028(77)90442-3.
[93] R.J. Jaccodine, Surface Energy of Germanium and Silicon, *Journal of the Electrochemical Society,* 110 (1963) 524-527, doi:10.1149/1.2425806.
[94] S.-W. Chung, J.-Y. Yu, J.R. Heath, Silicon nanowire devices, *Applied Physics Letters,* 76 (2000) 2068-2070, doi:10.1063/1.126257.
[95] K. Nogi, K. Ogino, A. McLean, W. Miller, The temperature coefficient of the surface tension of pure liquid metals, *Metallurgical and Materials Transactions B,* 17 (1986) 163-170, doi:10.1007/bf02670829.
[96] T.R. Hogness, THE SURFACE TENSIONS AND DENSITIES OF LIQUID MERCURY, CADMIUM, ZINC, LEAD, TIN AND BISMUTH, *Journal of the American Chemical Society,* 43 (1921) 1621-1628, doi:10.1021/ja01440a026.

[97] J.M. Molina, R. Voytovych, E. Louis, N. Eustathopoulos, The surface tension of liquid aluminium in high vacuum: The role of surface condition, *International Journal of Adhesion and Adhesives,* 27 (2007) 394-401, doi:10.1016/j.ijadhadh.2006.09.006.
[98] M.I. den Hertog, J.-L. Rouviere, F. Dhalluin, P.J. Desré, P. Gentile, P. Ferret, F. Oehler, T. Baron, Control of Gold Surface Diffusion on Si Nanowires, *Nano Letters,* 8 (2008) 1544-1550, doi:10.1021/nl073356i.
[99] P. Madras, E. Dailey, J. Drucker, Spreading of Liquid AuSi on Vapor−Liquid−Solid-Grown Si Nanowires, *Nano Letters,* 10 (2010) 1759-1763, doi:10.1021/nl100249j.
[100] L. Yu, F. Fortuna, B. O'Donnell, G. Patriache, P. Roca i Cabarrocas, Stability and evolution of low-surface-tension metal catalyzed growth of silicon nanowires, *Applied Physics Letters,* 98 (2011), doi:10.1063/1.3569817.
[101] Z. Pan, S. Dai, D.B. Beach, D.H. Lowndes, Temperature Dependence of Morphologies of Aligned Silicon Oxide Nanowire Assemblies Catalyzed by Molten Gallium, *Nano Letters,* 3 (2003) 1279-1284, doi:10.1021/nl0343203.
[102] O. Khyzhun, L. Sygellou, S. Ladas, Interfacial Oxidation of Ultrathin Nickel and Chromium Films on Yttria-Stabilized Zirconia†, *The Journal of Physical Chemistry B,* 109 (2004) 2302-2306, doi:10.1021/jp048875d.
[103] G.A. El-Shobaky, A.S. Ahmad, A.N. Al-Noaimi, H.G. El-Shobaky, Thermal decomposition of basic cobalt and copper carbonates, *Journal of Thermal Analysis and Calorimetry,* 46 (1996) 1801-1808, doi:10.1007/bf01980784.
[104] M. Iwamoto, Y. Yoda, N. Yamazoe, T. Seiyama, Study of metal oxide catalysts by temperature programmed desorption. 4. Oxygen adsorption on various metal oxides, *The Journal of Physical Chemistry,* 82 (1978) 2564-2570, doi:10.1021/j100513a006.
[105] J.H. Thomas, X-ray photoelectron spectroscopy study of hydrogen plasma interactions with a tin oxide surface, *Applied Physics Letters,* 42 (1983) 794-796, doi:10.1063/1.94097.
[106] O. Kuboi, Degradation of ITO Film in Glow-Discharge Plasma, *Japanese Journal of Applied Physics,* 20 (1981), doi:10.1143/JJAP.20.L783.
[107] G.V. Bianco, M.M. Giangregorio, P. Capezzuto, M. Losurdo, T.-H. Kim, A.S. Brown, G. Bruno, Plasma-plasmonics synergy in the Ga-catalyzed growth of Si-nanowires, *Materials Science and Engineering: B,* (2012), doi:10.1016/j.mseb.2011.09.030.
[108] I. Langmuir, TYPES OF VALENCE, *Science,* 54 (1921) 59-67, doi:10.1126/science.54.1386.59.
[109] L.M. Falicov, G.A. Somorjai, Correlation between Catalytic Activity and Bonding and Coordination-Number of Atoms and Molecules on Transition-Metal Surfaces - Theory and Experimental-Evidence, *Proceedings of the National Academy of Sciences of the United States of America,* 82 (1985) 2207-2211, doi:10.1073/pnas.82.8.2207.
[110] T.J. Clark, K. Lee, I. Manners, Transition-Metal-Catalyzed Dehydrocoupling: A Convenient Route to Bonds between Main-Group Elements, *Chemistry – A European Journal,* 12 (2006) 8634-8648, doi:10.1002/chem.200600981.
[111] T.D. Tilley, Mechanistic Aspects of Transition-Metal Catalyzed Dehydrogenative Silane Coupling Reactions, *Comments on Inorganic Chemistry,* 10 (1990) 37-51, doi:10.1080/02603599008048649.
[112] G. Bond, Catalysis by Metals, Academic Press (1962).
[113] M.J.S. Spencer, G.L. Nyberg, Adsorption of silane and methylsilane on gold surfaces, *Surface Science,* 573 (2004) 151-168, doi:10.1016/j.susc.2004.08.043.
[114] L.H. Dubois, B.R. Zegarski, The activated adsorption of silane on nickel, *Surface Science,* 204 (1988) 113-128, doi:10.1016/0039-6028(88)90271-3.
[115] E.M. McCash, M.A. Chesters, P. Gardener, S.F. Parker, The adsorption and decomposition of silane on Cu(111), *Surface Science,* 225 (1990) 273-280, doi:10.1016/0039-6028(90)90448-h.
[116] P. Roca i Cabarrocas, M. Stchakovsky, B. Drevillon, F. Fortuna, H. Bernas, Kinetics of formation of silicides in a-Si:H/Pd interfaces monitored by in situ ellipsometry and kelvin probe techniques,

Journal of Non-Crystalline Solids, 137–138, Part 2 (1991) 1055-1058, doi:10.1016/s0022-3093(05)80303-5.
[117] M.C. Kung, R.J. Davis, H.H. Kung, Understanding Au-Catalyzed Low-Temperature CO Oxidation, *The Journal of Physical Chemistry C,* 111 (2007) 11767-11775, doi:10.1021/jp072102i.
[118] P.J. Alet, L. Yu, G. Patriarche, S. Palacin, P. Roca i Cabarrocas, In situ generation of indium catalysts to grow crystalline silicon nanowires at low temperature on ITO, *Journal of Materials Chemistry,* 18 (2008) 5187-5189, doi:10.1039/B813046a.

4. Sn-catalyzed SiNW Growth

"Oh torre de la luz, triste hermosura."

In this chapter we detail the results of our optimization studies for the morphology of Sn-catalyzed nanowires. Several intriguing properties of plasma-assisted VLS growth with Sn catalysts are brought forward. We look into the unusual independence of growth rate on temperature, the apparent absence of catalyst drops at the nanowire tips, the relation between growth rate and the abundance of feed species. We also draw attention to challenges in achieving straight nanowire growth at 250 °C and explore the unusual faceting which develops over the sidewalls of Sn and In-catalyzed SiNWs grown at higher temperatures. These results offer some fresh insight into the VLS mechanism in general and draft an initial road map for future optimization studies into the morphology of Sn-catalyzed SiNWs.

"Tower of light, mournful beauty.", La Isla, Pablo Neruda, 1968-1974

1. Sn-catalysts and plasma-assisted VLS fabrication conditions

In view of considerations detailed in the previous chapter regarding contamination during the VLS growth process and fabrication costs, we adopted drops of liquid Sn to catalyze the growth of our SiNWs. This choice entailed parametric optimization studies as Sn has to date remained seldom exploited as a SiNW catalyst compared, for instance, with Au. This is in fact surprising given its history in crystallizing Si for solar cell applications by liquid phase epitaxy.[1-3] Filamentary silicon growth was reported in several studies where Sn was vaporized with Si in tube furnaces at high temperatures.[4-7] However little control over the system could be attained and the nanowire morphologies produced were typically erratic. The first report of customary VLS growth with Sn-catalysts only emerged in 2007, when Parlevliet and Cornish exposed a film of Sn to a pulsed silane plasma and obtained dense disordered arrays of bending silicon nanowires.[8, 9] In 2008, Yu et al. published a systematic study on the growth mechanism and properties of SiNWs catalyzed by Sn drops reduced from layers of SnO_2.[10] Several reports of Sn-catalyzed SiNW growth have since explored their compatibility with alternative fabrication techniques[11-13] and intricacies in their growth mechanism.[14-17] Recent reports have also emerged of Sn-catalyzed SiNWs integrated into photovoltaic devices.[9, 18, 19] Much of the progress which has permitted us to make this step from new materials to new devices is described in the present chapter.

1.1. Process conditions

The nanowires in this chapter were fabricated in two radio-frequency (13.56 kHz), plasma enhanced chemical vapor deposition (RF-PECVD) reactors, which will be referred to in the text as the ARCAM (Figure 4.1.a) and Plasfil reactors (Figure 4.1.b). Each reactor presented its own advantages. In Plasfil, growth temperatures of up to a nominal value of 700°C could be reached (although Kapton temperature probes suggested the real temperature at the sample surface could be lower than this value).

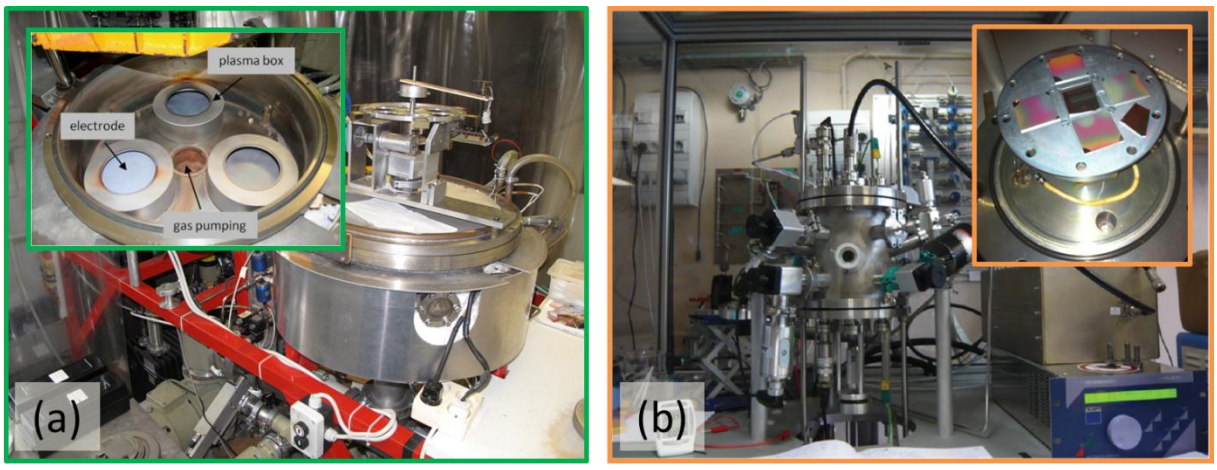

4.1 -- Arcam and Plasfil PECVD reactors.
Arcam (a) and Plasfil (b) plasma-enhanced chemical vapor deposition reactors. Insets show inside of the reactor chambers.

The ARCAM reactor could be heated no further than 275°C; however it offered greater flexibility in terms of the gases used. It was notably linked to trimethylboron and phosphine lines that made it possible to dope Si during deposition, which were necessary to make the solar cells presented in Chapter 5. The substrates used were typically inch by inch pieces of glass (1.1 mm thick) covered in an 80 nm layer of SnO_2 supplied by Asahi (Figure 4.2.b). Experiments were also conducted on thin layers of Sn (5 nm) evaporated in-house over corning glass (1.1 mm thick) (Figure 4.2.a).

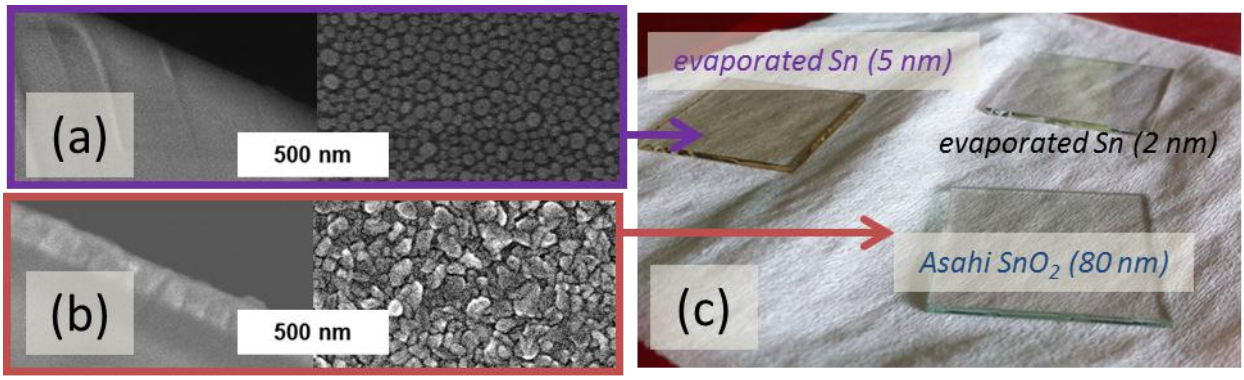

4.2 - Substrates used in the SiNW morphology optimization studies.
Two types of substrates were used in the optimization study for SiNW morphology. Inch by inch pieces of glass over which a few nm of Sn were evaporated (a) and substrates of glass covered in 80 nm of SnO_2 purchased from Asahi (b).

Table 4.1: Typical process conditions in the Plasfil reactor

	range of values tested	H-plasma	range of values tested	SiH_4-plasma
temperature (substrate)	180 – 600 °C	250 °C	250 – 700 °C	600 °C
temperature (RF electrode)	180 – 600 °C	200 °C	250 – 600 °C	400 °C
plasma power	20 – 450 mW	50 mW/cm²	20–450 mW	20 mW/cm²
chamber pressure	260 – 600 mTorr	260 mTorr	70 – 1000 mTorr	380 mTorr
hydrogen flow	100 – 200 sccm	100 sccm	0 – 200 sccm	100 sccm
silane flow		0	2 – 10 sccm	10 sccm
electrode distance		3 cm		3 cm
duration	1 – 10 minutes	5 minutes	1 – 120 minutes	15 minutes

The substrates were exposed to a H_2 plasma prior to VLS growth to reduce the metal oxide on their surface and form metallic drops. In the Plasfil reactor, the conditions of this plasma were typically a H_2 gas flow of 100 sccm, a pressure of 260 mTorr, an RF power density of 50 mW/cm² and a duration of 5 minutes. Following the H-plasma reduction step, the power applied to the plasma was turned off, the temperature of the chamber was increased (typically to 600°C), the H_2 pressure in the chamber

was increased to 1 Torr and the chamber was left to thermalize for 10 minutes. Growth conditions for the nanowire were then established, typically by introducing a 10 sccm silane flow into the chamber and bringing the gas pressure to 260 mTorr by adjusting the position of a butterfly valve leading to the gas pump. The chamber was left to thermalize for 10 minutes before igniting the plasma with an RF-power density of typically 20 mW/cm². We intentionally established a temperature gradient between the electrodes in the Plasfil reactor, setting the substrate heater at a temperature 50 – 200 °C higher than the RF electrode, to enhance the thermal diffusion of dust and powders away from the sample surface. These process conditions are summarized in Table 4.1.

Conditions in the ARCAM reactor required adjustment to produce similar nanowire growth. The temperature was limited to 275 °C, the H_2 plasma was conducted under a pressure of 600 mTorr for 3 minutes and the RF power density was reduced to 30 mW/cm². Plasma conditions could be adjusted while the chamber was empty and samples were rotated into it once they had stabilized. In the ARCAM reactor; all heaters were set to the same temperature. Typical process conditions for catalyst reduction and SiNW growth in the ARCAM reactor are detailed in Table 4.2.

Table 4.2: Typical process conditions in the ARCAM reactor

	range of values tested	H-plasma	range of values tested	SiH_4-plasma	range of values tested
temperature (substrate)		250 °C	250 – 275 °C	250 °C	250 – 700 °C
temperature (RF electrode)		200 °C	250 – 275 °C	250 °C	250 – 600 °C
plasma power		30 mW/cm²	30 mW	5 mW/cm²	5 – 30 mW
chamber pressure		600 mTorr	260 – 600 mTorr	70 mTorr	70 – 1200 mTorr
hydrogen flow		200 sccm	200 sccm	0 sccm	0 – 200 sccm
silane flow		0		50 sccm	2 – 10 sccm
electrode distance		2.8 cm	1.2 – 2.8 cm	2.8 cm	1.2 – 2.8 cm
duration		5 minutes	1 – 10 minutes	15 minutes	1 – 130 minutes

When the plasma did not ignite, the standard procedure was to close the valve to the process pump in order to briefly increase the pressure in the chamber. As soon as the plasma ignited, the valve was reopened and the chamber pressure was observed to stabilize at the intended value within seconds.

2. Parameters influencing the nanowire growth rate

We begin by describing the impact of the plasma conditions on the growth rate of the SiNWs. The growth rate insightfully summarizes the nanoscopic reactions involved in the VLS process. Varying, one by one, parameters which affect it and observing their respective impact offers information on the mechanism which we are trying to control.

2.1. The effect of temperature on growth rate

Substrates of glass/SnO_2 (80 nm) were exposed to hydrogen then silane plasmas both in the Plasfil and the ARCAM reactors under the process conditions described in Table 4.1-2 for growth durations spanning 2 to 130 minutes. Despite risks of catalyst loss both to the vapor phase and to precipitation within the nanowire material,[17, 20, 21] the growth rate remained linear. Recent (unpublished) results have shown that the nanowire length eventually saturates for growth durations of several hours. However, over the durations studied in this chapter, the growth rate of Sn-catalyzed SiNWs in Plasfil (0.42 $nm.s^{-1}$) and ARCAM (0.43 $nm.s^{-1}$) was virtually identical. Their appearance, however, was strikingly different. SiNWs grown in the Plasfil reactor were substantially thinner and straighter (Figure 4.3.a) than those grown in ARCAM (Figure 4.3.c). This suggests that although a difference in the growth temperature of 250 to 600 °C plays a key role in the diameter and morphology of Sn-catalyzed SiNWs, its impact on the growth rate is marginal (Figure 4.3.b). In contrast, the VLS growth of Au-catalyzed SiNWs under standard CVD conditions is a thermally activated process in which the nanowire growth rate is tightly correlated to the substrate temperature.[22] However the situation differs substantially in our system because neither the temperature nor the Sn catalysts are expected to dissociate the silane gas - this task is performed by the plasma.

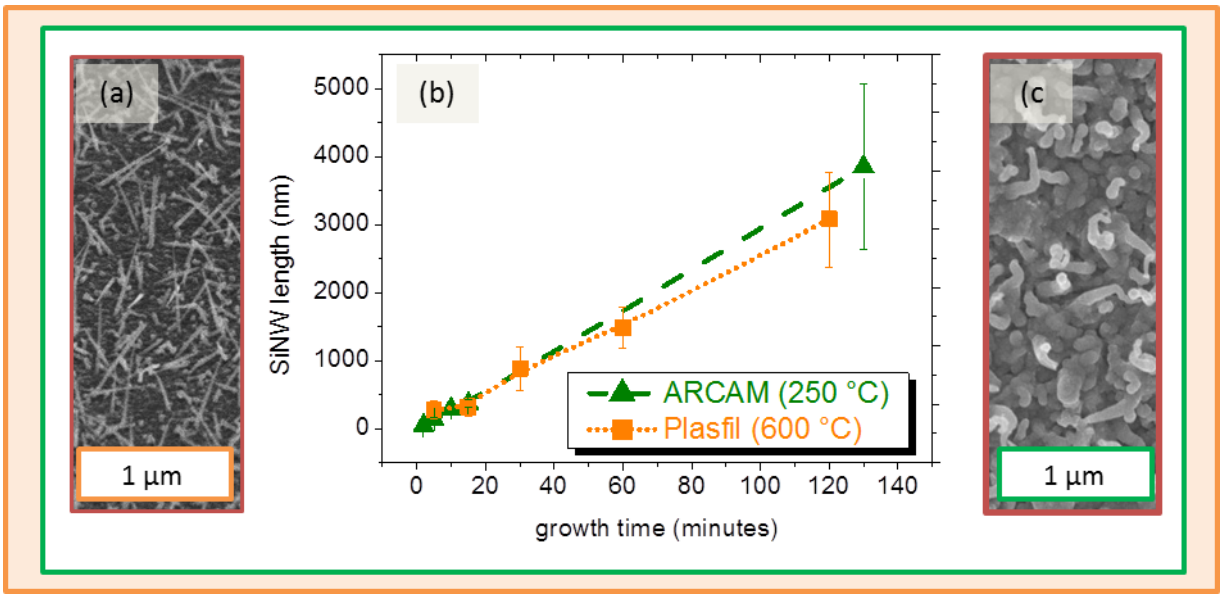

4.3 - Sn-catalyzed SiNW length as a function of growth time.
Sn-catalyzed SiNWs grown in the Plasfil and ARCAM reactor over durations spanning from 2 to 130 minutes (b) and SEM micrographs of Sn-catalyzed SiNWs grown in the Plasfil (a) and ARCAM (c) reactor for 15 minutes.

Closer inspection of the ARCAM samples on which nanowires were grown for 130 minutes revealed that the tip of the nanowires had retained the same diameter as observed on 15 minute growths (Figure 4.4). However the diameter at their base had grown considerably (Figure 4.4.a), showing that although VLS can proceed unperturbed for hours, the competing deposition of a-Si:H from the silane plasma continuously covers the nanowire sidewalls.

It was also noted that the nanowires grown in Plasfil (at 600 °C) were considerably tapered and often presented sharp tips at the end of which no catalyst drops were observed (Figure 4.5.a). Červenka et

al. reported similar needle-like structures when growing SiNWs from Au catalysts by PECVD. They attributed the thicker base to PECVD deposition on the nanowire sidewalls, although they noted with interest that the sidewall deposition was also crystalline.[23]

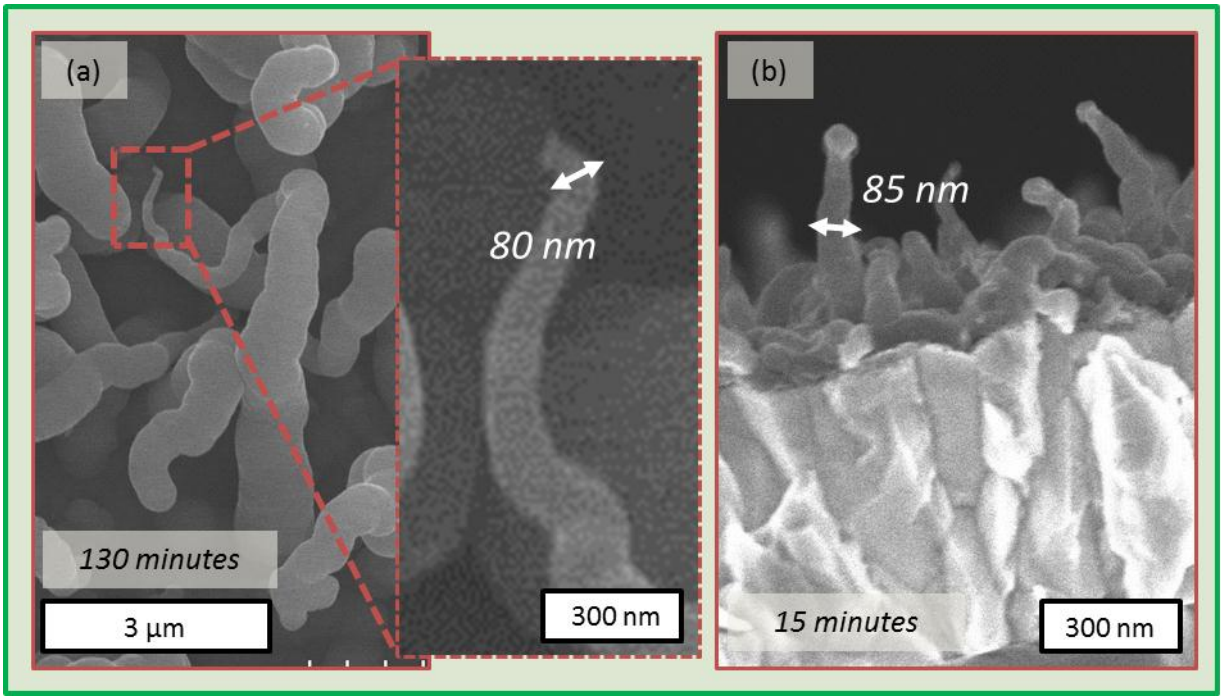

4.4 - Diameter of Sn-catalyzed SiNW grown in the ARCAM reactor.
SEM micrographs of Sn-catalyzed SiNWs grown on glass/SnO_2 substrates in the ARCAM reactor for durations of 130 minutes (a) and 15 minutes (b). Inset of Figure 4.4.a draws attention to the diameter of the nanowire tip, which has not changed throughout the growth process.

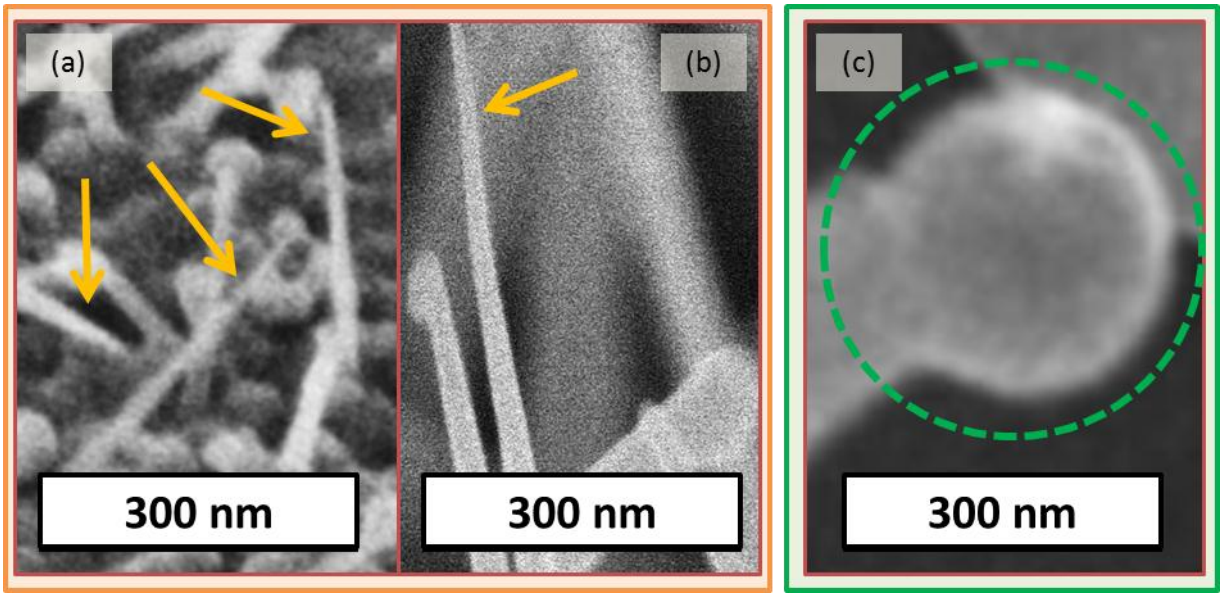

4.5 - Catalyst drops not found at the tip of Sn-catalyzed SiNWs grown at 600 °C.
SEM micrographs of Sn-catalyzed SiNWs grown on glass/SnO_2 substrates in the Plasfil reactor for 5 minutes (a) and 60 minutes (b), and in the ARCAM reactor for 130 minutes (c). Arrows designate needle-like nanowire tips apparently devoid of catalyst drops, while circles designate visible catalyst drops.

We were inclined to attribute the absence of catalyst drops to depletion (either to the gas phase or precipitation within the nanowire). However, the nanowires were observed to grow for durations exceeding the time it took for their catalyst drops to disappear. Figure 4.5 shows that many Sn-catalyzed SiNWs no longer exhibited catalyst drops at their tip after 5 minutes (Fig. 4.7.b). In spite of this, their growth proceeded at a constant rate for 60 minutes (Figures 4.5.b). In contrast, catalyst drops were generally visible at the tip of Sn-catalyzed SiNWs grown in the ARCAM reactor at 250 °C even after deposition times exceeding 2 hours (Figure 4.5.c). Another surprising property of the silicon nanowire arrays was that their density proved substantially lower than the density of Sn drops which catalyzed their growth (Figure 4.6). Following exposure to a silane plasma for 15 minutes, the density of nanowires at the substrate surface had decreased from the initial 1900 catalyst drops per µm² to fewer than 100 nanowires per µm² in the Plasfil reactor and 5 nanowires per µm² in the ARCAM reactor.

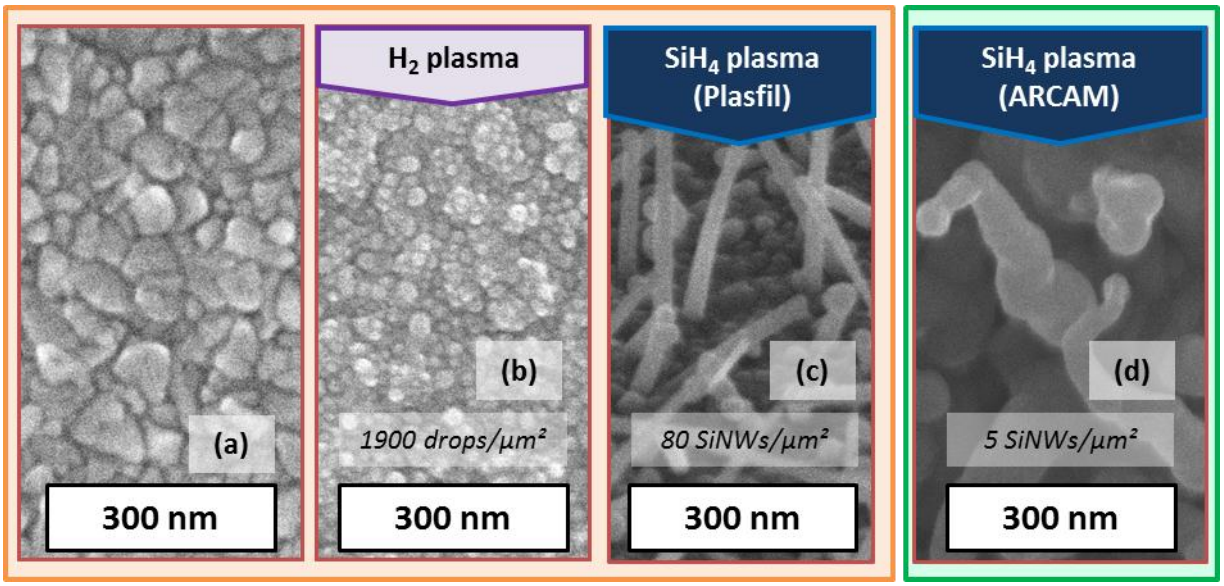

4.6 - Density of Sn-cataylzed SiNWs and catalyst drops.
SEM micrographs of the surface of a glass/SnO_2 substrate before treatment (a), following exposure to a H_2 plasma for 5 minutes (b), and following exposure to a silane plasma in either the Plasfil (c) or ARCAM (d) reactor for 15 minutes.

This decrease in the catalyst density may result from catalyst drops reconfiguring as they are exposed to the silane plasma. A similar process was observed in Chapter 2 when Si contamination altered the distribution of metal drops on the substrate surface (Figure 2.15). In favor of this interpretation, it was observed that the tip of the SiNWs generally presented catalyst drops with diameters larger (Figure 4.6.d) than the average Sn drops prior to VLS growth (Figure 4.6.d). However further studies indicated that this may not be the only factor. To gain further insight into the initial stages of the nanowire growth process, we submitted substrates of glass/SnO_2 to hydrogen and silane plasmas in the Plasfil reactor under conditions specified in Table 3.1 and halted their growth after 5 minutes. The density of nanowires on these samples was lower than that on samples exposed for 15 minutes (Figure 4.7) with a high number of shorter nanowires only beginning to grow. These observations fit

with findings of an incubation time during which catalysts incorporate silicon prior to initiating VLS and which can last several minutes.[24, 25] During this incubation time, the silane plasma is continuously depositing a-Si:H over the sample surface. If the catalysts cannot incorporate enough Si atoms to exceed their solubility and initiate VLS growth fast enough, they will foreseeably remain buried, possibly explaining the observed decrease in density.

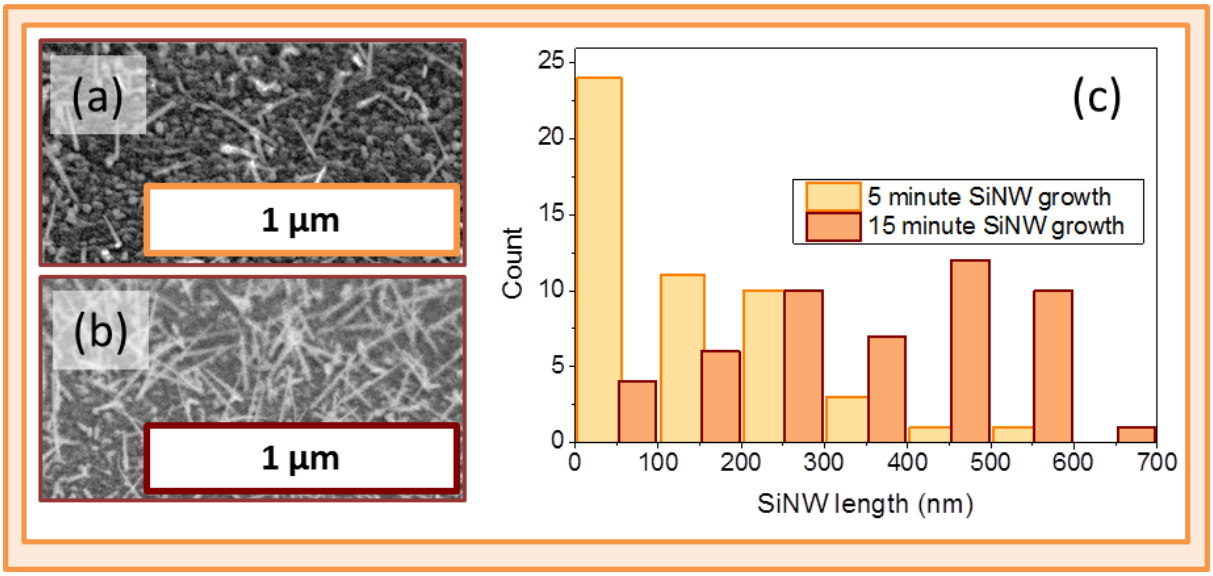

4.7 - Incubation period of Sn-catalyzed SiNWs grown in Plasfil.
SEM micrographs of Sn-catalyzed SiNWs grown on glass/SnO_2 substrates at 600 °C in the Plasfil reactor for durations of 5 minutes (a) and 15 minutes (b). Histogram of nanowire lengths in both samples (c).

2.2. The effect of silane pressure on growth rate

We studied the effect of the silane gas pressure on the growth rate of the SiNWs. Substrates of glass/SnO_2 (80 nm) were again exposed to hydrogen and silane plasmas under standard conditions (Table 4.1) in the Plasfil reactor. In this experiment, the growth time was fixed at 10 minutes and the total pressure in the system was varied from 70 to 1000 mTorr. As silane was diluted 1:10 in H_2, the partial Si pressure in the chamber ranged from 7 to 90 mTorr. The growth rate was observed to increase linearly with the partial pressure of SiH_4 in the chamber (Figure 4.8), suggesting that higher concentrations of Si in the gas phase lead to faster incorporation into the catalyst. It was also observed that the density of SiNWs on the sample surface decreased as they grew longer (Figure 4.8.a). Samples deposited under the maximal (90 mTorr) silane partial pressure exhibited considerably larger separation between each nanowire (Figure 4.8.e). This may result from increased reconfiguration (coalescence) when Sn drops are exposed to a higher pressure silane plasma. However it may also be related to higher rates of parasitic deposition from the silane plasma burying the catalysts of nanowires faster. The diameters at the base of nanowires grown under higher silane partial pressures were also observed to be substantially thicker (Figure 4.8.e). This foreseeably results from increased parasitic a-Si:H deposition on their sidewalls. Because their diameter exceeds the distance separating nanowires grown at lower pressure (Figure 4.8.b), some contribution to the decrease in density may also originate from nanowires merging with each other as they grow longer and their bases thicken.

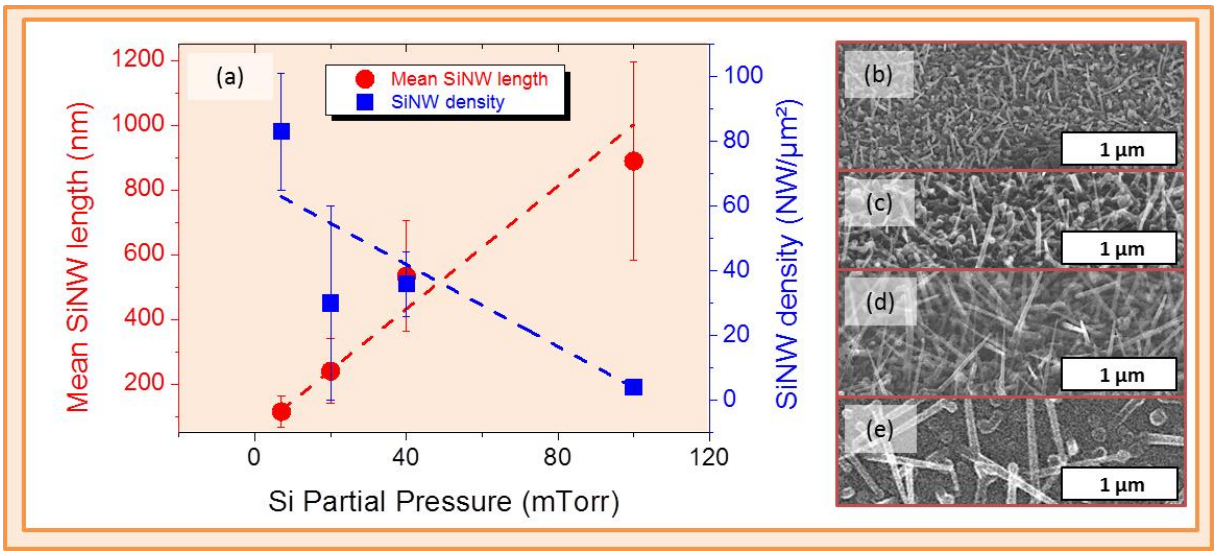

4.8 – Length and density of Sn-catalyzed SiNWs as a function of silane pressure.
SiNW length and density as a function of silane pressure during VLS growth for a duration of 10 minutes (a) for pressures of 7 mTorr (b), 20 mTorr (c), 40 mTorr (d) and 90 mTorr (e).

The direct relation between the abundance of the feed species and the nanowire growth rate has been reported on nanowires grown from other catalysts.[26] It has historically been used as evidence that, under certain conditions, species incorporation into the catalyst drop can be the rate-limiting step determining the nanowire growth rate.[27]

2.3. The effect of H_2 dilution on growth rate

In an attempt to rid the nanowires of the parasitic a-Si:H deposition on their sidewalls, we increased the concentration of H_2 gas in the plasma during VLS growth. Atomic hydrogen is known to etch a-Si:H and lead to plasma deposited layers of silicon with a higher crystal fraction.[28] The objective of the experiment was to continuously etch the parasitic a-Si:H growth on the nanowire sidewalls and produce thin, straight Sn-catalyzed SiNWs at low temperature. The experiment was conducted in the ARCAM reactor, using initially standard conditions (Table 4.2) on substrates of glass/SnO_2. The silane flow rate and total gas pressure in the chamber were kept constant while the hydrogen flow rate was progressively increased from 0 to 200 sccm so that its partial pressure contributed from 0 to 80 % of the total plasma pressure.

Nanowire growth in these samples remained twisted and kinked (Figure 4.9) with large diameters in comparison with the nanowires typically grown in Plasfil at higher temperatures (Figure 4.3.a). However the depositions differed considerably in that the density and length of the Sn-catalyzed SiNWs was observed to vary considerably according to the H_2 concentration in the plasma. When no H_2 was added, the nanowire density was low (Figure 4.9.a). A modest concentration of H_2 in the plasma increased both the length and density of the SiNWs (Figure 4.9.b), while a large proportion of H_2 in the plasma led to lower SiNW lengths and densities again (Figure 4.9.c). It was also noted that the average diameter of the Sn catalyst drops found at the tip of the nanowires decreased considerably as the H_2 concentration was increased. The experiment was repeated on substrates of

glass covered in an evaporated layer of Sn whose thickness was given as 2.6 nm by a quartz microbalance positioned close to the samples inside the evaporator. Although the nanowires grown were generally smaller, denser and less straight, the general behavior with respect to increases in the H_2 concentration were the same as with the glass/SnO_2 substrates.

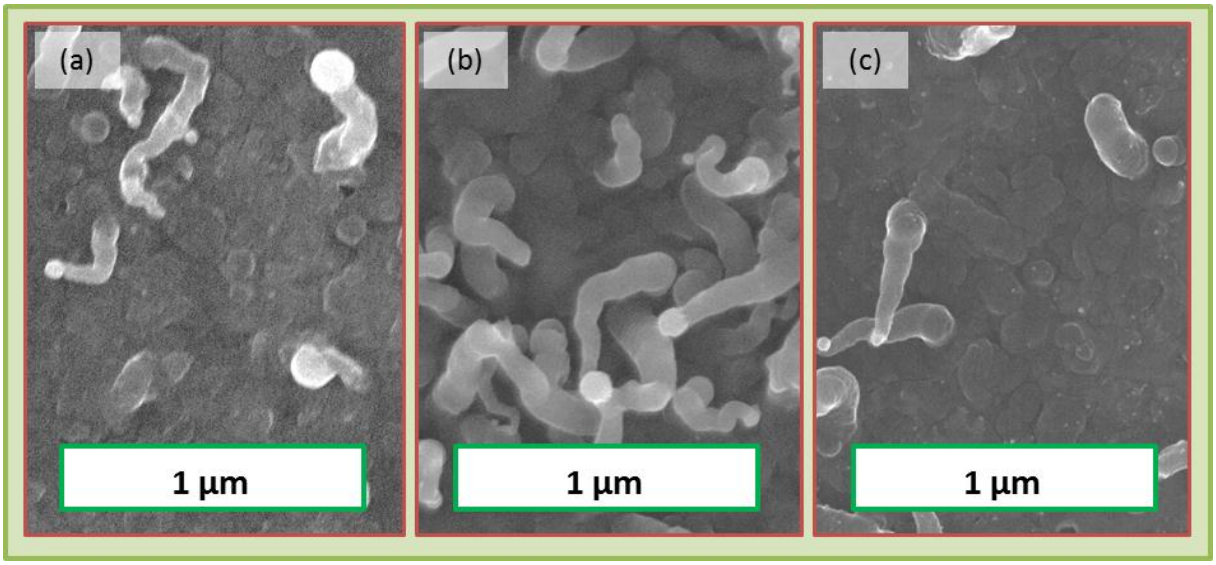

4.9 - Effect of hydrogen concentration on the growth rate of Sn-catalyzed SiNWs.
SEM micrographs of Sn-catalyzed SiNWs grown at 250 °C in the ARCAM reactor in silane plasmas with a hydrogen concentration of 0% (a), 23% (b) and 80% (c).

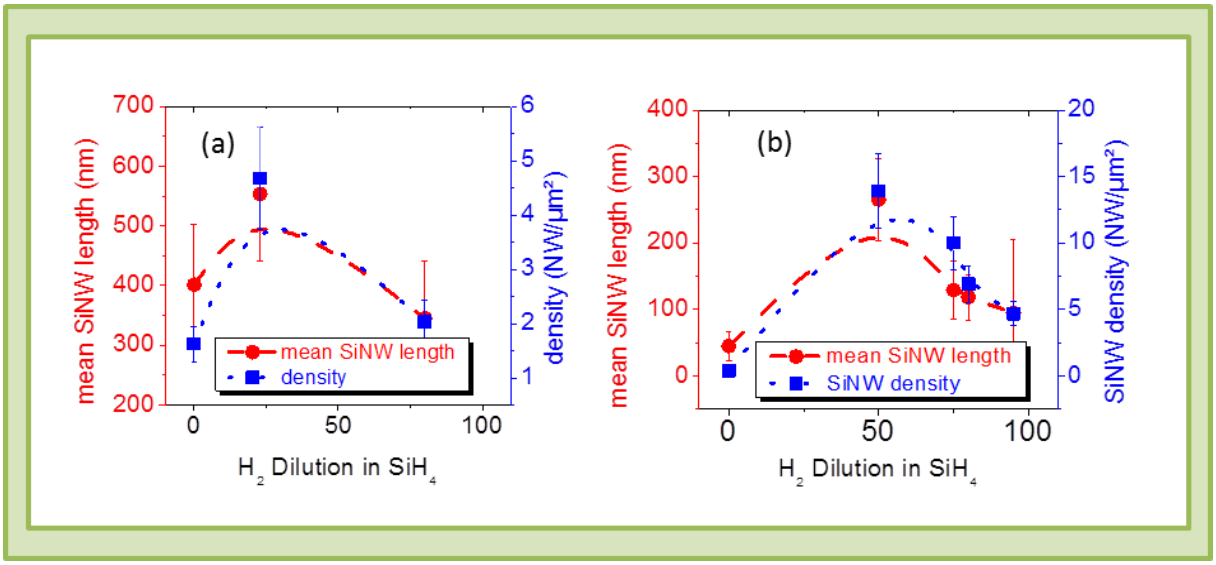

4.10 - Dimensions of Sn-catalyzed SiNWs grown under different H_2 concentrations.
The dependence of SiNW length and density on the concentration of H_2 in the SiH_4 plasma on substrates of glass/SnO_2 (a) and glass covered in evaporated Sn (4nm) (b).

With both kinds of substrates, the number and length of Sn-catalyzed SiNWs initially increased with the H_2 concentration in the plasma then decreased as the H_2 concentration dominated the gas mix (Figure 4.10). This non-linear relation may be due to the variety of roles which hydrogen plays in the growth of Sn-catalyzed SiNWs. It is known to reduce the oxidation at the catalyst surface but it also

dilutes the nanowire feed species as it is added to the plasma. When Sn drops are not exposed to a preliminary hydrogen plasma, they are unlikely to catalyze VLS growth at all. It is possible that some hydrogen is necessary during deposition to ensure the catalyst does not reoxidize. Atomic hydrogen is always present in our system during plasma assisted VLS as it is a by-product of the dissociation of silane molecules. Notwithstanding, an additional flow may optimize its concentration for keeping the catalyst surface reduced. However, adding hydrogen also reduces the partial pressure of silane in the plasma, which as seen in Figure 4.8, scales directly with the nanowire growth rate. A similar decrease in growth rate for Sn-catalyzed nanowires grown in silane plasmas under increased H_2 concentrations was observed by Rathi et al.[17] who also ascribed it to the reduced abundance of feed species in the plasma. The non-linear relation in Figures 4.10.a-b between the H_2 concentration and the nanowire growth presumably results from competition between its beneficial effect on growth rate in reducing the catalyst surface and its detrimental effect of diluting the feed species in the plasma.

2.4. The effect of plasma power on growth rate

Increasing the plasma power is known to increase the density and energy of ions in the plasma which in turn dissociates a higher fraction of silane molecules, alters the plasma chemistry and can increase the silicon deposition rate in standard PECVD deposition of a-Si:H films.[29] A glass substrate covered with SnO_2 was exposed to a hydrogen and silane plasma under standard Plasfil conditions (Table 4.1) increasing silane plasma power density from 20 to 300 mW/cm². The nanowires were observed to grow twice as long and substantially thicker (Figure 4.11.b) than usual (Figure 4.11.c). Their density was also observed to decrease (Figure 4.11.a).

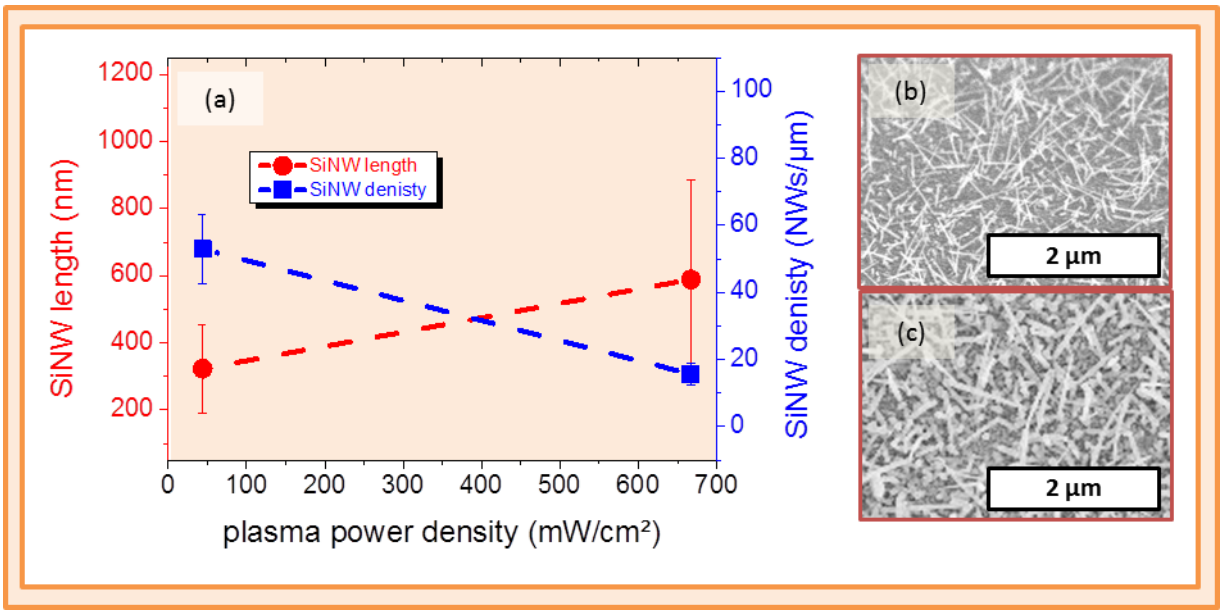

4.11 - Effect of plasma power on the growth rate of Sn-catalyzed SiNWs.
Sn-catalyzed SiNWs grown on glass/SnO_2 substrates at 600 °C in the Plasfil reactor for plasma power densities of 20 mW/cm² (a) and 300 mW/cm² (b).

Increases in SiNW growth rates have been reported when changing the feed species from a silane gas to a silane plasma.[30, 31] These results may follow the same logic as the relation between nanowire

growth and gas pressure. By dissociating silane molecules, the plasma effectively increases the abundance of reactive feed species in the environment of the catalyst drop. This may however prove an unadvisable approach to reduce nanowire growth times. We observed a modest increase in the length and diameter of the SiNWs (by a factor of 2) for a ten-fold increase in the plasma power. Such high power densities can lead to the formation of particles and dust in the plasma which contaminate the deposition and compromise its electronic properties.

In summary, within the experimental conditions studied, the growth rate of the Sn-catalyzed SiNWs remained unaffected by the temperature of the VLS growth process; however it responded strongly to changes in the abundance of the growth species. This was highlighted by varying the total silane pressure and the plasma power density, which resulted in the growth of longer nanowires. Adding hydrogen to the silane plasma was initially observed to enhance nanowire growth; however above a critical concentration, it was observed to hinder it (presumably as a result of diluting the silane in the plasma).

3. Straight and faceted SiNW growth

In Chapter 3, we presented the VLS growth process by stating that metal drops heated at temperatures higher than their eutectic point with the growth species can liquefy and catalyze the growth of vertical, crystalline nanowires. This description risks missing some of the key points governing the dynamics of the process. In practice, it is very challenging to achieve straight nanowire growth at the eutectic temperature and samples generally need to be heated to considerably higher temperatures to avoid kinks or bending in their structure.[32] The substrate temperature plays an important and complex role in the VLS growth process. It determines many factors in the system, including the mobility of adsorbed growth species, the hydrogen passivation of the substrate surface, the solubility of the species within the catalyst drop and their diffusion coefficient through the liquid metal.

3.1. The effect of temperature on growing straight SiNWs

We are primarily interested in growing Sn-catalyzed SiNWs straight because any kinks would constitute obstacles to the conformal coverage of the subsequent layers required to complete the radial PIN junctions (Chapter 5). Although vertical Sn-catalyzed SiNWs grew in the ARCAM reactor at temperatures as low as 250 °C (Figure 4.12.a), none of the process conditions explored succeeded in making them straight or reducing their kinks. Straight nanowire growth was only observed for samples made at higher temperature in the Plasfil reactor. We studied the impact of the substrate temperature by submitting substrates of glass/SnO_2 to the standard H_2 plasma conditions described in Table 4.1 and varying the nominal nanowire growth temperature from 300 °C to 600 °C. However straight VLS growth in the Plasfil reactor was only observed at 600 °C (Figure 4.12.e).

A similar trend emerges from the growth conditions reported in the literature. While the eutectic point of silicon with for Au, Sn, In and Ga indicates that SiNWs can be grown at temperatures as low as 363 °C, 231 °C, 156 °C and 30 °C respectively, straight growth is typically observed at temperatures

higher than 600 °C (Figure 4.13.e-h). It is also striking that the occasional reports of VLS growth at temperatures lower than 400 °C generally present bent and kinked SiNWs (Figures 4.13.a-d). The nanowires in Figure 4.13 were taken from reports of nanowire growth using different fabrication techniques, conditions and catalysts, yet the temperature has invariably stood out as the dominant factor governing their crystallinity. Why this happens may be related to the free energy of Si atoms at the interface between the catalyst drop and the nanowire tip. If they occupy energetically suboptimal (non-crystalline) sites, heating the sample may increase their scope for dissolving back into the catalyst or reconfiguring their bonds.

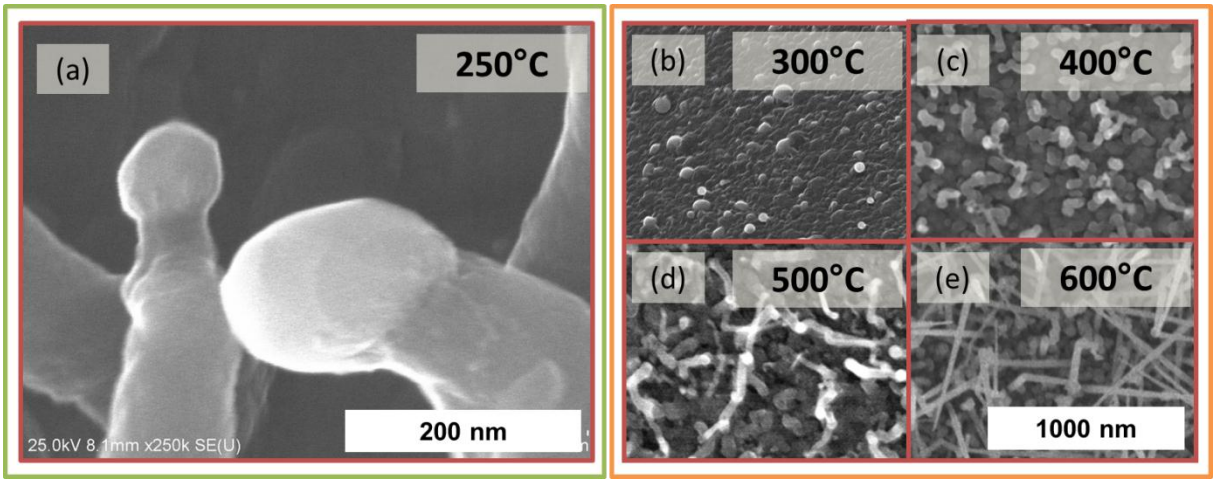

4.12 - Effect of temperature on the crystallinity of Sn-catalyzed SiNWs.
SEM micrographs of Sn-catalyzed SiNWs grown under the conditions described in Tables 4.1-2 on glass/SnO_2 substrates in the ARCAM reactor at 250 °C (a) and in the Plasfil reactor at 300 °C (b), 400 °C (c), 500 °C (d) and 600 °C (e).

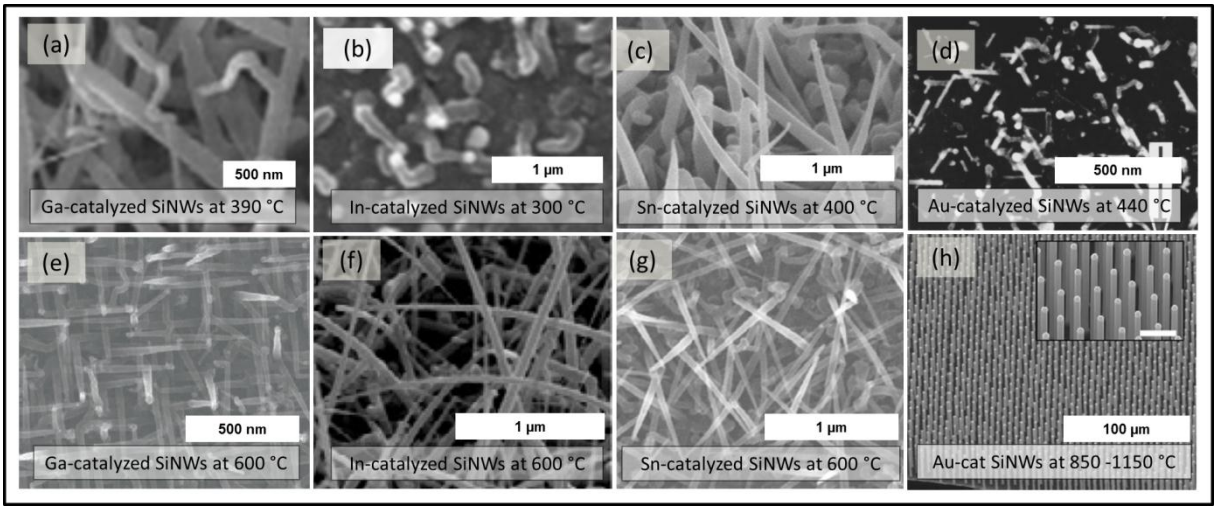

4.13 - Effect of temperature on the crystallinity of SiNWs grown with different catalysts.
Ga-catalyzed SiNWs grown at 390 °C under PECVD conditions [33] (a), In-catalyzed SiNWs grown at 300 °C using electron beam evaporation [34] (b), Sn-catalyzed SiNWs grown at 400 °C using H-radical assisted conditions [11] (c), Au-catalyzed SiNWs grown at 440 °C in a thermal CVD reactor [35] (d), Ga-catalyzed SiNWs grown at 600 °C under PECVD conditions [36] (e), Sn-catalyzed SiNWs grown at 600 °C under PECVD conditions [37] (f), In-catalyzed SiNWs grown at 600 °C under PECVD conditions on a crystalline substrate [14] (g), Au-catalyzed SiNWs grown at 850 to 1150 °C [38] (h).

This is undesirable from the perspective of our radial junction solar cells as part of the rationale for adopting Sn catalysts was to reduce their processing temperature. There is however scope for improvement. Isolated studies have reported straight nanowire growth at temperatures even lower than the eutectic. Wang et al. grew aligned SiNWs at 430 °C by adopting solid Al catalysts.[39] Renard et al. produced straight if inhomogeneous SiNWs with CuO catalysts at temperatures of 400 °C.[40] By using a plasma during the growth process, Aella et al. succeeded in reducing the temperature of VLS and fabricating highly crystalline Au-catalyzed SiNWs at 350 °C.[31] This same technique allowed Červenka et al. to produce straight Au-catalyzed SiNWs at temperatures as low as 250 °C.[23] The last two cases could be explained by the plasmas used in their growth conditions locally heating the catalysts. They are of particular interest in our case as the technique could foreseeably be transferred to Sn-catalyzed SiNWs.

3.2. High temperature faceting of Sn and In-catalyzed SiNWs

We also investigated whether heating the substrate beyond 600 °C affected the morphology of the nanowires any further. In this experiment, glass/ITO (100 nm) substrates were included in the same deposition runs as glass/SnO_2 substrates. The exact composition of the catalyst in samples grown on ITO covered substrates is unknown. However as the oxide is formed of In_2O_3 (90% by mass) and SnO_2 (10% by mass), the metal reduced at its surface is presumably an alloy composed predominantly of In. In the interest of brevity, we will refer to these samples simply as In-catalyzed SiNWs. Both types of substrates were simultaneously exposed to hydrogen and silane plasmas in the Plasfil reactor under process conditions described in Table 4.1 for a silane plasma duration of 1-2 hours and at growth temperatures ranging from 600°C to 700°C (Figure 4.14).

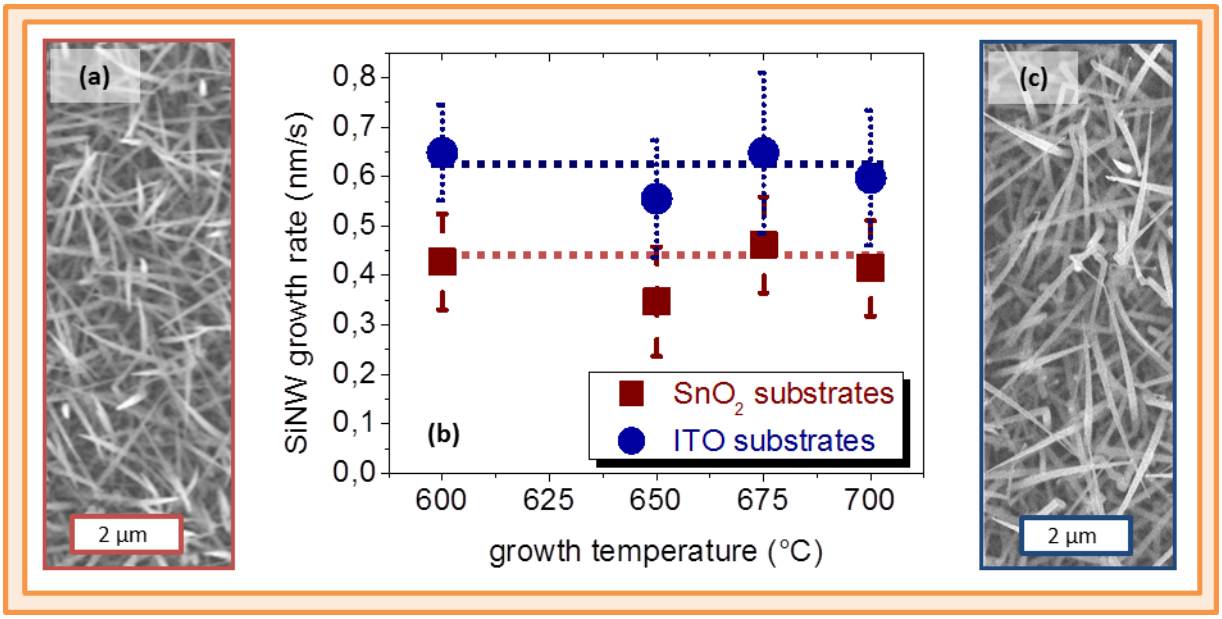

4.14 - Effect of high temperature on the growth rate of Sn and In-catalyzed SiNWs.
The effect of (nominal) growth temperature on SiNWs grown on glass/SnO_2 and glass/ITO substrates at temperatures ranging from 600 to 700 °C (b). SEM micrographs of depositions at 675 °C on substrates covered in SnO_2 (a) and ITO (b).

Again, the growth rate of the nanowires was not observed to vary within this temperature range (Figure 4.14); however it varied considerably according to the catalyst used (Figure 4.14.b). For deposition times of 1 hour and for temperatures spanning 600 to 700 °C, In-catalyzed SiNWs typically grew to lengths of 2300 nm, far exceeding the 1500 nm length observed for Sn-catalyzed SiNWs grown in the same runs (Figure 4.14.b). Catalyst drops were not always visible at the tip of the In-catalyzed SiNWs. Figure 4.15 shows that regardless of the growth temperature, some SiNWs display catalyst drops at their tip (circled) while others end in a tapered needle (indicated by an arrow). Even when a catalyst drop is visible at the tip of the nanowire, its diameter is considerably smaller compared to the diameter at the base of the nanowire itself. The fact that this needle structure is common to Sn, In and Au[23] suggests that it is related to the unusual process conditions (i.e. the plasma) used rather than a property of the uncommon metal we are using as a catalyst. Closer inspection of the Sn and In-catalyzed SiNWs grown at a nominal temperature of 700 °C revealed geometric facets over the SiNW sidewalls. In the case of In-catalyzed SiNWs grown at 650 °C, the cross-section of the nanowires was circular (Figure 4.16.a). However when the nominal growth temperature was increased to 700 °C, it became hexagonal, with planar facets intersecting at angles of 120° and extending along the entire length of the SiNW sidewalls.

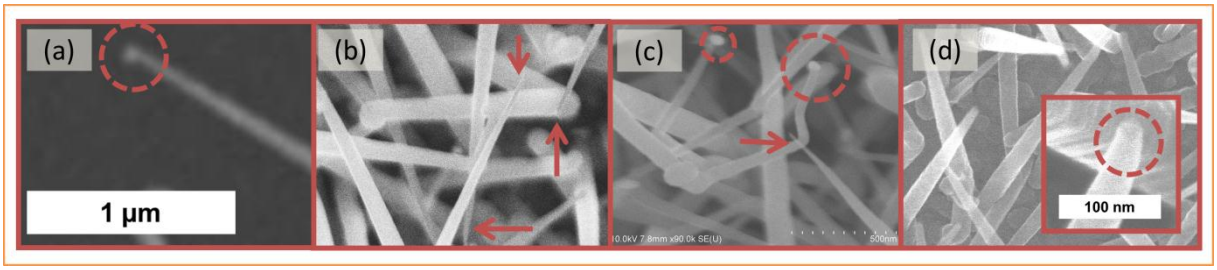

4.15 - Absence of catalysts at the tip of In-catalyzed SiNWs grown at high temperature.
SEM micrographs of In-catalyzed SiNWs grown at 600 °C (a), 650 °C (b), 675 °C (c) and 700 °C (d). Arrows designate nanowires where the catalyst is absent, circles designate visible catalyst drops at the nanowire tip.

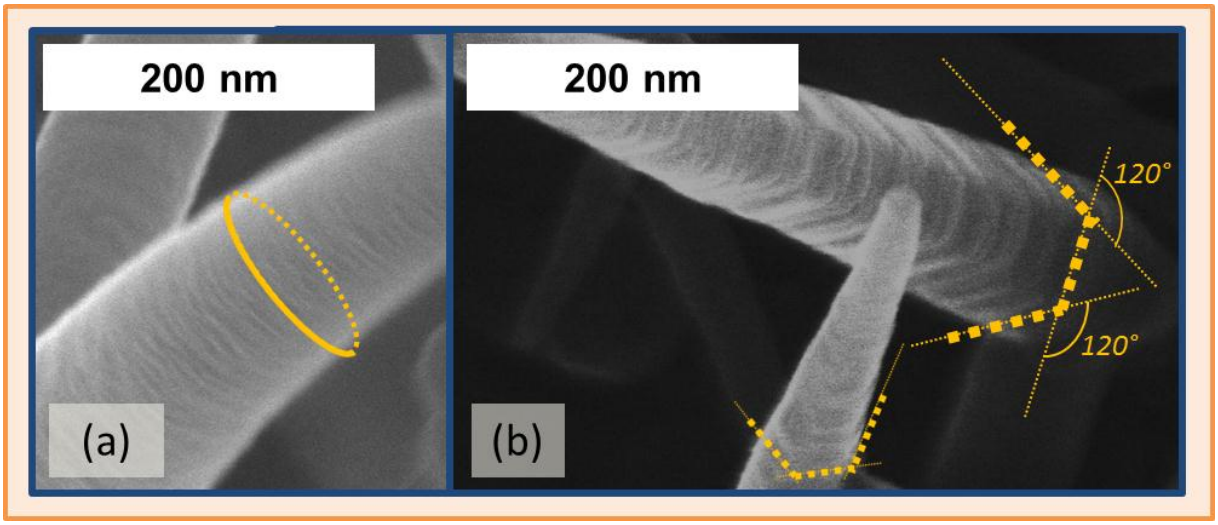

4.16 - Faceting over the sidewalls of In-catalyzed SiNWs grown at temperatures higher than 600 °C.
SEM micrographs of In-catalyzed SiNWs grown by PA-VLS at 650 °C displaying conventional, circular cross-sections (a) and at 700 °C presenting hexagonal facets (b).

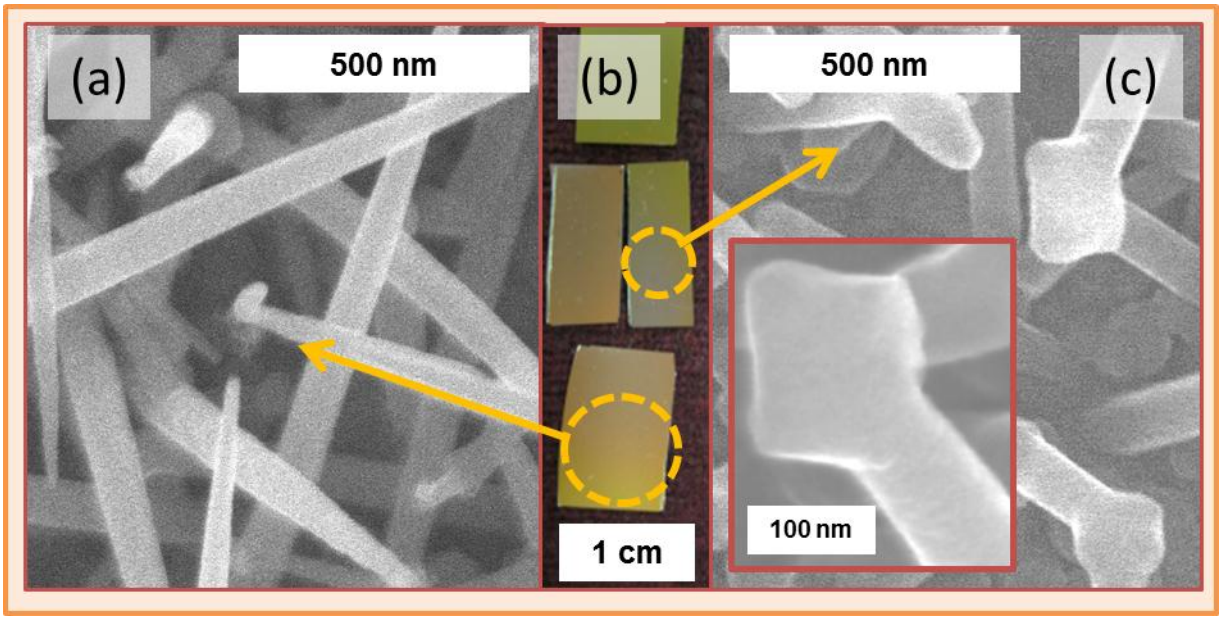

4.17 - Faceting over the sidewalls of Sn-catalyzed SiNWs grown at temperatures higher than 600 °C.
Sn-catalyzed SiNWs grown by PA-VLS at a nominal temperature of 700 °C displaying different morphologies depending on their position on the substrate holder. Samples furthest from the center (a) grew the cylindrical and tapered nanowires while samples grown closest to the center (c) exhibited facets.

Surprisingly, the Sn-catalyzed SiNWs displayed different degrees of faceting according to the position of the sample on the Plasfil substrate holder. Figure 4.17.b shows the position of the substrates as they were arranged within the reactor. Nanowires grown on the sample closest to the center of the substrate holder were observed to form angular structures with widths reaching twice the diameter of the nanowires at their tip. It is foreseeable that inhomogeneous heating of the substrate holder leads to hotter regions in the center.

3.3. Catalyst diameter and faceting in Sn-catalyzed SiNWs

To ensure homogeneous heating over the sample area, a pad of Sn (10 mm wide and 200 nm thick) was evaporated at the center of a Corning glass substrate and placed in the center of the Plasfil substrate holder. The substrate was exposed to a hydrogen and silane plasma under the conditions described in Table 4.1 at a nominal temperature of 650 °C. When the Sn surface was exposed to the oxide removing H_2 plasma, its edges spread out into droplets whose size decreased progressively from 1 µm in the center of the pad to 50 nm in its outer edge (Figure 4.18.a). The SiNWs grown from these Sn drops therefore also adopted a range of progressively smaller diameters. Remarkably, the facets observed on these Sn-catalyzed SiNWs were observed to depend on the diameter of their catalyst drop. For clarity, we have divided the area extending over a dozen microns from the edge of the Sn pad into four different regions which capture the diversity of facets observed on the sidewalls of these nanowires. Over the area originally occupied by the Sn pad, drops formed with diameters of up to 500 nm. However, only drops with diameters in the 100 – 200 nm range proved capable of catalyzing the growth of SiNWs (Figure 4.18.b). Some of these nanowires presented faceted sidewalls (Figure 4.18.c). The distribution of Sn drop diameters in this central region peaked at 120 nm and decreased progressively, with a few drops presenting diameters of over a micron (Figure 4.19.a).

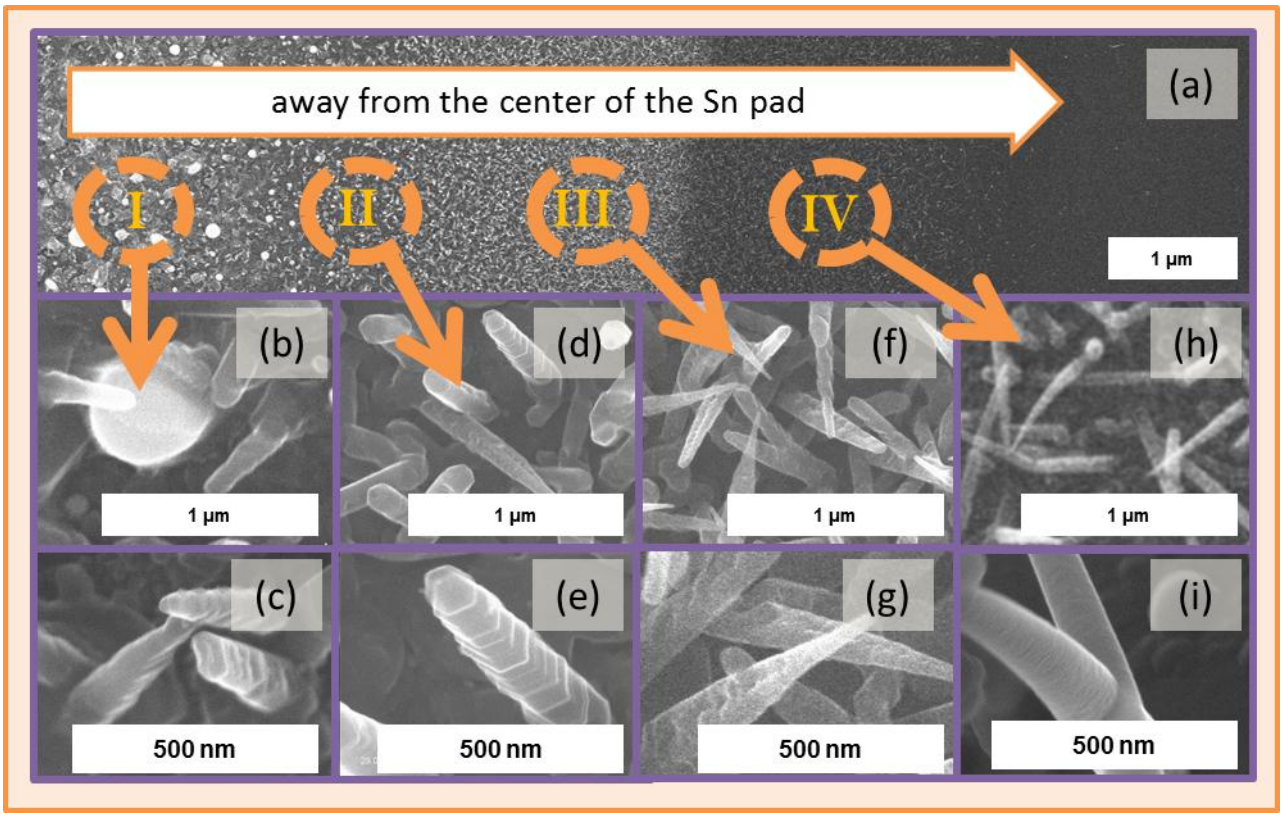

4.18 - Faceting on SiNWs of various diameters grown from catalyst which diffused about a localized Sn pad.
SEM micrographs of SiNWs grown by PA-VLS at 650 °C from a 10 x 10 mm² pad of evaporated Sn (a) revealing progressively smaller Sn drops from its central region which catalyze the growth of faceted SiNWs (b-g) to its outer halo which catalyze the growth of SiNWs the sidewalls remain smooth (h-i).

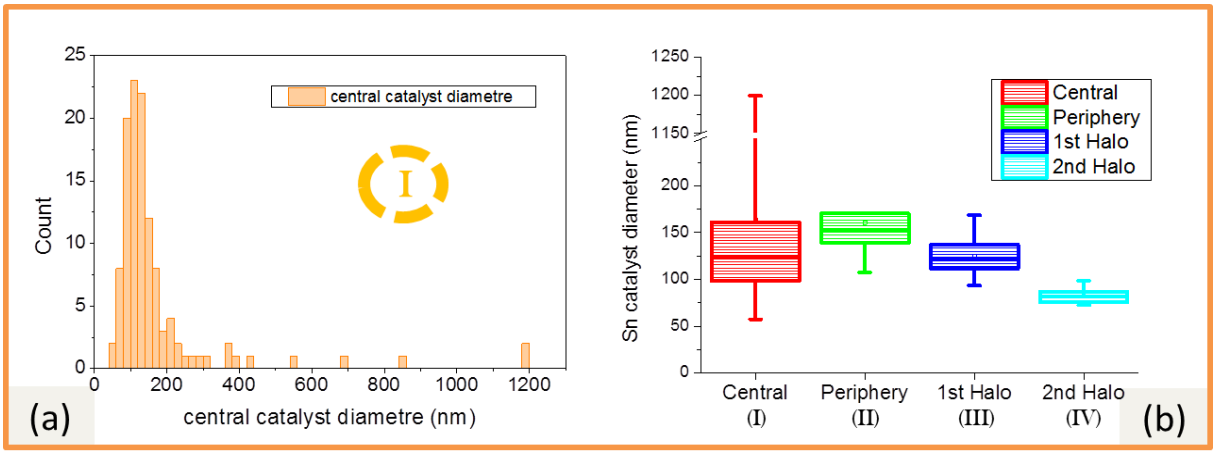

4.19 - Range of diameters of metal drops and SiNWs produced by a localized Sn pad.
The distribution of catalyst diameters in the central region of the Sn pad (a). Box plots of catalyst diameters indicate progressively smaller diameters as metal drops spread further from the center (roman numerals refer to Figure 4.18, fingers encompass the entire data range and boxes open on the 25th and close on the 75th percentile) (b).

In the vicinity of the evaporated Sn pad (region II as identified in Figure 4.18), no Sn drop diameters larger than 200 nm were observed; however the diameter of nanowires grown in this region was similar to that of the nanowires grown in the center, with an average diameter of 160 nm. The

sidewalls of many of these nanowires presented clear hexagonal facets (Figures 4.18.d-e). Further from the center of the metal pad, the density and diameter of catalysts progressively decreased (Figure 4.18.f-i). Nanowires grown in the first halo of smaller drops surrounding the Sn pad (region III as identified in Figure 4.18) presented a rough, inhomogeneous structure but no clear facets (Figure 4.18.f-g). Nanowires grown furthest from the central Sn pad, in region IV, present the familiar tapered cylindrical structure (Figure 4.18.h-i) of the nanowires grown at 600 °C (Figure 4.3.a). The diameter at the base of the nanowires tended to decrease for nanowires further from the center of the substrate (Figure 4.19.b). The fact that nanowire faceting and diameter were both observed to vary according to the proximity to the substrate center suggested that the two properties were related.

Further evidence of this was obtained from observations of nanowires spontaneously switching from faceted to cylindrical growth as the nanowire tapered during the growth process (Figure 4.20.c). In an attempt to maximize the temperature gradient across the sample surface, substrates of SnO_2 covered glass were positioned as far as possible from the chamber center. They were exposed to standard H_2 and silane plasma under conditions described in Table 4.1 at a nominal temperature of 650 °C and for a duration of 1 hour. The sample displayed a noticeable color gradient across its length (Figure 4.20.a), presumably as a result of the light scattering effect produced by the different structures on its surface.

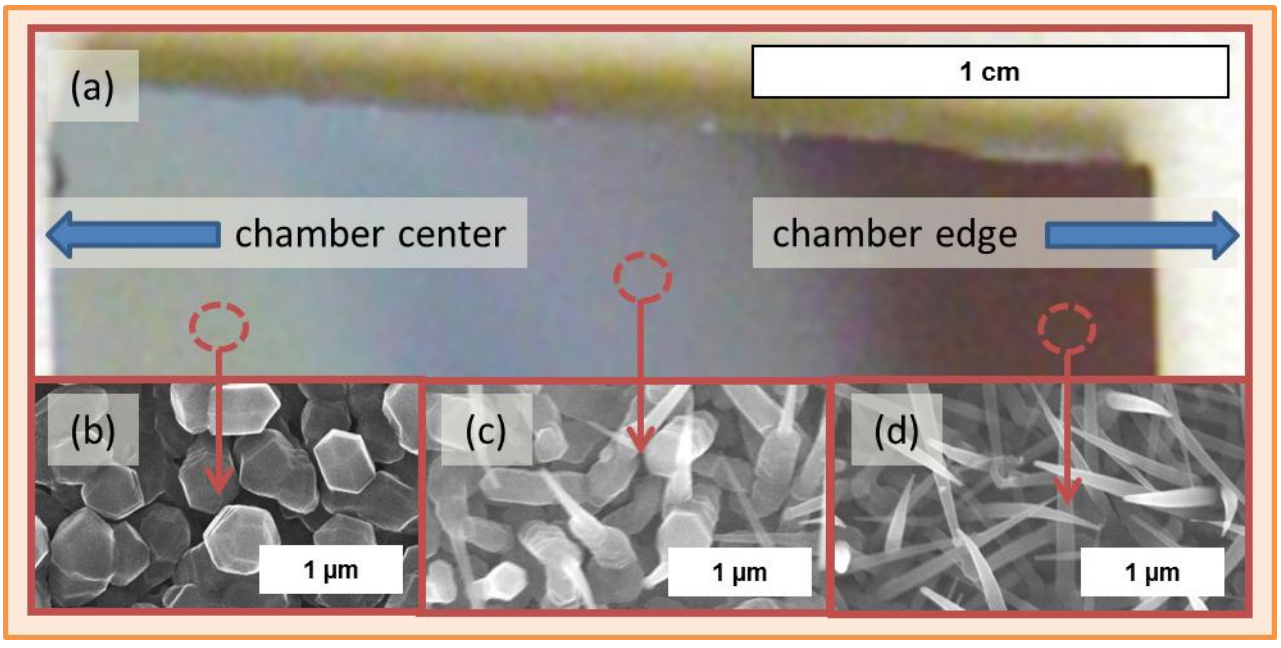

4.20 - Faceting on Sn-catalyzed SiNWs grown over a temperature gradient.
Photograph of the surface of a sample on which Sn-catalyzed SiNWs grown by PA-VLS on an SnO_2 substrate at 650 °C (a).

SEM observations revealed that over the area of the sample that was closest to the center of the reactor chamber (which was presumably hotter during the deposition process), Si grew in the form of hexagonal crystals several hundreds of nanometers wide which did not grow vertically (Figure 4.20.b). At the furthest extreme from the center (where the temperature was presumably lower), VLS growth

proceeded to form vertical, tapered cylindrical nanowires with diameters lower than 100 nm (Figure 4.20.d). The diameter of the hexagonal Si crystals was consistently larger than that of the cylindrical SiNWs, presumably as a result of the temperature gradient across the substrate causing catalyst drops closer to the center of the reactor to coarsen more than those on the edge. Astonishingly, in the central area of the sample (Figure 4.20.c), catalysts with diameters between 100 and 200 nm began catalyzing growth of the hexagonal faceted kind that was observed in Figure 4.18.b-e) then switched halfway through the growth process to the tapered cylindrical kind observed in Figure 4.20.d.

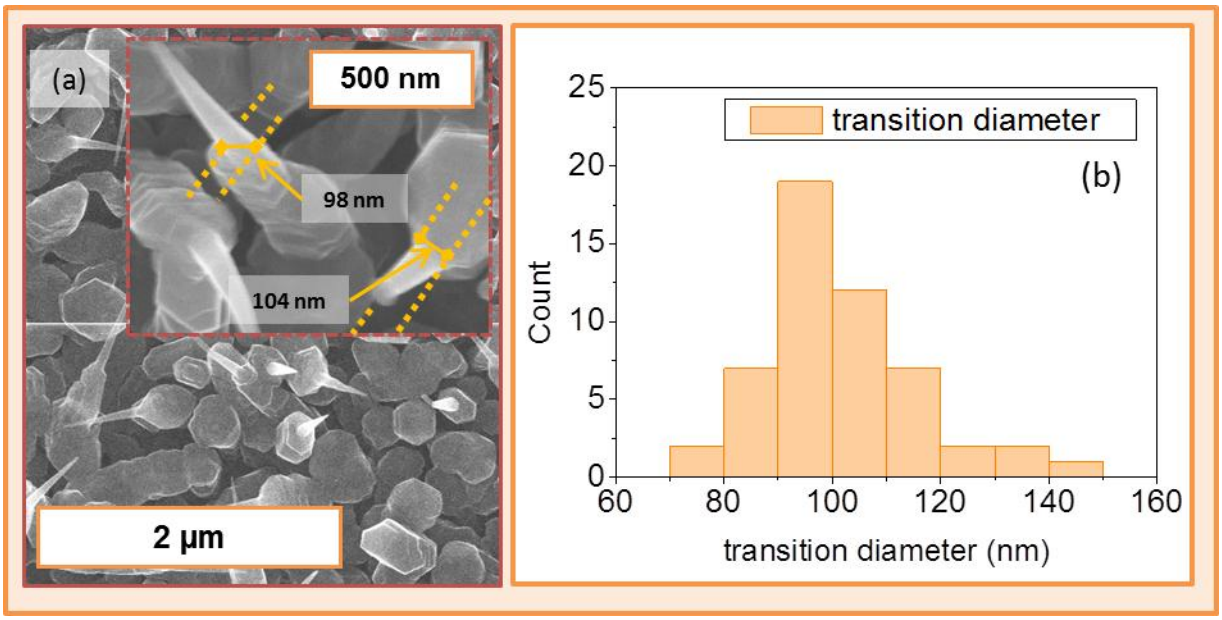

4.21 - Transition from faceted to cylindrical growth in Sn-catalyzed SiNWs.
SEM micrograph of Sn-catalyzed SiNWs grown on glass/SnO_2 at a nominal temperature of 650 °C (a). Distribution of transition diameters at which the nanowires switch from faceted to cylindrical growth (b). The inset of (a) draws attention to the transition diameter.

These results suggest that the diameter of the catalyst particle determines the facets which form over the sidewalls of the Sn-catalyzed SiNWs. The diameters of the Sn drops in Figure 4.21.a may initially have been large enough to initiate faceted SiNW growth; however as the nanowires grew and tapered, their diameter shrunk to the point where standard, cylindrical VLS growth took over. This transition diameter was measured from SEM images of the point at which the nanowires switched from one growth mode to the other (inset Figure 4.21.a). In most cases, the transition diameter was found between 90 and 110 nm (Figure 4.21.b) and its average value was of 98 nm. The reason the Sn drops can at times catalyze the growth of faceted SiNWs remains unclear; however it may be related to the catalyst dimensions exceeding the typical diffusion length of the Si atoms within it.[14] Cylindrical nanowires are believed to form one layer at a time, as Si atoms diffuse within the catalyst drop and nucleate at energetically favorable step sites at the edge of the forming layer.[41] However if the catalyst drop is large enough, the surface area of its interface with the SiNW tip may prove too broad to be swept by Si atoms before they nucleate. Instead, they may form nucleation sites on top of forming Si layers, seeding new layers before the previous ones are complete. This would lead to an uneven growth front and possibly polycrystalline facetted growth.

This explanation fits with observations of limited nanowire growth on very large catalyst drops. To test the limits of this interpretation, we exposed thick layers (100 nm) of Sn evaporated on glass substrates to the plasma conditions described in Table 4.1, fixing the plasma temperature both for the H_2 and SiH_4 plasma at 400 °C, leading to VLS growth on Sn drops with diameters exceeding 500 nm (Figure 4.22.a). Although silicon was observed to nucleate at the interface between these catalysts and the substrate, they did not form complete or regular layers but separate crystal shards.

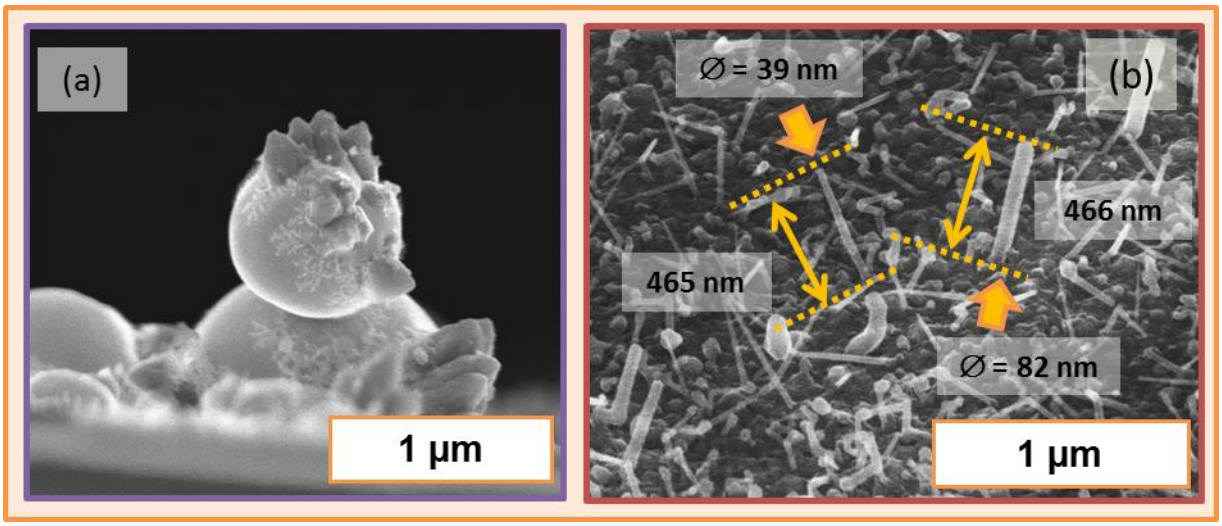

4.22 – Limiting diameters for faceting in Sn-catalyzed SiNWs.
Cross-sectional SEM micrograph of large-diameter Sn catalyst drops evaporated onto glass substrates and exposed to a hydrogen and silane plasma in the Plasfil reactor at 400 °C (a). Sn-catalyzed SiNWs grown in the Plasfil reactor at 600 °C on substrates of glass/SnO_2 (b).

The growth temperature, the catalyst drop diameter and nucleation rate may therefore play important roles in the faceting observed on the sidewalls of our Sn-catalyzed SiNWs. Together these three parameters define a window of conditions outside which faceting (or no nanowire growth at all) take place but inside which layer-by-layer cylindrical growth can be expected. For instance, if Si atoms inside the catalyst drop nucleate rapidly with respect to their diffusion rate, catalysts with diameters smaller than the diffusion length lead to layer-by-layer growth while larger ones lead to faceting. However, further from the limits of this window of conditions, no relation is expected between the three parameters and faceting. This is illustrated in Figure 4.22.b, which shows Sn-catalyzed SiNWs with different diameters, all lower than 100 nm, grown on glass/SnO_2 substrates under the standard conditions described in Table 4.1 for a duration of 10 minutes. As these smaller scales are all presumably lower than the Si diffusion length in the Sn catalyst, the larger diameter metal drops are not observed to catalyze faceted growth. In fact they do not even affect the nanowire growth rate (Figure 4.22.b).

4. Conclusion

In this section we detail our parametric studies investigating the effect of various plasma conditions on the morphology of Sn-catalyzed silicon nanowires and optimizing them to grow disordered arrays which can be incorporated into radial junction solar cells. By increasing the temperature, it proved possible to grow Sn-catalyzed SiNWs straight. By increasing the silane pressure and plasma power, we have shown that their growth rate can be increased from 0.4 to 15 nm/s. We have also developed plasma conditions to grow Sn-catalyzed SiNWs at temperatures as low as 250 °C. In so doing, we have exposed a number of intriguing properties in the VLS growth process using Sn catalysts. As expected, the plasma environment made it possible to grow silicon nanowires with Sn catalysts. However it may have affected other aspects of the growth process in ways which we had not foreseen. Unusually for VLS growth, the nanowire growth rate showed no relation to the substrate temperature. This presumably results from the fact that the gas species is dissociated not thermally but by the plasma. Also, the parasitic deposition directly from gas to solid phase is faster under PECVD than under conventional thermal CVD conditions. This may be related to the considerable decrease in the density of nanowires grown with respect to the density of catalyst drops formed on the substrate as the parasitic layer constantly risks burying catalyst drops.

One puzzling observation is that catalyst drops were no longer observed at the tip of Sn-catalyzed nanowires after 5 minutes of growth at temperatures higher than 600 °C. It is unclear whether the drop shrinks or wets the nanowire sidewalls, but it presumably remains present in some form as nanowire growth was observed to proceed at a linear rate for up to 2 hours. We have observed the same effect on nanowires grown from In drops and Cervenka et al. have reported similar findings with Au-catalyzed SiNWs also grown by plasma-assisted VLS.[23] This diversity of catalyst materials suggests that this effect is caused by the plasma environment, rather than by the Sn itself. However metal drops remained visible at the tip of Sn-catalyzed SiNWs also grown by plasma-assisted VLS at lower temperatures. Which combination of factors results in needle-nanowire growth raises interesting questions, as the growth mode may differ considerably from conventional VLS. We have also reported that crystalline facets can form over the sidewalls of Sn-catalyzed SiNWs grown at nominal temperatures higher than 650 °C. By performing plasma-assisted VLS growth with catalysts of various diameters, different degrees of faceting were observed. These findings were confirmed by observations of Sn-catalyzed SiNWs switching from faceted to standard growth as their diameter decreased due to tapering. We have inferred from these observations that, in the case of Sn-catalyzed SiNWs, nanowire growth does not always proceed layer-by-layer.

Perspectives

Although we have managed to grow SiNW arrays using Sn catalysts which can be incorporated into radial junction solar cells, the materials stand to gain considerably from further optimization. Nanowire growth was achieved at temperatures as low as 250 °C; however it required nominal process temperatures of 600 °C to grow straight. High temperatures are incompatible with current a-Si:H PV fabrication lines and waste one of the potential benefits of Sn catalysts. Reports of plasma-

assisted VLS growth of straight SiNWs at low temperature suggest that other process parameters can alleviate the dependence on substrate temperature.

The surface faceting of Sn-catalyzed SiNWs also opens technological opportunities as the roughness of nanowire sidewalls determines to a large extent their phonon spectrum. Controlling the faceting could therefore lead to a range of new applications, notably in thermoelectric energy conversion.[42] We inferred from the observations of faceting that layer-by-layer (cylindrical) nanowire growth is best achieved at low supersaturations and with smaller catalyst drops. This may offer guidance in future attempts to reduce the temperature of straight nanowire growth by minimizing the silane pressure, plasma power or the catalyst diameter. However, attempts at adopting smaller catalysts or reducing the nanowire growth rate so far have led to more catalysts being buried. One way around this problem may be to further explore high energy plasma conditions with high concentrations of H_2 in order to continuously etch the parasitic a-Si:H while the crystalline silicon grown from the plasma-assisted VLS remains intact.

BIBLIOGRAPHY

[1] G.E. Possin, Solution growth of silicon from liquid tin for application to photovoltaic solar cells, *Solid-State Electronics,* 27 (1984) 167-176, doi:10.1016/0038-1101(84)90108-4.
[2] F. Abdou, A. Fave, M. Lemiti, A. Laugier, C. Bernard, A. Pisch, Liquid phase epitaxy of silicon from tin alloys at low temperature, *Photovoltaic Specialists Conference, 2005. Conference Record of the Thirty-first IEEE*, 2005, pp. 1066-1069, doi:10.1109/pvsc.2005.1488318.
[3] B. Girault, F. Chevrier, A. Joullie, G. Bougnot, Liquid phase epitaxy of silicon at very low temperatures, *Journal of Crystal Growth,* 37 (1977) 169-177, doi:10.1016/0022-0248(77)90079-3.
[4] S.H. Sun, G.W. Meng, M.G. Zhang, Y.T. Tian, T. Xie, L.D. Zhang, Preparation and characterization of oriented silica nanowires, *Solid State Communications,* 128 (2003) 287-290, doi:10.1016/j.ssc.2003.08.021.
[5] C. Ye, L. Zhang, X. Fang, Y. Wang, P. Yan, J. Zhao, Hierarchical Structure: Silicon Nanowires Standing on Silica Microwires, *Advanced Materials,* 16 (2004) 1019-1023, doi:10.1002/adma.200306509.
[6] M. Shao, H. Hu, M. Li, H. Ban, M. Wang, J. Jiang, Karman vortex street assisted patterning in the growth of silicon nanowires, *Chemical Communications,* (2007) 793-794, doi:10.1039/B613473D.
[7] P. Wu, X. Zou, L. Chi, Q. Li, T. Xiao, Growth model of lantern-like amorphous silicon oxide nanowires, *Nanotechnology,* 18 (2007) 125601, doi:10.1088/0957-4484/18/12/125601.
[8] D. Parlevliet, J.C.L. Cornish, Silicon Nanowires: Growth Studies Using Pulsed PECVD, *MRS Online Proceedings Library,* 989 (2007), doi:10.1557/PROC-0989-A23-03.
[9] D. Parlevliet, P. Jennings, Thin film silicon nanowire photovoltaic devices produced with gold and tin catalysts, *Journal of Nanoparticle Research,* 13 (2011) 4431-4436, doi:10.1007/s11051-011-0478-9.
[10] L. Yu, P.-J. Alet, G. Picardi, I. Maurin, P.R.i. Cabarrocas, Synthesis, morphology and compositional evolution of silicon nanowires directly grown on SnO2 substrates, *Nanotechnology,* 19 (2008) 485605, doi:10.1088/0957-4484/19/48/485605.
[11] M. Jeon, K. Kamisako, Synthesis and characterization of silicon nanowires using tin catalyst for solar cells application, *Materials Letters,* 63 (2009) 777-779, doi:10.1016/j.matlet.2009.01.001.
[12] M. Jeon, H. Uchiyama, K. Kamisako, Characterization of Tin-catalyzed silicon nanowires synthesized by the hydrogen radical-assisted deposition method, *Materials Letters,* 63 (2009) 246-248, doi:10.1016/j.matlet.2008.10.005.
[13] S. Cheng, T. Ren, P. Ying, R. Yu, W. Zhang, J. Zhang, C. Li, Enhanced growth of crystalline-amorphous core-shell silicon nanowires by catalytic thermal CVD using in-situ generated tin catalyst, *SCIENCE CHINA Chemistry,* (2012) 1-7, doi:10.1007/s11426-012-4717-4.
[14] L. Yu, B. O'Donnell, J.L. Maurice, P. Roca i Cabarrocas, Core-shell structure and unique faceting of Sn-catalyzed silicon nanowires, *Applied Physics Letters,* 97 (2010), doi:10.1063/1.3464557.
[15] L. Yu, F. Fortuna, B. O'Donnell, G. Patriache, P. Roca i Cabarrocas, Stability and evolution of low-surface-tension metal catalyzed growth of silicon nanowires, *Applied Physics Letters,* 98 (2011), doi:10.1063/1.3569817.
[16] L. Yu, B. O'Donnell, P.J. Alet, S. Conesa-Boj, F. Peiro, J. Arbiol, P. Roca i Cabarrocas, Plasma-enhanced low temperature growth of silicon nanowires and hierarchical structures by using tin and indium catalysts, *Nanotechnology,* 20 (2009) 225604, doi:10.1088/0957-4484/20/22/225604.
[17] S.J. Rathi, B.N. Jariwala, J.D. Beach, P. Stradins, P.C. Taylor, X.J. Weng, Y. Ke, J.M. Redwing, S. Agarwal, R.T. Collins, Tin-Catalyzed Plasma-Assisted Growth of Silicon Nanowires, *Journal of Physical Chemistry C,* 115 (2011) 3833-3839, doi:10.1021/Jp1066428.
[18] J. Cho, B. O'Donnell, L. Yu, K.-H. Kim, I. Ngo, P. Roca i Cabarrocas, Sn-catalyzed silicon nanowire solar cells with 4.9% efficiency grown on glass, *Progress in Photovoltaics: Research and Applications,* (2012), doi:10.1002/pip.1245.

[19] B. O'Donnell, L. Yu, M. Foldyna, P. Roca i Cabarrocas, Silicon nanowire solar cells grown by PECVD, *Journal of Non-Crystalline Solids,* 358 (2012) 2299-2302, doi:10.1016/j.jnoncrysol.2011.11.026.
[20] J.E. Allen, E.R. Hemesath, D.E. Perea, J.L. Lensch-Falk, Z.Y. Li, F. Yin, M.H. Gass, P. Wang, A.L. Bleloch, R.E. Palmer, L.J. Lauhon, High-resolution detection of Au catalyst atoms in Si nanowires, *Nature Nanotechnology,* 3 (2008) 168-173, doi:10.1038/Nnano.2008.5.
[21] M.M.J.W. van Herpen, D.J.W. Klunder, W.A. Soer, R. Moors, V. Banine, Sn etching with hydrogen radicals to clean EUV optics, *Chemical Physics Letters,* 484 (2010) 197-199, doi:10.1016/j.cplett.2009.11.030.
[22] J. Kikkawa, Y. Ohno, S. Takeda, Growth rate of silicon nanowires, *Applied Physics Letters,* 86 (2005) 123109, doi:10.1063/1.1888034.
[23] J. Červenka, M. Ledinský, J. Stuchlík, H. Stuchlíková, S. Bakardjieva, K. Hruška, A. Fejfar, J. Kočka, The structure and growth mechanism of Si nanoneedles prepared by plasma-enhanced chemical vapor deposition, *Nanotechnology,* 21 (2010) 415604, doi:10.1088/0957-4484/21/41/415604.
[24] B. Kalache, P. Roca i Cabarrocas, A. Fontcuberta i Morral, Observation of incubation times in the nucleation of silicon nanowires obtained by the vapor-liquid-solid method, *Japanese Journal of Applied Physics,* 45 (2006) L190-L193, doi:10.1143/Jjap.45.L190.
[25] B.J. Kim, J. Tersoff, S. Kodambaka, M.C. Reuter, E.A. Stach, F.M. Ross, Kinetics of Individual Nucleation Events Observed in Nanoscale Vapor-Liquid-Solid Growth, *Science,* 322 (2008) 1070-1073, doi:10.1126/science.1163494.
[26] K.-K. Lew, J.M. Redwing, Growth characteristics of silicon nanowires synthesized by vapor–liquid–solid growth in nanoporous alumina templates, *Journal of Crystal Growth,* 254 (2003) 14-22, doi:10.1016/s0022-0248(03)01146-1.
[27] G.A. Bootsma, H.J. Gassen, A quantitative study on the growth of silicon whiskers from silane and germanium whiskers from germane, *Journal of Crystal Growth,* 10 (1971) 223-234, doi:10.1016/0022-0248(71)90188-6.
[28] A. Fontcuberta i Morral, P. Roca i Cabarrocas, Etching and hydrogen diffusion mechanisms during a hydrogen plasma treatment of silicon thin films, *Journal of Non-Crystalline Solids,* 299–302, Part 1 (2002) 196-200, doi:10.1016/s0022-3093(01)01001-8.
[29] U. Kroll, J. Meier, H. Keppner, A. Shah, S.D. Littlewood, I.E. Kelly, P. Giannoules, Origins of atmospheric contamination in amorphous silicon prepared by very high frequency (70 MHz) glow discharge, *Journal of Vacuum Science & Technology A: Vacuum, Surfaces, and Films,* 13 (1995) 2742-2746, doi:10.1116/1.579698.
[30] S. Hofmann, C. Ducati, R.J. Neill, S. Piscanec, A.C. Ferrari, J. Geng, R.E. Dunin-Borkowski, J. Robertson, Gold catalyzed growth of silicon nanowires by plasma enhanced chemical vapor deposition, *Journal of Applied Physics,* 94 (2003) 6005-6012, doi:10.1063/1.1614432.
[31] P. Aella, S. Ingole, W.T. Petuskey, S.T. Picraux, Influence of plasma stimulation on Si nanowire nucleation and orientation dependence, *Advanced Materials,* 19 (2007) 2603, doi:10.1002/adma.200602944.
[32] J. Westwater, D.P. Gosain, S. Tomiya, S. Usui, H. Ruda, Growth of silicon nanowires via gold/silane vapor-liquid-solid reaction, *Journal of Vacuum Science & Technology B,* 15 (1997) 554-557, doi:10.1116/1.589291.
[33] H. Griffiths, C. Xu, T. Barrass, M. Cooke, F. Iacopi, P. Vereecken, S. Esconjauregui, Plasma assisted growth of nanotubes and nanowires, *Surface and Coatings Technology,* 201 (2007) 9215-9220, doi:10.1016/j.surfcoat.2007.04.067.
[34] R.R. Kumar, K.N. Rao, A.R. Phani, Growth of silicon nanowires by electron beam evaporation using indium catalyst, *Materials Letters,* 66 (2012) 110-112, doi:10.1016/j.matlet.2011.08.064.
[35] J. Westwater, D.p. Gosain, K. Yamauchi, S. Usui, Nanoscale silicon whiskers formed by silane/gold reaction at 335 °C, *Materials Letters,* 24 (1995) 109-112, doi:10.1016/0167-577x(95)00091-7.

[36] I. Zardo, L. Yu, S. Conesa-Boj, S. Estrade, P.J. Alet, J. Roessler, M. Frimmer, P. Roca i Cabarrocas, F. Peiro, J. Arbiol, J.R. Morante, A.Fontcuberta i Morral, Gallium assisted plasma enhanced chemical vapor deposition of silicon nanowires, *Nanotechnology,* 20 (2009), doi:10.1088/0957-4484/20/15/155602.
[37] F. Iacopi, P.M. Vereecken, M. Schaekers, M. Caymax, N. Moelans, B. Blanpain, O. Richard, C. Detavernier, H. Griffiths, Plasma-enhanced chemical vapour deposition growth of Si nanowires with low melting point metal catalysts: an effective alternative to Au-mediated growth, *Nanotechnology,* 18 (2007), doi:10.1088/0957-4484/18/50/505307.
[38] B.M. Kayes, M.A. Filler, M.C. Putnam, M.D. Kelzenberg, N.S. Lewis, H.A. Atwater, Growth of vertically aligned Si wire arrays over large areas (> 1 cm(2)) with Au and Cu catalysts, *Applied Physics Letters,* 91 (2007), doi:10.1063/1.2779236.
[39] Y. Wang, V. Schmidt, S. Senz, U. Gosele, Epitaxial growth of silicon nanowires using an aluminium catalyst, *Nat Nano,* 1 (2006) 186-189, doi:10.1038/nnano.2006.133.
[40] V.T. Renard, M. Jublot, P. Gergaud, P. Cherns, D. Rouchon, A. Chabli, V. Jousseaume, Catalyst preparation for CMOS-compatible silicon nanowire synthesis, *Nat Nano,* 4 (2009) 654-657, doi:10.1038/nnano.2009.234.
[41] V.G. Dubrovskii, N.V. Sibirev, J.C. Harmand, F. Glas, Growth kinetics and crystal structure of semiconductor nanowires, *Physical Review B,* 78 (2008), doi:10.1103/Physrevb.78.235301.
[42] A.I. Hochbaum, R. Chen, R.D. Delgado, W. Liang, E.C. Garnett, M. Najarian, A. Majumdar, P. Yang, Enhanced thermoelectric performance of rough silicon nanowires, *Nature,* 451 (2008) 163-167, doi:10.1038/nature06381.

5. Radial junction solar cells

"Rosen, wild wie rote Flammen, sprühn aus dem Gewühl hervor;
Lilien, wie krystallne Pfeiler, schießen himmelhoch empor.
Und die Sterne, groß wie Sonnen, schaun herab mit Sehnsuchtsglut;
In der Lilien Riesenkelche strömet ihre Strahlenflut."

We present in this chapter photovoltaic devices that use the silicon nanowire arrays developed in the previous chapter to trap light and convert it into electricity. Having doped the SiNWs p-type, covered them in conformal layers of intrinsic and n-type a-Si:H and provided them with electrical contacts, we create radial PIN junctions. The glass substrates on which these devices are grown are flat, hence light trapping is provided by the silicon nanowires themselves. We document our improvement in the conformal coverage of the nanowires, our attempts at controlling the nanowire density, and optimizing their doping, length and window layer thickness, which gradually improved the performance of these radial junction solar cells from the first observable diode rectification to devices with short-circuit currents higher than in planar reference cells and energy conversion efficiencies of 6%.

"Roses, as wild as red hot flames, spring forth from the manic crowds. Lilies, soar like crystal towers, up towards the highest clouds;
And stars, as great as suns, shine down with feverish love ablaze, Till each great heart each lily bears overflows with stellar rays."
Die Harzreise, Heinrich Heine, 1824

1. Introducing radial junction photovoltaics

The term “radial junction” describes the unconventional direction of charge collection in our devices. In typical, planar photovoltaic cells, electrons and holes must diffuse vertically across the absorber to reach electrical contacts. In radial junctions, the absorber is engineered so as to be laterally surrounded by electrical contacts. We have explored this junction configuration in virtue of its ability to trap light. However other potential benefits have been ascribed to the radial junction structure which we will briefly attempt to outline in this introduction.

The blueprints for our work were first sketched out shortly after the discovery of the VLS-growth mechanism.[1] In 1978, Heinrich Diepers filed a patent for a photovoltaic device which trapped light in microscopic semiconductor rods[2] and A.A. Shchetinin published the first *J(V)* curves of silicon whisker solar cells.[3] Radial junctions did not provoke great interest immediately, but the field received a surge of attention with the emergence of nanotechnology.[4] Photovoltaic cells arguably offered a convenient stepping stone for research on nanowires. From a clean room perspective, the physical properties of nanowires can be put to the benefit of photovoltaic devices with relative simplicity (notably avoiding post-growth handling steps). The substrate is in electrical contact with the core of the nanowires, the nanowires naturally grow in the direction required and the device can be coated by thin-film deposition techniques to electrically contact the nanowire shells. As can be seen in Figure 5.1, arrays of SiNWs can be integrated into radial junction solar cells without so much as detaching them from their substrate.

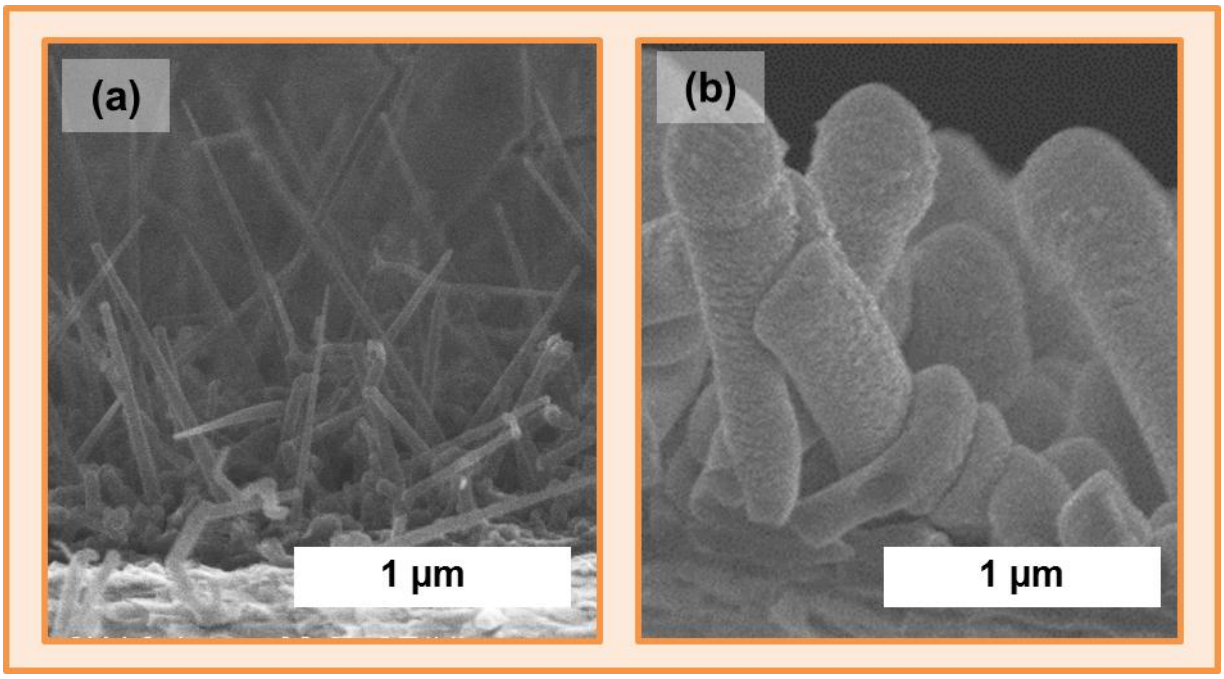

5.1 – Sn-catalyzed SiNWs and radial PIN junction solar cell grown by PECVD.
Cross-sectional SEM image of p-doped SiNWs (a) and radial PIN junctions built on nanowires grown under identical conditions and covered in intrinsic and n-type a-Si:H and an ITO electrical contact (b).

The first application of silicon nanowires in modern photovoltaics came in the field of excitonic (photoelectrochemical and organic) solar cells, where their high effective surface was coveted to improve the separation and extraction of charges from low-mobility absorbers.[5-10] The concept of an

all-silicon radial junction solar cell only emerged from its 30-year hiatus in 2005. The group of Peng at Tsinghua University championed its advantages for light trapping[4] the same year that the Atwater group at Caltech released a model of its advantages in reducing the carrier collection path in PV cells made of low quality material.[11] Studies on all-Si radial junction solar cells remained largely theoretical until, in August 2007, the Lieber group (which had pioneered the field of nanowire transistors) produced a PIN junction over a doped SiNW, contacted it, and tested its current-voltage characteristics.[12] The experiment demonstrated that, in spite of intricacies in making and handling them, nanoscopic radial junctions could generate power.

Box 6: A warning on wafers

Due to their high purity and thermal stability, Si wafers are commonly used as substrates for the growth of radial junction solar cells. In addition to the obstacles which wafers present in terms of the prospective commercialization of the technology, there is a risk that even a highly doped Si wafer contributes current to a PN junction formed at its surface. Measures can be taken to prevent this from happening. For instance the wafer can be thinned[13] or shaded under a reflective layer.[14] The safest approach however is simply to use a different substrate.

Much of the early work on radial junction solar cells was motivated by the prospect of increasing light absorption in thinner layers of material by orienting these layers along the same path as the direction of light propagation.[11] Quite unrelated from gains in trapping light within the plane of the cell, the intent was to benefit from the increased optical path length through the material and the radial junction was designed to provide ubiquitous electrical contacts along this vertical absorber (a technique sometimes referred to in the literature as “orthogonalizing the direction of light absorption and carrier collection”[15]). In essence, this can be seen as exploiting the larger volume of material which is packed in a radial junction by folding it in the shape of three dimensional pillars. However increasing the surface area of the device also increases its interfacial recombination. In practice, a compromise must be reached between the maximal nanowire length and minimal interface recombination.[13]

Following the emergence of single nanowire radial junctions, Tsakalakos et al. published results on arrays of radial PIN junctions grown together on metal foils in a process that required no crystalline Si wafers, no lithography and no nano-manipulation steps.[16] A 1 cm² array of p-doped SiNWs was covered in intrinsic and n-type a-Si:H and contacted millions of radial junctions within the same conformal layer of ITO. Although the performance of the device was limited, its diode rectification provided the first experimental evidence that arrays of radial junctions could be combined over macroscopic areas to operate in unison. Stelzner et al. confirmed these results and noted the enhanced optical absorption of arrays of SiNWs grown on glass substrates as compared to the absorption of a flat 375 µm thick Si wafer.[17] The use of nanowire-based photovoltaics branched out to axial PN junctions[18-21] and core-shell structures made from different materials.[22, 23] In 2008, Gunawan and Guha drove the energy conversion efficiency of an array of radial junctions grown on a crystalline Si substrate past the 1% benchmark.[24] By varying the thickness of the Au layer used to

catalyze the growth of their SiNWs, they also drew attention to the risk of metal contamination in the device inherent to the VLS growth process.

A recurring problem in these early radial junction cells was a loss in open-circuit voltage compared to their planar counterparts. Their built-in voltage was often lower than 300 mV, [12, 16, 17, 24, 25] barely half the value reached in planar silicon solar cells. Several groups have since drawn attention to the risk of contamination from the metal drops used to catalyze the nanowire growth.[26-30] For matters of convenience, nanowire growth has typically remained catalyzed by Au, which is notoriously detrimental to the electronic properties of Si.[31] Alternative fabrication methods, including chemically etching pillar structures out of Si wafers, succeeded in raising the open-circuit voltage and driving the energy conversion efficiency of radial junction cells up to 10%.[13, 32] Attempts were therefore pursued to remove the metal catalyst from bottom-up grown radial junction cells, for instance by dipping the device in metal etchants after nanowire growth.[24, 33] Recent achievements by the Gösele group in growing SiNWs from Al catalysts[34] were followed by studies on the use of alternative catalysts which might prove less detrimental as contaminants in the Si matrix than gold.[29] These include our own work on In and Sn catalysts.[28, 35-37] In 2010, the Atwater group combined metal removal techniques with Cu catalysts to produce an array of VLS-grown radial junctions with an unprecedented 7.9% energy conversion efficiency.[14] The devices offered encouraging results with respect to the potential of the technology. Further improvements could well tip the performance of radial junctions beyond those of established planar thin-film cells. However, in order to materialize this potential, the fabrication techniques required for making these cells need to be adapted to low cost methods and materials.

Box 7: Light trapping benefits of radial junction solar cells

The extent to which nanowire arrays are capable of trapping light remains unknown and they could potentially surpass the limits of current texturing techniques. Because the dimensions of the SiNWs used in radial junction solar cells are of the same order of magnitude as the wavelength of the radiation that they are designed to absorb, their interaction with photons cannot be described in terms of ray optics and there is substantial research involved in modeling the effect of the array morphology on its ultimate absorptance. Evidence has also emerged that plasmonic effects within individual nanowires could increase light absorption in the cell beyond Lambertian limits.

Our research has focused on such practicalities. Instead of Si wafers, we have adopted glass substrates; instead of using lithography techniques, we have positioned our catalyst drops by self-assembly; instead of high nanowire growth temperatures, we have used low melting point catalysts and have avoided wet chemical etching techniques in order to rely on vacuum equipment that can be integrated into an automated PECVD assembly line. One reason for this approach is purely practical. These are the tools we have experience working with at the PICM laboratory. The other is industrial. It will be easier to develop radial junctions commercially if they can be manufactured with the equipment in use in current a-Si:H fabrication lines. The objective was to draw on the advantages of radial junctions while remaining as close as possible to the fabrication process of commercialized a-Si:H solar cells.

2. Radial junctions grown at low temperature

Our solar cells were initially made in the ARCAM reactor using Asahi glass substrates covered in flat SnO_2 (80 nm thick). The ARCAM reactor was used on account of its connection to p-type and n-type doping gases and the benefit of separate chambers which avoid cross-contamination of dopants in the deposition chamber. The conditions for forming catalyst drops on their surface were derived from the studies presented in Chapter 2 and those for growing SiNWs from studies in Chapter 4. We begin with an overview of the complete fabrication process of our first devices. Many of the steps illustrated in Figure 5.2 were later amended; some even had to be replaced. Nonetheless the sequence offers a general idea of how the studies for individual layers of the cell fit into the final device.

2.1. Overview of the initial fabrication process

Glass substrates covered in 80 nm of SnO_2 were brought to a vacuum of 10^{-6} mbar in an RF-PECVD reactor (Figure 5.2.a). The substrates were exposed for 5 minutes to a H_2 plasma under a chamber pressure of 600 mTorr, an RF power density of 30 mW/cm² and a chamber temperature of 250 °C (Figure 5.2.b). Metal droplets were formed on the surface of the substrates as the H_2 plasma reduced the surface of the SnO_2 layer. The Sn droplets were then exposed to a silane plasma, to which 1 sccm of trimethylboron (TMB) (diluted in 98% H_2) was added in order to dope the nanowires p-type. The SiH_4 plus TMB plasma lasted for 15 minutes under a chamber pressure of 70 mTorr, an RF power density of 20 mW/cm² and a chamber temperature of 250 °C to catalyze the VLS-growth of p-type SiNWs (Figure 5.2.c).

Following SiNW growth, the temperature in the deposition chamber was dropped to 175 °C in order to solidify the Sn drops (and halt their catalytic activity), and samples were transferred to the chamber designated for intrinsic silicon deposition. Conformal layers of intrinsic a-Si:H were deposited over the doped nanowires by exposing the samples for 30 – 60 minute to a SiH_4 plasma under a chamber pressure of 110 mTorr and an RF power density of 10 mW/cm². Samples were then transferred to the n-type silicon chamber where they were exposed to a SiH_4 plus phosphine (PH_3) plasma under a pressure of 120 mTorr for 6 minutes to deposit an n-type a-Si:H silicon shell over the intrinsic layer (Figure 5.2.d). Samples were removed from the chamber and placed under vacuum in a Joule effect evaporator to contact the radial junctions with an evaporated layer of Al (Figure 5.2.e). The cells were then annealed in air at temperatures of 150 °C for 30 minutes prior to *J(V)* characterization.

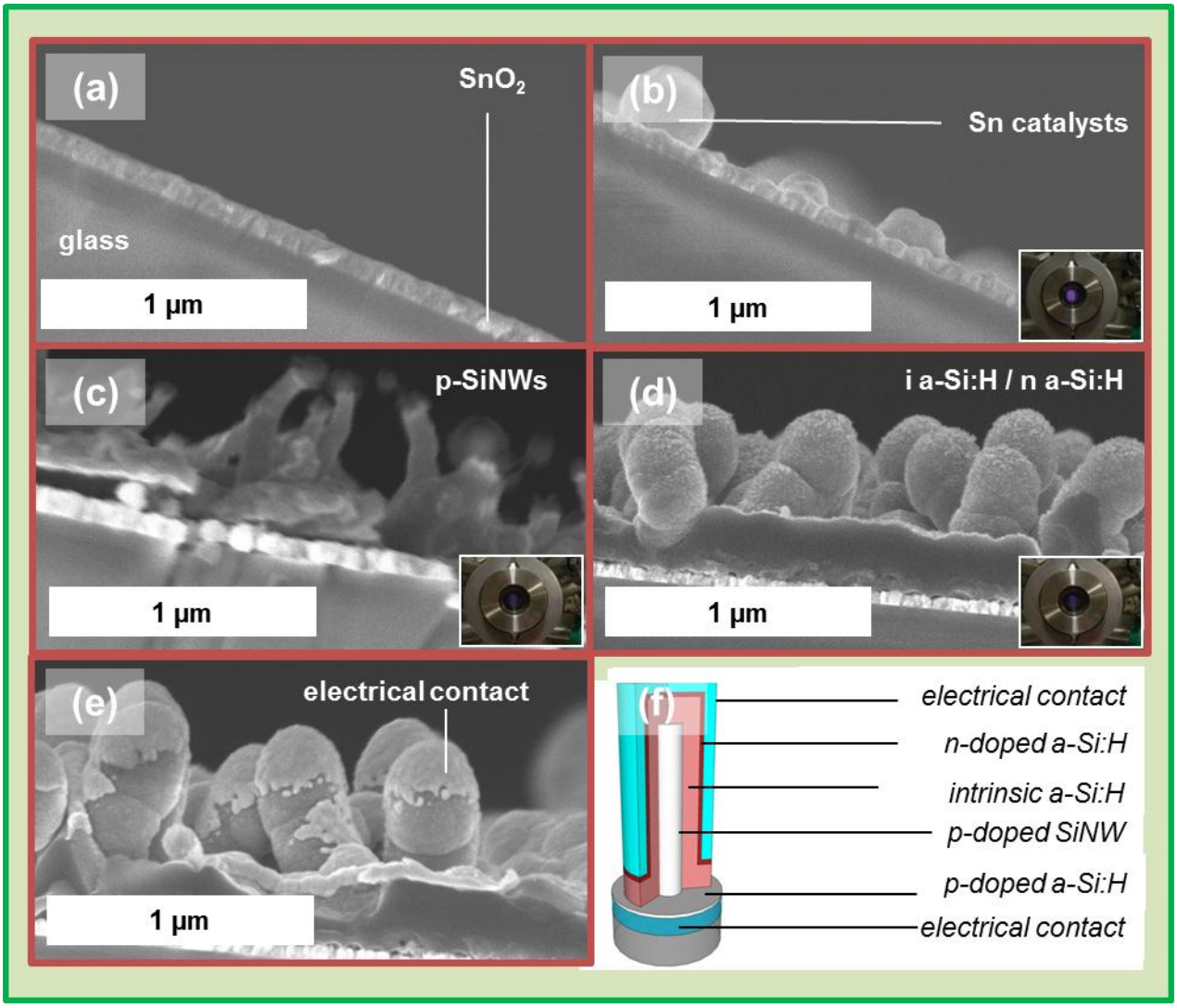

5.2 - Fabrication steps for our first radial junction devices.
SnO2 covered glass substrates (a) were exposed to a H_2 plasma to form liquid drops of Sn at their surface (b) which catalyzed the growth of p-type SiNWs when exposed to a SiH_4 plus TMB plasma (c). The SiNWs were exposed to a SiH_4 plasma and a SiH_4 plus PH_3 plasma at 175 °C to coat them in conformal layers of intrinsic and n-type a-Si:H (d). Al was evaporated over the radial PIN junctions in a Joule effect evaporator to cover their shells in an electrical metallic contact (e).

2.2. Choice of materials and conformal coverage

The choice of the materials used for the intrinsic and n-type layers covering the SiNWs is a delicate matter. Their bandgap defines the band diagram of the device, each material must be capable of conformal deposition over the abrupt texture of the SiNWs, and the plasma conditions used in each deposition must not damage the materials on which they are depositing. The consequences of poor choices regarding the last of these points was illustrated in our first attempts at covering the nanowires in an intrinsic layer of hydrogenated microcrystalline silicon (µc-Si:H). As described in Table 5.1, glass/SnO_2 substrates were exposed to a hydrogen plasma to produce the Sn catalyst drops at their surface. They were then exposed to a SiH_4 plus TMB plasma to grow p-type nanowires. The temperature was then decreased to 175 °C and a 500 nm layer of intrinsic µc-Si:H was deposited over the SiNWs, by exposing the samples to a silane and hydrogen plasma under a total pressure of 2 Torr, a power density of 88 mW/cm², respective H_2 and SiH_4 gas flow rates of 200 sccm and 6 sccm,

and for a duration of two hours. This was immediately followed by the deposition of a 20 nm layer of n-type a-Si:H

Table 5.1: Plasma conditions for RJPV with intrinsic layer of µc-Si (samples 90112b)

	H flux	SiH_4	TMB/PH_3	Pressure	plasma power	temperature	time
catalyst reduction	200	0	0/0 sccm	600 mTorr	31 mW/cm²	250 °C	3 minutes
p-SiNWs growth	0	50	1/0 sccm	70 mTorr	13 mW/cm²	250 °C	15 minutes
i-µSi:H growth	200	6	0/0 sccm	2 Torr	88 mW/cm²	150 °C	120 minutes
n-aSi:H growth	0	40	0/3 sccm	110 mTorr	6,3 mW/cm²	150 °C	6 minutes

The current-voltage characteristics of these devices displayed low current generation, poor open-circuit voltage and little rectification (Figure 5.3.c). These properties are symptomatic of a short-circuited solar cell. SEM cross-sections of the samples revealed that the number of radial junctions had been strongly reduced (Figure 5.3.a) in comparison with the number of nanowires grown under identical conditions when not covered in µc-Si:H (Figure 5.3.b). It was also observed that the sidewall surfaces of the radial junctions were uneven, indicating that the deposition of µc-Si:H was not conformal.

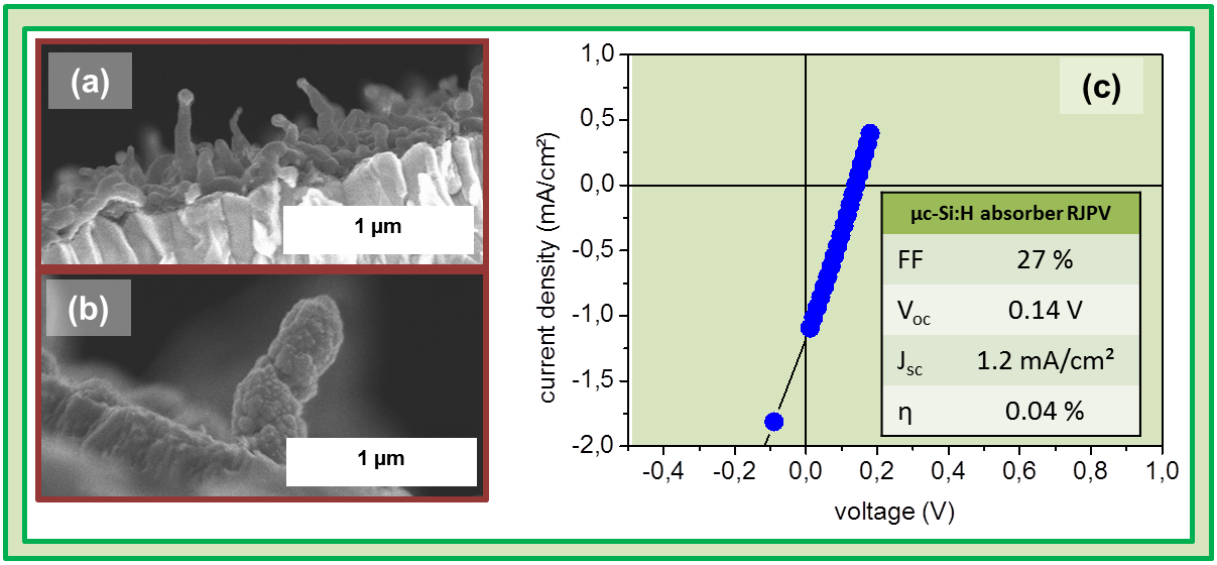

5.3 - Radial junction solar cells with µc-Si:H absorbers.
SiNWs doped p-type (a) and covered in an intrinsic µc-Si:H layer and n-type a-Si:H layer (b). *J(V)* characteristics of the device indicate a shunted diode behavior in this device (c).

The results initially raised concerns that conformal coverage could simply not be achieved by PECVD over the abrupt texture of silicon nanowires. However an investigation into the impact of the microcrystalline silicon plasma conditions on the nanowire samples revealed that the problem may be related to the high RF power and H_2 concentration necessary during the deposition of µc-Si:H. The exact mechanism through which atomic H crystallizes the (otherwise a-Si:H) deposition remains a topic of research, however it is generally believed to etch [38] or permeate [39] through the a-Si:H

deposition. In doing so, atomic hydrogen interacts with the sample on which the µc-Si:H is being deposited. To test the effect that it produces on our radial junctions, SiNWs were grown on glass/SnO_2 substrates and exposed to a H_2 plasma for 30 minutes. Standard conditions for the catalyst reduction plasma and the SiNW growth process were adopted and the subsequent H plasma was ignited at a temperature of 150 °C, under a pressure of 70 mTorr, a hydrogen flow rate of 200 sccm and a power of 190 mW/cm² (Table 2.2).

Table 5.2: Plasma conditions for removing SiNWs in a H_2 plasma (samples 90909c)

	H flux	SiH_4	TMB/PH_3	Pressure	plasma power	temperature	time
catalyst reduction	200	0	0/0 sccm	600 mTorr	31 mW/cm²	250 °C	3 minutes
p-SiNWs growth	0	50	1/0 sccm	70 mTorr	13 mW/cm²	250 °C	15 minutes
H_2 plasma	200	0	0/0 sccm	70 Torr	190 mW/cm²	150 °C	30 minutes

Following the H_2 plasma treatment, the SiNWs displayed smaller diameters and a rougher surface, their density appeared to have decreased and the sample was generally more translucent (Figure 5.4). These observations suggest that the hydrogen plasma removes Si atoms from the sample surface. The silicon deposited between the nanowires and at their surface is amorphous and prone to etching by atomic hydrogen.[39] This could explain the modification to the sample surface between the nanowires (Figure 5.4.b) and the increased optical transmission of the samples. Depositing µc-Si:H films requires an abundance of H atoms in a subsurface layer that can extend tens of nanometers into the material.[39, 40] The decrease in nanowire density may therefore be due to hydrogen atoms permeating the p-type layer and reducing the SnO_2 substrate beneath it. By doing so, it may liquefy the solid basis on which the nanowires are founded and cause them to break free and be swept away through the vacuum pumps of the plasma reactor.

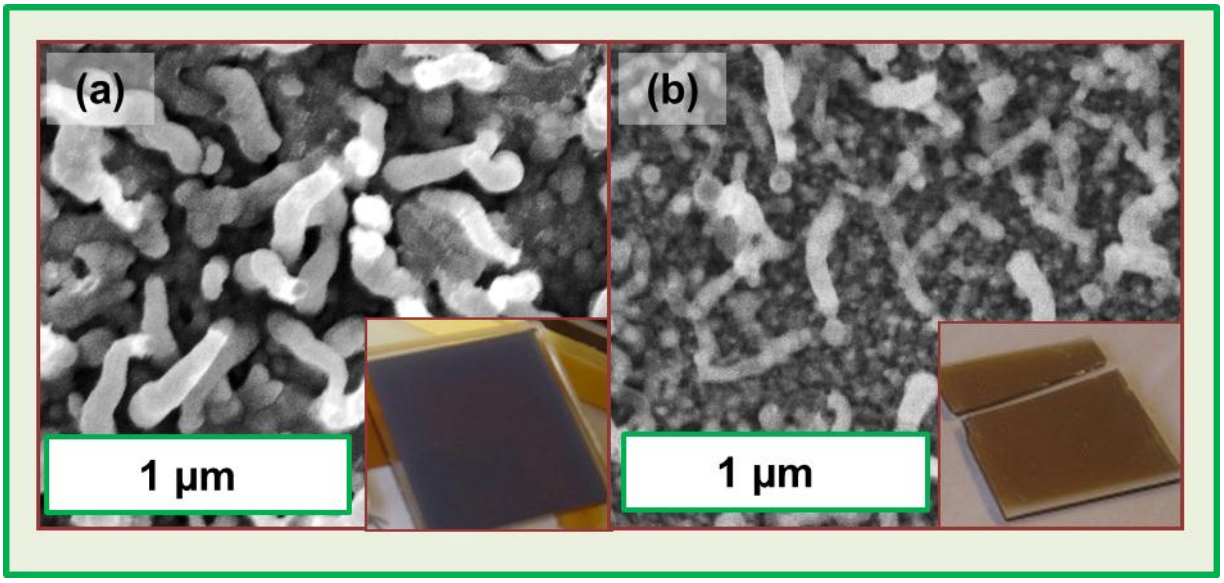

5.4 - Sn-catalyzed SiNWs exposed to a H_2 plasma.
SiNWs were grown under a silane plasma (a) then were exposed to a 30 minute H_2 plasma at 190 mW/cm² (b). Insets show photographs of the samples exposed to the same light source.

Also, if the atomic hydrogen in the plasma etches through the a-Si:H deposited between the nanowires completely, the intrinsic absorber will come in contact with the transparent conducting oxide and short-circuit the cell. This may explain the poor diode characteristic observed in Figure 5.3.c. We opted instead for an intrinsic a-Si:H in the following studies. Although the wider band gap of a-Si:H is less desirable for the band diagram of the device, the material can be deposited using less energetic plasma conditions than µc-Si:H. The adapted conditions are described in Table 5.3.

Table 5.3: Plasma conditions RJPV using an a-Si:H absorber (samples 90130a)

	H flux	SiH_4	TMB/PH_3	Pressure	plasma power	temperature	time
catalyst reduction	200	0	0/0 sccm	600 mTorr	31 mW/cm²	250 °C	3 minutes
p-SiNWs growth	0	50	1/0 sccm	70 mTorr	13 mW/cm²	250 °C	15 minutes
intrinsic a-Si:H	0	40	0/0 sccm	110 Torr	6.3 mW/cm²	150 °C	60 minutes
n-type a-Si:H	0	40	0/3 sccm	110 Torr	6.3 mW/cm²	150 °C	6 minutes

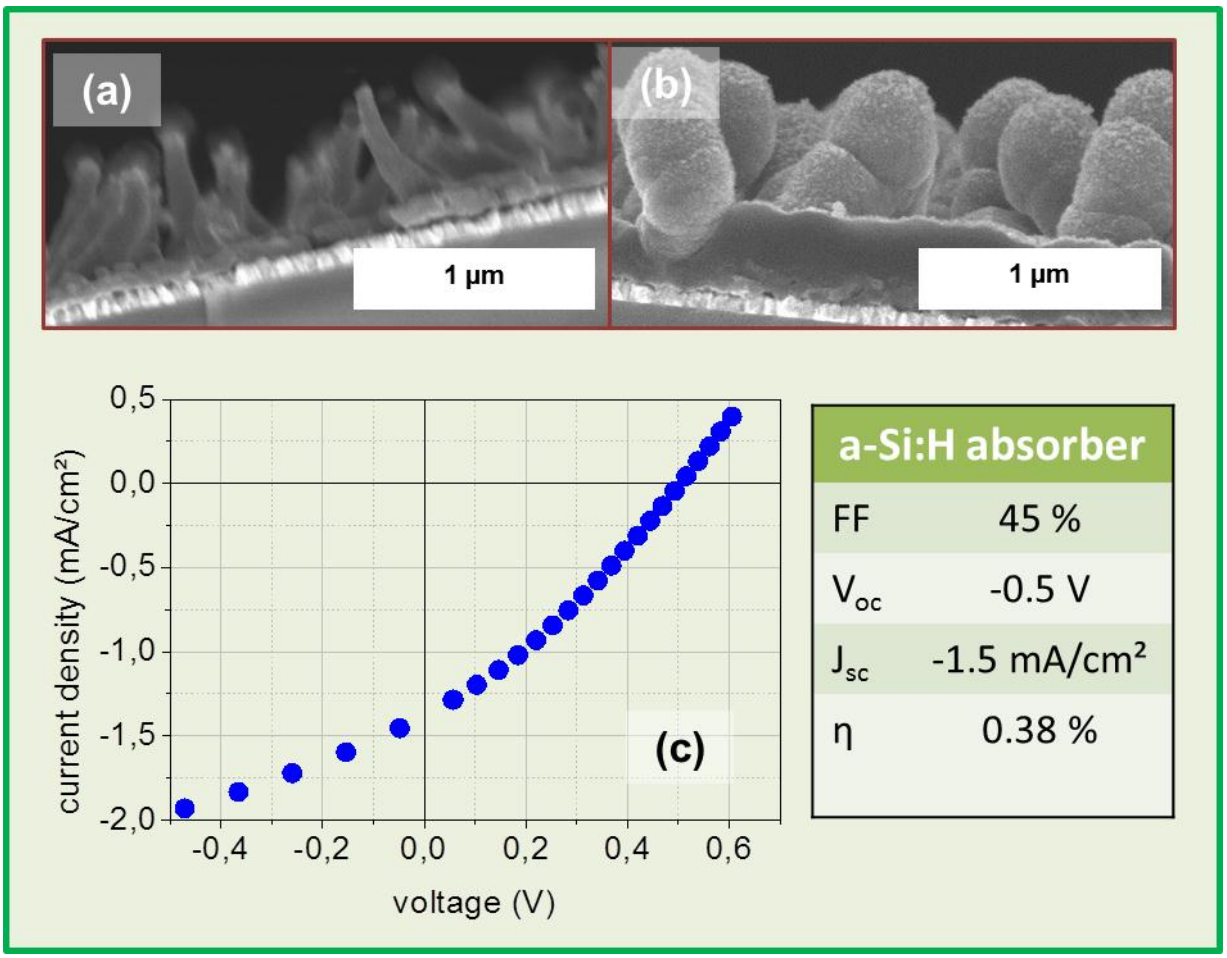

5.5 - Radial junction solar cells with a-Si:H absorbers.
SiNWs doped p-type (a) were grown in the ARCAM reactor and covered in intrinsic a-Si:H and n-type a-Si:H layers (b). The current voltage characteristics of these devices show the diode rectification of a solar cell (c).

These conditions led to a dense array of radial junctions at the sample surface (Figure 5.5.b). Although the short-circuit current and open-circuit voltage of the resulting device remained low, its fill factor was higher than in the cell deposited with the µc-Si:H absorber and the current-voltage characteristics clearly exhibited the rectification properties of a photo-diode (Figure 5.5.c). These results drew attention to the importance of conformal coverage over these highly textured surfaces to achieve a working junction and demonstrated that this requirement can be met using PECVD under adequate conditions.

2.3. Light trapping and the superstrate configuration

Our solar cells were initially designed in a substrate configuration (Figure 5.6.a) in which a metal contact was evaporated over their top layer and light was shone through the glass on which they were deposited. We inherited this approach from the standard fabrication process for the planar a-Si:H solar cells produced at the PICM laboratory. However, to take advantage of the light trapping effect of SiNWs, photons must be scattered across the nanowires,[41] not reflected within them. The nanowire tips therefore needed to be exposed to light, not covered in metal.

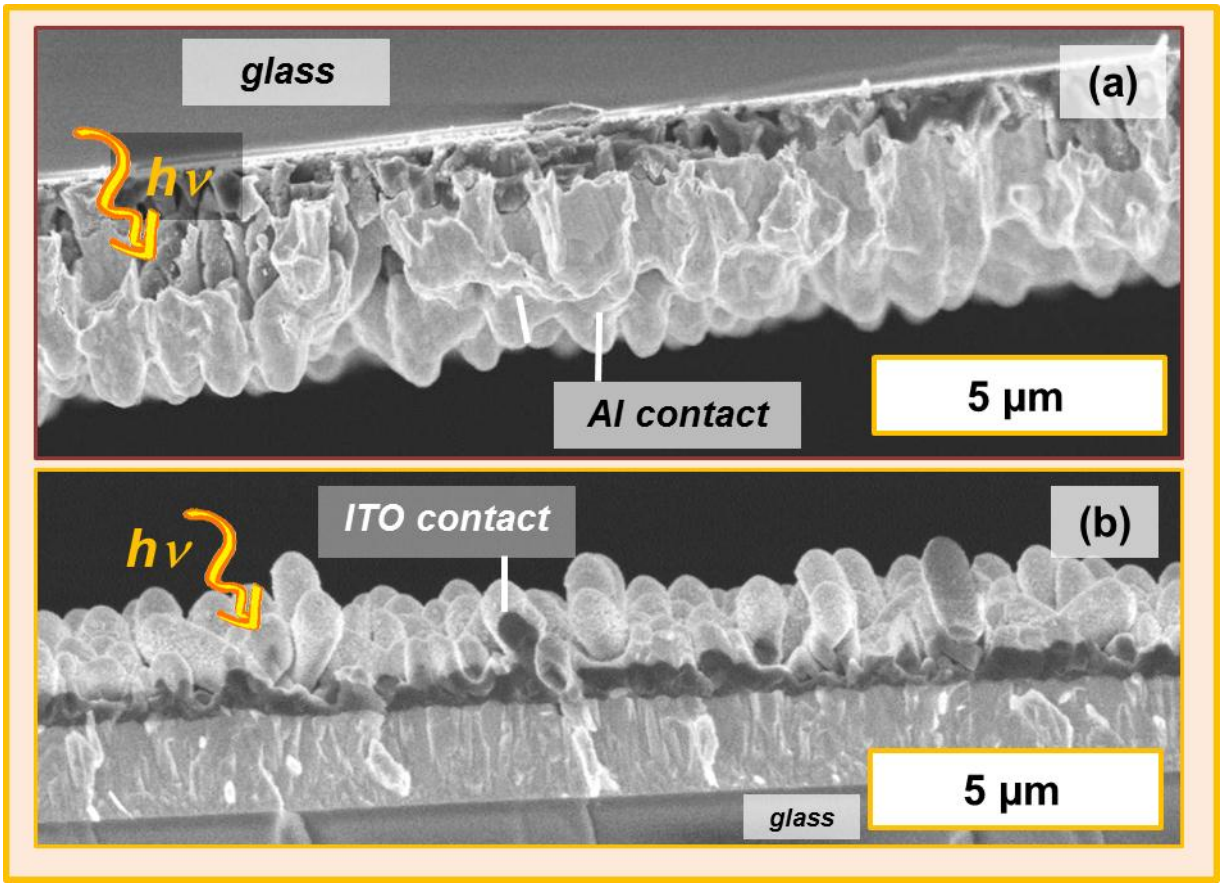

5.6 – Radial junction solar cells in substrate and superstrate configurations.
PIN radial junction solar cells grown in substrate configuration with Al evaporated over the n-layer (a), and in superstrate configuration with ITO sputtered over the n-layer (b).

We therefore replaced the evaporated metal contact by sputtering a layer of ITO over the radial junctions instead. Using similar conditions as the cells made in the previous section, we grew p-type SiNWs and covered them in intrinsic a-Si:H and n-type a-Si:H layers. These samples were then placed under vacuum in a physical vapor deposition system equipped with an ITO target. The sample was kept at room temperature under a gas flow of 40 sccm of Ar, at a pressure of 3.8 µbar and applying an RF plasma power of 2 W/cm². The target surface was cleaned by exposing it to the plasma for 2 minutes. The samples were then introduced under the target for 200 seconds to deposit a layer of ITO with a thickness corresponding to 200 nm over a flat glass reference substrate. These conditions are summarized in Table 5.4.

Table 5.4: ITO window layer sputtering conditions

	Ar flow	O_2	TMB/PH_3	Pressure	plasma power	temperature	time
ITO sputter	38	2	0/0 sccm	4.4 mTorr	2 W/cm²	37 °C	3.3 minutes

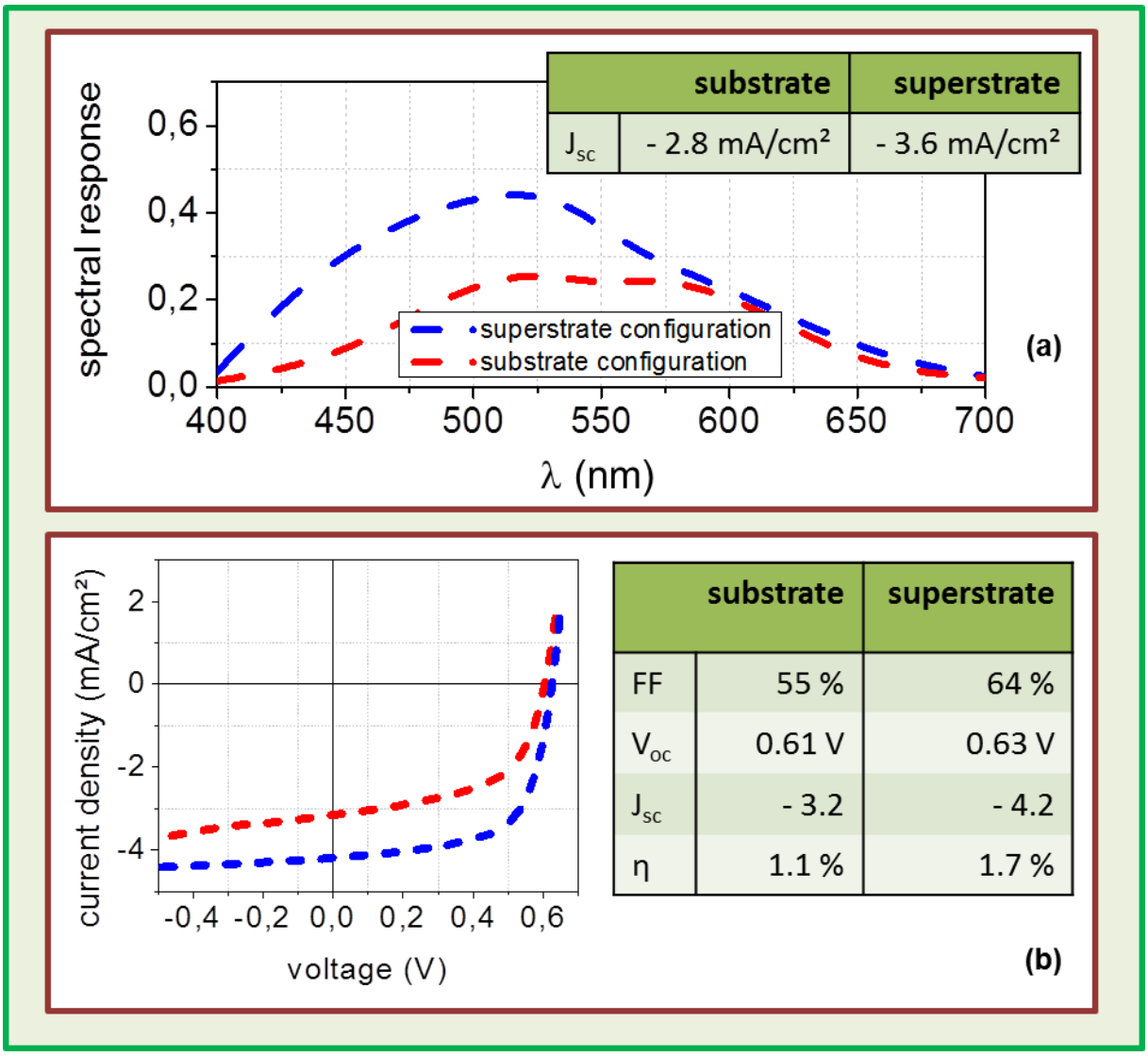

5.7 - SR and J(V) characteristics of substrate and superstrate solar cell configurations.
Spectral response (a) and current-voltage characteristics (b) of radial junction solar cells illuminated both through the glass (substrate configuration) and through the ITO (superstrate configuration).

Cross-sectional SEM micrographs revealed that the deposition of the ITO remained conformal to the radial junction structure (Figure 5.6.b). The spectral response and *J(V)* characteristics of the cells were then measured for both directions of light incidence. Shining light in the superstrate configuration (through the top ITO layer, rather than through the glass) increased the short-circuit current of the cell, in particular at lower wavelengths (Figure 5.7), suggesting that better light trapping was achieved in the superstrate configuration.

2.4. Light trapping and SiNW density

In view of optimizing light trapping within our devices, we attempted to control the density of nanowires grown at the sample surface. To do so, we prepared substrates which were known from our studies in Chapter 2 to produce catalyst drops with different diameters and densities when exposed to a hydrogen plasma. Glass/SnO_2 (80 nm) substrates were included to produce small catalyst droplets in high densities. Glass substrates over which ZnO was sputtered for 40 minutes and ITO was sputtered for 10 seconds were included to provide larger and sparser catalysts. And glass substrates over which the same ZnO layer was sputtered but the layer of ITO was sputtered for 20 seconds, were included to produce even larger and sparser catalyst drops. The deposition rate of ITO was measured as 1 nm.s^{-1} on flat glass substrates. We also included glass substrates covered in flat ZnO (1 µm) over which no ITO was deposited, to serve as reference planar junctions for the study (Figure 5.8).

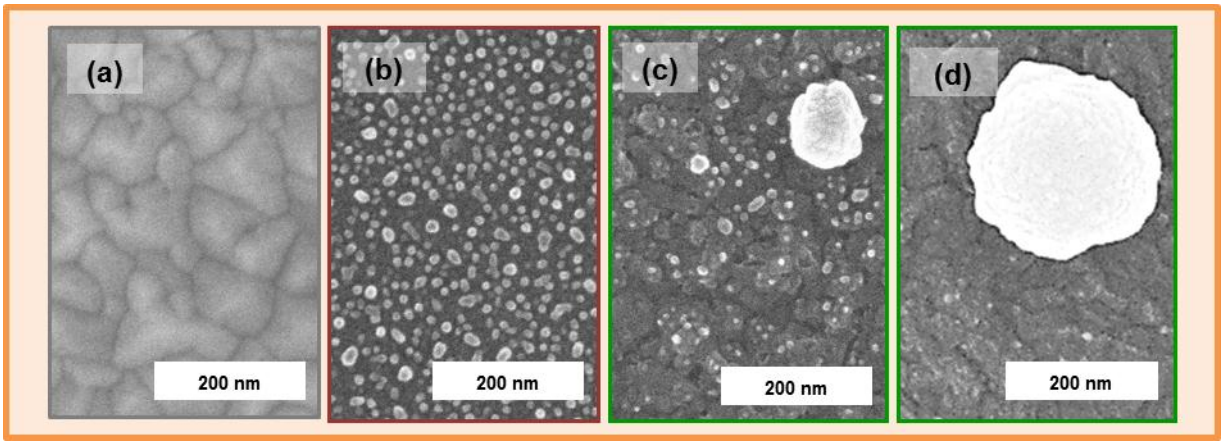

5.8 - Substrates used for radial junction array density studies.
The following substrates were reduced in a H_2 plasma to obtain different densities and diameters of catalyst drops: glass/ZnO (a), glass/SnO_2 (b), glass/ZnO/ITO (10s) (c) and glass/ZnO/ITO (20s).

Substrates were placed in the Nextral reactor, heated to 250 °C and exposed to a H_2 plasma under a gas flow rate of 200 sccm, a pressure of 600 mTorr and a plasma power density of 30 mW/cm² for 3 minutes. The p-type SiNWs were then grown in conditions similar to those used in the ARCAM reactor by feeding a silane and TMB at respective flow rates of 50 sccm and 1 sccm for 15 minutes, at a pressure of 70 mTorr and a plasma power density of 10 mW/cm². The temperature was then

reduced and conformal layers of intrinsic a-Si:H and n-type a-Si:H were deposited over the nanowires using the deposition conditions described in Table 5.5.

Table 5.5: Plasma conditions for RJPV with different nanowire densities (samples nx100519)

	H flux	SiH_4	TMB/PH_3	Pressure	plasma power	temperature	time
catalyst reduction	200	0	0/0 sccm	600 mTorr	31 mW/cm²	250 °C	3 minutes
p-SiNWs growth	0	50	1/0 sccm	70 mTorr	13 mW/cm²	250 °C	15 minutes
i-aSi:H growth	0	50	0/0 sccm	45 mTorr	6,3 mW/cm²	150 °C	60 minutes
n-aSi:H growth	0	40	0/3 sccm	110 mTorr	6,3 mW/cm²	150 °C	6 minutes

Nanowire samples were also made by exposing the substrates to only the catalyst reduction and SiNW growth steps and removing them from the reactor in order to observe the morphology of the nanowires formed via SEM. The ZnO substrate presented a flat surface, as was to be expected since no catalyst particles were present at its surface (Figure 5.9.a). The SnO_2 covered substrate presented a high density of short, thin nanowires (Figure 5.9.b). The samples deposited on 10 seconds of ITO presented fewer and larger SiNWs (Figure 5.9.c). Those deposited on 20 seconds of ITO presented fewer still, considerably longer SiNWs (Figure 5.9.d).

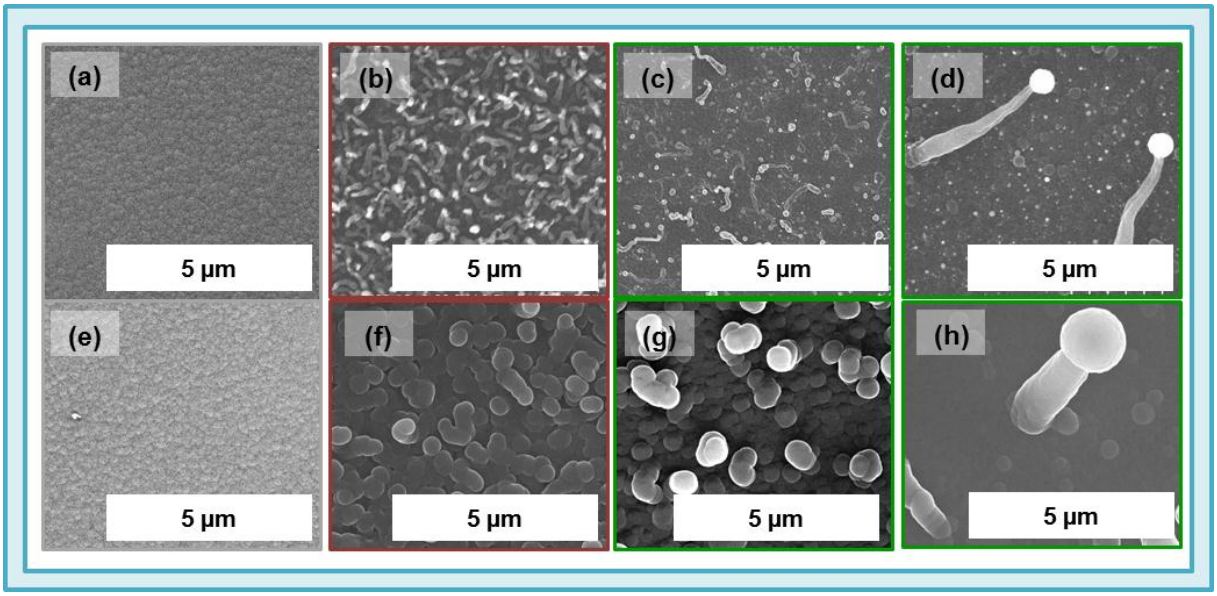

5.9 - Density of SiNW arrays according to different substrates.
SiNWs grown in the Nextral reactor on substrates of ZnO (a), SnO_2 (b), ZnO covered with 10 seconds (c) and 20 seconds of ITO sputtering (d). The p-type nanowires were then coated in conformal layers of intrinsic a-Si:H, n-type a-Si:H and ITO to produce radial junction solar cells in arrays with different densities (e-h).

SEM images were also obtained of the complete radial junction cells (Figure 5.9.e-f). They revealed that the cell deposited over the ZnO substrate remained flat (Figure 5.9.e). The cell deposited over SnO_2 showed a decrease in the number of radial junctions at its surface (Figure 5.9.f) compared to the number of nanowires prior to deposition (Figure 5.9.b). Considering the thickness of the conformal deposition and the initial proximity of the nanowires, it is foreseeable that radial junctions were buried together during the deposition of the intrinsic a-Si:H layer. In contrast, in the cell grown

on the substrate over which the ITO film was sputtered for 20 seconds, the nanowires were sparse and clearly separate (Figure 5.9.d). As a consequence the deposition of the intrinsic and n-type layers was more conformal (Figure 5.9.h).

In order to compare how well each of the different radial junction structures trapped light, optical absorptance measurements were performed on these cells using a Perkin-Elmer Lambda 950 spectrophotometer with an integrating sphere (Figure 5.10.a). The measurements indicated that all radial junction solar cells absorbed light better than the flat ZnO reference cell. However, the cell grown on the substrate covered in SnO_2 displayed higher optical absorptance than those grown on the substrates covered in ITO. The difference between the two may lie in the density of radial junctions. While in the case of the cells deposited on ITO, radial junctions were sparse, the cell grown on SnO_2 is completely covered in them.

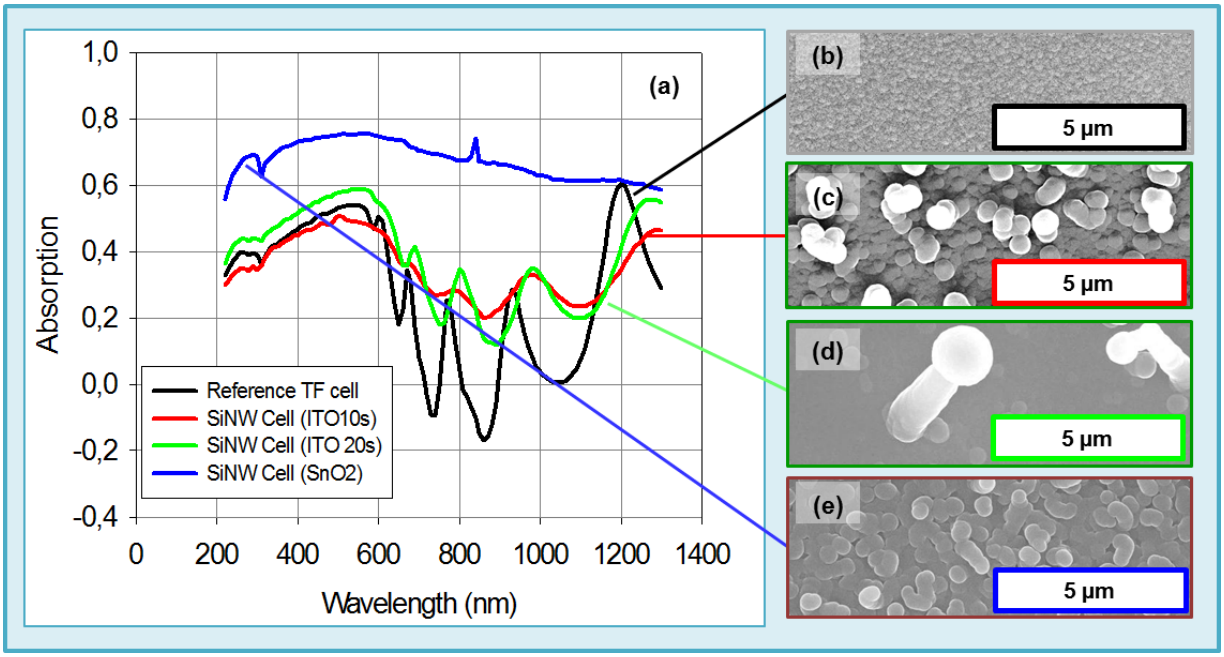

5.10 - Optical absorptance of radial junction solar cells with different array densities.
Optical absorptance measurements (a) performed on radial junction cells deposited in the same plasma run deposited over substrates of glass covered in ZnO (b), ZnO/ITO sputtered for 10 seconds (c), ZnO/ITO sputtered for 20 seconds (d) and SnO_2 (e).

However this increase in absorptance did not translate into improved photovoltaic performance. In principle, trapping more light in the cell would be expected to increase short-circuit current. In practice, as the *J(V)* characteristics of these cells demonstrated (Figure 5.11), other factors must be taken into account. The cell grown on SnO_2, with the highest density of SiNWs and the highest optical absorptance displayed a comparatively low short-circuit current (Figure 5.11). The gentle slope of its *J(V)* curve suggested that internal losses and current leakage through the diode were both high. In contrast, both cells grown on ITO present short-circuit currents in excess of 4 mA/cm² (Figure 5.11). The cell grown on 20 seconds of ITO, with scarce and large radial junctions proved less effective at trapping light; however its short-circuit current and open-circuit voltage were comparatively high.

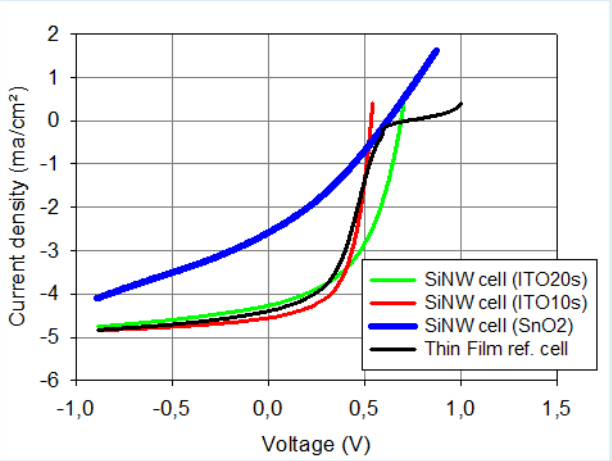

	ZnO	SnO_2	ITO (10 s)	ITO (20 s)
FF	41 %	31 %	56 %	49 %
V_{oc} (V)	0.68	0.62	0.53	0.69
J_{sc} (mA/cm²)	- 4.4	- 2.6	- 4.6	- 4.3
η	1.2 %	0.5 %	1.4 %	1.4 %

5.11 - J(V) characteristics of radial junction solar cells with different array densities.
J(V) characteristics of radial junction solar cells deposited in the same plasma run deposited over substrates of glass covered in ZnO, SnO_2 and ZnO/ITO sputtered for 10 seconds and 20 seconds.

This draws attention to the importance of growing devices with surface morphologies that will facilitate the extraction of charge carriers. The reference cell grown on flat ZnO suffers from a low open circuit voltage for a planar a-Si:H solar cells.[42] Its current-voltage curve also exhibits the typical S shape of a double diode (Figure 5.11). This may be due to contact issues between p-type a-Si:H and the ZnO or the lower doping efficiency of a-Si:H compared to crystalline Si.[43] There are several complications in comparing these cells. For instance, the series resistance of the sample grown on the SnO_2 substrate may differ from that on ZnO, or the large catalyst drops still visible at the tip of the radial junctions in the samples deposited on 20 seconds of ITO may cause additional recombination. However the results may generally offer the guideline that improving light trapping in radial junction solar cells can only be effective so long as the charge collection is guaranteed. A compromise must be found in optimizing the density of the radial junction arrays. Nanowires must be sufficiently dense to trap light but far enough apart to ensure conformal coverage of the subsequent layers.

3. Radial junctions grown at high temperature

One important obstacle to conformal coverage was that the nanowires in the previous studies had tended to grow bent and kinked. In Chapter 4, it was seen that nanowires were considerably straighter when grown at temperatures of 600 °C. We therefore compromised on the temperature used throughout our fabrication process and deposited a radial junction cell over SiNWs grown at 600 °C in the Plasfil reactor (Figure 5.12.a). The substrates used were glass/ITO (100 nm). Plasma conditions for the H_2 reduction and nanowire growth process were those described in Table 4.1 for a duration of 60 minutes. A 260 nm thick intrinsic layer was then deposited over the nanowires in Plasfil under a silane pressure of 260 mTorr, a temperature of 150 °C and an RF power of 10 mW/cm² (Figure 5.12.b). Samples were then transferred to the ARCAM reactor to deposit the n-type layer for 6 minutes under the standard conditions described above in Table 5.1. In this first attempt, the electrical contacts used were Al.

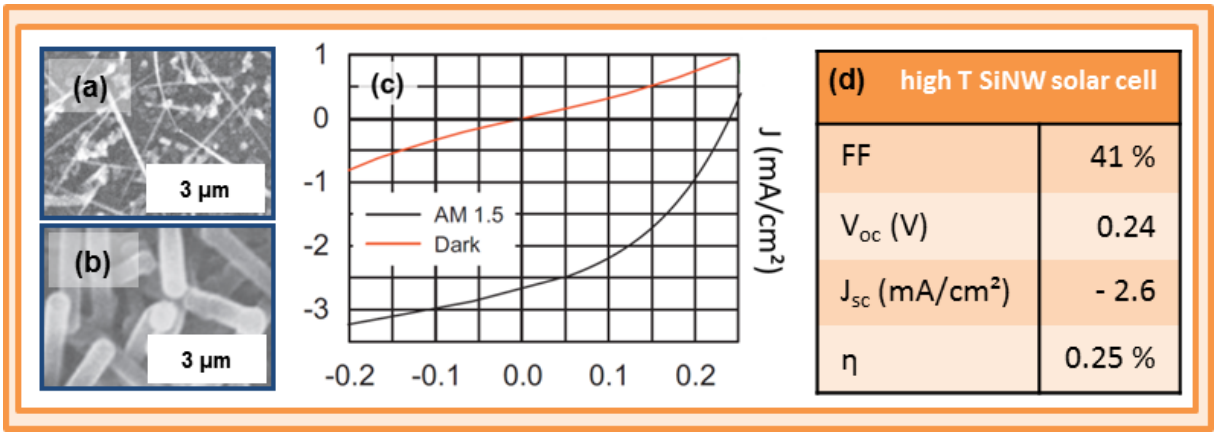

5.12 - Radial junction solar cells on intrinsic SiNWs grown at high temperature.
SiNWs were grown at 600 °C in the Plasfil reactor using catalysts reduced from a substrate of glass covered in ITO (a) and coated in n-type a-Si:H in the ARCAM reactor (b). Current-voltage measurements (c) and photovoltaic parameters (d) are shown.

At the time, the Plasfil reactor was not equipped with dopant gas lines. In consequence, the nanowires grown were nominally intrinsic. SEM microscopy reveals that the diameters of the final a-Si/SiNWs structures are generally uniform throughout their length (Figure 5.12.b), suggesting that coverage of the a-Si:H layer was conformal. Although undoped and unoptimized, *JV* measurements indicated that the devices presented a rectification behavior and a fill factor and short-circuit current comparable to the doped radial junction cells previously deposited at low temperature.

3.1. p-Type doping in the nanowires

To dope the SiNWs, a trimethylboron line was connected to the Plasfil reactor. Radial junction solar cells were then deposited over p-type SiNWs grown at 600 °C by adding TMB to the silane plasma during nanowire growth. In addition to the higher temperature of the nanowire growth process, several amendments were made to our solar cell design (Figure 5.13.a). Instead of reducing the TCO surface to produce catalyst drops, flat layers of ZnO:Al (~1 µm thick) were sputtered onto glass substrates to constitute the back contact for the solar cell. The metal catalyst for nanowire growth was then provided by evaporating a thin layer of Sn (~1 nm) on the surface of the ZnO. This substrate was favored over SnO_2 or ITO, as its transparency and conductivity was not observed to degrade when exposed to a H_2 plasma. The glass/ZnO:Al/Sn substrates were loaded into the Plasfil reactor and exposed to a hydrogen plasma for 3 minutes at 350 °C to form 50 nm wide Sn drops.

Table 5.6: Plasma conditions for RJPV with SiNWs grown at 600 °C (samples PF110502-04)

	H flux	SiH_4	TMB/PH_3	Pressure	plasma power	temperature	time
catalyst reduction	100	0	0/0 sccm	600 mTorr	50 mW/cm²	350 °C	3 minutes
p-SiNWs growth	0	10	0 - 2.5 sccm	350 mTorr	20 mW/cm²	600 °C	10 minutes
i-aSi:H growth	0	10	0/0 sccm	120 mTorr	20 mW/cm²	175 °C	60 minutes
n-aSi:H growth	0	40	0/10 sccm	110 mTorr	6,3 mW/cm²	150 °C	6 minutes

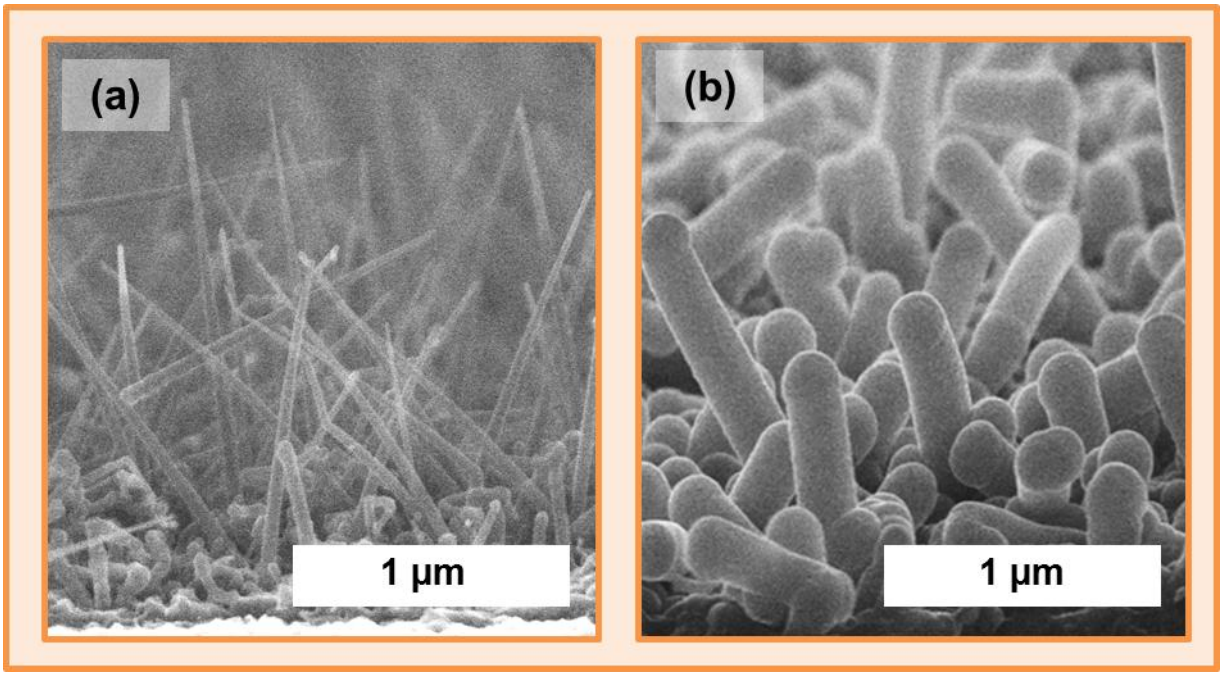

5.13 - Radial junction solar cells on p-type SiNWs grown.
Straight p-type SiNWs were grown from Sn catalysts evaporated on a ZnO substrate under a silane and TMB plasma at 600 °C (a) and covered in intrinsic and n-type a-Si:H (b).

Once the catalysts were formed, they were heated to 600 °C and exposed to a plasma of silane and trimethylboron (TMB) diluted in 98% H_2 for 10 minutes, causing them to catalyze the growth of p-type silicon nanowires (Figure 5.13.a). After SiNW growth, the temperature was dropped to 175 °C and the system was allowed to cool for an hour under a gas flow of H_2 at a constant pressure of 1 Torr. The samples were exposed to a silane plasma for 60 minutes to coat the p-type nanowires in an intrinsic layer of a-Si:H. They were then removed from the Plasfil and introduced into the ARCAM reactor where they were exposed to a silane plus phosphine plasma to deposit a conformal layer of n-type a-Si:H over their surface and complete the radial PIN junctions (Figure 5.13.b). Deposition conditions are detailed in Table 5.6. The cells were then covered in an ITO contact which was sputtered over mask-defined areas of 3.1 mm².

In order to study the effect of p-type doping in the SiNWs, a series of cells were fabricated in which the concentration of TMB (diluted in H_2) in the silane plasma was gradually increased. Its partial pressure was incremented from 0 to 52.5 mTorr of the total 350 mTorr pressure of the silane + diluted TMB in the chamber. The p-type Si nanowires were then incorporated into radial PIN junctions following the procedure described above, producing the cells illustrated in Figures 5.13.a-e. The open circuit voltage of the cells increased progressively as TMB was added to the nanowire growth conditions (Table 5.7). Their current-voltage characteristics showed a gradual improvement in both V_{oc} and fill factor (Figure 5.14.f). Beyond a TMB partial pressure of 42 mTorr, benefits from additional doping were observed to saturate. The highest open-circuit voltage in this run was 0.80V, a value close to the 0.89V observed in record planar a-Si:H solar cells.[44] The short-circuit current of all cells doped with TMB was over 10 mA/cm² and peaked at 13 mA/cm². The short-circuit current and open circuit voltage were markedly lower for the cell deposited on undoped nanowires. In fact the *JV* characteristic of this sample showed minimal fill factor and no diode rectification. This is expected given the low built-in potential of a cell with no p-type layer.

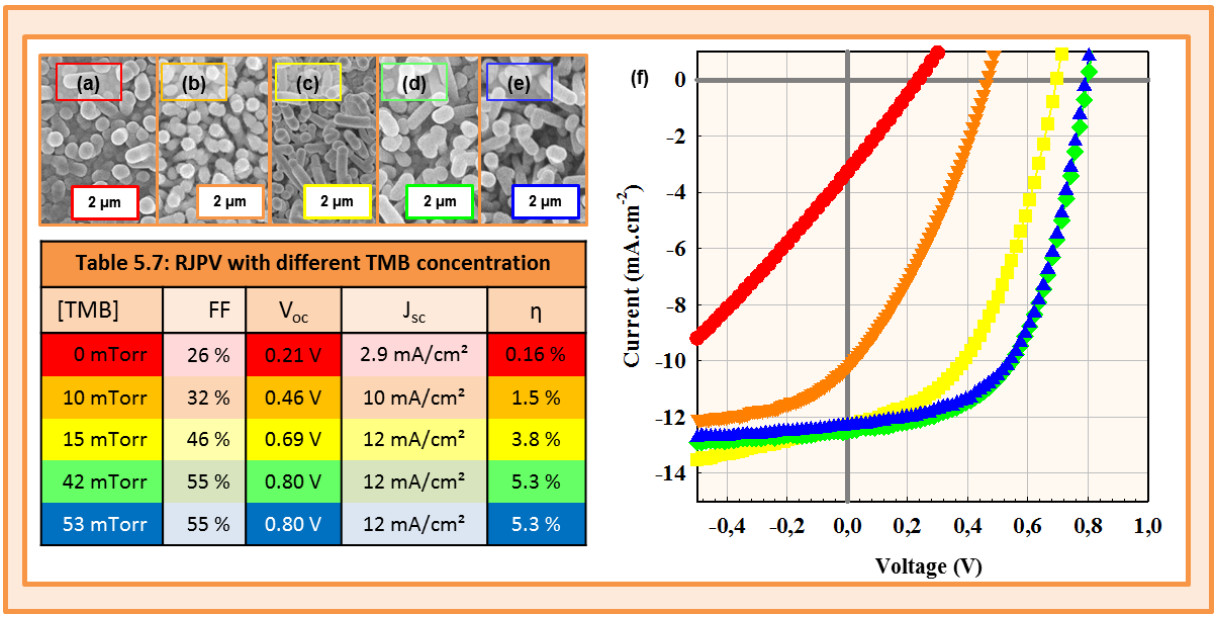

Table 5.7: RJPV with different TMB concentration

[TMB]	FF	V_{oc}	J_{sc}	η
0 mTorr	26 %	0.21 V	2.9 mA/cm²	0.16 %
10 mTorr	32 %	0.46 V	10 mA/cm²	1.5 %
15 mTorr	46 %	0.69 V	12 mA/cm²	3.8 %
42 mTorr	55 %	0.80 V	12 mA/cm²	5.3 %
53 mTorr	55 %	0.80 V	12 mA/cm²	5.3 %

5.14 - Radial junction solar cells with increasing TMB concentration during SiNWs growth.
Radial junction solar cells deposited over p-doped nanowires whose partial pressure of TMB in total a silane gas pressure of 350 mTorr was increased from 0 mTorr (a), 10 mTorr (b), 15 mTorr (c), 42 mTorr (d) to 53 mTorr (e). Their corresponding *JV* characteristics are displayed in (f) and PV parameters in Table 5.7.

3.2. Conformal coverage revisited

Although top view SEM images of the samples indicated that the deposition of a-Si:H layers remained remarkably conformal throughout most of the SiNW length (Figure 5.14.a-e), cross-sectional views revealed that this was not the case at the interface between the radial junctions and the substrate. Overshadowing by taller radial junctions left smaller ones stunted and all were generally thicker at their tip than at their base (Figure 5.15).

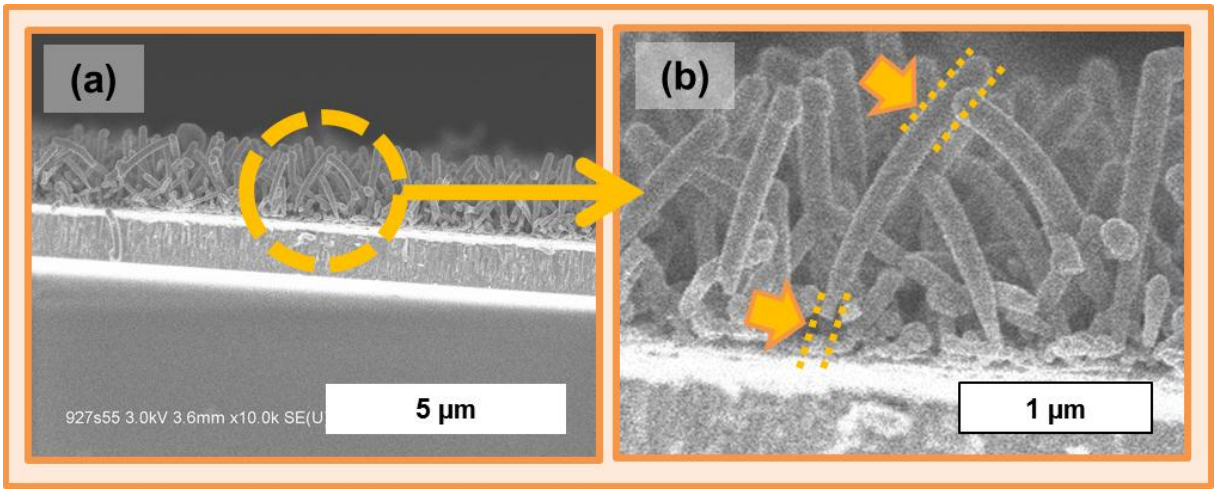

5.15 - Conformal coverage of layers over Sn-catalyzed SiNWs deposited at 600 °C.
PIN radial junction solar cells (without ITO) deposited over nanowires grown at 600 °C (a) exhibit uniform diameters over most of their length however the tightly packed bases are often observed to be thinner than their tips (b).

Similar complications were observed with the deposition of the ITO over the radial junctions. SEM images of the devices demonstrated that in the case of low nanowire densities, a 200 nm thick layer of ITO could be sputtered conformal to the radial junction surfaces (Figures 5.16.a-c). However above a given density and length of radial junctions, the ITO deposited preferentially at their tips, leaving stretches at their base poorly covered (Figure 5.16.b).

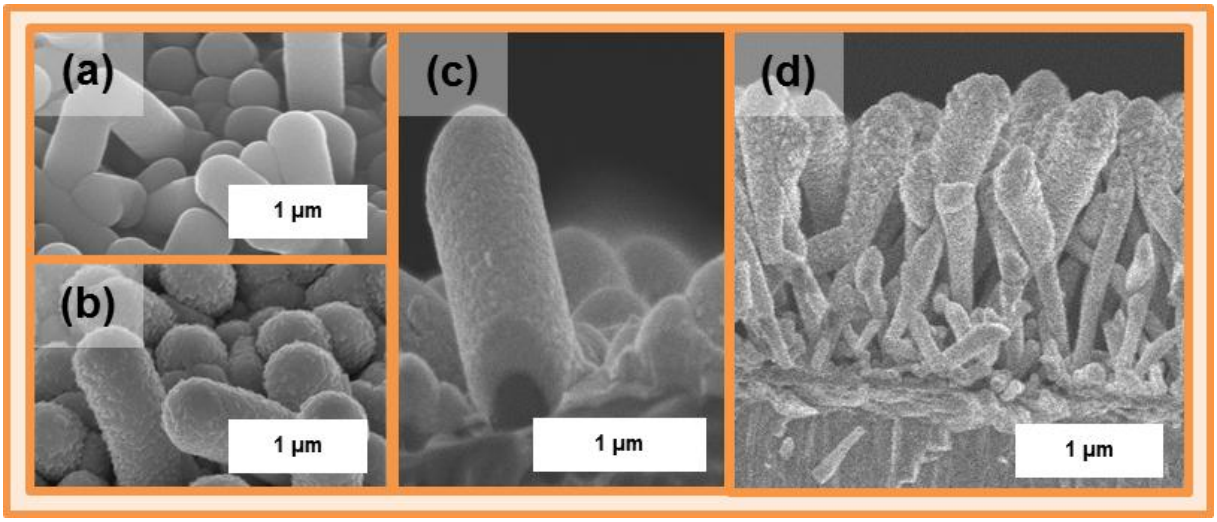

5.16 - Conformal coverage of ITO contacts on radial PIN junctions.
Radial junctions solar cells before (a) and after (b) sputtering the ITO contact layer. While individual nanowires can be covered conformally with ITO by physical vapor deposition (c), high densities of long radial junctions suffer from non-uniform deposition (d).

In brief, the coverage of the a-Si:H layers over the p-type SiNWs was more conformal for cases in which the nanowire density was lower and the nanowires themselves were shorter. This resembles the conclusion regarding the compromise between light trapping and conformal coverage in radial junctions grown at lower temperature (Figure 5.11) with the distinction that conformal coverage over SiNWs grown at 600 °C can be achieved over arrays which are considerably longer and denser, greatly increasing the potential gains in light trapping. Straight nanowires can also be expected to form fewer sites for recombination and largely avoid the problem of touching each other or being buried under the a-Si:H absorber layer. Their higher density may also constitute an advantage in terms of the collection area of the device as the arrays present less surface between nanowires where the p-type deposition consists of parasitic a-Si:H.

3.3. Comparison with planar junctions

To compare light trapping in radial junction solar cell with planar structures, three cells were deposited on glass substrates. The first was a radial junction solar cell grown on a ZnO layer (1 µm) thick covered in a film of Sn (1 nm). Catalyst drops and SiNWs were formed in the Plasfil reactor under the conditions described in Table 5.6 setting the TMB flow rate to 0.9 sccm and reducing the growth duration of the nanowires to 5 minutes. Our intention in growing nanowires was to facilitate the conformal coverage of the following intrinsic and n-type a-Si:H and ITO layers. The intrinsic a-Si:H was deposited in Plasfil, adopting conditions identical to Table 5.6 but extending the intrinsic layer deposition time to 90 minutes in order to ensure that the intrinsic layer covering the larger surface

area presented by the SiNW arrays would be at least as thick as in a planar structure. The devices were then transferred to the ARCAM reactor where they were exposed to the standard silane plus phosphine plasma for n-type a-Si:H deposition during 8 minutes. The samples were then contacted with a layer of ITO layer sputter for 7.5 minutes. The two reference samples were deposited in the ARCAM reactor under conditions optimized in-house for planar polymorphous silicon (pm-Si:H) cells.[45] One was deposited on a glass substrate covered in a flat layer of SnO_2 (80 nm) with a square resistance of 130 Ω□, the other on a glass substrate covered with textured SnO_2 (1 µm) with a square resistance of 15 Ω□. Both planar solar cells were back contacted with evaporated Al. The devices were designed to each have an intrinsic layer 300 nm thick (Figure 5.17.c-d). In the case of the radial junction solar cell, this meant covering the entire surface around the nanowire with 250 nm of Si, resulting in diameters 500 nm wide (Figure 5.17.b). All samples were annealed at 150 °C for 15 minutes and their J(V) characteristics were measured under AM1.5. The current-voltage characteristics of all three devices show commendable diode rectification and open-circuit voltages in excess of 0.80 V. However the short-circuit current of the radial junction cell was considerably higher than that of the flat reference cell. As short-circuit current scales with illumination,[46] this improvement can be associated to increased light trapping from the radial junctions. In fact, the short-circuit current of the radial junction cell comes close to that of the reference cell deposited on commercially textured SnO_2.

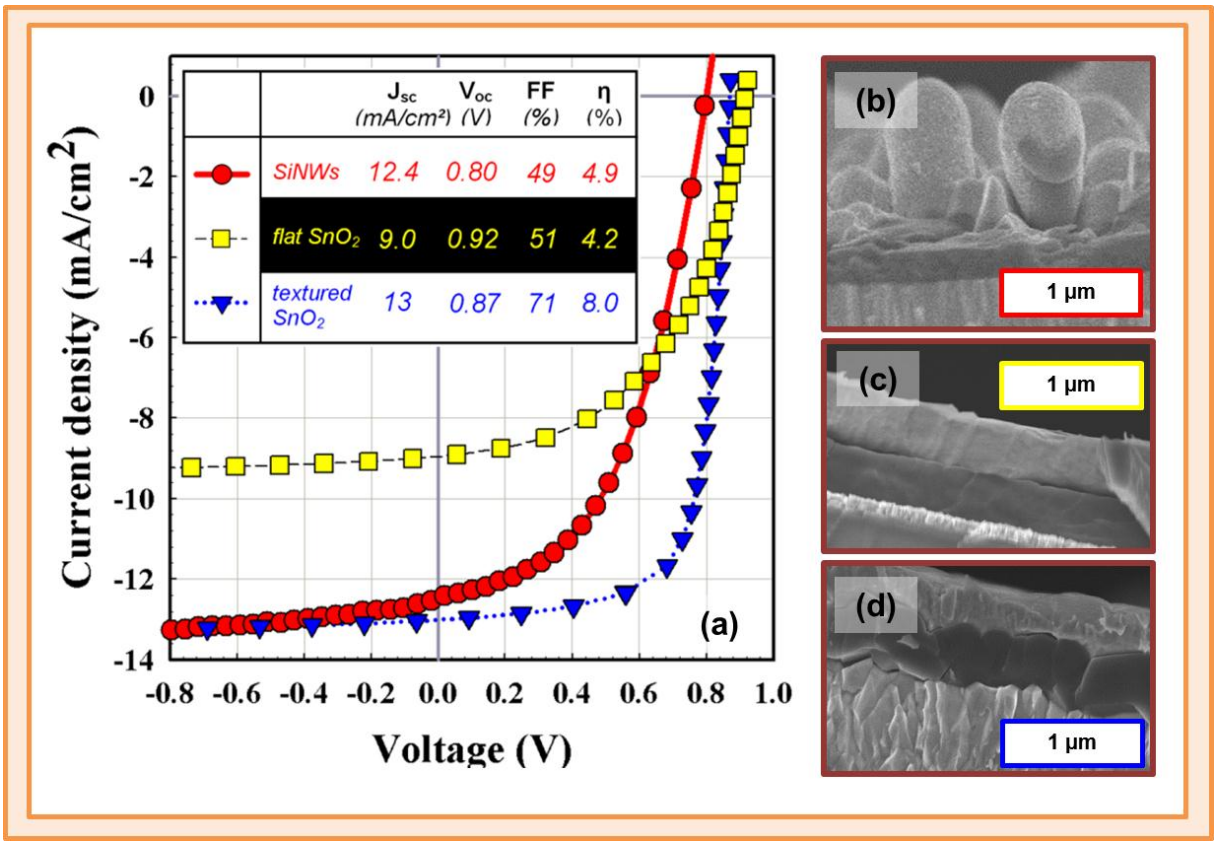

5.17 - J(V) characteristics of radial junction, planar and conventionally textured solar cells.
Current-voltage characteristics comparing light trapping in a radial junction solar cell, a planar hydrogenated polymorphous silicon cell deposited over a flat glass/SnO_2 substrate and a planar pm-Si:H cell deposited over a standard commercially textured Asahi substrate (a). Cross-sectional SEM images of the three samples (b-d).

However the low fill factor of the radial junction cell shows that the device continues to suffer from electrical losses. There are numerous potential flaws which could explain these losses, including inadequate conformal coverage, suboptimal intrinsic layer thickness, catalyst contamination… Another important point is that the texture of the reference SnO_2 substrate in Figure 5.17 has been chosen for its light trapping properties whereas the morphology of the radial junction cell formed at random. Further improvements in light trapping could therefore be expected from optimizing the diameter and density of the radial junction array.

4. Light trapping in radial junctions

According to both theoretical and experimental studies of light trapping in one-dimensional structures, optical absorptance is expected to increase in arrays with longer nanowires.[13, 47] In this final section we have attempted to improve the photon absorption in the radial junction cells by optimizing the length of the SiNWs on which they were grown. Based on these results, we will then look into why light is being lost in the device before summarizing the conclusions of this chapter.

4.1. Nanowire length

Glass/ZnO substrates were covered with layers of Sn, whose nominal thickness was given as 0.2, 0.5 and 5 nm by a quartz microbalance during their evaporation. They were exposed in the same run to a silane and TMB plasma for 30 minutes to grow nanowires on their surface and then covered in layers of intrinsic and n-type a-Si:H and ITO (under the conditions specified in Table 5.8), and annealed in air for one hour. Metal layers with different thickness were prepared because shorter nanowires were observed to grown on substrates covered in thinner layers of Sn (Figure 5.18.b-d). This peculiarity was not identified in our studies on nanowire growth in Chapter 4; however, the thickness of catalysts previously used was always greater than 1 nm. The fact that below this thickness, nanowires are observed to grow shorter could be attributed to the increased surface tension required to grow smaller diameter nanowires, which may lead to slower growth rates and fewer active catalysts.[48] Alternatively, the results may also support claims that the catalyst is progressively lost during the growth process, halting VLS if the system runs out of Sn.[26, 29, 49] The approach ensured the homogeneity of the plasma conditions over the entire series of samples and made it possible to grow nanowires 1 µm, 2 µm and 3 µm long on otherwise identical substrates in the same plasma deposition run.

Table 5.8: Plasma conditions for RJPV with different lengths (samples PF101210)

	H flux	SiH_4	TMB/PH_3	Pressure	plasma power	temperature	time
catalyst reduction	100	0	0/0 sccm	380 mTorr	50 mW/cm²	350 °C	3 minutes
p-SiNWs growth	0	10	0.9 sccm	340 mTorr	20 mW/cm²	600 °C	30 minutes
i-aSi:H growth	0	10	0/0 sccm	120 mTorr	20 mW/cm²	175 °C	240 minutes
n-aSi:H growth	0	40	0/10 sccm	110 mTorr	6.3 mW/cm²	175 °C	24 minutes
ITO sputter	[Ar]/[O_2] = 38/2 sccm			4.4 mTorr	2 W/cm²	37 °C	17 minutes
Annealing						150 °C	60 minutes

The SiNWs were then covered in a 240 minute deposition of intrinsic a-Si:H before being transferred to the ARCAM reactor for a 24 minute deposition of n-type a-Si:H, which corresponded to a nominal thickness of 70 nm on a flat substrate (Table 5.8). The deposition times for the intrinsic and n-type layers were increased compared to previous samples out of concern that the enhanced surface area presented by the highly textured surface of the nanowires would spread the conformal a-Si:H layers too thin.

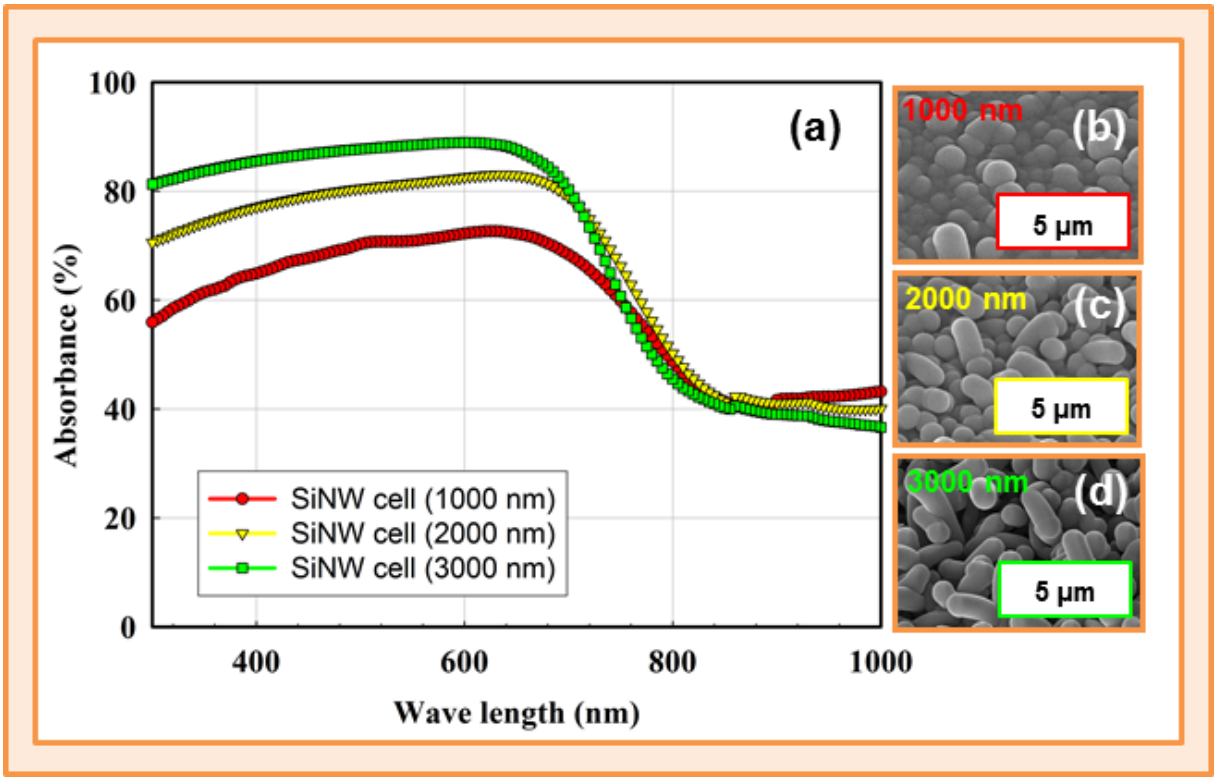

5.18 - Optical absorptance of radial junction solar cells grown on increasingly long SiNWs.
Optical absorptance measurements of radial junction solar cells deposited over p-type SiNWs lengths of 1000 nm (b), 2000 nm (c) and 3000 nm (d).

The optical absorptance of these samples was determined from reflectance and transmission measurements using a UV-Visible Perkin-Elmer Lambda 950 spectrophotometer with an integrating sphere (Figure 5.18.a). Silicon deposition time was identical for all cells; however the absorptance curves show that devices with longer nanowires absorb more light in the visible range than devices with shorter nanowires. Although it is encouraging to confirm that light trapping can be optimized by altering the nanowire morphology, our previous studies (Figure 5.11) have already shown that, by itself, this does not necessarily lead to improvements in the performance of the solar cells. The absorptance curves give little indication as to where in the device light interacts. Photons absorbed in defects, inactive layers or in the remnants of buried Sn catalysts will not contribute to the current generated by the cell. Nor will photo-excited electrons if they recombine. However, in this case light trapping was observed to correlate with short-circuit currents in the cell. *J(V)* characteristics of the same samples (Figure 5.19.d) reveal that all three devices rectify current, produce open-circuit voltages close to 0.8 V and present energy conversion efficiencies of 3.4% to 6%.

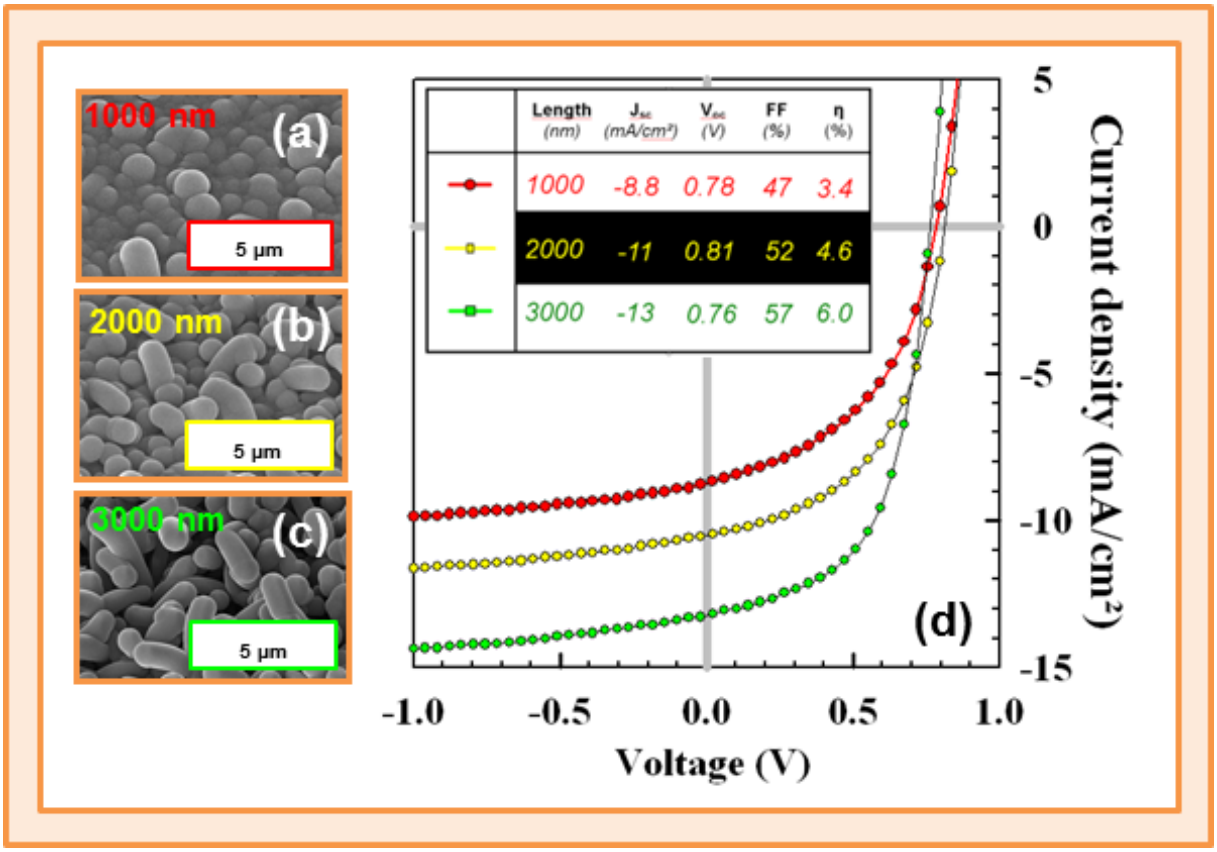

5.19 - J(V) characteristics of radial junction solar cells grown on increasingly long SiNWs.
Current-Voltage characteristics of radial junction solar cells deposited over p-type SiNWs with lengths of 1000 nm (b), 2000 nm (c) and 3000 nm (d).

The performance of cells deposited on shorter nanowires was limited to a large extent by their short-circuit current, which was observed to increase by 50% when the nanowires were extended from 1 to 3 µm. As mentioned above, the short-circuit current depends primarily on the intensity of light incident on the cell. The fact that the open-circuit voltage remains largely unaffected by the nanowire length suggests that improved light trapping is the primary cause for improvements in the energy conversion efficiency of the cells. Combining these observations with the absorptance spectra in Figure 5.19 provides compelling evidence of the benefits that radial junctions can offer in trapping light for solar cells. The radial junctions not only trap light, they trap it where it is needed and harness the charges it generates.

4.2. Window layer thickness and losses in the blue

One challenge that has plagued our cells since we first shined light through their ITO layers has been their disappointing charge collection at wavelengths lower than 500 nm. Figure 5.20.a illustrates the spectral response of the radial junction solar cell presented in Figure 5.17 (when assessing the relative merits of nanowires and ZnO texturing for trapping light in solar cells). It is compared with the polymorphous silicon cell deposited on textured SnO_2 in the same study. Differences in the spectral response between wavelengths of 600 to 700 nm can be explained by the lower bandgap of the a-Si:H intrinsic layer deposited in Plasfil for the radial junction cell (determined by spectroscopic ellipsometry to be 1.64 – 1.69 eV as compared to the 1.7 eV bandgap of the planar a-Si:H cell

deposited in the ARCAM reactor). However this does not explain the mismatch between the two curves at lower wavelengths. Absorptance measurements indicated that the cells do absorb light at these wavelengths (Figure 5.18.a); however the spectral response measurements (Figure 5.20.a) indicate that either it is not generating electron-hole pairs, or that these charges are not being collected.

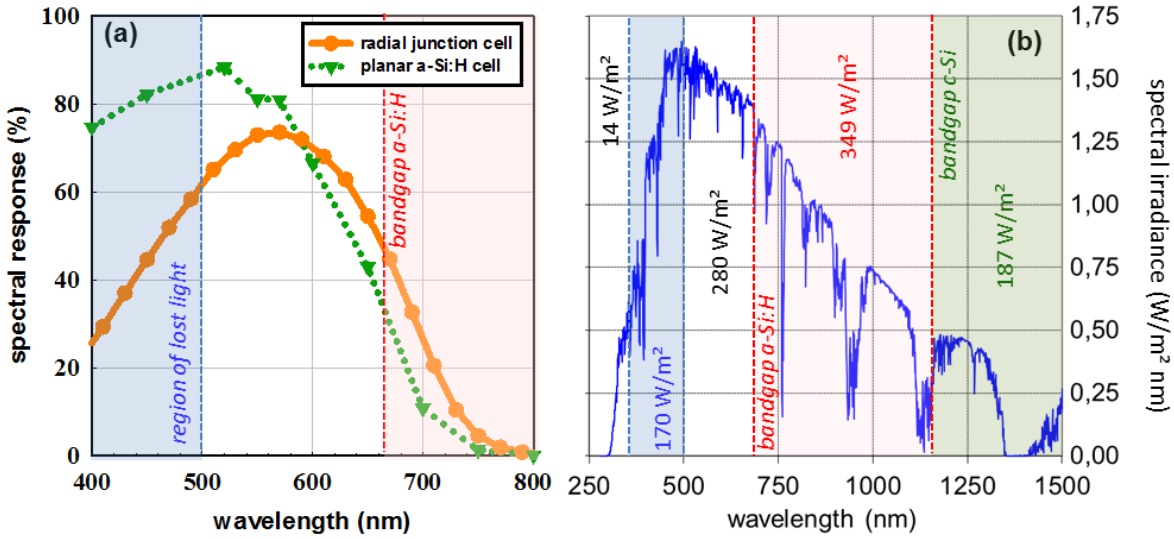

5.20 – Optical losses at low wavelengths in our radial junction solar cells.
Spectral response curves for radial junction and planar a-Si:H solar cells (a) and solar spectrum at air mass 1.5 (b).

The blue region of the AM1.5 solar spectrum indicated on Figure 5.20 represents 170 W/m² of sunlight. In other words, it accounts for 35% of the power available to a photovoltaic cell with a bandgap of 1.8 eV in the AM1.5 solar spectrum. If each photon in this region were to create an electron-hole pair, and each of these charges were collected, it would contribute 6.1 mA/cm² to the short-circuit current of the cell. In practice, this potential may not be fully exploited. But variations of 50% and more in the spectral response of radial junction and planar a-Si:H at these wavelengths (Figure 5.20.a) is a considerable loss that must be remedied if radial junction solar cells are to compete with conventional texturing techniques. On account of its higher energy, blue light has a penetration depth of only ~30 nm in a-Si:H devices.[50] It is expected to be absorbed close to the surface of the cell and is also liable to be lost in the TCO window layer and the n-type a-Si:H. In order to identify the extent of these losses, we deposited cells with varying thicknesses of ITO and n-type a-Si:H and observed the evolution of their spectral response.

Layers of Sn 0.5 nm thick were evaporated on substrates of glass covered in sputtered ZnO (1 µm thick). Deposition conditions were adapted from those used in the study on SiNW length. In order to avoid problems of conformal coverage, the SiNW growth time was reduced to 5 minutes and covered in an intrinsic a-Si:H layer for a duration of 90 minutes. All samples were coated in n-type a-Si:H in the ARCAM reactor for a duration of 8 minutes (with a nominal deposition rate of 0.05 nm s^{-1} on flat surfaces). To study the absorption in the ITO contact layer, each of four such samples was sputtered with an ITO layer through 3.1 mm² masks for a duration of 2.5, 3.3, 7.5 or 17 minutes (using

conditions that lead to a deposition rate of 0.5 nm s^{-1} on flat surfaces). These conditions are summarized in Table 5.9.

Table 5.9: Plasma conditions for RJPV with different n-aSi:H and ITO layers (samples PF110329-31a)

	H flux	SiH_4	TMB/PH_3	Pressure	plasma power	temperature	time
catalyst reduction	100	0	0/0 sccm	600 mTorr	50 mW/cm²	350 °C	3 minutes
p-SiNWs growth	0	10	0.9 sccm	230 mTorr	20 mW/cm²	600 °C	5 minutes
i-aSi:H growth	0	10	0/0 sccm	120 mTorr	20 mW/cm²	175 °C	90 minutes
n-aSi:H growth	0	40	10 sccm	110 mTorr	6.3 mW/cm²	175 °C	6 – 20 minutes
ITO sputter	[Ar]/[O_2] = 38/2 sccm			4.4 mTorr	2 W/cm²	37 °C	2.5 – 17 minutes
Annealing						150 °C	60 minutes

Scanning electron microscopy of the samples confirmed that the length and density of the radial junctions covered in ITO an generally homogeneous across all radial junction cells although their diameter increases with the thickness of the ITO layer sputtered over them (Figure 5.21.a-d). A cross-sectional SEM image of a region of the cell covered in ITO (sputtered for 7.5 minutes) reveals that the ITO deposition is not strictly conformal. It is thinner at the base of the radial junction than at its tip and thickest over flat areas between nanowires.

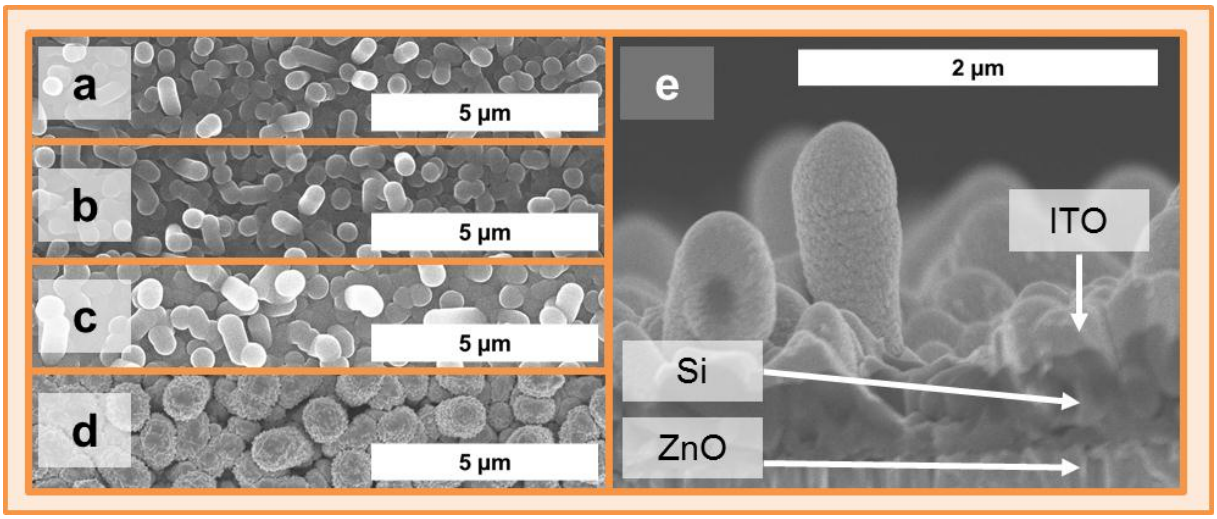

5.21 - Radial junction solar cells with increasingly thick ITO layers.
Top-view SEM images of radial junction solar cells contacted with ITO layers deposited for durations of 2.5 (a), 3.3 (b), 7.5 (c) and 17 minutes (d). Cross-sectional SEM image of the sample exposed to ITO sputtering during 7.5 minutes (e).

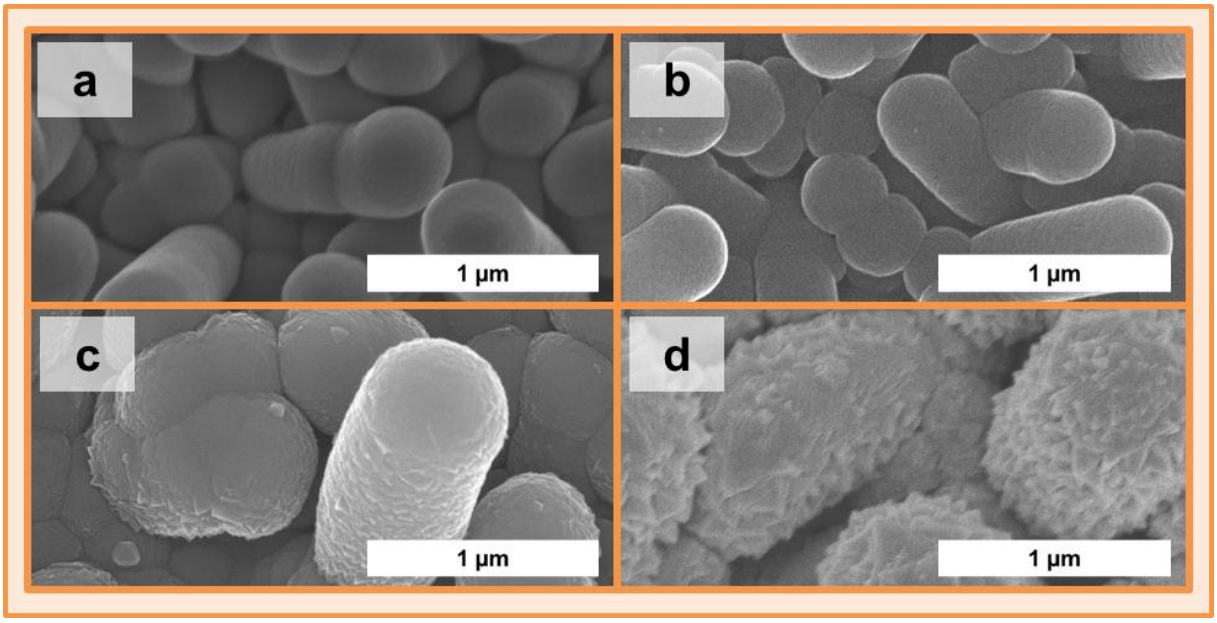

5.22 - Surface texture of increasingly thick ITO layers.
The morphology of smooth radial junction Si sidewalls (a) grows progressively more textured as the duration of ITO deposition is increased to 3.3 (b), 7.5 (c) and 17 minutes (d).

The ITO deposition was observed to affect the surface texture of the radial junction sidewalls. The smoothness of a-Si:H (Figure 5.22.a) gradually gave way to rough ITO crystallites. Within 7.5 minutes of ITO sputtering, sharp textured features on the scale of 10 nm had formed over the radial junctions (Figure 4.5.b). As of 17 minutes, ITO shards covered the entire length of the radial junctions and bridged much of the empty space between them (Figure 5.22.c). However, this fine structure over the surface of the radial junctions was not observed to affect their tendency to trap light.

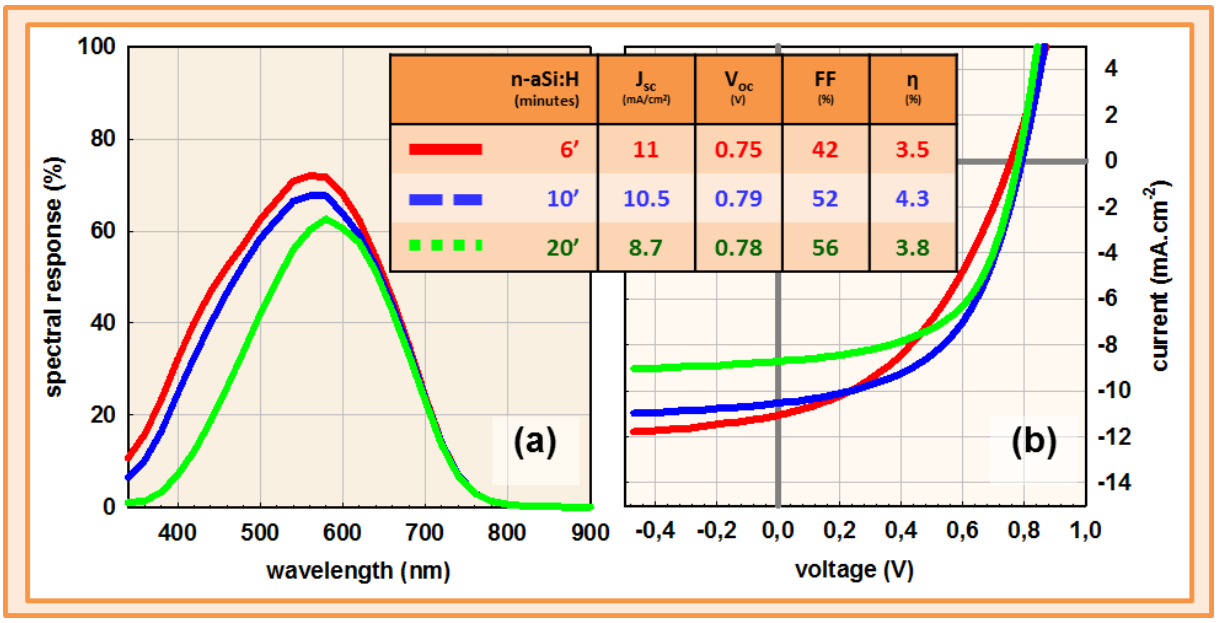

5.23 - Effect of ITO layer thickness on SR and J(V) characteristics of radial junction solar cells.
Figure 5.23 – Spectral response (a) and current-voltage characteristics (b) of radial junction solar cells over which ITO layers were deposited for durations of 2.5, 3.3, 7.5 and 17 minutes.

Spectral response and current-voltage characteristics were measured on these cells (Figure 5.23). Thicker layers of ITO reduced the spectral response of the cells only marginally (Figure 5.23.a) resulting in a short-circuit current increase of 0.8 mA/cm² for the cell with an ITO layer sputtered during 2.5 minutes as compared to 17 minutes. Even in the case of the cell with the thinnest layer of ITO, spectral response in the blue region remained lower than 60 %. In contrast, the *J(V)* characteristics show that thinning the layer of ITO can eventually lead to losses in fill factor (Figure 5.23) which can be ascribed to resistive losses in thin layers of ITO. In terms of energy conversion efficiency, the best compromise between conduction and transparency of the contact layer was found for cells sputtered with ITO for 7.5 minutes. However, within the range of thicknesses studied, little variation was noted in either property.

A more pronounced trend emerged when comparing the n-layer thickness to current collection in the cell. Identical cells were made according to the deposition conditions in Table 5.9, however the duration of the ITO sputtering was fixed this time at 7.5 minutes and the duration of the n-type a-Si:H deposition in the ARCAM reactor was varied over durations of 6, 10 and 20 minutes. All samples were annealed in air at 150 °C for 60 minutes following deposition (Table 5.9). For incident light with a wavelength of 500 nm, reducing the deposition time from 20 to 6 minutes was observed to increase the fraction of electron-hole pairs collected from 40% to 60% (Figure 5.24.a). However *J(V)* characteristics identified that, although reducing the thickness of the n-layer increased the short-current in the cell by 1.8 mA/cm², it also reduced its fill factor from 56% to 42% (Figure 5.24). Again, the cell with the thinnest window layer presented the highest short-circuit current but not the best energy conversion efficiency.

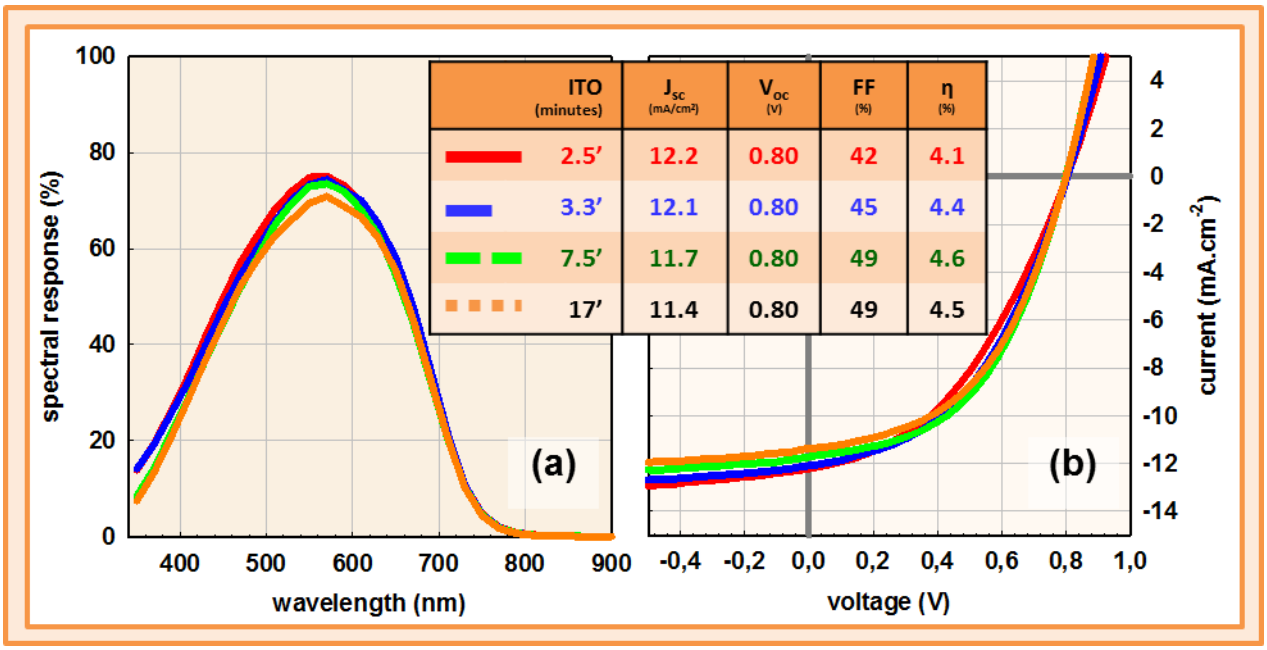

5.24 - Effect of n-layer thickness on SR and J(V) characteristics of radial junction solar cells.
Spectral response (a) and current-voltage characteristics (b) of radial junction solar cells deposited with n-type a-Si:H layers deposited for durations of 6, 10 and 20 minutes.

In summary, despite optical measurements showing considerable light absorptance at wavelengths lower than 500 nm in radial junction solar cells (Figure 5.18), spectral response measurements indicate that few charges excited by these photons are actually being collected (Figure 5.20). Thinning the window layers through which photons are transmitted to reach the cell absorber only led to marginal improvements in spectral response (Figure 5.23-24) and these gains were offset by losses in fill factor. The results suggest that the poor carrier collection at low wavelengths does not result from optical losses within the window layers of the cell. The spectral response curves could however be interpreted as electronic losses within the material. Considering the NIP structure of the radial junction (i.e. light is incident through the n-layer of the cell), high energy light is liable to produce electron-hole pairs close to the n-i interface. This constrains short-lived holes to diffuse across the entire intrinsic layer of the cell to reach the p-layer where they can be collected. Whereas in a PIN configuration, light is incident through the p-layer and excites electron-hole pairs close to the collection point for holes. The increased recombination of holes in the case of NIP configurations would explain the low spectral response for blue light.

5. Conclusion

The primary objective of the studies presented in this chapter was to demonstrate that the performance of low-cost photovoltaics could benefit from a radial junction configuration. Compelling optical models have described the interactions of light within SiNW arrays [47] and experimental studies have fitted some of these predictions.[4, 41, 51, 52] However, disconcertingly few studies have shown light trapping in SiNWs actually improving the performance of photovoltaic cells. At the beginning of this thesis, it remained unclear whether photons were ultimately absorbed in the silicon nanowires, in remnants of the Sn catalysts or in surface states at the nanowire sidewalls. That light could be absorbed in the intrinsic layer of a solar cell deposited over the SiNWs remained an assumption until our radial junction solar cells were observed to generate higher short-circuit currents than planar a-Si:H devices deposited under the same conditions (Figure 5.17). Later, the correlation between radial junction geometry, optical absorptance and short-circuit current (Figures 5.18-19) demonstrated beyond doubt that light was being both trapped and put to good use by the radial junctions. Gradual advances in the cell design, such as shining light through the tip of the nanowires rather than through their base (Figure 5.7), or growing the nanowires straight instead of kinked (Figure 5.12), progressively reduced losses in the cell to a level at which the effect of improved light trapping could be identified. Already, in their current form, radial junctions were observed to rival the light trapping properties of commercially textured SnO_2. If electronic losses in the device can be dealt with and the geometry of the radial junctions optimized, they could broaden the prospects of light trapping in thin-film silicon solar cells, reducing the thickness of material required to absorb the solar spectrum and therefore improving the efficiency and competitiveness of this technology.

In conclusion, we have demonstrated that radial junction solar cells can be built bottom-up using low-cost materials and techniques compatible with current a-Si:H production lines to convert solar energy with an efficiency of 6%. The nanowires at the core of the radial junctions were grown by VLS using Sn catalysts to minimize the impact of metal contamination within the Si and keep the entire fabrication process at temperatures lower than 250 – 600 °C. The substrates used were glass, and all

fabrication steps, including texturing, were compatible with a one-pump-down process. The texture provided by the radial junctions was observed to trap enough light to produce short-circuit current densities of up to 13 mA/cm², coming close to what can be achieved with optimized textured substrates used in planar a-Si:H solar cells. Open-circuit voltages in the cell reached 800 mV, suggesting that contamination from the catalyst has been largely averted. By considering both performance and cost-effectiveness, we have developed a technique to make radial junction solar cells which is closely compatible with established equipment used in current a-Si:H production lines. Although these proof-of-concept devices must now be optimized to reveal their full potential, the results provide an encouraging benchmark for the capabilities of radial junction solar cells and invite further research into materializing their prospects.

Perspectives

Although the results in this chapter have provided evidence of the benefits radial junctions can offer in terms of light trapping, the ultimate goal of increasing energy conversion efficiencies in a-Si:H solar cells by reducing the thickness of their intrinsic absorber remains to be reached. In these first attempts, intrinsic a-Si:H layers with thicknesses ranging from 200 nm to 600 nm (Figure 5.17 4.2, 4.6 & 4.7) were adopted largely to avoid diode shunts in the event of sub-optimal conformal coverage. However, in recent work, our team at LPICM has obtained short-circuit currents as high as 13 mA/cm² with intrinsic layers as thin as 80 nm,[53] offering hope that the lessons learnt on these initial attempts can be transferred to thinner absorbers. One area for further improvement was that high efficiency cells were only achieved on straight SiNWs.

Further improvements in our devices could easily be gained from replacing the transparent substrates (used throughout these studies in virtue of their suitability for optical studies) with reflective ones. All the more so, considering that annealing ZnO at temperatures above 500 °C under vacuum has been shown to decrease its conductivity.[54] Also blue spectral response could foreseeably be increased by doping the nanowires n-type and adopting an NIP configuration. A more gentle deposition technique (ALD, MBE…) or better suited PECVD conditions could facilitate conformal coverage. Other flaws in our radial junction devices may require more ambitious approaches to patch. Fill factors remained lower than 60% and improvements to open-circuit voltage resulting from optimizing p-type doping saturated at values of 0.8 V. While these results compare favorably with published values for Au catalyzed radial junction solar cells,[14, 16] regaining the full 67% fill factor and 0.88 V open-circuit voltage that can be achieved with planar a-Si:H solar cells will require further investigations into the intricacies of Sn-catalyzed SiNWs. Defects in the nanowires, the interface with the absorber and the impact of the thickness of the intrinsic layer have remained largely undocumented throughout these studies. There are also further steps which can be taken towards minimizing contamination from the catalyst as Sn has been reported to form volatile hydrides when exposed to atomic H[29, 55] and might be removed entirely when exposed to a H_2 plasma following SiNW growth. An important topic for further improvement is to reduce the SiNW growth temperature. High energy conversion efficiencies were only observed on radial junction cells with straight SiNWs, which could only be formed at temperatures of 600 °C. This is regrettable as standard a-Si:H PECVD fabrication lines typically operate at temperatures lower than 300 °C. However, functioning (albeit low-efficiency) radial junction cells were fabricated at 250 °C (Figure 5.11) and

potential paths for achieving straight growth at these temperatures were identified in Chapter 4. Controlling the morphology of SiNWs using growth parameters other than temperature is a key topic for future research. In terms of optics, we have reported effects of nanowire length on light trapping; however, although we managed to gain a limited degree of control over the density of radial junctions by varying the configuration of the metal drops catalyzing their growth (Figure 5.11), preliminary results indicated only marginal gains in optical absorptance (which were largely offset by the reduced conformity of the covering layers). Controlling the self-assembly of liquid metal drops is nonetheless a topic that holds both considerable challenges and promise. Our efforts in controlling the density of In drops have recently shown results in terms of increasing short-circuit currents in radial junction cells and we expect them to continue.[53] _ENREF_16_53

When these processes have been optimized, the challenge is to build radial junction silicon cells with absorbers as thin as possible and investigate whether they do limit deterioration from the Staebler-Wronski effect. Ultimately, the greatest prospect of the technology resides in radial µc-Si:H/a-Si:H tandem structures with unprecedentedly thin absorbers. Because silicon nanowires grow in crystalline form, they also offer an exciting opportunity to deposit the bottom µc-Si:H cell epitaxially. The prospect of increased light trapping offered by the radial junctions may also reduce the delay required for µc-Si:H deposition.

BIBLIOGRAPHY

[1] R.S. Wagner, W.C. Ellis, Vapor-liquid-solid mechanism of single crystal growth, *Applied Physics Letters,* 4 (1964) 89-90, doi:10.1063/1.1753975.
[2] H. Diepers, Solar cell comprising semiconductive whiskers, US Patent 4099986, *Siemens Aktiengesellschaft,*(1978).
[3] A.A. Shchetinin, A.I. Drozhzhin, N.K. Sedykh, E.P. Novokreshchenova, Photoconverters based on silicon-crystal whiskers, *Measurement Techniques,* 21 (1978) 502-504, doi:10.1007/bf00817420.
[4] K.Q. Peng, Y. Xu, Y. Wu, Y.J. Yan, S.T. Lee, J. Zhu, Aligned single-crystalline Si nanowire arrays for photovoltaic applications, *Small,* 1 (2005) 1062-1067, doi:10.1002/smll.200500137.
[5] M. Firon, B. Drevillon, A. Fontcuberta i Morral, S. Palacin, P. Roca i Cabarrocas, Photoactive nanocomposite and method for the production thereof, US Patent 7713779, *Commissariat à l'Energie Atomique,*(2005).
[6] M. Law, L.E. Greene, J.C. Johnson, R. Saykally, P. Yang, Nanowire dye-sensitized solar cells, *Nature Materials,* 4 (2005) 455-459, doi:10.1038/nmat1387.
[7] P.-J. Alet, S. Palacin, P. Roca i Cabarrocas, B. Kalache, M. Firon, R. de Bettignies, Hybrid solar cells based on thin-film silicon and P3HT, *The European Physical Journal - Applied Physics,* 36 (2006) 231-234, doi:10.1051/epjap:2006145.
[8] C.J. Novotny, E.T. Yu, P.K.L. Yu, InP Nanowire/Polymer Hybrid Photodiode, *Nano Letters,* 8 (2008) 775-779, doi:10.1021/nl072372c.
[9] J.-S. Huang, C.-Y. Hsiao, S.-J. Syu, J.-J. Chao, C.-F. Lin, Well-aligned single-crystalline silicon nanowire hybrid solar cells on glass, *Solar Energy Materials and Solar Cells,* 93 (2009) 621-624, doi:10.1016/j.solmat.2008.12.016.
[10] A.P. Goodey, S.M. Eichfeld, K.-K. Lew, J.M. Redwing, T.E. Mallouk, Silicon Nanowire Array Photoelectrochemical Cells, *Journal of the American Chemical Society,* 129 (2007) 12344-12345, doi:10.1021/ja073125d.
[11] B.M. Kayes, H.A. Atwater, N.S. Lewis, Comparison of the device physics principles of planar and radial p-n junction nanorod solar cells, *Journal of Applied Physics,* 97 (2005) 114302, doi:10.1063/1.1901835.
[12] B.Z. Tian, X.L. Zheng, T.J. Kempa, Y. Fang, N.F. Yu, G.H. Yu, J.L. Huang, C.M. Lieber, Coaxial silicon nanowires as solar cells and nanoelectronic power sources, *Nature,* 449 (2007) 885-U888, doi:10.1038/Nature06181.
[13] E. Garnett, P.D. Yang, Light Trapping in Silicon Nanowire Solar Cells, *Nano Letters,* 10 (2010) 1082-1087, doi:10.1021/Nl100161z.
[14] M.C. Putnam, S.W. Boettcher, M.D. Kelzenberg, D.B. Turner-Evans, J.M. Spurgeon, E.L. Warren, R.M. Briggs, N.S. Lewis, H.A. Atwater, Si microwire-array solar cells, *Energy & Environmental Science,* 3 (2010) 1037-1041, doi:10.1039/c0ee00014k.
[15] M.D. Kelzenberg, D.B. Turner-Evans, B.M. Kayes, M.A. Filler, M.C. Putnam, N.S. Lewis, H.A. Atwater, Photovoltaic Measurements in Single-Nanowire Silicon Solar Cells, *Nano Letters,* 8 (2008) 710-714, doi:10.1021/nl072622p.
[16] L. Tsakalakos, J. Balch, J. Fronheiser, B.A. Korevaar, O. Sulima, J. Rand, Silicon nanowire solar cells, *Applied Physics Letters,* 91 (2007) 233117, doi:10.1063/1.2821113.
[17] T. Stelzner, M. Pietsch, G. Andra, F. Falk, E. Ose, S. Christiansen, Silicon nanowire-based solar cells, *Nanotechnology,* 19 (2008), doi:10.1088/0957-4484/19/29/295203.
[18] T.J. Kempa, B.Z. Tian, D.R. Kim, J.S. Hu, X.L. Zheng, C.M. Lieber, Single and Tandem Axial p-i-n Nanowire Photovoltaic Devices, *Nano Letters,* 8 (2008) 3456-3460, doi:10.1021/Nl8023438.
[19] V. Sivakov, G. Andra, A. Gawlik, A. Berger, J. Plentz, F. Falk, S.H. Christiansen, Silicon Nanowire-Based Solar Cells on Glass: Synthesis, Optical Properties, and Cell Parameters, *Nano Letters,* 9 (2009) 1549-1554, doi:10.1021/Nl803641f.
[20] E. Tutuc, J. Appenzeller, M.C. Reuter, S. Guha, Realization of a Linear Germanium Nanowire p−n Junction, *Nano Letters,* 6 (2006) 2070-2074, doi:10.1021/nl061338f.

[21] S. Hoffmann, J. Bauer, C. Ronning, T. Stelzner, J. Michler, C. Ballif, V. Sivakov, S.H. Christiansen, Axial p-n Junctions Realized in Silicon Nanowires by Ion Implantation, *Nano Letters,* 9 (2009) 1341-1344, doi:10.1021/nl802977m.
[22] C. Colombo, M. Heibeta, M. Gratzel, A.Fontcuberta i Morral, Gallium arsenide p-i-n radial structures for photovoltaic applications, *Applied Physics Letters,* 94 (2009) 173108, doi:10.1063/1.3125435.
[23] Y. Dong, B. Tian, T.J. Kempa, C.M. Lieber, Coaxial Group III−Nitride Nanowire Photovoltaics, *Nano Letters,* 9 (2009) 2183-2187, doi:10.1021/nl900858v.
[24] O. Gunawan, S. Guha, Characteristics of vapor–liquid–solid grown silicon nanowire solar cells, *Solar Energy Materials and Solar Cells,* 93 (2009) 1388-1393, doi:10.1016/j.solmat.2009.02.024.
[25] S. Perraud, S. Poncet, S. Noël, M. Levis, P. Faucherand, E. Rouvière, P. Thony, C. Jaussaud, R. Delsol, Full process for integrating silicon nanowire arrays into solar cells, *Solar Energy Materials and Solar Cells,* 93 (2009) 1568-1571, doi:10.1016/j.solmat.2009.04.009.
[26] J.E. Allen, E.R. Hemesath, D.E. Perea, J.L. Lensch-Falk, Z.Y. Li, F. Yin, M.H. Gass, P. Wang, A.L. Bleloch, R.E. Palmer, L.J. Lauhon, High-resolution detection of Au catalyst atoms in Si nanowires, *Nature Nanotechnology,* 3 (2008) 168-173, doi:10.1038/Nnano.2008.5.
[27] M.C. Putnam, M.A. Filler, B.M. Kayes, M.D. Kelzenberg, Y.B. Guan, N.S. Lewis, J.M. Eiler, H.A. Atwater, Secondary Ion Mass Spectrometry of Vapor-Liquid-Solid Grown, Au-Catalyzed, Si Wires, *Nano Letters,* 8 (2008) 3109-3113, doi:10.1021/Nl801234y.
[28] L. Yu, B. O'Donnell, P.J. Alet, S. Conesa-Boj, F. Peiro, J. Arbiol, P. Roca i Cabarrocas, Plasma-enhanced low temperature growth of silicon nanowires and hierarchical structures by using tin and indium catalysts, *Nanotechnology,* 20 (2009) 225604, doi:10.1088/0957-4484/20/22/225604.
[29] S.J. Rathi, B.N. Jariwala, J.D. Beach, P. Stradins, P.C. Taylor, X.J. Weng, Y. Ke, J.M. Redwing, S. Agarwal, R.T. Collins, Tin-Catalyzed Plasma-Assisted Growth of Silicon Nanowires, *Journal of Physical Chemistry C,* 115 (2011) 3833-3839, doi:10.1021/Jp1066428.
[30] V. Schmidt, J.V. Wittemann, S. Senz, U. Gosele, Silicon Nanowires: A Review on Aspects of their Growth and their Electrical Properties, *Advanced Materials,* 21 (2009) 2681-2702, doi:10.1002/adma.200803754.
[31] W.M. Bullis, Properties of gold in silicon, *Solid-State Electronics,* 9 (1966) 143-168, doi:10.1016/0038-1101(66)90085-2.
[32] Y.R. Lu, A. Lal, High-Efficiency Ordered Silicon Nano-Conical-Frustum Array Solar Cells by Self-Powered Parallel Electron Lithography, *Nano Letters,* 10 (2010) 4651-4656, doi:10.1021/nl102867o.
[33] C.E. Kendrick, H.P. Yoon, Y.A. Yuwen, G.D. Barber, H. Shen, T.E. Mallouk, E.C. Dickey, T.S. Mayer, J.M. Redwing, Radial junction silicon wire array solar cells fabricated by gold-catalyzed vapor-liquid-solid growth, *Applied Physics Letters,* 97 (2010) 143108, doi:10.1063/1.3496044.
[34] Y. Wang, V. Schmidt, S. Senz, U. Gosele, Epitaxial growth of silicon nanowires using an aluminium catalyst, *Nat Nano,* 1 (2006) 186-189, doi:10.1038/nnano.2006.133.
[35] L. Yu, B. O'Donnell, J.L. Maurice, P. Roca i Cabarrocas, Core-shell structure and unique faceting of Sn-catalyzed silicon nanowires, *Applied Physics Letters,* 97 (2010), doi:10.1063/1.3464557.
[36] L. Yu, F. Fortuna, B. O'Donnell, G. Patriache, P. Roca i Cabarrocas, Stability and evolution of low-surface-tension metal catalyzed growth of silicon nanowires, *Applied Physics Letters,* 98 (2011), doi:10.1063/1.3569817.
[37] L. Yu, B. O'Donnell, P.-J. Alet, P. Roca i Cabarrocas, All-in-situ fabrication and characterization of silicon nanowires on TCO/glass substrates for photovoltaic application, *Solar Energy Materials and Solar Cells,* 94 (2010) 1855-1859, doi:10.1016/j.solmat.2010.06.021.
[38] C.C. Tsai, G.B. Anderson, R. Thompson, B. Wacker, Control of silicon network structure in plasma deposition, *Journal of Non-Crystalline Solids,* 114, Part 1 (1989) 151-153, doi:10.1016/0022-3093(89)90096-3.
[39] A. Matsuda, Microcrystalline silicon. Growth and device application, *Journal of Non-Crystalline Solids,* 338 (2004) 1-12, doi:10.1016/j.jnoncrysol.2004.02.012.

[40] A. Fontcuberta i Morral, P. Roca i Cabarrocas, Etching and hydrogen diffusion mechanisms during a hydrogen plasma treatment of silicon thin films, *Journal of Non-Crystalline Solids,* 299–302, Part 1 (2002) 196-200, doi:10.1016/s0022-3093(01)01001-8.
[41] O.L. Muskens, J.G. Rivas, R.E. Algra, E.P.A.M. Bakkers, A. Lagendijk, Design of light scattering in nanowire materials for photovoltaic applications, *Nano Letters,* 8 (2008) 2638-2642, doi:10.1021/Nl0808076.
[42] S. Benagli, D. Borrello, E. Vallat-Sauvain, J. Meier, U. Kroll, J. Hötzel, J. Spitznagel, J. Steinhauser, L. Castens, Y. Djeridane, High-efficiency amorphous silicon devices on LPCVD-ZNO TCO prepared in industrial KAI-M R&D reactor, *24th European Photovoltaic Solar Energy Conference*, Hamburg, 2009, pp. 2293 - 2298, doi:10.4229/24thEUPVSEC2009-3BO.9.3.
[43] R.A. Street, Doping and the Fermi Energy in Amorphous Silicon, *Physical Review Letters,* 49 (1982) 1187-1190, doi:10.1103/PhysRevLett.49.1187.
[44] M.A. Green, K. Emery, Y. Hishikawa, W. Warta, E.D. Dunlop, Solar cell efficiency tables (version 39), *Progress in Photovoltaics: Research and Applications,* 20 (2012) 12-20, doi:10.1002/pip.2163.
[45] E. Johnson, K.-H. Kim, P.Roca i Cabarrocas, In-Situ Observation of High Deposition Rate Hydrogenated Polymorphous Silicon Cell Degradation through Variable Intensity Method Measurements, *MRS Proceedings,* 1153 (2009), doi:10.1557/PROC-1153-A07-09
[46] M. Wolf, H. Rauschenbach, Series resistance effects on solar cell measurements, *Advanced Energy Conversion,* 3 (1963) 455-479, doi:10.1016/0365-1789(63)90063-8.
[47] L. Hu, G. Chen, Analysis of optical absorption in silicon nanowire Arrays for photovoltaic applications, *Nano Letters,* 7 (2007) 3249-3252, doi:10.1021/Nl071018b.
[48] V. Schmidt, S. Senz, U. Gösele, Diameter dependence of the growth velocity of silicon nanowires synthesized via the vapor-liquid-solid mechanism, *Physical Review B,* 75 (2007) 045335, doi:10.1103/PhysRevB.75.045335.
[49] J.B. Hannon, S. Kodambaka, F.M. Ross, R.M. Tromp, The influence of the surface migration of gold on the growth of silicon nanowires, *Nature,* 440 (2006) 69-71, doi:10.1038/Nature04574.
[50] J. Takada, M. Yamaguchi, N. Fukada, K. Nishimura, Y. Tawada, Thermal-Degradation of a-Si-H Solar-Cells by Dopant Diffusion, *Japanese Journal of Applied Physics Part 1-Regular Papers Short Notes & Review Papers,* 26 (1987) 889-892, doi:10.1143/JJAP.26.889.
[51] R.A. Street, W.S. Wong, C. Paulson, Analytic model for diffuse reflectivity of silicon nanowire mats, *Nano Letters,* 9 (2009) 3494-3497, doi:10.1021/Nl901683y.
[52] L. Tsakalakos, J. Balch, J. Fronheiser, M.Y. Shih, S.F. LeBoeuf, M. Pietrzykowski, P.J. Codella, B.A. Korevaar, O. Sulima, J. Rand, A. Davuluru, U. Rapol, Strong broadband optical absorption in silicon nanowire films, *Journal of Nanophotonics,* 1 (2007), doi:10.1117/1.2768999.
[53] L. Yu, B. O'Donnell, M. Foldyna, P. Roca i Cabarrocas, Radial junction amorphous silicon solar cells on PECVD-grown silicon nanowires, *Nanotechnology,* 23 (2012) 194011, doi:10.1088/0957-4484/23/19/194011.
[54] C. Charpentier, P. Prod'Homme, L. Francke, P. Roca i Cabarrocas, Microstructural, Optical and Electrical Properties Of Post-Annealed ZnO:Al Thin Films., *MRS Proceedings,* 1394 (2012), doi:10.1557/opl.2012.258.
[55] M.M.J.W. van Herpen, D.J.W. Klunder, W.A. Soer, R. Moors, V. Banine, Sn etching with hydrogen radicals to clean EUV optics, *Chemical Physics Letters,* 484 (2010) 197-199, doi:10.1016/j.cplett.2009.11.030.

Conclusion

Throughout this thesis, we have explored the prospects of radial junction solar cells to trap light and reduce the thickness of the absorber layer in low-cost a-Si:H and µc-Si:H based photovoltaics. To date, the majority of VLS-grown silicon radial junction solar cells have been fabricated using gold catalysts, which are known to introduce effective recombination levels in the Si bandgap. As these devices have systematically suffered from considerable electronic losses, we have developed techniques to replace the catalysts with post-transition metals.

Sn, In, Bi, Ga and Al were singled out as promising VLS catalysts in virtue of the comparatively shallow energy levels which they introduce in the Si bandgap, their low eutectic points with Si, and their abundance. We have presented a compendium of recent reports on the suitability of post-transition metals for VLS and argued against the precepts that the Si solubility and surface tension of a metal may determine its ability to catalyze stable nanowire growth. This literature overview brings out one striking point which most post-transition metal catalysts have in common. They require a reactive environment, most commonly a plasma, to catalyze VLS growth. Several possible contributions of the plasma have been identified. We have drawn attention to its capacity to reduce the oxide layer which forms at the surface of post-transition metals, facilitating Si incorporation into the catalyst and nanowire growth. Its impact on the nanowire growth rate was assessed in light of the increased chemical potential it confers to the gas species during VLS growth. Most importantly, it assists the VLS growth process in breaking down the gas species. We advance that this is of capital importance for growing SiNWs with post-transition metals given that their d and s electronic subshells are full, making it less likely for the feed species to adsorb and dissociate on their surface. The only notable exception is Al, which catalyzes SiNW growth under CVD conditions in spite of complete d and s subshells, inviting further research on this topic.

We pursued attempts to form liquid drops of Sn and In to catalyze the growth of our SiNWs. To keep all fabrication steps of the radial junction solar cells in line with a one-pump-down process, we studied approaches to control the configuration of the metal drops by self-assembly. Their diameter and density were observed to vary primarily according to the amount of metal provided, the temperature at which they were exposed to a hydrogen plasma, and the nature of the substrate on which they formed. Although it was possible to control the size and spacing of In drops formed over ZnO substrates, the prospect of optimization at diameters much lower than 100 nm remained elusive. We also failed to decorrelate the density of drops in each configuration from their diameter. However smaller diameter Sn drops were obtained by evaporating films of Sn on glass/ZnO substrates and reducing the surface of glass/SnO_2. These samples provided us with the substrates needed for our work on Sn-catalyzed nanowire growth and radial junction solar cells.

Studies on the growth of Sn-catalyzed SiNWs revealed that the nanowire growth rate could be enhanced by increasing the silane pressure and plasma power, and optimizing the H_2 dilution during the PAVLS growth process. Surprisingly, heating the substrate was not observed to affect the growth rate although it did improve the crystal structure of the nanowires. At nominal temperatures in excess of 600 °C, Sn and In-catalyzed SiNWs were observed to develop crystalline facets over their

sidewalls. The presence of facets was linked to the diameter of the Sn catalysts following observations of VLS growth reverting from faceted to cylindrical growth as the nanowire tapered. The density of nanowires proved substantially lower than that of Sn drops initially reduced at the sample surface, suggesting that the Sn drops are either buried or redistribute when exposed to silicon. Another practical obstacle was that the Sn-catalyzed silicon nanowires were only observed to grow straight at nominal substrate temperatures of 600 °C. This calls for further optimization of the nanowire growth conditions to achieve similar results at temperatures closer to the eutectic.

Incorporating these SiNWs into radial junction solar cells presented several challenges. The plasma conditions of the layers covering them were adapted to avoid high atomic hydrogen concentrations liable to damage the nanowire array. Conformal coverage of their abrupt surface made it necessary to increase the growth temperature of the VLS process to a nominal value of 600 °C in order to obtain straight and separate nanowires. Controlling the concentration of TMB within the silane plasma during nanowire growth was instrumental in achieving adequate doping in the materials. The length of the radial junctions was optimized to reach a compromise between conformal coverage and light trapping within the device. We also adapted the substrate used, the direction of light incidence within the cell, and the thickness of the window layers. These advances led to the fabrication of radial junction solar cells with energy conversion efficiencies of 6%. The devices demonstrated that a PIN junction could be formed by plasma deposition over the highly textured surfaces presented by SiNWs. It also proved that light trapping in these structures can produce short-circuit current densities of up to 13 mA/cm² on solar cells with 3.1 mm² areas. These results were shown to exceed the performance of planar a-Si:H devices deposited under the same conditions, and came close to that of optimally textured SnO_2 substrates. We have presented evidence that the light trapped by the radial junctions contributes to the photovoltaic effect by comparing measurements of the optical absorptance and short-circuit current of devices grown with progressively longer nanowires. Open-circuit voltages in the cell of 800 mV and fill factors close to 60% suggest that contamination from the catalyst was largely averted in these devices compared to literature reports on SiNW radial junction cells catalyzed with Au. Their fabrication process is also largely compatible with established PECVD equipment used in a-Si:H production lines and a one-pump-down process.

Radial junction solar cells in general – and our devices in particular – have come a long way over the past four years and yet we have only begun to scratch the surface of this technology. This is a good thing. With each new understanding come technological improvements and a windfall of interesting scientific questions. While much work remains to understand the intricacies of these devices and benefit from their full potential, the results in this thesis have shown that radial junction cells can be made by PECVD and provide an encouraging milestone in the development of this technology.

APPENDIX: MEASURED AND NOMINAL TEMPERATURE

It has been mentioned in Chapter 4 that the actual substrate temperature in the Plasfil reactor is foreseeably lower than the nominal value measured at the heater. Recent experimental evidence has emerged that this difference can be substantial.

A thermocouple was introduced into the Plasfil reactor and placed at the surface of glass, n-type crystalline silicon and Kapton substrate. The reactor was in each case placed under vacuum and progressively heated to 650 °C (nominal temperature) under H_2 gas pressures of 260 and 1000 mTorr. The gas pressure and substrates used were designed to replicate experimental conditions during SiNW growth.

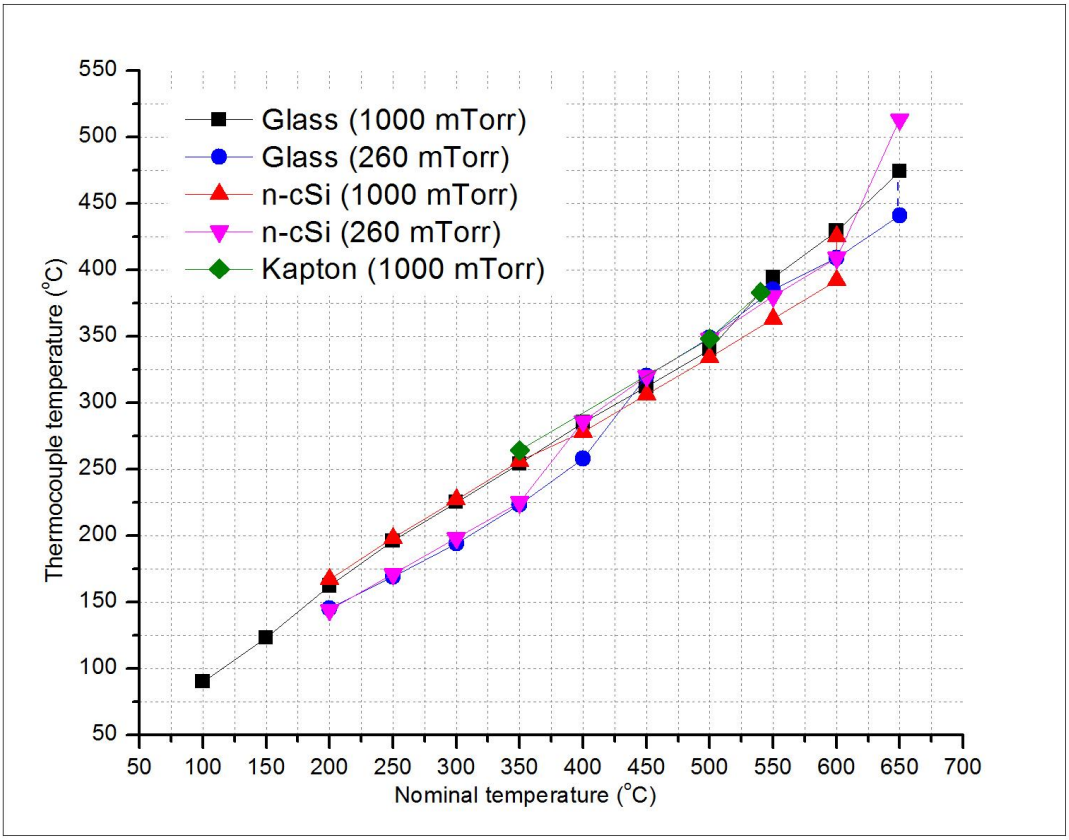

Appendix: Nominal temperature of the substrate heater in the Plasfil reactor as a function of the temperature measured using an in-situ thermocouple.

The temperature measured by the thermocouple was systematically lower than the nominal temperature of the heater, with discrepancies reaching 175 °C at the higher temperatures used in the previous studies during SiNW growth. As a consequence, the standard temperature required for straight SiNW growth in Chapters 4 and 5 lies in fact between 400 and 425 °C, rather than 600 °C.

This observation affects two of the conclusions drawn in these studies. First, as the highest temperatures achievable in the reactor are too low to thermally dissociate silane and, we have no

1. J. Westwater, D.p. Gosain, K. Yamauchi, S. Usui, Nanoscale silicon whiskers formed by silane/gold reaction at 335 °C, Materials Letters, 24 (1995) 109-112, doi:10.1016/0167-577x(95)00091-7

direct evidence that post-transition metals are incapable of catalyzing the growth of SiNWs under standard (thermally activated) CVD conditions. However we can still conclude that they do not catalytically favor the reaction in the way that Au has been observed to[1] as the growth temperatures studied remain considerably higher than the eutectic points of the Sn-Si, In-Si and Bi-Si systems).

The second point is that straight SiNWs and the entire fabrication process for our higher efficiency solar cells can be performed at temperatures lower than 425 °C. This is of interest from an industrial perspective as it falls within the higher range of plasma reactors currently used in thin-film fabrication lines.

LIST OF PUBLICATIONS

L. Yu, B. O'Donnell, P.J. Alet, S. Conesa-Boj, F. Peiro, J. Arbiol, P. Roca i Cabarrocas, "Plasma-enhanced low temperature growth of silicon nanowires and hierarchical structures by using tin and indium catalysts" *Nanotechnology*, 20 (2009) 225604.

I. Ngo, B. O'Donnell, J. Alvarez, M. Gueunier-Farret, J.-P. Kleider, L. Yu, P. Roca i Cabarrocas, "Catalyst formation and growth of Sn- and In-catalyzed silicon nanowires" *MRS Conference Proceedings* (2010).

L. Yu, B. O'Donnell, P.J. Alet, P. Roca i Cabarrocas, "All-in-situ fabrication and characterization of silicon nanowires on TCO/glass substrates for photovoltaic application" *Solar Energy Materials and Solar Cells*, 94 (2010) 1855-1859.

L. Yu, B. O'Donnell, J.L. Maurice, P.Roca i Cabarrocas, "Core-shell structure and unique faceting of Sn-catalyzed silicon nanowires", *Appled Physics Letters*, 97 (2010).

L. Yu, W. Chen, B. O'Donnell, G. Patriarche, S. Bouchoule, P. Pareige, R. Rogel, A.C. Salaun, L. Pichon, P. Roca i Cabarrocas, "Growth-in-place deployment of in-plane silicon nanowires", *Appled Physics Letters*, 99 (2011) 203104-203103.

L. Yu, F. Fortuna, B. O'Donnell, G. Patriache, P. Roca i Cabarrocas, "Stability and evolution of low-surface-tension metal catalyzed growth of silicon nanowires", *Applied Physics Letters*, 98 (2011).

J. Cho, B. O'Donnell, L. Yu, K.-H. Kim, I. Ngo, P. Roca i Cabarrocas, "Sn-catalyzed silicon nanowire solar cells with 4.9% efficiency grown on glass", *Progress in Photovoltaics: Research and Applications* (2012).

B. O'Donnell, L. Yu, M. Foldyna, P. Roca i Cabarrocas, "Silicon nanowire solar cells grown by PECVD", *Journal of Non-Crystalline Solids* (2012).

L. Yu, F. Fortuna, B. O'Donnell, T. Jeon, M. Foldyna, G. Picardi, P. Roca i Cabarrocas, "Bismuth-Catalyzed and Doped Silicon Nanowires for One-Pump-Down Fabrication of Radial Junction Solar Cells", *Nano Letters* 12 (2012) 4153-4158.

L. Yu, B. O'Donnell, M. Foldyna, P. Roca i Cabarrocas, "Radial junction amorphous silicon solar cells on PECVD-grown silicon nanowires", *Nanotechnology* 23 (2012) 194011.

M. Foldyna, L. Yu, B. O'Donnell, P. Roca i Cabarrocas, "Optical absorption in vertical silicon nanowires for solar cell applications" *Proceedings of the SPIE* pp. 811110 (2011)

L. Yu, M. Foldyna, B. O'Donnell, G. Picardi, P. Roca i Cabarrocas, "Building radial junction thin-film solar cells on silicon nanowires", *SPIE Newsroom* (2012).

ACKNOWLEDGEMENTS

None of these solar cells would have seen the light without the priceless guidance and help from my coworkers, mentors and friends. I am very much indebted to my laboratory for its unwavering support and trust over the years, in particular to Linwei Yu and Pere Roca i Cabarrocas who were with me on each step of the way and to Jinyoun Cho, my old brother in arms and partner in crime. My deepest gratitude goes to Jimmy Kim, Romain Pangu, Laurent Kroely, Emmanuel Thefurber, Fulvio Michelis, Sergei Abolmasov and Marty Brown for their relentless patience in alleviating my ignorance and making me smile. I would also like to thank Gary Rose, Fred Farci, Jérôme Charliac, Cyril Jadaud, Fred Liège and Eric Paillassa who turned myriads of the everyday problems we encountered into opportunities. The work in this thesis was invigorated by the bright young minds I had the pleasure of working with. Thank you very much to Irène Ngo, Lamia Ammoura, Hakim Arezki, Mun-Ho Song, and to Soumyadeep Misra who is now bearing the nanowire torch. My thanks also to Thierry Gacoin, Anna Fontcuberta i Morral, Jean-Paul Kleider and David Queré for their council and help on the numerous occasions we outstepped the boundaries of our own expertise. I would also like to express my gratitude to my sponsors at Total S.A, in particular to Loïc Frank and Marc Vermeersch, and to the French National Center for Scientific Research for the support and independence they gave me throughout my research.

It has been a privilege to work at the LPICM in the company of such decent people and sharp minds. I treasure memories of the calm kindness of Parsathi Chatterjee, Holger Vach, Antonello Martino, Fatima Bouanis, Rachida Boubekri, Poncho Torres Rios and Junzhuan Wang; of the efficiency and almost maternal amenity of Laurence Corbel, Chantale Geneste and Carine Roger-Roulling; of the cynical pragmatism of Pavel Bulkin, Sergei Abolmasov, Alexei Abramov and Dimitri Daineka (curiously balanced by the cheerfulness of Tatiana Novikova); of the heated nanowire debates with Costel Cojocaru, Rym Boukhicha and Martin Foldyna; of the cosmopolitan flair of Ka-Hyun Kim, Kihwan Kim, Chang Seok Lee, Jinyoun Cho, Taewoo Jeon, Chang-Hyun Kim, Younho Heo Park, Mun-Ho Song and Taeha Hwang; of the sense of ephemeral but deeply rooted community I shared with Paz Carreras, Rohit Prasana, Yassine Djeridane, Pierre-Jean Alet, Ken Ogata, Boris Morel, Louis Gorintin, Wilfried Favre, Djicknoum Diouf, José Alvarez and Peiqing Yu; of the warm and now familiar handshake of Razvigor Ossikovski, Enric Garcia-Caurel, Mario Moreno, Marc Chatelet, Bicher Haj Ibrahim, Maher Oudwan, Jacqueline Tran, Anirban Dhar, Laurent Baraton, Dennis Tondelier, Jean-Eric Bourrée, Yvan Bonnassieux and Veinardi Suendo; and of the random and priceless fous rires with Stefano Granata, Erik Johnson, Clément Fallet, Elisabeth Warren, Ana Klimovic, Paul Finger, Omid Yaghmazadeh and Marc Chaigneau.

I owe this opportunity to my family, who have supported me in everything I have done, to David Eeckhout, Olivier Moerens and Thierry Camus, who patiently taught me to enjoy learning, to Ian Howarth, Pierre Seneor and Sara Ducci, who patiently guided me through university, and to Bernard Drévillon who hired me and has patiently dealt with the choice since. Last, I would like to thank the people who made these past four years worthwhile beyond the confines of science. Thank you Elise Warcoin for sheltering me throughout the storm. Thanks Pierre Jouy, Chip Nguyen, Pepiniello Martino, Patosh Bouchon and Charlie Cayron for the DQN community. Thanks Hélène Besson, André Chanbubu, Sami Ellouze, Math Warcoin, Olive Chedru and Ptinico Morin for the beer, laughter and zombies that have been my home these past two years. Thanks Nico Guénot, Stéphane Zimmerman, Doc Caputo and Céline Guénot for France – it's simply gorgeous. And thanks Vicky McGroon, Hyeok Kim, Zin Nam, Bastien Michel, Kenjij Hirata, Songzhe Han, Zixian Jiang, Tie Cheng and Willem Rischau for the friendship and delightful chaos you weaved into our lives.

COLOR CODE

For clarity, the frames of figures throughout this thesis have been color coded in order to identify the reactor and the substrates used in each experiment. This information is also detailed in the figure captions however the color code provides an additional indicator when comparing samples.

The color of the outer frame of each figure and each table designates the reactor used to make the sample. **Green is used for the ARCAM reactor, Orange is used for the Plasfil reactor and Blue is used for the Nextral reactor** (only used in one study).

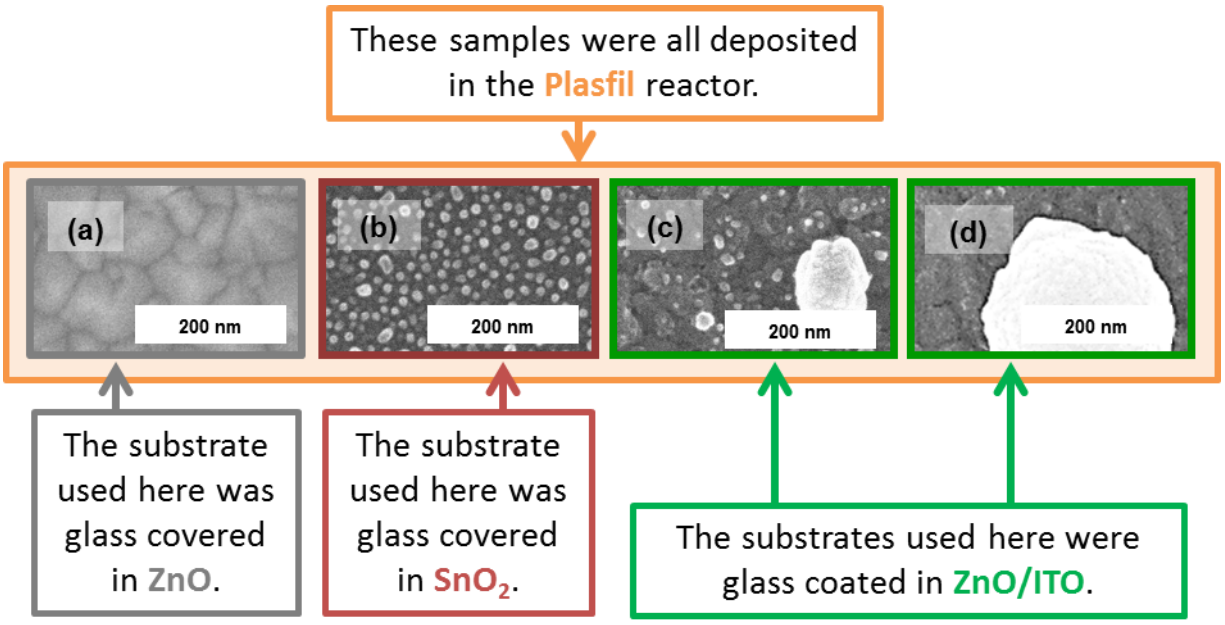

For each SEM micrograph, the frame of the image indicates the substrate used. **Burgundy Red designates Glass/SnO_2 substrate, Orange designates Glass/ZnO/Sn(1 nm) substrate, Blue designates Glass/ITO substrate (or cSi/ITO substrate), Green designates Glass/ZnO/ITO substrate, Purple designates Glass/Sn, or cSi/Sn, Black designates ZnO/Bi (evaporated), Grey designates ZnO with no nanowire catalysts.**

The color surrounding the scale bar inside SEM images relates to the conditions of that particular sample with respect to the graph next to it (for instance if the data points corresponding to sample A are red, the SEM image of sample A will have a red bordered scale bar)

.

ABSTRACT

In this thesis, disordered arrays of vertical silicon nanowires are used to trap light in a novel structure for PECVD-deposited silicon solar cells. The abrupt surface of these structures can absorb light efficiently and be manufactured in the same vacuum run as the other layers of the cell, offering the prospect of dispensing with the additional fabrication steps conventionally required to texture the substrates of thin-film photovoltaics. Drops of liquid tin and indium, designed to catalyze the growth of silicon nanowires, were deposited and arranged by self-assembly techniques on transparent conducting oxide substrates under vacuum to obtain metal drop configurations with diameters and densities spanning several orders of magnitude. In discussing the suitability of different metals to catalyze the growth of silicon nanowires, we have highlighted distinctions between the behavior of transition and post-transition metals for vapor-liquid-solid growth and studied in particular the case of silicon nanowires catalyzed by tin. Nanowires doped P-type were grown in disordered arrays designed to trap light and covered in conformal layers of intrinsic and N-type hydrogenated amorphous silicon, and an indium-tin-oxide electrical contact to produce networks of 10 million radial PIN junctions connected over areas of 3.1 mm². These cells were deposited over untextured substrates using techniques which are compatible with a single pump-down process. Optimizing their fabrication process led to open-circuit voltages of 0.8 V, short-circuit currents of 13 mA/cm² and energy conversion efficiencies of 6%, rivalling that of planar PIN structures deposited with established texturing techniques and setting a new record for this technology.

Keywords: silicon nanowire, photovoltaics, PECVD, tin, indium, radial junction, post-transition metals.

RESUME

Cette thèse présente une structure novatrice de cellules solaires déposées par plasma qui permet de piéger la lumière au moyen d'un réseau de nanofils de silicium. Ces structures ouvrent de nouvelles perspectives pour augmenter l'efficacité de conversion énergétique et permettent de contourner les étapes de texturation du substrat typiquement requises lors de la fabrication de cellules solaires en couches minces de silicium. Les gouttes d'étain et d'indium servant à catalyser la croissance des nanofils ont été extraites de couches d'oxydes transparents conducteurs par un plasma d'hydrogène et agencées sous vide pour obtenir des diamètres et des densités couvrant plusieurs ordres de grandeur. Plusieurs anomalies liées à la croissance de nanofils de silicium catalysée par des gouttes d'étain ont été recensées pour étudier les subtilités du mécanisme de croissance Vapeur-Liquide-Solide. Nous identifions notamment des différences fondamentales entre l'effet catalytique de métaux ayant des orbitales électronique d incomplètes (Au, Pt, Cu,…) et remplies (Sn, In, Ga, Bi,…). Des réseaux de nanofils dopés de type P ont ensuite été recouverts de façon conforme par des couches de silicium amorphe hydrogéné intrinsèque et dopés de type N, ainsi que d'un contact électrique d'oxyde d'indium dopé à l'étain pour former des réseaux de 10 millions de jonctions PIN radiales couvrant des surfaces de 3,1 mm². Ces cellules ont été déposées entièrement par des méthodes de fabrication sous vide sur des substrats non texturés. Leur optimisation a mené à des tensions à circuit ouvert de 0,8 V, des courants de court-circuit de 13 mA/cm² et des efficacités de conversion énergétiques de 6%, rivalisant avec des cellules planaires texturées par des méthodes établies et marquant un nouveau record pour cette technologie.

Mots clés : nanofil de silicium, photovoltaïque, PECVD, étain, indium, jonction radiale, catalyse.